University of New Mexico
UNM Digital Repository

Earth and Planetary Sciences ETDs | Electronic Theses and Dissertations

Summer 7-13-2022

Single-crystal elasticity of clinopyroxenes and the viscosity of kimberlite magma under high pressure-temperature conditions

Ming Hao
University of New Mexico - Main Campus

Follow this and additional works at: https://digitalrepository.unm.edu/eps_etds

 Part of the Geology Commons, and the Mineral Physics Commons

Recommended Citation

Hao, Ming. "Single-crystal elasticity of clinopyroxenes and the viscosity of kimberlite magma under high pressure-temperature conditions." (2022). https://digitalrepository.unm.edu/eps_etds/327

This Dissertation is brought to you for free and open access by the Electronic Theses and Dissertations at UNM Digital Repository. It has been accepted for inclusion in Earth and Planetary Sciences ETDs by an authorized administrator of UNM Digital Repository. For more information, please contact disc@unm.edu.

Ming Hao

Candidate

Department of Earth and Planetary Sciences

Department

This dissertation is approved, and it is acceptable in quality and form for publication:

Approved by the Dissertation Committee:

Jin Zhang , Chairperson

Brandon Schmandt

Adrian Brearley

Przemek Dera

Joshua P Townsend

Single-crystal elasticity of clinopyroxenes and the viscosity of kimberlite magma under high pressure-temperature conditions

BY

Ming Hao

B.S., Geology, Peking University, 2017

DISSERTATION

Submitted in Partial Fulfillment of the

Requirements for the Degree of

Doctor of Philosophy

Earth and Planetary Sciences

The University of New Mexico

Albuquerque, New Mexico

August, 2022

ACKNOWLEDGMENTS

I heartily acknowledge Dr. Jin Zhang, my advisor and dissertation chair, for all the help and guidance in the past five years. Jin is a really nice and supportive person, who is not only my guide in the field of mineral physics, but also the mentor of my life. I would like to express my sincere gratitude to Jin for her instruction about the experimental and communication skills during my entire Ph.D. study. I would like to thank Jin for spending her time with me to help clarify my confusion of my Ph.D. research goals as well as the future directions of my life path.

I also would like to thank all the faculties, staffs, and friends in and out of the department and institute, in particular, my committee members, Dr. Brandon Schmandt, Dr. Adrian Brearley, Dr. Joshua P. Townsend, and Dr. Przemek Dera, for their valuable suggestions and encouragement throughout my entire Ph.D. study. In particular, I would like to say special thanks to two people: Brandon, who is my second advisor and has introduced the giant world of seismology to me and Przemek for his help of X-ray diffraction experiments and the last-minute acceptance of the request to serve on my committee.

In addition, I would like to thank Dr. Dongzhou Zhang, Dr. Rostislav Hrubiak, Dr. Curtis Kenney-Benson, Dr. Sergey Tkachev, and Dr. Vitali Prakapenka for their enormous amount of support and help for the synchrotron experiments carried out at Advanced Photon Source (in particular duing the pandemic!), which are essential for the completion of my Ph.D. dissertation. Many thanks to Mike Spilde, and Dr. Sergey Tkachev for their help with Electron Microprobe Analysis experiments and gas loading of the diamond anvil cells. Thanks to Caroline Pierotti for her help with sample preparation, Dr. Mingqiang Hou for his help of loading Paris-Edinburgh cell, Zhiyuan Ren for his help with the Brillouin and synchrotron

experiments. I also want to thank Dr. Peter Olson who shared his knowledge with me on various geodynamic problems, and Dr. Qin Wang for her generous help with the omphacite project.

I would like to express my special gratitude to Wen-Yi Zhou, who is both my important science collaborator and fiancée. Thank you for the support and encouragement for my research and life. And finally, to my mom and dad, without your love and support, I cannot go through all the difficulties and get here.

Single-crystal elasticity of clinopyroxenes and the viscosity of kimberlite magma under high pressure-temperature conditions

by

Ming Hao

B.S., Geology, Peking University, 2017

Ph.D., Earth and Planetary Sciences, the University of New Mexico, 2022

ABSTRACT

Clinopyroxene is not only an important mineral phase in the pyrolitic upper mantle, but also one of the dominated mineral phases in the subducted or delaminated eclogitic materials in the deep Earth. Identifying and locating these eclogitic materials requires the knowledge of the thermoelastic properties of clinopyroxene under high pressure-temperature conditions. In this dissertation, we have measured the single-crystal elastic properties of jadeite and omphacite, which are major clinopyroxene phases in the eclogitic materials, up to 18 GPa 700 K by Brillouin spectroscopy and utilized these data to identify the eclogitic heterogeneities in the mantle.

We also measured the viscosity of kimberlite magma, which carries eclogite xenoliths, diamonds, and other deep mantle phases to the Earth's surface through an ultra-fast eruption trajectory. We found the viscosity of volatile-rich kimberlite magma is extremely low under high pressure-temperature conditions and utilized these data to model the kimberlite magma ascent and eruption process.

TABLE OF CONTENTS

LIST OF TABLES

LIST OF FIGURES

Chapter I

Introduction

1. The single-crystal elastic properties of clinopyroxene

Clinopyroxene with chemical formula $(Ca,Na)(Mg,Al,Fe)(Si,Al)_2O_6$ is one of the major mineral phases in the Earth's upper mantle (e.g., Anderson & Bass, 1986; Bass & Anderson, 1984; Ringwood, 1975). As shown in figure I.1, the classic upper mantle model rock pyrolite, which was developed based on the melting relationships between mafic-ultramafic rocks, contains 10-30 vol% clinopyroxene in the shallower part of the mantle, which gradually dissolves into majoritic garnet from 300 km to 500 km depth (Ringwood, 1975; Irifune et al., 1986; Mainprice, 2015). To constrain the seismic properties of the Earth's upper mantle (e.g., density and anisotropic seismic velocities), it is important to understand the single-crystal elasticity of clinopyroxene.

Various seismic observations have suggested that the Earth's upper mantle is heterogeneous both laterally and vertically (e.g., Schmandt & Humphreys, 2010; French & Romanowicz, 2014; Ritsema et al., 2011). Subduction and delamination are the two important geological processes that can bring the oceanic or continental crustal materials to the deep Earth and contribute to the observed seismic heterogeneity (Kay & Kay, 1993; Schmandt & Humphreys, 2010). For example, many of the fast seismic anomalies under north America are potentially related to the subduction of Farallon plate (Schmandt & Humphreys, 2010). Levander et al. (2011) also identified a teardrop-shaped seismic anomaly with up to 3% higher Vp under Colorado Plateau, which are likely caused by the lithosphere delamination. In addition to these seismic observations, the trace element and isotope data of mantle xenoliths

and oceanic island basalts also suggest subduction and delamination contributes to the enriched geochemical reservoirs (Hofmann, 1997; Chauvel et al., 1992). For example, the enriched mantle 1 (EM-1), which shows low $^{206}Pb/^{204}Pb$ and high $^{208}Pb/^{206}Pb$ values, is related with the recycled ancient sediments; the enriched mantle 2 (EM-2) with high $^{207}Pb/^{204}Pb$ and low Nb/U

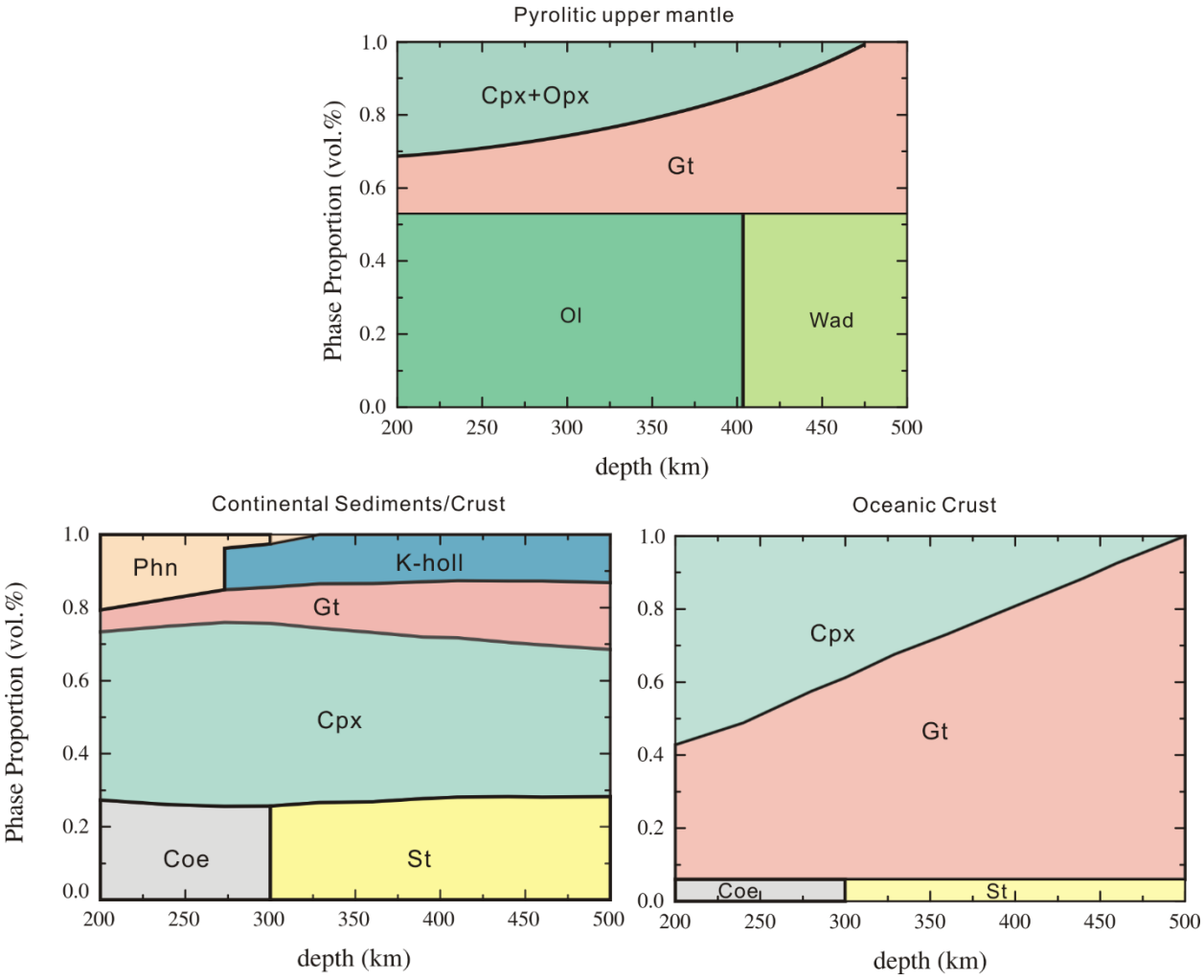

Figure I.1. Phase diagrams of the pyrolitic upper mantle (Ringwood, 1975; Irifune et al., 1986; Mainprice, 2015), subducted continental crusts (Wu et al., 2009), and oceanic crust (Aoki & Takahashi, 2004). (Cpx: clinopyroxene; Opx: orthopyroxene; Gt: garnet; Ol: olivine; Wad: wadsleyite; Phn: phengite; K-holl: K-hollandite; Coe: coesite; St: stishovite)

represents the subducted oceanic crust. Those enriched mantle sources are the important reservoirs for the incompatible elements (e.g., REE) and heat-generation elements (e.g., U, Th, and K). Thus, identification of those heterogeneities in the Earth's mantle is necessary for us to understand these geophysical and geochemical observations.

Subducted slabs have layered structures, which usually include a 7-10 km thick basaltic crust possibly with a thin sedimentary layer on top of it. The basaltic slab crust transforms into denser eclogite at depth > ~60 km (Ahrens & Schubert, 1975), which provides important driving force for subduction. As shown in the figure I.1, the Na,Al-bearing clinopyroxene (omphacite) composes more than 60 vol% of eclogite at the uppermost mantle and gradually transforms into majoritic garnet (Aoki & Takahashi, 2004). Due to the sluggish kinetics of omphacite to majorite transition and the cold geotherms in the subduction zones, omphacite is likely to exist down to depths greater than 500 km (Van Mierlo et al., 2013; Nishi et al., 2013). In addition to the slab crust, the felsic continental sediments or subducted continental crust will also transform to eclogitic materials in the upper mantle (figure I.1; Wu et al., 2009; Irifune et al., 1994). Because of the high Na_2O content (~2.7-5.6 wt%; Wu et al., 2009; Rudnick & Fountain, 1995), the clinopyroxene in the subducted continental sediments/crust is close to pure jadeite ($NaAlSi_2O_6$). Different from the clinopyroxenes in the pyrolitic upper mantle and subducted oceanic crust, the jadeite in the continental sediments/crust is the dominated phase throughout the entire upper mantle (40-50 vol%) and remains stable down to the mantle transition zone (~410-660 km depth; Wu et al., 2009; Irifune et al., 1994). Therefore, the elastic properties of clinopyroxenes, such as omphacite and jadeite at high pressure-temperature conditions, are necessary to understand the seismic properties and observations of the subducted eclogitic materials in the Earth's upper mantle.

Delamination, which contributes to the mantle convection and geochemical heterogeneities, is also an important process in the Earth's upper mantle (Bird, 1979; Kay & Kay, 1993). During the delamination process, the basaltic or andesitic lower continental crust may transform into denser eclogitic materials at high pressure-temperature conditions. When the gravitationally unstable lower continental crust interacted with the mantle flow in the subduction zone mantle wedge or in the asthenosphere, the eclogitic materials will be peeled off and sink into the Earth's upper mantle (Kay & Kay, 1993). Considering clinopyroxenes are among the major mineral phases in the eclogitic materials, the single-crystal elastic properties of clinopyroxenes under the high pressure-temperature conditions help us constrain the seismic properties of the delaminated continental lower crust and further help locate them.

In this dissertation, we are interested in the densities of various clinopyroxenes in the mantle. The high pressure-temperature thermal equations of state (EOS) of different clinopyroxenes are still not well constrained partially due to the low crystal symmetry. Most of the previous EOS measurements of clinopyroxene are conducted at high-pressure and room-temperature conditions. For example, the most recent EOS study of clinopyroxene is the single-crystal X-ray diffraction experiments on omphacite at room-temperature and high-pressure conditions (Zhang et al., 2016). Zhao et al. (1997), Zhao (1998), and Nishihara et al. (2003) are the only EOS studies at simultaneous high pressure-temperature conditions. However, the pressures reached in those previous studies are lower than 10 GPa, which cannot cover the entire pressure stability filed of clinopyroxene (~17-18 GPa, figure I.1). In addition, the polycrystalline nature of the samples used in those studies may also result in additional uncertainties due to deviatoric stresses developed between the mineral grains at high pressure-temperature conditions. Therefore, we conducted thermal EOS measurements using diamond

anvil cell combined with single-crystal X-ray diffraction techniques at Sector 13-BMC and 13-BMD, GSECARS, Advanced Photon Source.

In addition, the high pressure-temperature sound velocities of clinopyroxene are not well studied either. The only elasticity measurements of clinopyroxene at simultaneous high pressure-temperature conditions are performed on polycrystalline diopside ($CaMgSi_2O_6$) up to 8 GPa and 1073 K (Li & Neuville, 2010), and thus the single-crystal elastic moduli C_{ij}s are missing. The individual C_{ij}s, from which anisotropy information can be calculated, can only be acquired from single-crystal elasticity measurements. However, the only single-crystal high-pressure elastic study for clinopyroxene is again for the diopside end member (Sang & Bass, 2014). No high-pressure or high-temperature single-crystal elasticity study is available for upper mantle clinopyroxenes with other compositions. For example, the single-crystal elasticity of jadeite has only been measured once at ambient condition 30 years ago (Kandelin & Weidner, 1988).

Therefore, in this dissertation, we conducted single-crystal EOS and Brillouin spectroscopy measurements for natural jadeite and omphacite up to 18 GPa and 700 K. Based on the measured thermoelastic properties of jadeite and omphacite, we modeled various seismic properties of the subducted oceanic crust, continent-derived sediments/crust, and the delaminated lower continental crust and applied to the real Earth.

2. The viscosity of kimberlite magma

The volatile-rich kimberlite magma is one of the most important terrestrial magmas due to its ultra-deep origin. As the only natural diamond-bearing magma, kimberlite magma originates from depth > 200 km, possibly down to the mantle transition zone (Wilson & Head

Iii, 2007; Foley et al., 2019; Nickel & Green, 1985; Mitchell, 2013). Considering its ultra-deep origin, kimberlite magma and the xenoliths carried within it are important geochemical probes of the Earth's mantle (Pearson et al., 2019; Tappe et al., 2017). For example, the major elemental compositions (such as Mg/Si ratios) of kimberlite magma and mantle xenoliths provide crucial geochemical data for the local lithospheric mantle (Pearson et al., 2019). The comparison of the isotopes (such as $^{187}Os/^{188}Os$) and trace elements (such as Ba/Nb and Ce/Pb) between ocean island basalts and the kimberlite magma can also help us understand the enriched geochemical reservoirs (such as EM-1) in the deep Earth (Pearson et al., 2019; Tappe et al., 2013; Araujo et al., 2001).

Kimberlite magma may originate from the carbonated slab crust (Sun & Dasgupta, 2019) or partially melted CO_2-bearing peridotite (Dasgupta et al., 2013). The chemical compositions of kimberlite samples collected in the field vary a lot (Wilson & Head Iii, 2007; Kamenetsky et al., 2009). For example, the SiO_2 content varies from 25.6 wt% to 40 wt% and the MgO content ranges from 25.2 wt% to 38.6 wt%. In addition to the potential alteration and weathering process after the kimberlite magma crystallizes at the surface, during its ascent process, the reactions between the kimberlite magma and the nearby rocks can contribute to the geochemical complexity of kimberlite samples collected in the field. For example, the interaction between the primitive kimberlite magma and the enriched geochemical reservoirs could result in different $^{87}Sr/^{86}Sr$ ratio (Pearson et al., 2019; Smith et al., 1985). The migration speed of kimberlite magma in the deep Earth has significant influence on these chemical reactions during its ascent and eruption process. Previous simulation models show that the eruption process of kimberlite magma would be extremely fast (~5-20 m/s) if the viscosity is low enough to reach the turbulent regime (e.g., Sparks et al., 2006).

However, our understanding about the viscosity of volatile-rich kimberlite magma is still limited. Previous in-situ falling-sphere viscometry experiments suggested extremely low viscosities of pure calcite and dolomite melts (<0.01 Pa·s), which are more than an order of magnitude lower than that of MORB (Kono et al., 2014; Sakamaki et al., 2013). Considering the high CO_2 content in kimberlite magma, its viscosity is likely low. However, the only existing experimental study on kimberlite magma viscosity by Persikov et al. (2017) using quenched falling sphere experiments suggested that the viscosity of kimberlite magma is comparable to or even higher than MORB under high pressure-temperature conditions. Such high viscosity values do not support the fast ascent speed of the kimberlite magma, as suggested by previous simulation models (Sparks et al., 2006; Wilson & Head Iii, 2007). Moreover, Persikov et al. (2017) also found that the H_2O content did not affect the viscosity of kimberlite, which is counterintuitive and different from all the other silicate magmas (Robert et al., 2013; Whittington et al., 2009).

To fill in this knowledge gap, in this dissertation, we measured the viscosity of kimberlite magma with 2-8 wt% CO_2 and 0-5 wt% H_2O up to 5.3 GPa 2173 K inside a Paris-Edinburgh Press using in-situ falling-sphere viscometry technique at Sector 16-BM-B, HPCAT, Advanced Photon Source. Based on the updated viscosity data obtained in this dissertation, we further modeled the kimberlite magma ascent and eruption processes starting at a depth of 220 km and extended to the Earth's surface.

References

Ahrens, T. J., & Schubert, G. (1975). Gabbro-eclogite reaction rate and its geophysical significance. *Reviews of Geophysics*, *13*(2), 383-400.

Anderson, D. L., & Bass, J. D. (1986). Transition region of the Earth's upper mantle. *Nature*, *320*(6060), 321.

Aoki, I., & Takahashi, E. (2004). Density of MORB eclogite in the upper mantle. *Physics of the Earth and Planetary Interiors*, *143*, 129-143.

Araujo, A., Carlson, R. W., Gaspar, J. C., & Bizzi, L. A. (2001). Petrology of kamafugites and kimberlites from the Alto Paranaiba alkaline province, Minas Gerais, Brazil. *Contributions to Mineralogy and Petrology*, *142*(2), 163-177.

Bass, J. D., & Anderson, D. L. (1984). Composition of the upper mantle: Geophysical tests of two petrological models. *Geophysical Research Letters*, *11*(3), 229-232.

Bird, P. (1979). Continental delamination and the Colorado Plateau. *Journal of Geophysical Research: Solid Earth*, *84*(B13), 7561-7571.

Chauvel, C., Hofmann, A. W., & Vidal, P. (1992). HIMU-EM: the French Polynesian connection. *Earth and Planetary Science Letters*, *110*(1-4), 99-119.

Dasgupta, R., Mallik, A., Tsuno, K., Withers, A. C., Hirth, G., & Hirschmann, M. M. (2013). Carbon-dioxide-rich silicate melt in the Earth's upper mantle. *Nature*, *493*(7431), 211-215.

Foley, S. F., Yaxley, G. M., & Kjarsgaard, B. A. (2019). Kimberlites from source to surface: insights from experiments. *Elements: An International Magazine of Mineralogy, Geochemistry, and Petrology*, *15*(6), 393-398.

French, S. W., & Romanowicz, B. A. (2014). Whole-mantle radially anisotropic shear velocity structure from spectral-element waveform tomography. *Geophysical Journal International*, *199*(3), 1303-1327.

Hofmann, A. W. (1997). Mantle geochemistry: the message from oceanic volcanism. *Nature*, *385*(6613), 219.

Irifune, T., Ringwood, A. E., & Hibberson, W. O. (1994). Subduction of continental crust and terrigenous and pelagic sediments: an experimental study. *Earth and Planetary Science Letters*, *126*(4), 351-368.

Irifune, T., Sekine, T., Ringwood, A. E., & Hibberson, W. O. (1986). The eclogite-garnetite transformation at high pressure and some geophysical implications. *Earth and Planetary Science Letters*, *77*(2), 245-256.

Kamenetsky, V. S., Kamenetsky, M. B., Weiss, Y., Navon, O., Nielsen, T. F., & Mernagh, T. P. (2009). How unique is the Udachnaya-East kimberlite? Comparison with kimberlites from the Slave Craton (Canada) and SW Greenland. *Lithos*, *112*, 334-346.

Kandelin, J., & Weidner, D. J. (1988). The single-crystal elastic properties of jadeite. *Physics of the Earth and Planetary Interiors*, *50*(3), 251-260.

Kay, R. W., & Kay, S. M. (1993). Delamination and delamination magmatism. *Tectonophysics*, *219*(1-3), 177-189.

Levander, A., Schmandt, B., Miller, M. S., Liu, K., Karlstrom, K. E., Crow, R. S., ... & Humphreys, E. D. (2011). Continuing Colorado plateau uplift by delamination-style convective lithospheric downwelling. *Nature*, *472*(7344), 461-465.

Li, B., & Neuville, D. R. (2010). Elasticity of diopside to 8 GPa and 1073 K and implications for the upper mantle. *Physics of the Earth and Planetary interiors*, *183*(3-4), 398-403.

Mainprice, D. (2015). 2.20—Seismic anisotropy of the deep earth from a mineral and rock physics perspective. *Treatise on Geophysics*, 487-538.

Mitchell, R. H. (2013). *Kimberlites: mineralogy, geochemistry, and petrology*. Springer Science & Business Media.

Nickel, K. G., & Green, D. H. (1985). Empirical geothermobarometry for garnet peridotites and implications for the nature of the lithosphere, kimberlites and diamonds. *Earth and Planetary Science Letters*, *73*(1), 158-170.

Nishi, M., Kubo, T., Ohfuji, H., Kato, T., Nishihara, Y., & Irifune, T. (2013). Slow Si–Al interdiffusion in garnet and stagnation of subducting slabs. *Earth and Planetary Science Letters*, *361*, 44-49.

Nishihara, Y., Takahashi, E., Matsukage, K., & Kikegawa, T. (2003). Thermal equation of state of omphacite. *American Mineralogist*, *88*(1), 80-86.

Pearson, D. G., Woodhead, J., & Janney, P. E. (2019). Kimberlites as geochemical probes of Earth's mantle. *Elements: An International Magazine of Mineralogy, Geochemistry, and Petrology*, *15*(6), 387-392.

Persikov, E. S., Bukhtiyarov, P. G., & Sokol, A. G. (2017). Viscosity of hydrous kimberlite and basaltic melts at high pressures. *Russian Geology and Geophysics*, *58*(9), 1093-1100.

Ringwood, A. E. (1975). Composition and Petrology of the Earth's Mantle. *MacGraw-Hill*, *618*.

Ritsema, J., Deuss, A. A., Van Heijst, H. J., & Woodhouse, J. H. (2011). S40RTS: a degree-40 shear-velocity model for the mantle from new Rayleigh wave dispersion, teleseismic traveltime and normal-mode splitting function measurements. *Geophysical Journal International*, *184*(3), 1223-1236.

Robert, G., Whittington, A. G., Stechern, A., & Behrens, H. (2013). The effect of water on the viscosity of a synthetic calc-alkaline basaltic andesite. *Chemical Geology*, *346*, 135-148.

Rudnick, R. L., & Fountain, D. M. (1995). Nature and composition of the continental crust: a lower crustal perspective. *Reviews of geophysics*, *33*(3), 267-309.

Sang, L., & Bass, J. D. (2014). Single-crystal elasticity of diopside to 14 GPa by Brillouin scattering. *Physics of the Earth and Planetary Interiors*, *228*, 75-79.

Schmandt, B., & Humphreys, E. (2010). Complex subduction and small-scale convection revealed by body-wave tomography of the western United States upper mantle. *Earth and Planetary Science Letters*, *297*(3-4), 435-445.

Smith, C. B., Gurney, J. J., Ebrahim, N., Skinner, E. M. W., & Clement, C. R. (1985). Geochemical character of southern African kimberlites: a new approach based on isotopic constraints. *Transactions of the Geological Society of South Africa*, *88*(2), 267-280.

Sparks, R. S. J., Baker, L., Brown, R. J., Field, M., Schumacher, J., Stripp, G., & Walters, A. (2006). Dynamical constraints on kimberlite volcanism. *Journal of Volcanology and Geothermal Research*, *155*(1-2), 18-48.

Sun, C., & Dasgupta, R. (2019). Slab–mantle interaction, carbon transport, and kimberlite generation in the deep upper mantle. *Earth and Planetary Science Letters*, *506*, 38-52.

Tappe, S., Pearson, D. G., Kjarsgaard, B. A., Nowell, G., & Dowall, D. (2013). Mantle transition zone input to kimberlite magmatism near a subduction zone: origin of anomalous Nd–Hf isotope systematics at Lac de Gras, Canada. *Earth and Planetary Science Letters*, *371*, 235-251.

Tappe, S., Romer, R. L., Stracke, A., Steenfelt, A., Smart, K. A., Muehlenbachs, K., & Torsvik, T. H. (2017). Sources and mobility of carbonate melts beneath cratons, with implications for deep carbon cycling, metasomatism and rift initiation. *Earth and Planetary Science Letters*, *466*, 152-167.

Van Mierlo, W. L., Langenhorst, F., Frost, D. J., & Rubie, D. C. (2013). Stagnation of subducting slabs in the transition zone due to slow diffusion in majoritic garnet. *Nature Geoscience*, *6*(5), 400.

Whittington, A. G., Hellwig, B. M., Behrens, H., Joachim, B., Stechern, A., & Vetere, F. (2009). The viscosity of hydrous dacitic liquids: implications for the rheology of evolving silicic magmas. *Bulletin of Volcanology*, *71*(2), 185-199.

Wilson, L., & Head Iii, J. W. (2007). An integrated model of kimberlite ascent and eruption. *Nature*, *447*(7140), 53-57.

Wu, Y., Fei, Y., Jin, Z., & Liu, X. (2009). The fate of subducted upper continental crust: an experimental study. *Earth and Planetary Science Letters*, *282*(1-4), 275-284.

Zhang, D., Hu, Y., & Dera, P. K. (2016). Compressional behavior of omphacite to 47 GPa. *Physics and Chemistry of Minerals*, *43*(10), 707-715.

Zhao, Y., RB, V. D., & JZ, Z. (1998). Thermoelastic equation of state of monoclinic pyroxene: CaMgSi2O6 diopside. *The Review of High Pressure Science and Technology*, *7*, 25-27.

Zhao, Y., Von Dreele, R. B., Shankland, T. J., Weidner, D. J., Zhang, J., Wang, Y., & Gasparik, T. (1997). Thermoelastic equation of state of jadeite NaAlSi2O6: An energy-dispersive Reitveld Refinement Study of low symmetry and multiple phases diffraction. *Geophysical Research Letters*, *24*(1), 5-8.

Chapter II

High-pressure single-crystal elasticity and thermal equation of state of omphacite and their implications for the seismic properties of eclogite in the Earth's interior

Abstract

Omphacite is a major mineral phase of eclogite, which provides the main driving force for the slab subduction into the Earth's interior. We have measured the single-crystal elastic moduli of omphacite at high pressures for the first time up to 18 GPa at ambient temperature using Brillouin spectroscopy. A least-squares fit of the velocity-pressure data to the third-order finite strain equation of state yields K_{S0}'=4.5(3), G_0'=1.6(1) with ρ_0=3.34(1) g/cm^3, K_{S0}=123(3) GPa, and G_0=74(2) GPa. In addition, the synchrotron single-crystal X-ray diffraction data have been collected up to 18 GPa and 700 K. The fitting to Holland-Powell thermal-pressure equation of state yields K_{T0}'=4.6(5) and α_0=2.7(8) $\times 10^{-5}$ K^{-1}. Based on the obtained thermoelastic parameters of omphacite, the anisotropic seismic velocities of eclogite are modeled and compared with pyrolite between 200 to 500 km. The largest contrast between the eclogite and pyrolite in terms of seismic properties is observed between ~310 to 410 km.

1. Introduction

Omphacite is a clinopyroxene (Cpx) solid solution of Fe-bearing diopside ($CaMgSi_2O_6$) and jadeite ($NaAlSi_2O_6$), and is stable up to about 500 km depth in the Earth's interior (Irifune et al., 1986). It is also a major mineral component of eclogite (up to 75 vol%). Basalt, which makes up most of the Earth's oceanic crust, transforms into eclogite at the depth > ~60 km (Ahrens & Schubert, 1975). Previous studies have suggested that eclogite remains denser than the surrounding mantle down to the base of the transition zone, and therefore is considered one

of the main driving forces for the slab subduction (Peacock, 1996; Anderson, 2007; Xu et al., 2008; Moghadam et al., 2010). Subducted eclogite is also an important source of the chemical heterogeneities in the Earth's mantle (Kay & Kay, 1993; Peacock, 1996; Anderson, 2007; Xu et al., 2008; Moghadam et al., 2010). Previous studies have proposed to utilize the unique seismic properties of eclogite to identify possible subduction channels and eclogite-rich regions in the Earth's interior (e.g., Mauler et al., 2000; Abalos et al., 2011). Due to the elastically isotropic nature of garnet and the relatively small proportion (< 10 vol%) of the silica minerals in eclogite (e.g. Irifune et al., 2008; Liu et al., 2000; Sinogeikin & Bass, 2002; Aoki & Takahashi, 2004), the seismic anisotropy of eclogite is primarily caused by the lattice preferred orientation of omphacite, including L-type, S-type, and SL-type (e.g. Zhang et al., 2006; Zhang & Green, 2007). Thus, in order to model the seismic properties of eclogite in the Earth's interior, measurements of the density and single-crystal elastic properties of omphacite under relevant pressure(P)-temperature(T) conditions are needed.

Depending on the thermal history, natural omphacite crystals can display either a disordered C2/c or an ordered P2/n symmetry (Clark & Papike, 1968; Fleet et al., 1978). The P2/n and C2/c structures are similar, and the P2/n→C2/c phase transition at high-T has no resolvable effect on the equation of state (EOS) of omphacite (Nishihara et al., 2003; Pandolfo et al., 2012a, 2012b). This study primarily focuses on the evolution of the elastic properties, rather than the crystal structure of omphacite as a function of depth in the Earth's interior. Therefore, we do not differentiate the two structures of omphacite here.

Previous EOS studies on omphacite are mainly limited by the investigated P or T range or both (e.g., McCormick et al., 1989; Pavese et al., 2000; Pavese et al., 2001; Nishihara et al., 2003; Pandolfo et al., 2012a, 2012b; Pandolfo et al., 2015). For example, Zhang et al. (2016)

performed single-crystal X-ray diffraction (XRD) experiments on omphacite up to 47 GPa 300 K. Pandolfo et al. (2012b) measured the thermal expansion coefficients of omphacite up to 1073 K at 1 atm. The only available in situ high P-T EOS study for omphacite is performed on polycrystalline samples using multi-anvil press up to 10 GPa, and thus is unable to cover the entire P stability field of omphacite in the Earth's interior (Nishihara et al., 2003). On the other hand, although the sound velocities of the Mg,Ca end member diopside have been studied at various P-T conditions (Matsui & Busing, 1984; Levien et al., 1979; Isaak & Ohno, 2003; Isaak et al., 2006; Li & Neuville, 2010; Sang et al., 2011; Walker, 2012; Sang & Bass, 2014), the single-crystal elastic properties of omphacite has only been measured at ambient condition (Bhagat et al., 1992), or investigated computationally at high-P 0 K conditions (Skelton & Walker, 2015). The lack of experimentally determined thermoelastic properties of omphacite, which is the most abundant mineral phase in eclogite, restricts our understanding of the subduction process as well as the possible seismic identification of eclogitic materials in the Earth's interior.

To fill in this knowledge gap, we performed high P-T single-crystal XRD measurements on natural P2/n omphacite crystals up to 18 GPa 700 K at GeoSoilEnviroCARS (GSECARS), Advanced Photon Source (APS), Argonne National Laboratory (ANL), as well as single-crystal Brillouin spectroscopy measurements of the same crystals up to 18 GPa 300 K at the high-P laser spectroscopy laboratory at University of New Mexico (UNM). The thermal EOS, single-crystal elastic moduli (C_{ij}), aggregate compressional (Vp) and shear (Vs) velocities, adiabatic bulk modulus (K_S), shear modulus (G) and their P dependences are determined and utilized for calculating the seismic properties of eclogite in this study.

2. Experimental methods

The *P2/n* omphacite crystals were hand-picked from a natural eclogite rock. The composition $Na_{0.289}Mg_{0.633}Ca_{0.68}Fe_{0.108}Al_{0.323}Si_{1.975}O_6$ was determined by electron probe microanalysis (EPMA), using the JEOL 8200 Electron Microprobe facility hosted by the Institute of Meteoritics at UNM. The JEOL 8200 Electron Microprobe is equipped with 5 wavelength dispersive (WD) X-ray spectrometers and an ultrathin-window energy dispersive X-ray spectrometer. The WD spectrometers are fitted with multiple analyzing crystals to provide quantitative analysis of all elements from Be to U. Selected crystals with ~1 mm size were used for EPMA analysis, operating at 15 kV accelerating voltage and 20 nA beam current. The beam spot size is smaller than 1 μm. The detailed analysis results can be found in Table II.S2. Normalizing the chemical analysis in terms of diopside and jadeite yields a simplified composition of $Diopside_{70.5}Jadeite_{29.5}$. The crystals were then double-side polished into pellets with ~15 μm thickness. They were scratch-free and inclusion-free under optical examination. The polished samples were then cut into pieces with ~40 μm width for diamond anvil cell (DAC) loading.

Symmetric piston-cylinder DACs and BX90 DACs with standard 60° and 90° opening WC backing seats were used for Brillouin and XRD measurements (Kantor et al., 2012). Re gaskets were pre-indented to 50-55 μm thickness with a pair of 350 μm culet diamonds, and 235-240 μm diameter holes were drilled into the gaskets and served as sample chambers. Neon was gas loaded as the P-transmitting medium at GSECARS, APS, ANL (Rivers et al., 2008). For synchrotron high P-T XRD experiments, gold EOS was used for estimating the experimental Ps. The P derivatives of the isothermal bulk modulus (K_{T0}') of gold vary from 5.0 to 6.2 in previous EOS studies (e.g., Anderson et al., 1989; Dorogokunets & Oganov, 2007; Shim et al., 2002; Fei et al., 2004; Tsuchiya, 2003; Greeff & Graf, 2004; Fei et al., 2007). At

18 GPa 700K, the maximum difference between the Ps determined using different gold EOS is ~0.3 GPa. In this study, we adopted the internally consistent thermal EOS of gold from Fei et al. (2007). For ambient-T high-P Brillouin spectroscopy experiments, 2 ruby spheres were loaded into each DAC and used as the P standard (Mao et al., 1978). The maximum P difference between the ruby spheres before and after the experiment is 0.2 GPa.

Ambient and high P-T single-crystal XRD experiments were carried out at GSECARS experimental station 13-BM-D and 13-BM-C. The X-ray opening angles for symmetric piston-cylinder DACs and BX90 DACs are ±14° and ±24°, respectively. At 13-BM-D, the X-ray is monochromated to 37.0 keV and focused to 6 μm × 15 μm. A stationary Perkin-Elmer image plate is used as a detector. Diffraction images were collected at 1°/step under step-scan mode and the exposure time was 5 s/°. At 13-BM-C, the X-ray beam energy is 28.6 keV and the beam size is ~15 μm × 15 μm. The MAR165 Charge Coupled Device detector is placed on a rotational detector arm. 2 different detector positions were used. One detector position was perpendicular to the incident X-ray beam and the other detector position was rotated about the horizontal axis by 20° (Zhang et al., 2017). We collected both the wide-scan and 1°/step step-scan images with 3 s/° exposure time. LaB6 powder was used to calibrate the detector geometry parameters in both stations.

For measurements at ambient condition, the polished plate-like crystals were oriented with their plane normals parallel to the incoming X-ray beam. The obtained ambient unit cell parameters were averaged from the 3 grains measured with different orientations: a=9.584(7) Å, b=8.83(2) Å, c=5.2504(4) Å, and β=105.27(9)°. The calculated density ρ_0 is 3.34(1) g/cm^3 at ambient condition. The face normals of the measured 3 samples are (-0.1516, -0.9691, 0.1947), (0.2421, 0.2987, -0.9231), and (0.6512, -0.759, -0.0050), close to (010), (001), and

(1-10) directions. The angular uncertainties for the measured face normals are approximately 1-2° (Weidner & Carleton, 1977). For high P-T single-crystal XRD measurements, we used resistively heated DACs with Pt heaters to reach 373K, 500K, and 700K at high-P conditions. The DACs were oriented in the way that the DAC axes were parallel to the incoming X-ray beam. The T was estimated from the 2 K-type thermal couples attached to the diamond anvils. The difference between the 2 T readings was smaller than 10 K.

The Brillouin spectroscopy experiments were performed at the high-P laser spectroscopy laboratory at UNM up to 18 GPa. A 300mW 532 nm single-mode diode-pumped solid-state laser was used as a light source. The measurements were carried out using a 50° symmetric forward scattering geometry. The scattering angle was calibrated to be 50.37(5)° using a standard silica glass Corning 7980 (Zhang et al., 2011, 2015). The pair of diamonds were oriented to ensure that the fast and slow directions matched each other. We used the 3 pre-oriented omphacite crystals measured at 13-BM-D for the Brillouin measurements at 7 different Ps. At each P, Vp and Vs were measured at 13 different Chi angles (0, 30, 60, 90, 120, 150, 180, 195, 225, 255, 285, 315, 345) along the 360° azimuth to avoid any geometrical errors. All Brillouin spectra are with excellent signal-to-noise ratios. A typical Brillouin spectrum collected at 18 GPa is shown in Figure II.S7.

3. Results and discussion

3.1. Thermal EOS of omphacite

The single-crystal XRD images were analyzed using the ATREX IDL software package (Dera et al., 2013) to obtain the unit cell parameters (Table II.S3). Due to the use of

crystals with different orientations in different experimental runs, we only performed thermal EOS fit to the unit cell volumes.

The ambient isothermal bulk modulus K_{T0} was calculated from the Reuss bond of the adiabatic bulk modulus K_{S0}^{R} using equation II.S1 (Supporting Information) and the value of 118.7 GPa was fixed in the thermal EOS fitting process. As pointed by Angel et al. (2018), the use of thermal Birch-Murnaghan EOS may suffer from the unphysical assumptions of constant $\partial K_T/\partial T$ and K_T' within the explored P-T range, thus we chose to use the Holland-Powell thermal-P EOS instead in this study (Holland & Powell, 2011; Birch, 1947; equation II.S2-II.S4, Supporting Information). With fixed V_0 and K_{T0}, the fitting yields K_{T0}'=4.6(5) and α_0=2.7(8) $\times 10^{-5}$ K^{-1} (Figure II.1). Our obtained K_{T0}' and α_0 values agree well with Pandolfo et al. (2012a, b), Zhang et al. (2016), and Nishihara et al. (2003).

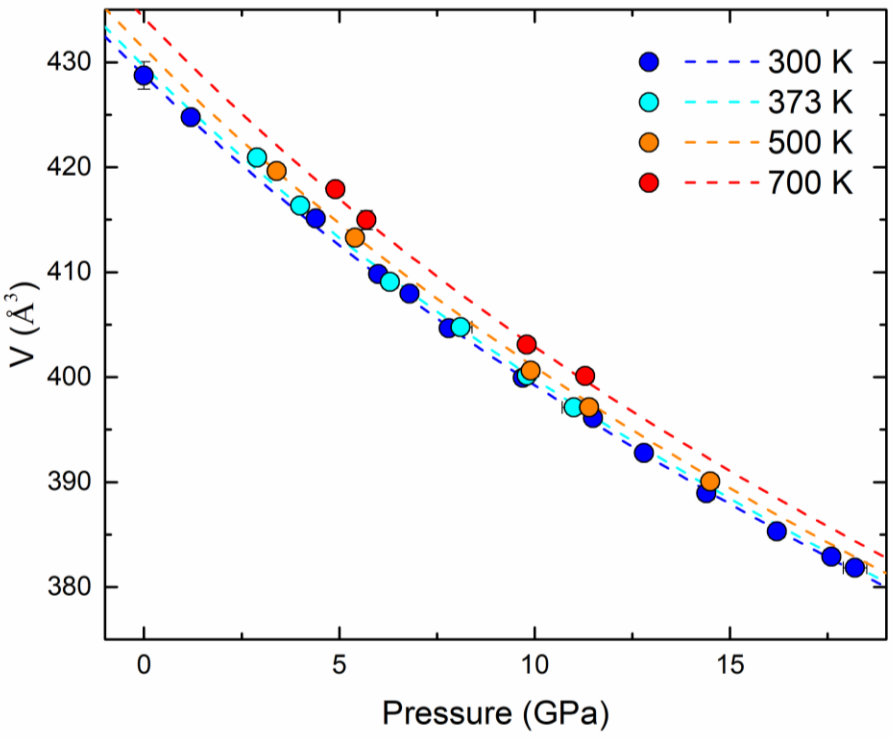

Figure II.1. P-V-T data of omphacite with calculated isothermal compression curves.

3.2. High-P single-crystal elastic properties of omphacite

With known ρ_0 measured by single-crystal XRD, a least squares inversion of the Christoffel equation was used to calculate the best-fit values for the 13-independent C_{ij}s of

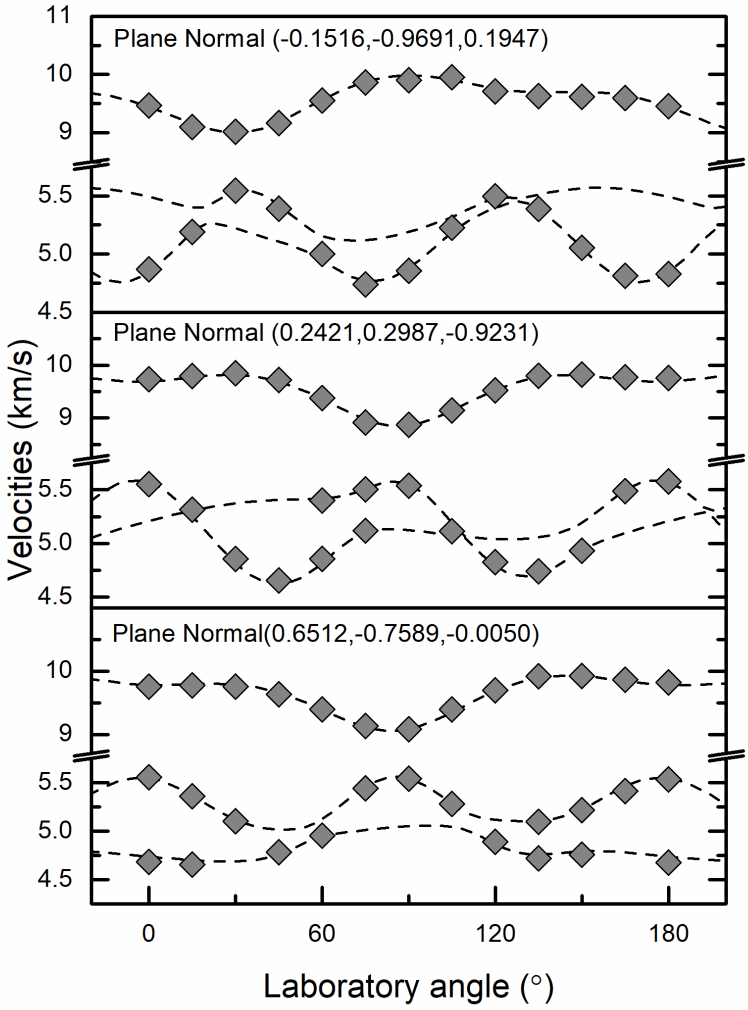

Figure II.2. Measured acoustic velocities of omphacite as a function of laboratory Chi angles within the sample plane at 18 GPa. Dashed lines are the acoustic velocities calculated from the best-fit single-crystal elasticity model; diamonds are the experimentally determined velocities. Errors are within the size of the symbols.

omphacite at ambient condition (Weidner & Carleton, 1977). The final results have a root-mean-square residual between the observed and modeled velocities of less than 50 m/s. The ambient aggregate elastic properties K_{S0} and G_0 were calculated using the Voigt-Reuss-Hill (VRH) averaging scheme (Hill, 1963). As shown in Table II.S4, most C_{ij}s for the $Diopside_{70.5}Jadeite_{29.5}$ sample determined in this study are smaller than the values of a $Diopside_{34.1}Jadeite_{65.9}$ omphacite sample measured by Bhagat et al. (1992).

The high-P densities, single-crystal and aggregate elastic properties were calculated iteratively. Given an initial guess of the sample's high-P densities, a set of C_{ij}s, K_S, G, Vp, and Vs can be calculated by the least squares inversion of the Christoffel equation at each P. Note, the Vp and Vs are independent of the assumed density values, and thus, they represent the true

	1 atm	3.0(1) GPa	6.0(1) GPa	8.9(1) GPa	12.0(1) GPa	15.0(1) GPa	18.0(1) GPa
ρ (g/cm^3)	3.340	3.419	3.492	3.558	3.625	3.686	3.744
C_{11} (GPa)	231.5(8)	259(1)	277.2(8)	294.3(7)	315.3(8)	333.2(7)	348.6(6)
C_{22} (GPa)	201(1)	213(2)	229(1)	247(1)	262(1)	277(1)	289(1)
C_{33} (GPa)	253.8(8)	275(1)	297.6(8)	314.2(7)	326.3(8)	346.8(8)	356.7(6)
C_{44} (GPa)	79.1(5)	82.3(6)	86.0(6)	87.6(5)	91.0(6)	92.5(6)	97.7(6)
C_{55} (GPa)	68.9(4)	70.7(5)	74.0(5)	78.4(4)	81.9(4)	84.5(4)	88.1(3)
C_{66} (GPa)	74.0(4)	80.3(7)	89.7(5)	95.7(6)	101.4(5)	109.6(5)	119.1(5)
C_{12} (GPa)	84.4(9)	96(1)	107.6(8)	120.7(8)	131.6(9)	144.5(9)	146.7(9)
C_{13} (GPa)	76(1)	85(1)	93(1)	104.2(9)	118(1)	122(1)	132.6(8)
C_{23} (GPa)	60(2)	71(2)	77(2)	89(2)	89(2)	99(2)	120(2)
C_{15} (GPa)	7.6(5)	5.6(6)	5.6(5)	4.4(4)	4.6(5)	6.3(5)	6.5(4)
C_{25} (GPa)	5.4(10)	4(1)	5.9(9)	6(1)	10(1)	11(1)	22(1)
C_{35} (GPa)	39.8(5)	33.2(6)	28.5(5)	26.4(4)	23.8(5)	21.5(5)	23.2(4)
C_{46} (GPa)	5.9(4)	6.4(6)	7.0(5)	7.2(6)	6.5(6)	2.2(6)	-1.8(5)
K_S^R (GPa)	119.9(5)	134.7(6)	146.7(6)	161.3(5)	171.3(6)	183.4(6)	193.6(5)
G^R (GPa)	71.9(2)	76.7(3)	82.2(3)	85.8(3)	90.0(3)	94.0(3)	97.8(2)
K_S^V (GPa)	125.3(5)	138.8(6)	150.8(6)	164.8(5)	175.8(6)	187.6(6)	199.2(5)
G^V (GPa)	75.4(2)	79.7(3)	85.0(3)	88.4(3)	92.5(3)	96.7(3)	100.7(2)
K_S^{VRH} (GPa)	123(3)	137(3)	149(2)	163(2)	174(3)	186(3)	196(3)
G^{VRH} (GPa)	74(2)	78(2)	84(2)	87(2)	91(2)	95(2)	99(2)
Vp (km/s)	8.13(4)	8.40(3)	8.63(3)	8.86(2)	9.02(3)	9.21(3)	9.37(3)
Vs (Km/s)	4.70(3)	4.78(3)	4.89(3)	4.95(2)	5.02(2)	5.09(2)	5.15(2)

Table II.1. Single-crystal and aggregate elastic properties of omphacite at different pressures determined in this study.

aggregate Vp and Vs under high-P conditions. With fixed ρ_0=3.34(1) g/cm^3, K_{S0}=123(3) GPa, and G_0=74(2) GPa, we can then fit the obtained P-Vp-Vs data set to the 3rd order finite-strain EOS (Davies, 1974; Davies & Dziewonski, 1975), and calculate the true high-P densities as well as the P derivatives of K_S and G. Finally, we recalculated the high-P single-crystal

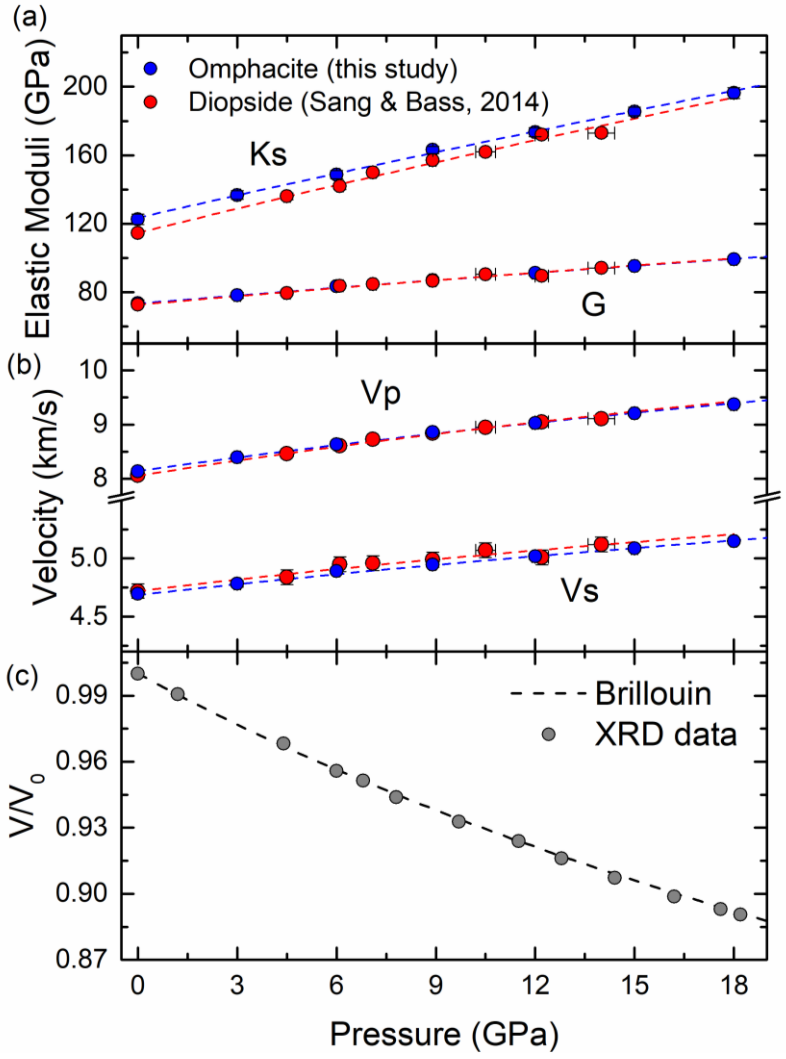

Figure II.3. (a) and (b) The high-P K_S, G, Vp, and Vs of omphacite in this study are compared with the previous study of diopside (Sang & Bass, 2014). (c) The high-P normalized volumes V/V_0 calculated from the finite strain inversion of the sound velocity data are compared with direct measurements from XRD experiments.

elasticity models with updated true densities. The calculated velocities from the final single-crystal C_{ij} model at 18 GPa are plotted with the measured velocities in Figure II.2. The V/V_0 values calculated from the finite strain EOS also agree well with the XRD measurements (Figure II.3c). All the C_{ij}s, K_S, G, Vp, Vs, and density values at different Ps are listed in Table II.1. The aggregate elastic properties of omphacite are found to display a close-to-linear P dependence within the explored P range. K_{S0}' and G_0' are determined to be 4.5(3), 1.6(1) with fixed ρ_0=3.34(1) g/cm^3, K_{S0}=123(3) GPa, and G_0=74(2) GPa. The K_{S0}' is indistinguishable from K_{T0}' considering their experimental uncertainties. Figure II.3a and II.3b show the K_S, G, Vp, and Vs of the omphacite in this study and the comparison with previous measurements of diopside (Sang & Bass, 2014). The K_{S0} and G_0 of jadeite (Kandelin & Weidner, 1988) are ~27% and ~19% higher than those of diopside, suggesting that the increase of jadeite component in Cpx stiffens the crystal structure, and results in higher K_{S0} and G_0. However, the K_{S0}' and G_0' of diopside are slightly larger than omphacite. Thus, the K_S and G differences between diopside and omphacite decrease with P (Figure II.3a). As a matter of fact, the shear moduli of omphacite and diopside are indistinguishable at P higher than 6 GPa. The Vp and Vs of diopside and omphacite are very similar over the entire P measurement range (<0.05 km/s difference, Figure 3b).

This study provides the first set of experimentally determined C_{ij}s of omphacite under high-P conditions (Table II.1, Figure II.4). The dashed lines in Figure II.4 are the finite strain fitting results of all C_{ij}s following the procedures listed in Zhang et al. (2018). Most of the C_{ij}s have close-to-linear P dependences up to 18 GPa, except C_{35} and C_{46}. Skelton and Walker (2015) have calculated the P derivatives for all the C_{ij}s of omphacite at 0 K. According to their results, C_{15}, C_{25}, C_{35}, and C_{46} have negative P derivatives, which are in agreement with the

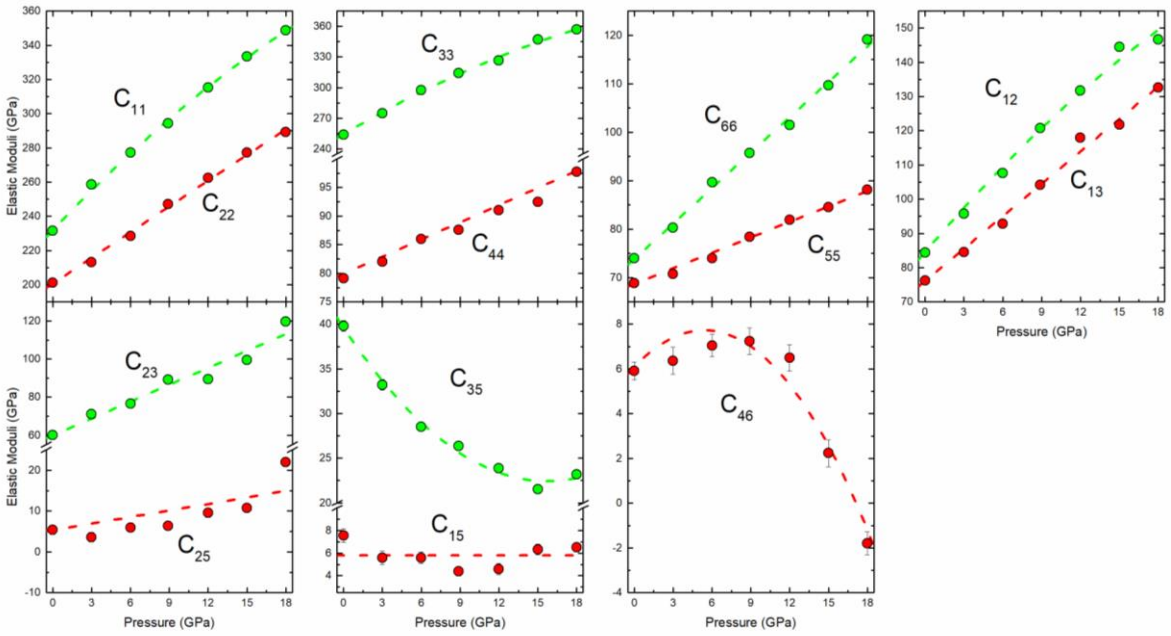

Figure II.4. Single-crystal elastic moduli of omphacite at high-P conditions. The dashed lines represent the best fit finite-strain elastic models.

experimental measurements of diopside (Sang & Bass, 2014). In this study, dC_{25}/dP is slightly positive and dC_{15}/dP is close to 0. Compared with previous studies, Skelton and Walker (2015) calculated the high-P elastic properties at 0 K which is different from 300K in this study. Sang and Bass (2014) performed the measurements for pure diopside end member whereas the omphacite crystals used in this study has ~29.5% jadeite component. The T and compositional difference might cause the deviation from these two previous studies.

3.3. Elastic anisotropy of omphacite at high-P conditions

Omphacite, garnet, and high-P silica phase are the major constituents of eclogite. Omphacite is the major anisotropy contributor due to the small volume% of the silica phase and the elastically isotropic nature of the garnet. Thus, in order to study the anisotropic seismic

properties of eclogite in the Earth's interior, it is important to understand the evolution of the elastic anisotropy of omphacite at high-P conditions.

In order to describe the elastic anisotropy of minerals, we have used 4 different anisotropy indices: Universal Anisotropy Index (A^U), the Vp and Vs azimuthal anisotropy A^{Vp} and A^{Vs}, and Vs polarization anisotropy D^{Vs}, which are defined in equations II.S5-II.S8 in the Supporting Information. A^U is used as a measure of the overall elastic anisotropy for materials with arbitrary symmetry (Ranganathan & Ostoja-Starzewski, 2008). A^{Vp} or A^{Vs} represents the maximum velocity difference of all Vp or Vs propagating along different directions. D^{Vs} describes the maximum velocity difference between 2 orthogonally polarized shear waves propagating along the same direction.

Utilizing the obtained C_{ij}s for omphacite, we calculated all 4 anisotropy indices up to 18 GPa, and also compared our obtained values with olivine, diopside, and orthopyroxene (Figure II.5, Zhang et al., 2018; Sang & Bass, 2014; Zhang & Bass, 2016). For consistency, we adopted the same finite strain approach used in this study to reanalyze all the data presented in previous studies. The calculated P dependences of all the C_{ij}s for olivine, diopside, and orthopyroxene are shown in Table II.S5. Among all 4 different minerals, orthopyroxene has the lowest elastic anisotropy indices in its entire P stability field (Zhang et al., 2012). At ambient- T high-P conditions, diopside has the highest anisotropy of A^U, A^{Vs}, and D^{Vs}, whereas olivine has slightly higher A^{Vp} than diopside. At P<~12 GPa, the elastic anisotropy of olivine, omphacite, and diopside all decrease with P. At P>~12 GPa, the A^U, A^{Vs}, and D^{Vs} of diopside, as well as the D^{Vs} of omphacite increase with P. This is in agreement with previous theoretical calculation results on omphacite and jadeite (Walker, 2012; Skelton & Walker, 2015). Within

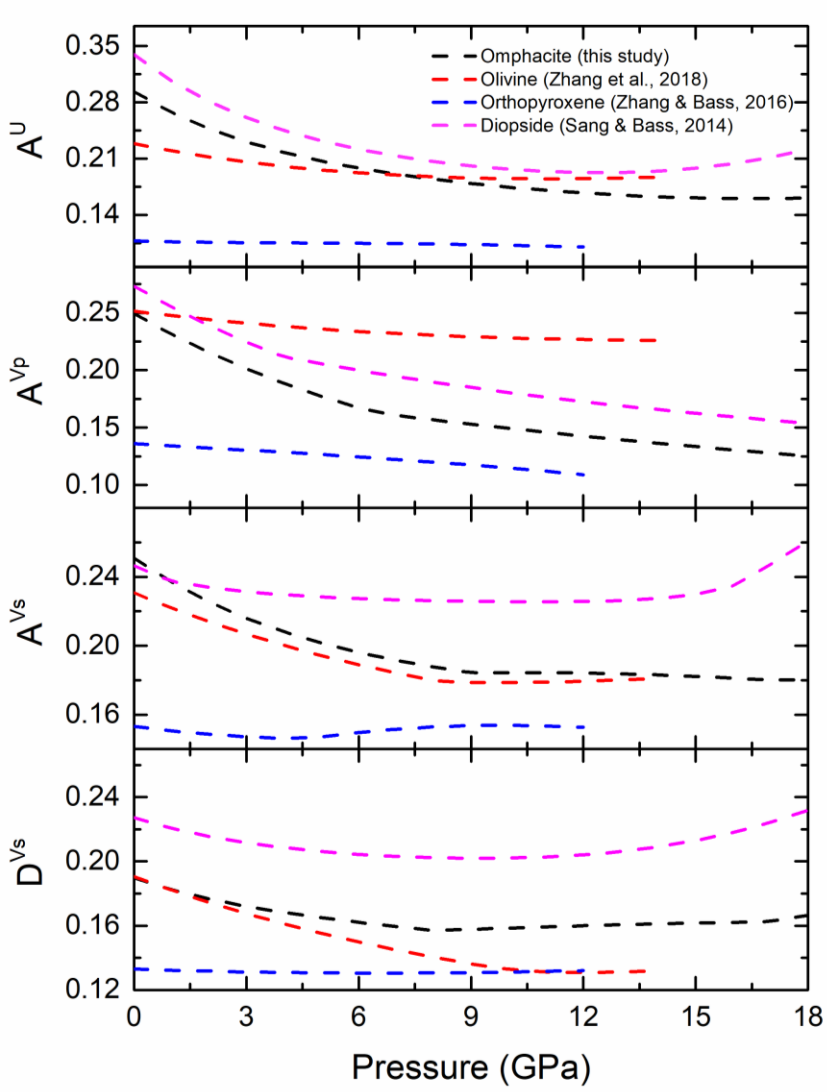

Figure II.5. The anisotropy indices (A^U, A^{Vp}, A^{Vs} and D^{Vs}) of omphacite, olivine (Zhang et al., 2018) and Orthopyroxene (Zhang & Bass, 2016).

the investigated P range, omphacite has higher A^{Vs} and D^{Vs} yet lower A^{Vp} compared with olivine. Omphacite is a strong anisotropy contributor in the regions where eclogite lithology is expected.

3.4. Geophysical implication

Recycled eclogitic, or basaltic component, is one of the most important chemical heterogeneities in the Earth's interior (Xu et al., 2008; Stixrude & Lithgow-Bertelloni, 2012). Due to the slow chemical diffusion and inefficient mixing, those chemical heterogeneities could be preserved through geological time (Ballmer et al., 2017). Locating the potentially eclogite-rich regions in the Earth's interior requires a better understanding of the seismic properties of eclogite (e.g., Abalos et al., 2011). Utilizing the thermoelastic parameters of omphacite and other relevant minerals, we modeled the isotropic Vp, Vs, and the elastic anisotropy profiles of eclogite along mantle adiabats from 200 km to 500 km depth (Katsura et al., 2010). Then we compared our results of eclogite with the ambient upper mantle model rock pyrolite. The thermoelastic parameters for the relevant mineral phases are listed in Table II.S6 (Li & Neuville, 2010; Irifune et al., 2008; Liu et al., 2000; Sinogeikin & Bass, 2002; Suzuki & Anderson, 1983; Reichmann et al., 2002; Gwanmesia et al., 2014; Fei, 1995; Arimoto et al., 2015; Chen et al., 2017; Kulik et al., 2018; Yang & Wu, 2014; Zhang et al., 2018; Zhang & Bass, 2016; Sang & Bass, 2014).

The aggregate velocities of eclogite are calculated based on the petrological models of Aoki and Takahashi (2004) from 200 km to 500 km depth, and the velocities of pyrolite are adopted from Xu et al. (2008) (Figure II.6a). It is worth noting that both the phase proportions and the chemical compositions of the minerals in eclogite change with depth. Previous studies have suggested different high-P petrological models of eclogite. Irifune et al. (1986) proposed that stishovite gradually exsoluted from the eclogite matrix, whereas Aoki and Takahashi (2004) and Xu et al. (2008) claimed that the coesite could be stabilized at depths <300 km. In the latter case, the coesite-stishovite transition can result in a velocity jump at ~310 km depth. Further studies are needed to clarify this issue.

The maximum A^{Vp} and D^{Vs} anisotropy of pyrolite and eclogite are estimated based on the proportions and P-dependent elastic anisotropy of different anisotropic minerals (Figure II.6). We only considered the P effect due to the lack of the single-crystal elasticity measurements at high-T conditions. Finite strain approach was employed to reanalyze all previous data to ensure the consistency of the anisotropy comparison. Unfortunately, the C_{ij}s of coesite have not been experimentally determined at high-P conditions. Thus, a constant elastic anisotropy value was assumed within its stability field (Weidner & Carleton, 1977).

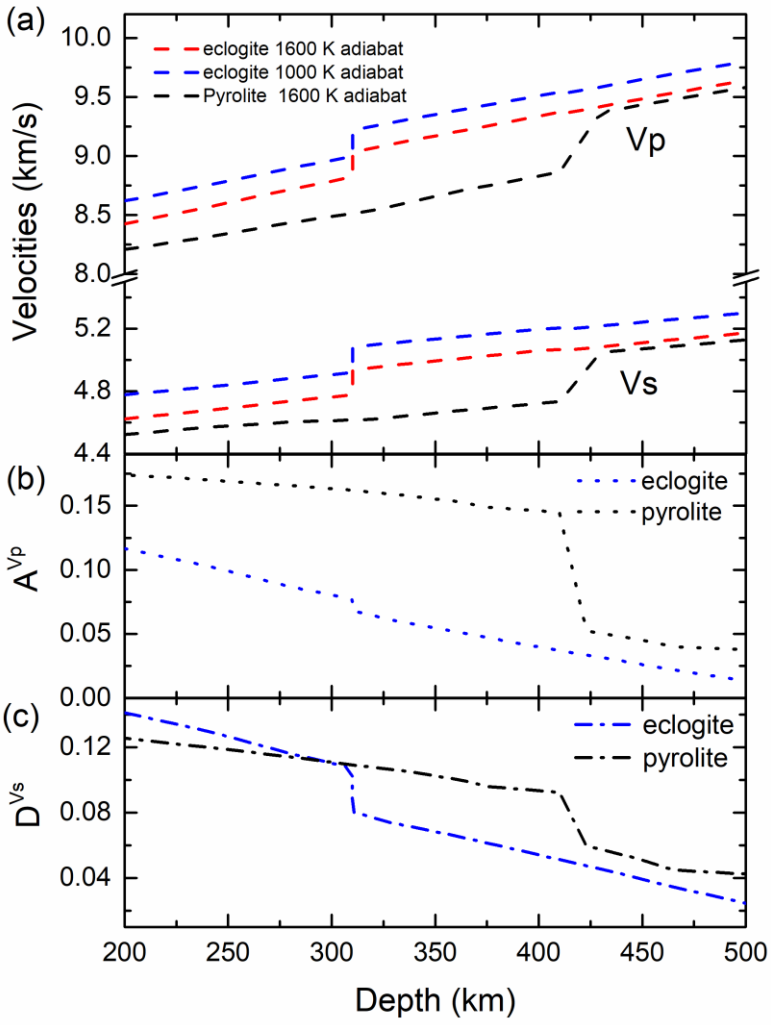

Figure II.6. The Vp, Vs, D^{Vs}, and A^{Vp} of pyrolite and eclogite in the Earth's interior.

Between 200-500 km depth, the obtained isotropic velocities of eclogite are always higher than pyrolite along the 1600 K adiabat. The maximum Vp (~5.7%) and Vs (~7.1%) difference between the eclogite and pyrolite is at the depth range between 310 km and 410 km, primarily due to the coesite-stishovite and olivine-wadsleyite transitions. The coesite-stishovite transition increases the Vp and Vs of eclogite by 2.3% and 3.3%, whereas the olivine-wadsleyite phase transition elevates the Vp and Vs of pyrolite by 5.1 % and 6.2 %, respectively. At depth >410 km, the velocities of pyrolite and eclogite are essentially identical (<0.9% difference), within the experimental uncertainty and seismic resolution. This result implies that, at least within the upper part of the transition zone, enrichment of eclogitic materials is unlikely to cause any compositional induced seismic anomalies. Considering eclogite is recycled back into the Earth's mantle through slab subduction, the T of eclogite can be several hundred K lower than the ambient mantle (e.g. Syracuse et al., 2010). We thus calculated velocity profiles along a colder 1000 K adiabat (Figure II.6a), and the Vp and Vs of eclogite are elevated by ~2.0% and 2.8%. In a realistic scenario, the maximum velocity difference of pyrolite and eclogite could be anywhere between 5.7%-7.7% for Vp, 7.1%-9.9% for Vs between 310 to 410 km.

The maximum difference of A^{Vp} and D^{Vs} between pyrolite and eclogite is also observed between 310 km and 410 km depth. At the 410 discontinuity, the olivine-wadsleyite transition decreases the A^{Vp} and D^{Vs} of pyrolite significantly due to the abrupt anisotropy drop across this phase transition (Zhang et al. 2018). At about 400 km, the A^{Vp} of pyrolite is ~3 times higher than eclogite. For the D^{Vs}, the trend is more interesting. At shallower depth eclogite has higher D^{Vs} than pyrolite because of the large proportion and high anisotropy of omphacite. This difference diminishes with depth due to the fast decrease of omphacite anisotropy as well

as the dissolution of omphacite into the garnet structure. The coesite-stishovite transition takes place at ~310 km depth. Stishovite is less anisotropic than coesite at this depth. Thus, the D^{Vs} of eclogite drops from 10.7% to 8.1% at 310 km, and the D^{Vs} of pyrolite is ~75% higher than eclogite at 410 km.

The maximum isotropic and anisotropic velocities contrast between pyrolite and eclogite is at 310-410 km, making it an optimal depth range for seismologists to search for eclogite-rich heterogeneities in the Earth's interior. The ~5%-7% velocity difference between eclogite and pyrolite also needs to be taken into account when estimating the slab temperatures between 310-410 km depth. Otherwise, the slab temperature could be underestimated by a few hundred K without considering the possible lithology difference.

4. Conclusion

We have determined the thermal EOS and the single-crystal elastic properties of omphacite using synchrotron single-crystal XRD and Brillouin spectroscopy. The derived thermoelastic properties for omphacite are: K_{T0}=118.7 GPa, K_{T0}'=4.6(5), α_0=2.7(8) $\times 10^{-5}$ K^{-1}, K_{S0}=123(3) GPa, G_0=74(2) GPa, K_{S0}'=4.5(3), and G_0'=1.6(1). Based on the modeled isotropic and anisotropic seismic properties of eclogite along different mantle adiabats, we found the maximum isotropic and anisotropic velocity contrast between the eclogite and ambient pyrolitic mantle is at 310-410 km depth. Due to the ~5% - 7% higher velocities of eclogite compared with pyrolite between 310 and 410 km depth, the slab temperature estimation based on pure T-induced seismic velocity increase can be off without considering the existence of eclogitic lithology.

Acknowledgments

The authors would like to thank Jane Silverstone for providing the omphacite sample, Mike Spilde for the help with EPMA experiment at the Institute of Meteoritics at UNM and Sergey Tkachev for the Neon gas loading of the DACs and the help with the room P-T XRD measurements for determining the crystal orientation at GSECARS. This work is supported by the National Science Foundation (NSF) under Grant EAR 1646527 (JZ) and the start-up fund from UNM (JZ). The use of the gas-loading system, 13-BM-D, and 13-BM-C beamlines are supported by COMPRES, the Consortium for Materials Properties Research in Earth Sciences under NSF Cooperative Agreement EAR 1661511, and GSECARS funded by NSF (EAR - 1634415) and Department of Energy (DOE) – GeoSciences (DE-FG02-94ER14466). This research used resources of the APS, a U.S. DOE Office of Science User Facility operated for the DOE Office of Science by Argonne National Laboratory under Contract NO. DE-AC02-06CH11357. The data presented in this study are available in the Supporting Information.

References

Ábalos, B., Fountain, D. M., Ibarguchi, J. G., & Puelles, P. (2011). Eclogite as a seismic marker in subduction channels: Seismic velocities, anisotropy, and petrofabric of Cabo Ortegal eclogite tectonites (Spain). *Bulletin*, *123*(3-4), 439-456.

Ahrens, T. J., & Schubert, G. (1975). Gabbro-eclogite reaction rate and its geophysical significance. *Reviews of Geophysics*, *13*(2), 383-400.

Anderson, D. L. (2007), New Theory of the Earth, Cambridge University Press, New York.

Anderson, O. L., Isaak, D. G., & Yamamoto, S. (1989). Anharmonicity and the equation of state for gold. *Journal of Applied Physics*, *65*(4), 1534-1543.

Angel, R. J., Alvaro, M., & Nestola, F. (2018). 40 years of mineral elasticity: a critical review and a new parameterisation of equations of state for mantle olivines and diamond inclusions. *Physics and Chemistry of Minerals*, *45(2)*, 95-113.

Aoki, I., & Takahashi, E. (2004). Density of MORB eclogite in the upper mantle. *Physics of the Earth and Planetary Interiors*, *143*, 129-143.

Arimoto, T., Gréaux, S., Irifune, T., Zhou, C., & Higo, Y. (2015). Sound velocities of Fe3Al2Si3O12 almandine up to 19 GPa and 1700 K. *Physics of the Earth and Planetary Interiors*, *246*, 1-8.

Ballmer, M. D., Houser, C., Hernlund, J. W., Wentzcovitch, R. M., & Hirose, K. (2017). Persistence of strong silica-enriched domains in the Earth's lower mantle. *Nature Geoscience*, *10*(3), 236.

Bhagat, S. S., Bass, J. D., & Smyth, J. R. (1992). Single-crystal elastic properties of omphacite-C2/c by Brillouin spectroscopy. *Journal of Geophysical Research: Solid Earth*, *97*(B5), 6843-6848.

Birch, F. (1947). Finite elastic strain of cubic crystals. *Physical review*, *71*(11), 809.

Chen, T., Liebermann, R. C., Zou, Y., Li, Y., Qi, X., & Li, B. (2017). Tracking silica in Earth's upper mantle using new sound velocity data for coesite to 5.8 GPa and 1073 K. *Geophysical Research Letters*, *44*(15), 7757-7765.

Clark, J. R., & Papike, J. J. (1968). Crystal-chemical characterization of omphacites. *American Mineralogist: Journal of Earth and Planetary Materials*, *53*(5-6), 840-868.

Davies, G. F. (1974). Effective elastic moduli under hydrostatic stress—I. quasi-harmonic theory. *Journal of Physics and Chemistry of Solids*, *35*(11), 1513-1520.

Davies, G. F., & Dziewonski, A. M. (1975). Homogeneity and constitution of the Earth's lower mantle and outer core. *Physics of the Earth and Planetary Interiors*, *10*(4), 336-343.

Dera, P., Zhuravlev, K., Prakapenka, V., Rivers, M. L., Finkelstein, G. J., Grubor-Urosevic, O., et al. (2013). High pressure single-crystal micro X-ray diffraction analysis with GSE_ADA/RSV software. *High Pressure Research*, *33*(3), 466-484.

Dorogokupets, P. I., & Oganov, A. R. (2007). Ruby, metals, and MgO as alternative pressure scales: A semiempirical description of shock-wave, ultrasonic, x-ray, and thermochemical data at high temperatures and pressures. *Physical Review B*, *75*(2), 024115.

Fei, Y. (1995). Thermal expansion. In T. J. Ahrens *Mineral physics & crystallography: a handbook of physical constants* (Vol. 2, pp. 29-44). Washington, DC: American Geophysical Union.

Fei, Y., Ricolleau, A., Frank, M., Mibe, K., Shen, G., & Prakapenka, V. (2007). Toward an internally consistent pressure scale. *Proceedings of the National Academy of Sciences*, *104*(22), 9182-9186.

Fei, Y., Van Orman, J., Li, J., Van Westrenen, W., Sanloup, C., Minarik, W., ... & Funakoshi, K. I. (2004). Experimentally determined postspinel transformation boundary in Mg2SiO4 using MgO as an internal pressure standard and its geophysical implications. *Journal of Geophysical Research: Solid Earth*, *109*(B2).

Fleet, M. E., Herzberg, C. T., Bancroft, G. M., & Aldridge, L. P. (1978). Omphacite studies; I, The P2/n--> C2/c transformation. *American Mineralogist*, *63*(11-12), 1100-1106.

Greeff, C. W., & Graf, M. J. (2004). Lattice dynamics and the high-pressure equation of state of Au. *Physical Review B*, *69*(5), 054107.

Gwanmesia, G. D., Wang, L., Heady, A., & Liebermann, R. C. (2014). Elasticity and sound velocities of polycrystalline grossular garnet (Ca3Al2Si3O12) at simultaneous high pressures and high temperatures. *Physics of the Earth and Planetary Interiors*, *228*, 80-87.

Hill, R. (1963). Elastic properties of reinforced solids: some theoretical principles. *Journal of the Mechanics and Physics of Solids*, *11*(5), 357-372.

Holland, T. J. B., & Powell, R. (2011). An improved and extended internally consistent thermodynamic dataset for phases of petrological interest, involving a new equation of state for solids. *Journal of Metamorphic Geology*, *29*(3), 333-383.

Irifune, T., Higo, Y., Inoue, T., Kono, Y., Ohfuji, H., & Funakoshi, K. (2008). Sound velocities of majorite garnet and the composition of the mantle transition region. *Nature*, *451*(7180), 814.

Irifune, T., Sekine, T., Ringwood, A. E., & Hibberson, W. O. (1986). The eclogite-garnetite transformation at high pressure and some geophysical implications. *Earth and Planetary Science Letters*, *77*(2), 245-256.

Isaak, D. G., & Ohno, I. (2003). Elastic constants of chrome-diopside: application of resonant ultrasound spectroscopy to monoclinic single-crystals. *Physics and Chemistry of Minerals*, *30*(7), 430-439.

Isaak, D. G., Ohno, I., & Lee, P. C. (2006). The elastic constants of monoclinic single-crystal chrome-diopside to 1,300 K. *Physics and Chemistry of Minerals*, *32*(10), 691-699.

Kandelin, J., & Weidner, D. J. (1988). The single-crystal elastic properties of jadeite. *Physics of the Earth and Planetary Interiors*, *50*(3), 251-260.

Kantor, I., Prakapenka, V., Kantor, A., Dera, P., Kurnosov, A., Sinogeikin, S., et al. (2012). BX90: A new diamond anvil cell design for X-ray diffraction and optical measurements. *Review of Scientific Instruments*, *83*(12), 125102.

Katsura, T., Yoneda, A., Yamazaki, D., Yoshino, T., & Ito, E. (2010). Adiabatic temperature profile in the mantle. *Physics of the Earth and Planetary Interiors*, *183*(1-2), 212-218.

Kay, R. W., & Kay, S. M. (1993). Delamination and delamination magmatism. *Tectonophysics, 219*(1-3), 177-189.

Kulik, E., Murzin, V., Kawaguchi, S., Nishiyama, N., & Katsura, T. (2018). Thermal expansion of coesite determined by synchrotron powder X-ray diffraction. *Physics and Chemistry of Minerals*, 1-9.

Levien, L., Weidner, D. J., & Prewitt, C. T. (1979). Elasticity of diopside. *Physics and Chemistry of Minerals*, *4*(2), 105-113.

Li, B., & Neuville, D. R. (2010). Elasticity of diopside to 8 GPa and 1073 K and implications for the upper mantle. *Physics of the Earth and Planetary interiors*, *183*(3-4), 398-403.

Liu, J., Chen, G., Gwanmesia, G. D., & Liebermann, R. C. (2000). Elastic wave velocities of pyrope–majorite garnets (Py62Mj38 and Py50Mj50) to 9 GPa. *Physics of the Earth and Planetary Interiors*, *120*(1-2), 153-163.

Mao, H. K., Bell, P. M., Shaner, J. T., & Steinberg, D. J. (1978). Specific volume measurements of Cu, Mo, Pd, and Ag and calibration of the ruby R 1 fluorescence pressure gauge from 0.06 to 1 Mbar. *Journal of applied physics*, *49*(6), 3276-3283.

Matsui, M., & Busing, W. R. (1984). Calculation of the elastic constants and high-pressure properties of diopside, CaMgSi/sub 2/O/sub 6. *American Mineralogist*, *69*, 1090-1095

Mauler, A., Burlini, L., Kunze, K., Philippot, P., & Burg, J. P. (2000). P-wave anisotropy in eclogites and relationship to the omphacite crystallographic fabric. *Physics and Chemistry of the Earth, Part A: Solid Earth and Geodesy*, *25*(2), 119-126.

McCormick, T. C., Hazen, R. M., & Angel, R. J. (1989). Compressibility of omphacite to 60 kbar; role of vacancies. *American Mineralogist, 74*(11-12), 1287-1292.

Moghadam, R. H., Trepmann, C. A., Stöckhert, B., & Renner, J. (2010). Rheology of synthetic omphacite aggregates at high pressure and high temperature. *Journal of Petrology, 51*(4), 921-945.

Nishihara, Y., Takahashi, E., Matsukage, K., & Kikegawa, T. (2003). Thermal equation of state of omphacite. *American Mineralogist, 88*(1), 80-86.

Pandolfo, F., Cámara, F., Domeneghetti, M. C., Alvaro, M., Nestola, F., Karato, S. I., & Amulele, G. (2015). Volume thermal expansion along the jadeite–diopside join. *Physics and Chemistry of Minerals, 42*(1), 1-14.

Pandolfo, F., Nestola, F., Cámara, F., & Domeneghetti, M. C. (2012a). High-pressure behavior of space group P 2/n omphacite. *American Mineralogist, 97*(2-3), 407-414.

Pandolfo, F., Nestola, F., Cámara, F., & Domeneghetti, M. C. (2012b). New thermoelastic parameters of natural C2/c omphacite. *Physics and Chemistry of Minerals, 39*(4), 295-304.

Pavese, A., Bocchio, R., & Ivaldi, G. (2000). In situ high temperature single crystal X-ray diffraction study of a natural omphacite. *Mineralogical Magazine,* 64(6), 983–993.

Pavese, A., Diella, V., Levy, D., & Hanfland, M. (2001). Synchrotron X-ray powder diffraction study of natural P2/n-omphacites at high-pressure conditions. *Physics and Chemistry of Minerals, 28*(1), 9-16.

Peacock, S. M. (1996). Thermal and petrologic structure of subduction zones. *Subduction: top to bottom, 96,* 119-133.

Ranganathan, S. I., & Ostoja-Starzewski, M. (2008). Universal elastic anisotropy index. *Physical Review Letters, 101*(5), 055504.

Reichmann, H. J., Sinogeikin, S. V., Bass, J. D., & Gasparik, T. (2002). Elastic Moduli of Jadeite-Enstatite Majorite. *Geophysical research letters, 29*(19).

Supporting Information

II.1. Calculation of the ambient isothermal bulk modulus K_{T0}

In a typical high-P single-crystal XRD experiment, the sample crystal is loaded in a DAC with soft P-transmitting media and is subject to a relatively uniform stress field. Therefore, it would be expected to obey the Reuss (iso-stress) bound of the bulk modulus. The ambient isothermal bulk modulus K_{T0} can be calculated from the Reuss bond of the adiabatic bulk modulus K_{S0}^{R} using the equation:

$$K_{T0} = \frac{K_{S0}^{R}}{1+\alpha\gamma_G T} \quad \text{(II.S1)}$$

Where α is the thermal expansion coefficient; γ_G is the Grüneisen parameter. The Reuss bond K_{S0}^{R} is calculated from the ambient C_{ij} tensor measured in this study (Section 3.2). The term $\alpha\gamma_G T$ is estimated to be ~ 0.01 for pyroxenes at 300 K (Nishihara et al., 2003). Thus, K_{T0} is calculated to be 118.7 GPa.

II.2. Definition of the Holland-Powell thermal-P EOS

The Holland-Powell thermal-P EOS is defined as:

$$P(V,T) = P(V,T_0) + P_{th}(V,T) \quad \text{(II.S2)}$$

$P(V, T_0)$ term corresponds to the P calculated with the 3rd order Birch-Murnaghan EOS (Birch, 1947). The thermal-P term $P_{th}(V, T)$ is calculated from:

$$P_{th}(V,T) = P\left(V,T_{ref}\right) + \alpha_0 K_{T0}\left(\frac{\theta_E}{\xi_0}\right)\left(\frac{1}{exp\left(\frac{\theta_E}{T}\right)-1} - \frac{1}{exp\left(\frac{\theta_E}{T_{ref}}\right)-1}\right) \quad \text{(II.S3)}$$

where T_{ref} is 300 K in this study, and θ_E is the Einstein temperature, which is fixed to 520 K for omphacite according to Holland and Powell (2011). The ξ_0 can be calculated by:

$$\xi_0 = \frac{\left(\frac{\theta_E}{T_{ref}}\right)^2 exp\left(\frac{\theta_E}{T_{ref}}\right)}{\left(exp\left(\frac{\theta_E}{T_{ref}}\right)-1\right)^2}. \quad \text{(II.S4)}$$

II.3. Definition of the anisotropy indices:

Universal Anisotropy Index (A^U) is defined as:

$$A^U = 5\frac{G^V}{G^R} + \frac{K_S{}^V}{K_S{}^R} - 6 \quad \text{(II.S5)}$$

The superscripts R and V refer to the Reuss and Voigt bounds of the homogeneous isotropic aggregate under VRH averaging scheme (Hill, 1963).

The Vp and Vs azimuthal anisotropy A^{Vp} and A^{Vs}, and Vs polarization anisotropy D^{Vs} are defined as:

$$A^{Vp} = \frac{Vp_{max} - Vp_{min}}{Vp_{VRH}} \quad \text{(II.S6)}$$

$$A^{Vs} = \frac{Vs_{max} - Vs_{min}}{Vs_{VRH}} \quad \text{(II.S7)}$$

$$D^{Vs} = \frac{|Vs_1 - Vs_2|_{max}}{Vs_{VRH}} \quad \text{(II.S8)}$$

The subscript VRH represents the VRH average calculated from the known C_{ij}s (Hill, 1963).

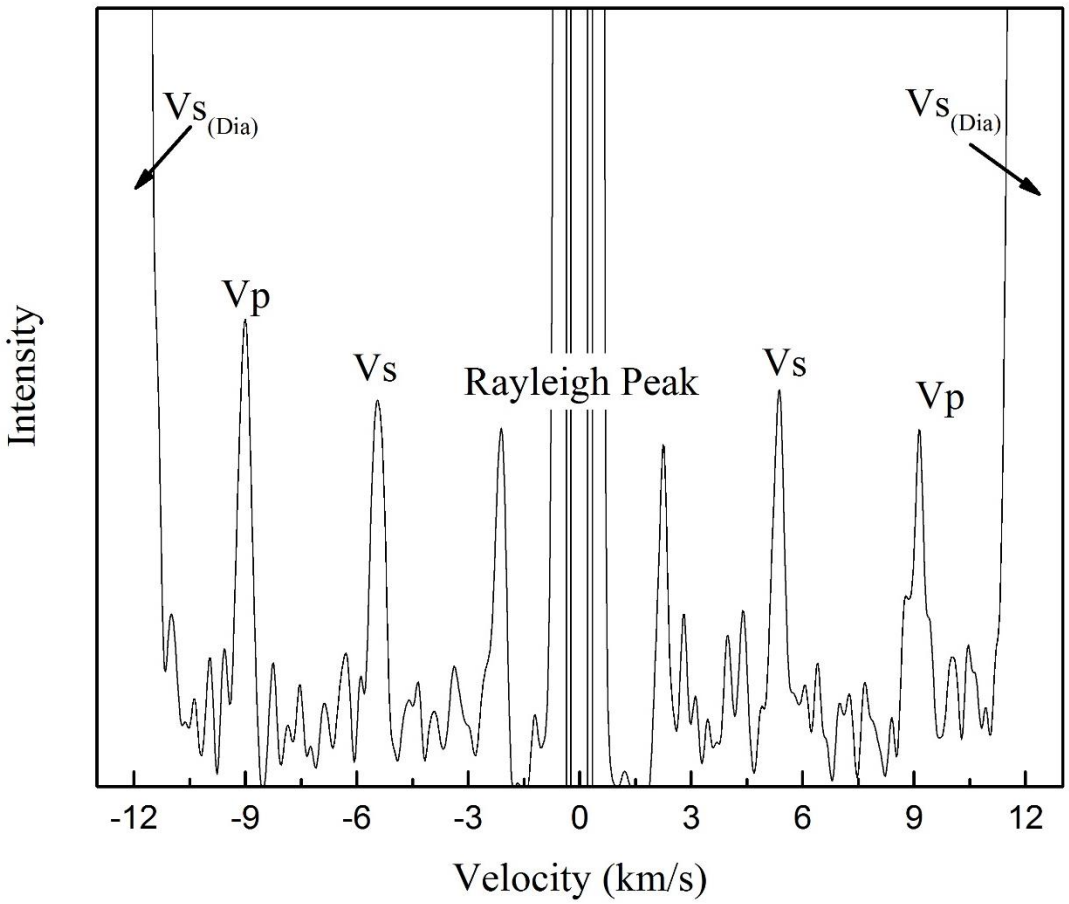

Figure II.S7. A typical the Brillouin spectrum at 18 GPa. One or two Vs associated with one Vp are observed. Neon peaks are too weak at 18 GPa to be observed.

Elements	Wt%	Component	Mole percent
Na	3.07	$NaAlSi_2O_6$	27.2
Mg	7.10	$NaFeSi_2O_6$	1.6

Al	4.02	$CaAl_2SiO6$	2.5
Si	25.58	$Ca_2Si_2O_6$	32.6
Ca	12.57	$Mg_2Si_2O_6$	31.5
Fe	2.79	$Fe_2Si_2O_6$	4.6
O	44.28	Total	100
Total	99.42		

Table II.S2. Chemical composition of the omphacite sample. The EPMA is performed using the JEOL 8200 Electron Microprobe facility hosted by the Institute of Meteroritics at UNM. Experimental conditions can be found from the main text section 2.

T (K)	P (GPA)	a (Å)	b (Å)	c (Å)	β (°)	V ($Å^3$)	Peak number
298	0	9.584(7)	8.83(2)	5.2504(4)	105.27(9)	429(1)	990
298	1.2(1)	9.547(6)	8.797(7)	5.246(2)	105.42(4)	424.7(4)	244
298	4.4(1)	9.499(5)	8.739(6)	5.196(1)	105.78(3)	415.1(4)	282
298	6.0(1)	9.478(4)	8.688(5)	5.175(1)	105.92(2)	409.8(3)	278
298	6.8(1)	9.468(5)	8.675(5)	5.166(1)	105.97(2)	407.9(3)	271
298	7.8(1)	9.452(5)	8.650(5)	5.151(1)	106.07(2)	404.7(3)	266
298	9.7(2)	9.421(5)	8.625(6)	5.123(2)	106.10(3)	399.9(4)	264
298	11.5(1)	9.403(5)	8.579(6)	5.113(1)	106.23(3)	396.1(4)	220
298	12.8(1)	9.394(5)	8.542(5)	5.099(1)	106.27(2)	392.8(3)	273
298	14.4(2)	9.376(5)	8.507(5)	5.082(1)	106.36(2)	388.9(3)	283
298	16.2(2)	9.360(5)	8.469(5)	5.067(1)	106.42(2)	385.3(3)	291
298	17.6(1)	9.342(4)	8.449(5)	5.057(1)	106.42(2)	382.9(3)	275
298	18.2(3)	9.339(4)	8.445(4)	5.048(1)	106.47(2)	381.8(3)	259
373	2.9(2)	9.557(5)	8.729(7)	5.229(2)	105.231(7)	420.9(4)	278
373	4.0(1)	9.534(4)	8.681(6)	5.217(2)	105.37(4)	416.3(3)	315
373	6.3(2)	9.505(4)	8.618(5)	5.182(1)	105.52(3)	409.1(3)	302
373	8.1(3)	9.483(4)	8.585(5)	5.162(2)	105.62(4)	404.7(3)	318
373	9.8(1)	9.464(4)	8.548(5)	5.140(2)	105.77(3)	400.2(3)	280
373	11(3)	9.447(3)	8.512(5)	5.132(2)	105.78(3)	397.1(3)	287
500	3.4(2)	9.556(4)	8.706(5)	5.228(2)	105.26(4)	419.6(4)	305
500	5.4(2)	9.522(4)	8.675(5)	5.192(2)	105.51(4)	413.3(4)	292
500	9.9(2)	9.461(5)	8.549(6)	5.146(2)	105.73(4)	400.6(4)	303
500	11.4(2)	9.448(5)	8.522(6)	5.127(2)	105.83(4)	397.1(4)	288
500	14.5(2)	9.404(4)	8.459(5)	5.098(2)	105.91(4)	390.0(3)	285
700	4.9(2)	9.55(1)	8.711(2)	5.204(1)	105.26(3)	417.9(5)	92
700	5.7(1)	9.52(2)	8.705(5)	5.201(2)	105.65(6)	415.0(9)	339
700	9.8(2)	9.473(9)	8.588(2)	5.150(1)	105.80(3)	403.1(4)	278
700	11.3(2)	9.459(4)	8.551(5)	5.140(1)	105.77(3)	400.1(3)	305

Table II.S3. Unit cell parameters of the omphacite at various P-T conditions.

	This study	Bhagat et al. [1992]
ρ (g/cm^3)	3.34(1)	3.327(2)
composition	$Diopside_{70.5}Jadeite_{29.5}$	$Diopside_{34.1}Jadeite_{65.9}$
C_{11} (GPa)	231.5(8)	257(1)
C_{22} (GPa)	201(1)	216.2(8)
C_{33} (GPa)	253.8(8)	260.2(7)
C_{44} (GPa)	79.1(5)	80.2(6)
C_{55} (GPa)	68.9(4)	70.6(4)
C_{66} (GPa)	74.0(4)	85.8(5)
C_{12} (GPa)	84.4(9)	86(1)
C_{13} (GPa)	76(1)	76(1)
C_{23} (GPa)	60(2)	71(1)
C_{15} (GPa)	7.6(5)	7.1(6)
C_{25} (GPa)	5(1)	13(1)
C_{35} (GPa)	39.8(5)	33.7(8)
C_{46} (GPa)	5.9(4)	10.2(3)
K_S^R (GPa)	119.9(5)	128.0(5)
G^R (GPa)	71.9(2)	77.7(2)
K_S^V (GPa)	125.3(5)	133.5(5)
G^V (GPa)	75.4(2)	80.6(2)
K_S (GPa)	123(3)	130.8(5)
G (GPa)	74(2)	79.2(2)
Vp (km/s)	8.13(4)	8.43(4)
Vs (Km/s)	4.70(3)	4.88(3)

Table II.S4. Single-crystal elastic properties of omphacite at ambient condition.

	Omphacite			Diopside (Sang & Bass, 2014)		
	M_0 (GPa)	$\partial M/\partial P$	$\partial M^2/\partial P^2$ (GPa^{-1})	M_0 (GPa)	$\partial M/\partial P$	$\partial M^2/\partial P^2$ (GPa^{-1})
C_{11}	231.5(8)	8.3(3)	-0.24(6)	229.0(4)	6.7(2)	-0.16(4)
C_{22}	201(1)	4.92(7)	0	179.0(4)	6.7(3)	-0.23(6)
C_{33}	253.8(8)	7.8(3)	-0.29(5)	242.5(4)	7.9(2)	-0.28(4)
C_{44}	79.1(5)	0.96(3)	0	78.9(3)	1.5(1)	0
C_{55}	68.9(4)	1.03(2)	0	68.1(2)	2.2(2)	-0.15(4)
C_{66}	74.0(4)	2.41(4)	0	78.2(3)	2.05(9)	0
C_{12}	84.4(9)	4.6(4)	-0.13(6)	78.0(7)	4.9(6)	-0.3(1)
C_{13}	76(1)	3.13(7)	0	69.8(6)	4.5(2)	-0.18(4)
C_{23}	60(2)	2.94(15)	0	58.0(7)	3.2(2)	0
C_{15}	5.8(5)	0	0	9.9(3)	-0.8(1)	0.10(3)
C_{25}	5.4(10)	0.5(1)	0	6.1(5)	-1.1(2)	0
C_{35}	39.8(5)	-2.3(1)	0.18(2)	40.9(3)	-1.3(2)	0.05(3)
C_{46}	5.9(4)	0.73(3)	-0.148(6)	6.6(2)	-1.7(3)	0.26(7)
	Olivine (Zhang et al., 2018)			Orthopyroxene (Zhang & Bass, 2016)		
	M_0 (GPa)	$\partial M/\partial P$	$\partial M^2/\partial P^2$ (GPa^{-1})	M_0 (GPa)	$\partial M/\partial P$	$\partial M^2/\partial P^2$ (GPa^{-1})
C_{11}	320.1(6)	7.2(3)	-0.05(1)	232.2(5)	12.6(4)	-1.3(1)
C_{22}	197.1(6)	5.9(1)	-0.08(1)	175.7(7)	10.2(4)	-0.8(1)
C_{33}	233.4(8)	5.3(1)	-0.03(1)	222.9(6)	13.5(6)	-1.3(2)
C_{44}	63.6(5)	1.91(4)	-0.037(2)	82.2(4)	3.0(2)	-0.42(5)
C_{55}	77.3(4)	1.53(5)	-0.023(2)	77.3(3)	2.6(2)	-0.34(8)
C_{66}	78(2)	2.11(6)	-0.024(2)	78.1(6)	4.4(5)	-0.6(2)
C_{12}	70(1)	3.8(1)	-0.03(1)	79.5(9)	6.9(3)	-0.5(1)
C_{13}	70.9(6)	3.7(1)	-0.011(4)	61.2(6)	8.6(5)	-0.9(2)
C_{23}	75.6(8)	3.35(7)	0	54.1(8)	8.4(4)	-0.7(1)

Table II.S5. Pressure derivatives of the single-crystal elastic moduli of omphacite, diopside, olivine and orthopyroxene. $\partial M/\partial P$ and $\partial M^2/\partial P^2$ values presented here are the first and second pressure derivatives defined by the finite strain equations of state in Davies (1974). M_0 is the value at ambient condition and is fixed.

Mineral	Density (g/cm^3)	K_{S0} (GPa)	dK_S/dP	dK_S/dT (GPa/K)	G_0 (GPa)	dG/dP	dG/dT (GPa/K)	a_0 (10^{-4} K^{-1})	a_1 (10^{-8} K^{-2})	a_2 (K)
Omphacite[1]	3.34(1)	123(3)	4.5(3)	-0.012(1)	74(2)	1.6(1)	-0.011(1)	0.27(8)	0	0
Pyrope[2,3,4,5,8]	3.56(2)	164.4(5)	4.4(1)	-0.014(3)	94.9(2)	1.15(6)	-0.011(2)	0.288	0.2787	-0.5521
Mg-majorite[2,3,4,5,8]	3.56(2)	162(5)	4.4(1)	-0.014(3)	86.2(2)	1.15(6)	-0.011(2)	0.288	0.2787	-0.5521
Jd-majorite[6,7]	3.644(7)	178(4)	4.47(2)	-0.0138(3)	125(2)	1.29(5)	-0.0128(2)	0.1951	0.8089	-0.4972
Grossular[7,8]	3.605(2)	171.2(8)	4.47(2)	-0.0138(3)	107.4(2)	1.29(5)	-0.0128(2)	0.1951	0.8089	-0.4972
Almandine[9]	4.3188(2)	174.2(12)	4.61(14)	-0.0267(7)	94.9(7)	1.06(6)	-0.0131(8)	0.26(5)	2.3(14)	0
Coesite[10,11]	2.91(2)	106.5(6)	2.7(15)	-0.0016(16)	60.7(3)	0.33(5)	-0.0044(5)	0.106(14)	-0.028(166)	-0.48(12)
Stishovite[12]										

1. Li and Neuville (2010) 2. Irifune et al. (2008) 3. Liu et al. (2000) 4. Sinogeikin and Bass (2002) 5. Suzuki and Anderson (1983) 6. Reichmann et al. (2002) 7. Gwanmesia et al. (2014) 8. Fei (1995) 9. Arimoto et al. (2015) 10. Chen et al. (2017) 11. Kulik et al. (2018) 12. Yang and Wu (2014)

Table II.S6. Thermo-elastic parameters of all the relevant mineral phases for calculating the aggregate elastic properties of eclogite. The a_0, a_1 and a_2 are the thermal expansion parameters, defined in Fei's (1995): $a(T)=a_0+a_1T+a_2T^{-2}$. The thermal expansion parameters obtained from Fei (1995) are without uncertainties. The aggregate sound velocity data of stishovite are directly obtained from the theoretical calculation study by Yang and Wu (2014). The parameters (except the thermal expansion parameters) for pyrope and coesite are recalculated based on the experimental values presented in Irifune et al. (2008) and Chen et al. (2017).

Chapter III

The single-crystal elastic properties of the jadeite-diopside solid solution and their implications for the composition dependent seismic properties of eclogite

Abstract

The 13 single-crystal adiabatic elastic moduli (C_{ij}) of a *C2/c* jadeite sample close to the ideal composition ($NaAlSi_2O_6$) and a natural *P2/n* diopside-rich omphacite sample have been measured at ambient condition by Brillouin spectroscopy. The obtained C_{ij}s for the jadeite sample are: C_{11} = 265.4(9) GPa, C_{22} = 247(1) GPa, C_{33} = 274(1) GPa, C_{44} = 85.8(7) GPa, C_{55} = 69.3(5) GPa, C_{66} = 93.0(7) GPa, C_{12} = 84(1) GPa, C_{13} = 66(1) GPa, C_{23} = 87(2) GPa, C_{15} = 5.4(7) GPa, C_{25} = 17(1) GPa, C_{35} = 28.7(6) GPa, C_{46} = 14.6(6) GPa. Voigt-Reuss-Hill averaging of the C_{ij}s yields aggregate bulk modulus K_S = 138(3) GPa and shear modulus G=84(2) GPa for jadeite. Systematic analysis combing previous single-crystal elasticity measurements within the diopside-jadeite solid solution indicates that the linear trends are valid for most C_{ij}s. The *Vp* and *Vs* of omphacite decrease with Di content, though the velocity changes are small as Di component exceeds 70%. We also found that both the isotropic *Vp* and *Vs* as well as the seismic anisotropy of eclogite changed strongly with the bulk chemical composition. The relationship between the anisotropic velocities of eclogite and the chemical composition can be a useful tool to trace the origin of the eclogitic materials in the Earth's mantle.

1. Introduction

Clinopyroxene (Cpx) is one of the major mineral phases in the Earth's upper mantle (Ringwood, 1975; Anderson & Bass, 1984). The chemical composition of the upper mantle

Cpx is close to Fe-bearing diopside (Di, $CaMgSi_2O_6$), with significant jadeite (Jd, $NaAlSi_2O_6$) component (e.g., Nestola et al., 2016). The crust of the subducted slabs and the delaminated lithosphere from continental roots form eclogite at depth >70-100 km (Irifune et al., 1986; Kay & Kay, 1993). Cpx constitutes up to 70% of natural eclogite. The Cpx in eclogite is essentially Fe-bearing omphacite, which is the solid solution between Di and Jd. The coupled substitution of (Ca, Mg) for (Na, Al) in the Di-Jd solid solution stiffens the crystal structure, which has been confirmed by both the high-pressure single-crystal X-ray diffraction experiments and the sound velocity measurements (Pandolfo et al., 2012; Nestola et al., 2006; Sang et al., 2011; Kandelin & Weidner, 1988; Zhang et al., 2016). The bulk (K_S) and shear (G) moduli of the end member Jd are ~25% and ~18% higher, respectively, than the end member Di (Sang et al., 2011; Kandelin & Weidner, 1988). In the Di-Jd solid solution, the chemical composition strongly influences the elastic properties and therefore, should be considered for modeling the seismic properties of pyrolite and eclogite.

The general chemical formula of Cpx is $(M2M1)Si_2O_6$. The M2 site is usually occupied by cations with larger ionic radii, such as Ca^{2+} and Na^{+}. The M1 site is slightly smaller, thus preferred by smaller cations, such as Mg^{2+} and Al^{3+}. At low-temperature conditions, the cations in the M1 and M2 sites are usually ordered, and the omphacite crystals show a lower *P2/n* symmetry, compared with the higher *C2/c* symmetry of the Di and Jd end members. As temperature increases, the ordering of the cations degrades in both the M1 and M2 sites, and eventually, the ordered *P2/n* structure will convert to a completely disordered *C2/c* structure at temperatures higher than ~725 ℃ (Fleet et al., 1978; Carpenter, 1980).

Previous high-pressure equation of state studies in the Di-Jd solid solution (e.g., Pandolfo et al., 2012; Nestola et al., 2006; Zhang et al., 2016) provided constraints to the

composition dependent isothermal bulk modulus (K_T). However, determination of the seismic velocities and elastic anisotropy requires direct single-crystal sound velocity measurements. The single-crystal elastic properties of Cpx with close to upper mantle chemical compositions have been studied previously (Levien et al., 1979; Sang et al., 2011; Collins & Brown, 1998; Isaak & Ohno, 2003; Bhagat et al., 1992; Walker, 2012; Norris, 2008; Skelton & Walker, 2015). Levien et al. (1979) first measured the single-crystal elasticity of the Di end member using Brillouin spectroscopy, and the results were improved in a more recent study by Sang et al. (2011). Isaak and Ohno (2003) measured a Cr-bearing Di using resonant ultrasound spectroscopy, which agrees well with Sang et al. (2011), suggesting that the incorporation of small amounts of Cr has no resolvable effect on the elastic properties. A Cpx with more realistic and complicated upper mantle composition was measured by Collins and Brown (1998) using the stimulated light scattering technique. They found some irregular trends that deviate from linear mixing models for C_{55}, C_{66}, and C_{35}. Omphacite has only once been measured at ambient condition by Bhagat et al. (1992). The sample used by Bhagat et al. (1992) is Jd-rich, whereas no single-crystal elasticity measurements are available for the Di-rich omphacites. Walker (2012) and Skelton and Walker (2015) theoretically calculated the C_{ij}s of Di, Jd, and $Di_{50}Jd_{50}$ at 0 K. They found that the linear mixing model did not work for C_{11}, C_{12}, C_{13}, and C_{23}. However, it remains unknown whether their conclusion still holds at temperatures higher than 0 K.

To improve our understanding of the single-crystal elastic properties of omphacite in the Di-Jd solid solution, we have measured the elastic properties of a *C2/c* Jd and a *P2/n* Di-rich omphacite at ambient condition. The accuracy and precision of the single-crystal Brillouin spectroscopy measurements are much better compared to several decades ago (Zhang et al.,

2011; Bass & Zhang, 2015). Employing the new results obtained in this study, we reanalyzed the elastic properties of the Di-Jd solid solution and explored the compositional effects on the seismic properties of eclogite over a wide compositional range.

2. Experimental methods

The compositions of the natural Jd and omphacite samples were measured by electron probe microanalysis (EPMA), using the JEOL 8200 Electron Microprobe facility hosted by the Institute of Meteoritics at University of New Mexico (UNM). Approximately 1 mm size crystals were polished and used for EPMA analysis, operating at 15 kV accelerating voltage and 20 nA beam current. The element standards were albite for Na, forsterite for Mg, almandine for Al and Fe, diopside for Si and Ca. Oxygen was calculated by stoichiometry from the cations. The detailed analysis results are summarized in Table III.1. Normalizing the chemical analysis in terms of Di and Jd yields simplified compositions of $Di_{3.2}Jd_{96.8}$ for the Jd sample, $Di_{70.5}Jd_{29.5}$ for the omphacite sample. The crystals were then double-side polished into pellets with ~15 μm thickness. They were scratch-free and inclusion-free under optical examination.

The unit-cell parameters and crystallographic orientations for all samples were determined by single-crystal X-ray diffraction at GeoSoilEnviroCARS experimental station

Elements	$Di_{70.5}Jd_{29.5}$ (Wt%)	$Di_{3.2}Jd_{96.8}$ (Wt%)
Na_2O	4.13	14.65
MgO	11.77	0.42
Al_2O_3	7.59	24.42
SiO_2	54.73	59.62
CaO	17.59	0.81
FeO	3.59	0.69
Total	99.42	100.62

Table III.1. The chemical composition of the Cpx samples used in this study.

13-BM-D, Advanced Photon Source, Argonne National Laboratory. The X-ray was monochromated to 37.0 keV and focused to 3-4 μm × 7-8 μm. A stationary Perkin-Elmer image plate was used as the detector. Diffraction images were collected at 1°/step for the ±16° opening and the exposure time was 5 s/°. The obtained unit-cell parameters are: a = 9.439(5), b = 8.583(4), c = 5.228(1) Å, β = 107.50(2)°, and V_0 = 404.0(3) Å^3 (density ρ = 3.302(5) g/cm^3) for $Di_{3.2}Jd_{96.8}$; a = 9.632(3), b = 8.843(3), c = 5.245(1) Å, β = 106.31(2)°, and V_0 = 428.8(2) Å^3 (density ρ = 3.339(2) g/cm^3) for $Di_{70.5}Jd_{29.5}$. The space groups are also confirmed to be *C2/c* and *P2/n* for the Jd and omphacite sample, respectively.

For each sample, we used 3 different orientations for the single-crystal Brillouin spectroscopy measurements. The face normals of the measured samples are: (-0.692, 0.714, -

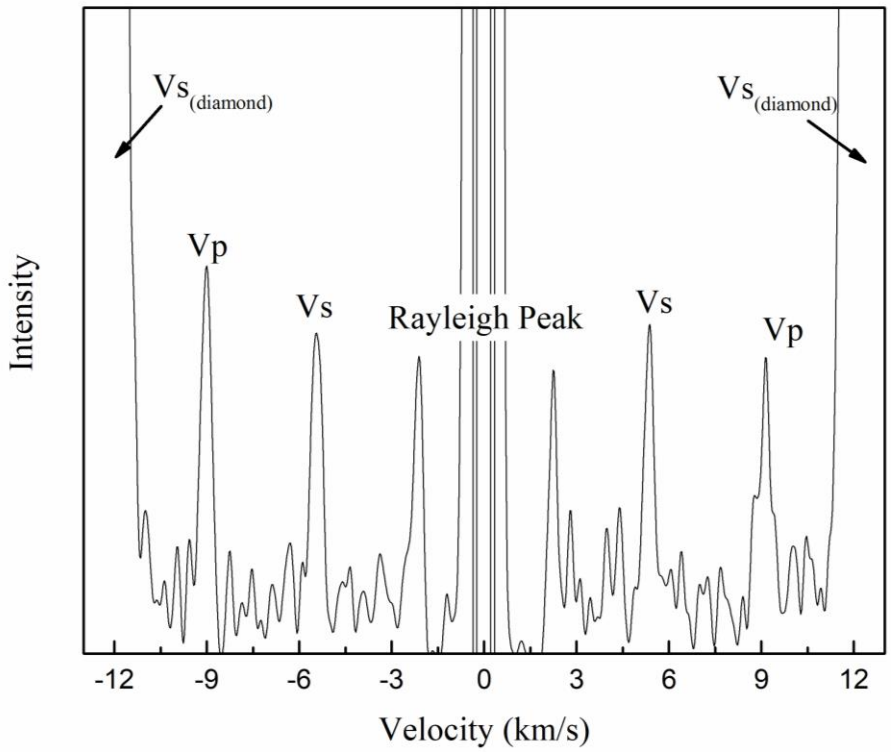

Figure III.1. A typical the Brillouin spectrum showing one *Vs* and one *Vp* from the sample.

0.106), (0.116, 0.993, -0.021), and (-0.043, 0.13, -0.999) for $Di_{3.2}Jd_{96.8}$; (-0.044, 0.979, 0.197), (0.242, 0.299, -0.923), and (0.697, 0.717, -0.016) for $Di_{70.5}Jd_{29.5}$. The accuracy of the measured plane normals is 0.5° or better.

The Brillouin spectroscopy experiments were performed in the high-pressure laser spectroscopy laboratory at UNM. We used a 300 mW 532 nm single-mode diode-pumped solid-state laser as the light source. The measurements were carried out using a 50° symmetric forward scattering geometry. The scattering angle was calibrated to be 50.37(5)° using a standard silica glass Corning 7980 (Zhang et al., 2011, 2015). For each crystal, shear velocities (*Vs*) and compressional velocities (*Vp*) were measured at 13 different χ angles (0, 30, 60, 90, 120, 150, 180, 195, 225, 255, 285, 315, 345) along the 360° azimuth to avoid any geometrical errors. All Brillouin spectra are with excellent signal-to-noise ratios. A typical Brillouin spectrum is shown on Figure III.1.

3. Results and discussion

A least square inversion of the Christoffel equation was used to calculate the best-fit values for the 13-independent C_{ij}s at ambient condition (Weidner & Carleton, 1977). The measured velocities associated with the velocity model predicted by the C_{ij} model of Jd are shown on Figure III.2. The ambient K_S and G were calculated using the Voigt-Reuss-Hill (VRH) averaging scheme (Hill, 1963). The K_S and G are 138(3) GPa and 84(2) GPa for $Di_{3.2}Jd_{96.8}$, and 123(3) GPa and 73(2) GPa for $Di_{70.5}Jd_{29.5}$, respectively.

Table III. 2 shows a complete list of the C_{ij}s obtained in this study alongside with both the results of the end member Jd measured by Kandelin and Weidner (1988), and those of the Jd-rich omphacite determined by Bhagat et al. (1992). The C_{ij}s of the $Di_{3.2}Jd_{96.8}$ sample

measured in this study are in general agreement, yet with much smaller uncertainties, compared with Kandelin and Weidner (1988). The small amount of the Di component in our Jd sample may explain the smaller C_{12} and K_S determined in this study. As expected, most C_{ij}s of the $Di_{70.5}Jd_{29.5}$ sample measured in this study are smaller than the values of the $Di_{34.1}Jd_{65.9}$

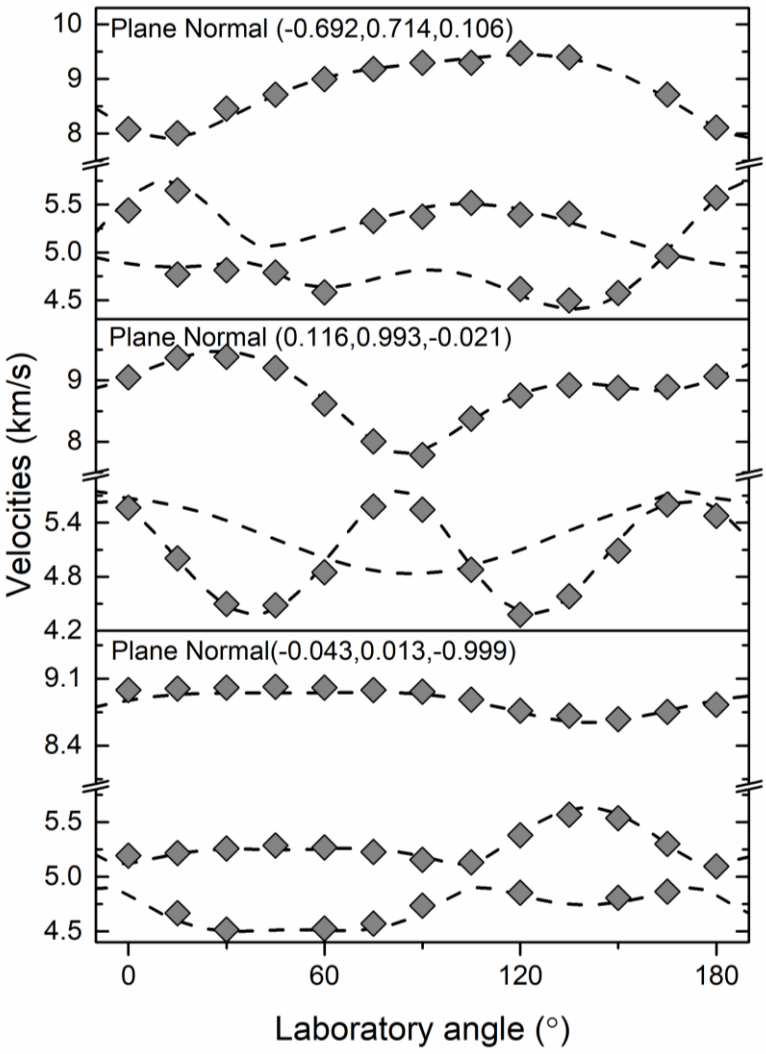

Figure III.2. Measured acoustic velocities of Jd as a function of laboratory χ angles within the sample plane. Dashed lines are the acoustic velocities calculated from the best-fit single-crystal elasticity model; diamonds are the experimentally determined velocities. Errors are within the size of the symbols.

omphacite measured by Bhagat et al. (1992).

Figure III.3 shows the elastic moduli change as a function of chemical composition in the Di-Jd solid solution (Kandelin & Weidner, 1988; Sang et al., 2011; Bhagat et al., 1992;

	Jd		Omphacite	
ρ (g/cm^3)	3.302(5)	3.33	3.339(2)	3.327(2)
composition	$Di_{3.2}Jd_{96.8}$ This study	Jd Kandelin and Weidner (1988)	$Di_{70.5}Jd_{29.5}$ This study	$Di_{34.1}Jd_{65.9}$ Bhagat et al. (1992)
C_{11} (GPa)	265.4(9)	274(4)	231.7(8)	257(1)
C_{22} (GPa)	247(1)	253(4)	202(1)	216.2(8)
C_{33} (GPa)	274(1)	282(3)	255.2(9)	260.2(7)
C_{44} (GPa)	85.8(7)	88(2)	78.4(5)	80.2(6)
C_{55} (GPa)	69.3(5)	65(4)	68.9(5)	70.6(4)
C_{66} (GPa)	93.0(7)	94(2)	73.6(4)	85.8(5)
C_{12} (GPa)	85(1)	94(2)	85(1)	86(1)
C_{13} (GPa)	66(1)	71(8)	77(1)	76(1)
C_{23} (GPa)	87(2)	82(4)	58(2)	71(1)
C_{15} (GPa)	5.4(7)	4(3)	7.8(5)	7.1(6)
C_{25} (GPa)	17(1)	14(4)	6(1)	13(1)
C_{35} (GPa)	28.7(6)	28(3)	39.5(5)	33.7(8)
C_{46} (GPa)	14.6(6)	13(1)	6.3(4)	10.2(3)
$K_S{}^R$ (GPa)	135.9(7)	141(2)	119.7(6)	128.0(5)
G^R (GPa)	82.7(3)	83(2)	72.0(3)	77.7(2)
$K_S{}^V$ (GPa)	140.1(7)	145(2)	125.3(6)	133.5(5)
G^V (GPa)	86.3(3)	87(1)	75.5(3)	80.6(2)
K_S (GPa)	138(3)	143(2)	122(3)	130.8(5)
G (GPa)	84(2)	85(2)	74(2)	79.2(2)
V_p (km/s)	8.71(4)	8.77(5)	8.13(4)	8.43(4)
V_s (Km/s)	5.06(3)	5.05(5)	4.70(3)	4.88(3)
RMS error (m/s)	42.2	\	38.8	49

Table III.2. Single-crystal elastic properties of different Cpx samples at ambient condition. The superscripts R and V refer to the Reuss and Voigt bounds of the homogeneous isotropic aggregate under VRH averaging scheme.

Collins & Brown, 1998; Isaak & Ohno, 2003). We have utilized the following empirical polynomial function to describe the compositional dependence of the elastic moduli:

$$E = a_0 + a_1 * c + a_2 * c^2 \quad \text{(III.1)}$$

where E represents the elastic properties, including the C_{ij}s, K_S, and G; c is the proportion of the Di component in the Di-Jd solid solution; a_0, a_1, and a_2 are the fitting parameters shown in Table III.3. The red shaded regions in Figure III.3 represent the 95% confidence intervals. Similar to the negative correlation between the Di content and the K_T determined by previous X-ray diffraction experiments, the directly measured K_S and G linearly decrease with the Di

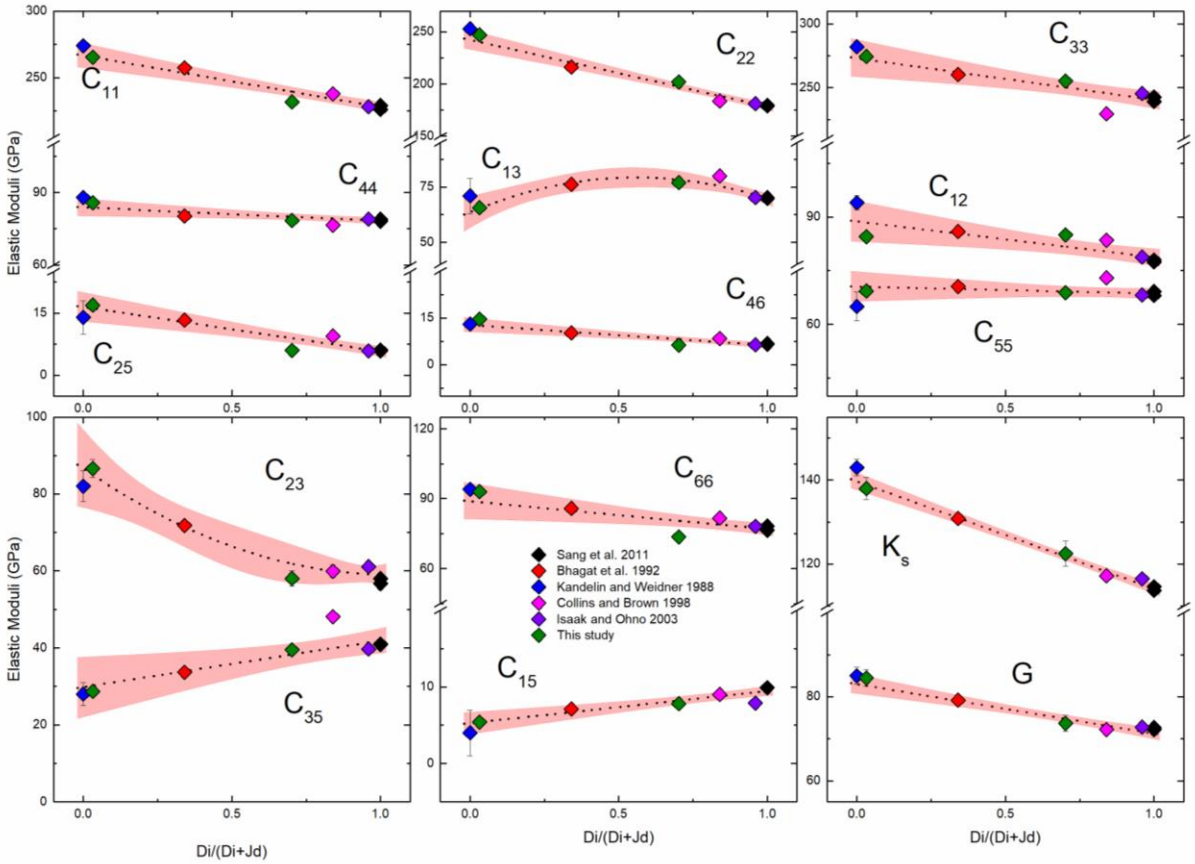

Figure III.3. C_{ij}s, K_S, and G as a function of chemical composition in the Di-Jd solid solution. The red shaded regions represent the 95% confidence intervals.

content as well. Actually, all single-crystal elastic moduli show close-to-linear relationships with the Jd and Di content, except C_{13} and C_{23}. The C_{13} and C_{23} of omphacite are slightly higher and lower, respectively, than the predicted values from linear mixing models. The omphacite sample we measured is Cr-free. In Figure III.3, most of the elastic moduli measured by Isaak and Ohno (2003) are actually within the shaded 95% confidence intervals. This confirms that a small amount of Cr does not have a noticeable influence on the elastic properties of Di as reported by Sang et al. (2011). It is also worth noting that the C_{33}, C_{55}, and C_{35} of the sample measured by Collins and Brown (1998) lie outside the trends determined from other measurements which may be explained by the high Tschermak's content (12mol%) of the sample measured by Collins and Brown (1998).

Skelton and Walker (2015) theoretically calculated the elastic properties of $Di_{50}Jd_{50}$ omphacite and compared with Walker (2012) to investigate the elasticity change within the

Elastic moduli	a_0	a_1	a_2
C_{11} (GPa)	267(4)	-39(4)	0
C_{22} (GPa)	243(4)	-64(4)	0
C_{33} (GPa)	273(6)	-33(7)	0
C_{44} (GPa)	84(1)	-5(2)	0
C_{55} (GPa)	71(2)	-2(2)	0
C_{66} (GPa)	89(4)	-12(4)	0
C_{12} (GPa)	89(2)	-10(3)	0
C_{13} (GPa)	64(3)	56(12)	-50(10)
C_{23} (GPa)	87(4)	-53(16)	26(13)
C_{15} (GPa)	5.3(7)	4.2(9)	0
C_{25} (GPa)	17(1)	-11(2)	0
C_{35} (GPa)	30(3)	12(4)	0
C_{46} (GPa)	12.8(9)	-6(1)	0
K_S (GPa)	139.7(8)	-26(1)	0
G (GPa)	83.1(9)	-12(1)	0

Table III.3. The polynomial fitting results for the compositional dependence of the elastic moduli in the Di-Jd solid solution. a_0, a_1 and a_2 are defined in Equation (III.1).

Di-Jd solid solution at 0 K. They found out that the C_{11}, C_{12}, C_{13}, and C_{23} of omphacite were off from the linear mixing trend of Di and Jd. In this study, the C_{13} and C_{23} of omphacite are indeed slightly higher and lower than the values predicted by the linear mixing model. However, the C_{11} and C_{12} actually agree well (Figure III.3). The difference between this study and Skelton and Walker (2015) may result from the temperature difference. Our measurements were carried out at room temperature whereas their calculation was performed at 0 K. Skelton and Walker (2015) suggested that the differential cation ordering between the M1 site and M2 site in omphacite caused the nonlinear mixing. In particular, the cations in the M2 site are more disordered than M1 at low temperatures. Elevating the temperature would disorder the cations within the crystal structure and result in a close to linear mixing trend. This might explain the absence of the nonlinear mixing trend in C_{11} and C_{12} observed in this study. The differences between the measured values and the predicted linear mixing values of C_{13} and C_{23} are also smaller than what were calculated by Skelton and Walker (2015). Further computational investigations at room-temperature condition can help us quantitatively understand the differences between this experimental study and previous theoretical investigations, as well as critically evaluate our explanations above.

4. Geophysical implications

Based on the measured single-crystal elastic properties, we calculated the aggregate *Vs* and *Vp* within the Di-Jd solid solution (Figure III.4a). Both the *Vp* and *Vs* display a nonlinear decrease with the Di content. The composition induced velocity change is negligible as the Di component exceeds 70%.

The Jd component of omphacite in natural eclogite varies from ~10% to ~65% (e.g., Coleman et al., 1965; Bhagat et al., 1992; Smyth et al., 1991). Based on the compositional

dependence of the omphacite velocities obtained in this study, and the existing sound velocity measurements of garnets (Sinogeikin & Bass, 2002; Gwanmesia et al., 2014; Arimoto et al., 2015), we calculated the *Vp* and *Vs* of 3 different eclogites at ambient condition assuming the Voigt averaging scheme (Table III.4, Coleman et al., 1965; Voigt, 1889). The *Vp* and *Vs* of eclogite increase with the Jd component in omphacite. In particular, the *Vp* and *Vs* differences between the eclogites 1 and 3 are as large as 3%. The bulk chemical composition of eclogite

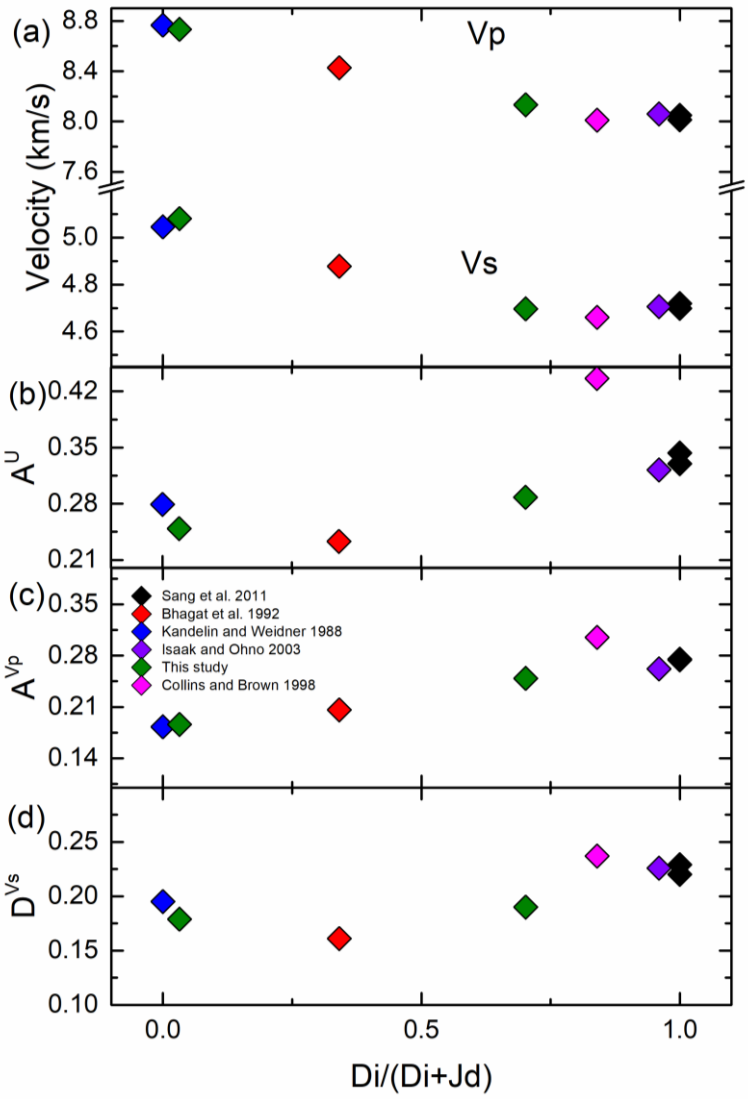

Figure III.4. The velocities, A^U, A^{Vp}, and D^{Vs} as a function of chemical composition.

depends on its parent rock. If the parent rock of eclogite has a strong continental and/or sediment component, the omphacite in eclogite will be enriched in Na and Al, and thus high in Jd content (Irifune et al., 1994). The relationship between the absolute velocities of eclogite and the chemical composition can be a useful tool to trace the origin of the eclogitic materials in the mantle.

Due to the elastically isotropic nature of the garnet, omphacite is the major anisotropy contributor in eclogite. Thus, in order to study the anisotropic seismic properties of eclogite, it is important to investigate the composition dependent elastic anisotropy in the Di-Jd solid solution.

In this study, universal anisotropy index (A^U), azimuthal *Vp* anisotropy (A^{Vp}) and radial *Vs* anisotropy (D^{Vs}) are calculated in the Di-Jd solid solution.

A^U is used as a measure of the overall elastic anisotropy for materials with arbitrary symmetry (Ranganathan & Ostoja-Starzewski, 2008):

		Eclogite 1	Eclogite 2	Eclogite 3
Omphacite	Jd	10.5%	21.0%	45.5%
	Di	59.5%	49.0%	24.5%
Garnet	Pyrope	20.1%	13.5%	4.8%
	Grossular	3.6%	4.8%	6.9%
	Almandine	5.7%	11.7%	18.3%
Vs (km/s)		4.76	4.79	4.90
Vp (km/s)		8.26	8.36	8.51

Table III.4. The end member mineral proportions, and calculated *Vp* and *Vs,* for the 3 eclogite samples. We assume the volume proportion of omphacite and garnet are 70% and 30% for all 3 eclogites.

$$A^U = 5\frac{G^V}{G^R} + \frac{{K_S}^V}{{K_S}^R} - 6 \quad \text{(III.2)}$$

where the superscripts R and V refer to the Reuss and Voigt bounds of the homogeneous isotropic aggregate under VRH averaging scheme.

A^{Vp} represents the maximum velocity difference of all *Vp* propagating along different directions:

$$A^{Vp} = \frac{Vp_{max} - Vp_{min}}{Vp} \quad \text{(III.3)}$$

D^{Vs}, which describes the maximum velocity difference between the 2 orthogonally polarized shear waves propagating along the same direction, is defined as:

$$D^{Vs} = \frac{|Vs_1 - Vs_2|_{max}}{Vs}. \quad \text{(III.4)}$$

Figure III.4b, III.4c, and III.4d show the anisotropy indices change as a function of chemical composition in the Di-Jd solid solution. The calculated anisotropy indices, especially the A^U and A^{Vp}, of the Cpx sample measured by Collins and Brown (1998), lie outside the trends determined from all the other studies. This again may be explained by its high Tschermak's content (12mol%). The Di end member has the highest A^U, A^{Vp}, and A^{Vs} within the Di-Jd solid solution. The A^{Vp} decreases linearly as the Jd component increases. The A^{Vp} of the Di end member is 60% higher than that of the Jd end member. The trends in D^{Vs} and A^U are not as clear. Jd-rich omphacite seems to have similar D^{Vs} and A^U as Jd. Nevertheless, the enrichment of Jd component in omphacite is likely to decrease the overall elastic anisotropy of Cpx. The single-crystal elasticity data presented in this study can serve as the basis for future anisotropy modeling based on the lattice preferred orientation of the omphacite crystals in

natural eclogite within a wide range of chemical compositions (Zhang et al., 2006; Zhang & Green, 2007).

Acknowledgement

The authors would like to thank Jane Silverstone (UNM), Jay Bass (UIUC) for providing the samples used in this study, Mike Spilde for the help with EPMA experiment at the Institute of Meteoritics at UNM. This work is supported by the National Science Foundation (NSF) under Grant EAR 1646527 (JZ) and the start-up fund from UNM (JZ). This research used resources of the APS, a U.S. DOE Office of Science User Facility operated for the DOE Office of Science by Argonne National Laboratory under Contract NO. DE-AC02-06CH11357.

References

Anderson, D.L. and Bass, J.D. (1984) Mineralogy and composition of the upper mantle. Geophysical Research Letters, 11, 637-40.

Arimoto, T., Gréaux, S., Irifune, T., Zhou, C., and Higo, Y. (2015) Sound velocities of $Fe_3Al_2Si_3O_{12}$ almandine up to 19 GPa and 1700 K. Physics of the Earth and Planetary Interiors, 246, 1-8.

Bass, J.D. and Zhang, J.S. (2015) Techniques for measuring high P/T elasticity. Schubert, Oxford.

Bhagat, S.S., Bass, J.D., and Smyth, J.R. (1992) Single-crystal elastic properties of omphacite-C2/c by Brillouin spectroscopy. Journal of Geophysical Research: Solid Earth, 97, 6843-6848.

Carpenter, M.A. (1980) Mechanisms of exsolution in sodic pyroxenes. Contributions to Mineralogy and Petrology, 71, 289-300.

Coleman, R.G., Lee, D.E., Beatty, L.B., and Brannock, W.W. (1965) Eclogites and eclogites: their differences and similarities. Geological Society of America Bulletin, 76, 483-508.

Collins, M.D. and Brown, J.M. (1998) Elasticity of an upper mantle clinopyroxene. Physics and Chemistry of Minerals, 26, 7–13.

Fleet, M.E., Herzberg, C.T., Bancroft, G.M., and Aldridge, L.P. (1978) Omphacite studies; I, The *P2/n* → *C2/c* transformation. American Mineralogist, 63, 1100-1106.

Gwanmesia, G.D., Wang, L., Heady, A., and Liebermann, R.C. (2014) Elasticity and sound velocities of polycrystalline grossular garnet ($Ca_3Al_2Si_3O_{12}$) at simultaneous high pressures and high temperatures. Physics of the Earth and Planetary Interiors, 228, 80-87.

Hill, R. (1963) Elastic properties of reinforced solids: some theoretical principles. Journal of the Mechanics and Physics of Solids, 11, 357-372.

Irifune, T., Ringwood, A.E., and Hibberson, W.O. (1994) Subduction of continental crust and terrigenous and pelagic sediments: an experimental study. Earth and Planetary Science Letters, 126, 351-368.

Irifune, T., Sekine, T., Ringwood, A.E., and Hibberson, W.O. (1986) The eclogite-garnetite transformation at high pressure and some geophysical implications. Earth and Planetary Science Letters, 77, 245-256.

Isaak, D.G. and Ohno, I. (2003) Elastic constants of chrome-diopside: application of resonant ultrasound spectroscopy to monoclinic single-crystals. Physics and Chemistry of Minerals, 30, 430–439.

Kandelin, J. and Weidner, D.J. (1988) The single-crystal elastic properties of jadeite. Physics of the Earth and Planetary Interiors, 50, 251–260.

Kay, R.W. and Kay, S.M. (1993) Delamination and delamination magmatism. Tectonophysics, 219, 177-189.

Levien, L., Weidner, D.J., and Prewitt, C.T. (1979) Elasticity of diopside. Physics and Chemistry of Minerals, 4, 105-113.

Nestola, F., Ballaran, T.B., Liebske, C., Bruno, M., and Tribaudino, M. (2006) High-pressure behaviour along the jadeite $NaAlSi_2O_6$–aegirine $NaFeSi_2O_6$ solid solution up to 10 GPa. Physics and Chemistry of minerals, 33, 417-425.

Nestola, F., Alvaro, M., Casati, M.N., Wilhelm, H., Kleppe, A.K., Jephcoat, A.P., Domeneghetti, M.C., and Harris, J.W. (2016) Source assemblage types for cratonic diamonds from X-ray synchrotron diffraction. Lithos, 265, 334-338.

Norris, S. (2008) Elastic properties of jadeite. Undergraduate Senior Thesis. University of Illinois.

Pandolfo, F., Nestola, F., Cámara, F., and Domeneghetti, M.C. (2012) New thermoelastic parameters of natural *C2/c* omphacite. Physics and Chemistry of Minerals, 39, 295-304.

Ranganathan, S.I. and Ostoja-Starzewski, M. (2008) Universal elastic anisotropy index. Physical Review Letters, 101, 055504.

Ringwood, A.E. (1975) Composition and Petrology of the Earth's Mantle. McGraw-Hill, New York.

Sang, L., Vanpeteghem, C.B., Sinogeikin, S.V., and Bass, J.D. (2011) The elastic properties of diopside, $CaMgSi_2O_6$. American Mineralogist, 96, 224-227.

Sinogeikin, S.V. and Bass, J.D. (2002) Elasticity of Majorite and a Majorite-Pyrope solid solution to high pressure: Implications for the Transition Zone. Geophysical Research Letters, 29, 4-1.

Skelton, R. and Walker, A.M. (2015) The effect of cation order on the elasticity of omphacite from atomistic calculations. Physics and Chemistry of Minerals, 42, 677-691.

Smyth, J.R., Bell, D.R., and Rossman, G.R. (1991) Incorporation of hydroxyl in upper-mantle clinopyroxenes. Nature, 351, 732.

Voigt, W. (1889) Ueber die Beziehung zwischen den beiden Elasticitätsconstanten isotroper Körper. Annalen der physik, 274, 573-587.

Walker, A.M. (2012) The effect of pressure on the elastic properties and seismic anisotropy of diopside and jadeite from atomic scale simulation. Physics of the Earth and Planetary Interiors, 192, 81-89.

Weidner, D.J. and Carleton, H.R. (1977) Elasticity of coesite. Journal of Geophysical Research, 82, 1334-1346.

Zhang, D., Hu, Y., and Dera, P.K. (2016) Compressional behavior of omphacite to 47 GPa. Physics and Chemistry of Minerals, 43, 707-715.

Zhang, J.S., Bass, J.D., and Zhu, G. (2015) Single-crystal Brillouin spectroscopy with CO_2 laser heating and variable q. Review of Scientific Instruments, 86, 063905.

Zhang, J.S., Bass, J.D., Taniguchi, T., Goncharov, A. F., Chang, Y. Y., and Jacobsen, S. D. (2011) Elasticity of cubic boron nitride under ambient conditions. Journal of Applied Physics, 109, 063521.

Zhang, J. and Green, H.W. (2007) Experimental investigation of eclogite rheology and its fabrics at high temperature and pressure. Journal of Metamorphic Geology, 25, 97-115.

Zhang, J., Green II, H.W., and Bozhilov, K.N. (2006) Rheology of omphacite at high temperature and pressure and significance of its lattice preferred orientations. Earth and Planetary Science Letters, 246, 432-443.

Chapter IV

The seismically fastest chemical heterogeneity in the Earth's deep upper mantle—implications from the single-crystal thermoelastic properties of jadeite

Abstract

Jadeite is a major mineral phase (up to 50 vol%) in the subducted sediments/crust with continental origin, which are one of the major heterogeneities and important enriched geochemical reservoirs (such as EM-1 and EM-2) for incompatible elements in the Earth's interior. Identifying and locating the enriched geochemical heterogeneities requires knowledge of the elastic properties of relevant mineral phases at high pressure-temperature conditions. Unfortunately, the single-crystal elastic properties of jadeite have never been measured at high-pressure conditions, partially due to its low crystal symmetry. In this study, we have measured the single-crystal elastic moduli of jadeite at high pressures for the first time up to 18 GPa at the ambient temperature condition using Brillouin spectroscopy. Fitting the third-order finite strain equation of state to the velocity-pressure data yields K_{S0}'=3.9(1), G_0'=1.09(4) with ρ_0=3.302(5) g/cm^3, K_{S0}=138(3) GPa, and G_0=84(2) GPa. In addition, we have also conducted synchrotron single-crystal X-ray diffraction experiments up to 25 GPa and 700 K. The fitting of a Holland-Powell type thermal-pressure Birch-Murnaghan equation of state yields K_{T0}'=3.8(2) and α_0=3.4(5) $\times 10^{-5}$ K^{-1}. Based on the obtained thermoelastic parameters of jadeite, the density and seismic velocities of continent-derived sediments/crust are modeled at the depth range from 200 to 500 km. The seismic velocities of the subducted continental sediments/crust become extremely fast at depths greater than ~300 km, up to 11.8% and 14.7% faster than the Vp and Vs of the ambient mantle, and 5.6% and 7.3% faster than the Vp and Vs

of the subducted oceanic crust. The existence of even a small amount of the subducted continental sediments/crust can result in strong seismic anomalies in the Earth's interior.

1. Introduction

Jadeite ($NaAlSi_2O_6$) is a major mineral phase (up to 50 vol%) in the subducted sediments/crust with continental origin and can exist up to 500 km depth in the Earth's interior (Irifune et al., 1994; Wu et al., 2009). The geochemical data, especially isotopic and trace-element geochemistry of oceanic island basalts (OIB), show that the subducted continental sediments/crust are one of the major enriched geochemical heterogeneities in the Earth's mantle (Hofmann, 1997). In particular, the enriched mantle 1 (EM-1) sources are consistent with the recycled ancient continental sediments/crust and the enriched mantle 2 (EM-2) sources are polluted by continent-derived sediments (e.g., Chauvel et al., 1992). Both EM-1 and EM-2 are the main geochemical reservoirs for the incompatible elements (e.g., U, Th, and K) and isotopes (e.g., ^{143}Nd, ^{87}Sr, and ^{40}Ar) in the Earth's interior (e.g. Hofmann, 1997). The enriched geochemical reservoirs have important geophysical implications as well. For example, the enrichment of K plays a significant role in the thermal evolution of the Earth (e.g., Arevalo et al., 2009). Considering the incompatible nature of K, continental crust and the continent-derived sediments on the ocean floor are the primary sources of the K in the Earth's interior, in addition to the possible important primitive K reservoirs formed early in the Earth's history (e.g., Corgne et al., 2007). Therefore, identification of the subducted sediments/crust in the mantle is crucial for both the geochemical and geophysical evolution of the Earth (e.g., Kufner et al., 2016).

Seismology provides by far the most precise images of the Earth's interior. Identifying the locality and estimating the size of the subducted continental sediments/crust in the Earth's

interior requires the knowledge of the elastic properties of all the relevant mineral phases, especially jadeite, due to its high volume fraction (Irifune et al., 1994; Wu et al., 2009). Previous studies have suggested the possible fast seismic velocities of the subducted continental sediments/crust in the deep upper mantle in presence of stishovite (e.g., Kawai & Tsuchiya, 2015). However, if jadeite is acoustically very slow at high-pressure (P) conditions, due to its abundance (Irifune et al., 1994; Wu et al., 2009), the continental sediments/crust can be seismically slow even with stishovite's presence. In addition, constraining the thermoelastic properties of jadeite is also helpful for modeling the velocity profiles of the subducted oceanic slab crust, considering the fact that the seismic velocities of the slab crust also strongly depend on the molar fraction of the jadeite component in the eclogitic omphacite crystals (Hao et al., 2019a). Thus, in order to model the seismic properties of these geochemical heterogeneities in the Earth's interior, measurements of the single-crystal thermoelastic properties of jadeite under relevant P-temperature (T) conditions are necessary.

Previous equation of state (EOS) studies of jadeite are limited in both P and T (e.g., Zhao et al., 1997; Cameron et al., 1973; Nestola et al., 2006; McCarthy et al., 2008; Tribaudino et al., 2008; Posner et al., 2014; Pandolfo et al., 2015). For example, Posner et al. (2014) performed single-crystal X-ray diffraction (XRD) measurements of jadeite up to 30.4 GPa at 300 K. Pandolfo et al. (2015) measured the thermal expansion coefficients of jadeite up to 1073 K at 1 atm. Zhao et al. (1997) performed the only in situ high P-T EOS study for polycrystalline jadeite up to 8.2 GPa, which is not enough to cover its entire stability range in the Earth's upper mantle. On the other hand, as the acoustically fastest chemical endmember of Clinopyroxene (Cpx), the single-crystal elastic properties of jadeite have been only experimentally determined at ambient condition (Kandelin & Weidner, 1988; Hao et al., 2019a;

Norris, 2008) or computed at 0 K and high-P conditions using first-principles calculation (Kawai & Tsuchiya, 2010; Walker, 2012).

Therefore, in this study, we conducted single-crystal Brillouin spectroscopy measurements of natural jadeite crystals up to 18 GPa 300 K at the high-P laser spectroscopy laboratory at University of New Mexico (UNM), and also investigated the thermal EOS of jadeite by performing synchrotron single-crystal XRD experiments on the same crystals up to 25 GPa and 700 K at GeoSoilEnviroCARS (GSECARS), Advanced Photon Source (APS), Argonne National Laboratory (ANL). We then calculated the seismic properties of the subducted oceanic crust and continent-derived sediments/crust using the thermoelastic properties of all relevant phases determined in this and previous studies.

2. Experimental methods

The jadeite crystals (space group *C2/c*) were hand-picked from a natural jadeitite. The chemical composition of the jadeite crystals was determined using a JEOL 8200 Electron Microprobe with 20 nA beam current and 15 kV accelerating voltage at the Institute of Meteoritics, UNM. The composition was determined as $Na_{0.954}Mg_{0.021}Ca_{0.029}Fe_{0.019}Al_{0.966}Si_{2.002}O_6$. Table IV.S2 shows the detailed analysis results. The selected crystals were then double-side polished into platelets with ~15 μm thickness. They were scratch-free under optical examination. The polished samples were then cut into pieces with ~45 μm width for diamond anvil cell (DAC) loading.

Symmetric piston-cylinder DACs and BX90 DACs with standard 60° and 90° opening WC backing seats and 300-350 μm cutlet diamonds were used for Brillouin and XRD experiments. Re gaskets were pre-indented to 45-55 μm thickness. 210-235 μm diameter holes

were drilled into the pre-indented gaskets and served as sample chambers. Neon was gas-loaded as the P-transmitting medium at GSECARS, APS, ANL. Gold EOS was used for estimating the experimental Ps for XRD measurements (Fei et al., 2007). For Brillouin measurements, 2 ruby spheres were loaded into each DAC and used as the P standard (Mao et al., 1978). The P differences between the Ps measured from the 2 ruby spheres before and after the completion of the Brillouin scattering measurements at 13 different crystallographic angles of each individual run were smaller than 0.2 GPa.

High-P single-crystal XRD experiments were carried out at GSECARS experimental station 13-BM-C. The X-ray opening angles for symmetric piston-cylinder DACs and BX90 DACs are ±14° and ±24°, respectively. The X-ray beam energy is 28.6 keV and the beam size is ~12 μm × 18 μm. A MAR165 Charge Coupled Device placed on a dedicated rotational arm was used as the detector. NIST standard LaB_6 powder was used to calibrate the detector geometry parameters. 2 different detector positions were used: one was perpendicular to the incident X-ray beam and the other was rotated about the horizontal axis by 20°. We collected both the wide-scan and 1°/step step-scan images with 2 s/° exposure time.

For measurements at ambient condition, the polished plate-like crystals were oriented with their plane normals parallel to the incoming X-ray beam. The averaged unit cell parameters from the measured 3 crystals at ambient condition were: a=9.439(5) Å, b=8.583(4) Å, c=5.228(1) Å, and β=107.50(2)°. The calculated ambient density ρ_0 was 3.302(5) g/cm^3. The plane normals of the measured 3 samples were (-0.692, -0.714, 0.106), (0.116, 0.993, -0.021), and (-0.905, 0.302, 0.302). The angular uncertainties were approximately 0.5°. For high P-T single-crystal XRD measurements, we used Pt heaters to heat the sample chamber to 373K, 500K, and 700K at high-P conditions. 2 K-type thermocouples were attached to the

diamonds to measure the T. The difference between the 2 T readings was always smaller than 10 K up to the maximum experimental T of 700 K.

Brillouin spectroscopy experiments were performed at the high-P laser spectroscopy laboratory at UNM. The light source was a 300mW 532 nm single-mode diode-pumped solid-state laser. The measurements were carried out using a 50° symmetric forward scattering geometry. Using a standard silica glass Corning 7980, the scattering angle was calibrated to be 50.42(5)°. The fast and slow directions of the 2 diamond anvils were oriented to match each other. We used the 3 pre-oriented jadeite crystals for the Brillouin measurements at 7 different Ps. To avoid any geometrical errors, compressional (Vp) and shear (Vs) velocities were measured at 13 different Chi angles (0, 30, 60, 90, 120, 150, 180, 195, 225, 255, 285, 315, 345) along the 360° azimuth at each P. All Brillouin spectra show excellent signal-to-noise ratios. Figure IV.S7 shows a typical Brillouin spectrum collected at 18 GPa.

3. Results and discussion

3.1. Thermal EOS of jadeite

Using the ATREX IDL software package (Dera et al., 2013), the single-crystal XRD images were analyzed to obtain the unit cell parameters at each P-T condition (Table IV.S3). Then we performed thermal EOS fit of the obtained unit cell volumes. The conventional isothermal EOS (e.g., Birch-Murnaghan EOS) assumed constant $\partial K_T/\partial T$ and K_T' in the P-T space, which is thermodynamically problematic because $\partial K_T/\partial T = 0$ at T=0 K and K_T' should increase with T (Angel et al., 2018). Thus, the EOS used in this study was modified based on the Birch-Murnaghan EOS with the isochoric thermal-P correction term from Holland and

Powell (2011). The details of the thermal-P EOS are summarized in the Supporting Information Text IV.S1 (Equation IV.S1-IV.S3).

The well-known trade-offs between the ambient isothermal bulk modulus K_{T0} and its P derivative K_{T0}' resulted in the large variations in previous studies, with K_{T0} and K_{T0}' ranging from 125 GPa, 5.0 to 136 GPa, 3.3, respectively (Zhao et al., 1997; Nestola et al., 2006; McCarthy et al., 2008; Posner et al., 2014). Therefore, in this study, we fixed K_{T0} to 134.6 GPa based on the Reuss bound of the adiabatic bulk modulus K_{S0}^{R} determined from high-precision Brillouin spectroscopy experiments (Supporting Information, Text IV.S2, Equation IV.S4). With fixed V_0 and K_{T0}, the thermal EOS fitting yielded K_{T0}'=3.8(2) with α_0=3.4(5) $\times 10^{-5}$ K^{-1} (Figure IV.1). Compared with previous studies, α_0 is slightly higher whereas K_{T0}' is in the

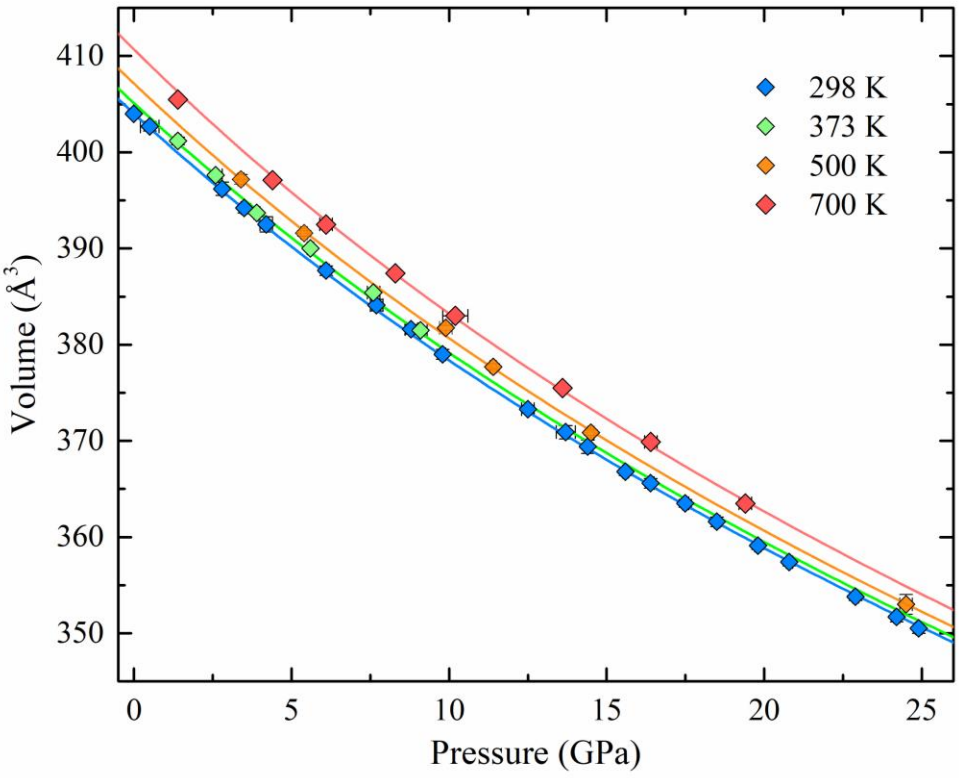

Figure IV.1. P-V-T EOS of jadeite with calculated isothermal compression curves.

middle of the range determined from previous studies (Nestola et al., 2006; McCarthy et al., 2008; Posner et al., 2014; Zhao et al., 1997; Figure IV.S8).

3.2. High-P single-crystal elastic properties of jadeite

The best-fit values for the 13-independent elastic moduli (C_{ij}) of jadeite at ambient condition were obtained using a least-squares inversion of the Christoffel equation with known ρ_0. The root-mean-square (RMS) residuals between the observed and modeled velocities of the results were less than 50 m/s. Using the Voigt-Reuss-Hill (VRH) averaging scheme, the ambient adiabatic bulk (K_{S0}) and shear moduli (G_0) were calculated. The high-P densities and elastic properties were iteratively calculated. First, using the least-squares inversion of the Christoffel equation, the C_{ij}s, K_S, G, Vp, and Vs can be calculated at each P with an initial guess of the sample's density. The Vp and Vs are independent of the assumed density values and therefore represent the true high-P aggregate velocities. Fixing ρ_0, K_{S0}, and G_0 to 3.302(5) g/cm^3, 138(3) GPa, and 84(2) GPa, respectively, we can then use the 3rd order finite-strain EOS to fit the P-Vp-Vs data to obtain the P derivatives of K_S and G, as well as the true high-P densities (Davies & Dziewonski, 1975). Finally, we updated the high-P C_{ij}s, K_S, and G using true densities. For low symmetry minerals, such as monoclinic jadeite, it is essential to choose the proper combination of crystallographic orientations in order to reliably invert the full single-crystal C_{ij}s. Therefore, we performed the inversion sensitivity test for the 13 C_{ij}s using the velocities measured along the 39 different crystallographic directions. All the technical details are shown in the Supporting Information Text IV.S3, Equation IV.S5. The sensitivity test results are shown in Figure IV.S9. According to Figure IV.S9, the only C_{ij} that can be improved with more measurements along more crystallographic directions is C_{15}, which plays a very minor role in calculating the anisotropic aggregate elastic properties. Figure IV.S10

shows the measured velocities and the calculated velocities from the best-fit C_{ij} model at 18 GPa, and the RMS error is 32m/s. All the Vp, Vs, C_{ij}s, K_S, G, and density values at each P are listed in Table IV.1.

The K_{S0}' and G_0' were determined to be 3.9(1), 1.09(4) with fixed ρ_0=3.302(5) g/cm^3, K_{S0}=138(3) GPa, and G_0=84(2) GPa. The K_{S0}' is consistent with K_{T0}' considering their experimental uncertainties. The K_S, G, Vp, and Vs of jadeite, omphacite, and diopside at different Ps are plotted together in Figure IV.2 for comparison (Hao et al., 2019b; Sang & Bass, 2014). We chose to plot the elasticity data measured using Brillouin spectroscopy method only

	1 atm	3.0(1) GPa	6.0(1) GPa	9.0(1) GPa	12.0(1) GPa	15.0(1) GPa	18.0(1) GPa
ρ (g/cm^3)	3.302(5)	3.372	3.437	3.5	3.56	3.617	3.671
C_{11} (GPa)	265.4(9)	281(1)	302.4(8)	312.9(9)	335.3(8)	353(1)	365.3(8)
C_{22} (GPa)	247(1)	267(1)	279(1)	292(1)	308(1)	317(1)	328(1)
C_{33} (GPa)	274(1)	284.5(7)	300.6(6)	317.1(6)	332.2(6)	346.7(7)	360.1(6)
C_{44} (GPa)	85.8(7)	89.5(5)	94.3(5)	95.0(5)	97.4(5)	102.6(7)	107.1(5)
C_{55} (GPa)	69.3(5)	70.1(4)	73.5(3)	78.4(3)	76.6(3)	79.4(4)	82.4(3)
C_{66} (GPa)	93.0(7)	98.0(9)	100.5(7)	108.8(6)	109.4(7)	112(1)	115.2(9)
C_{12} (GPa)	85(1)	93(2)	108(1)	117(1)	130(1)	153(2)	165(1)
C_{13} (GPa)	66(1)	70.5(9)	79.8(8)	93.8(8)	99.2(7)	107.2(9)	116.8(7)
C_{23} (GPa)	87(2)	91(1)	96.5(9)	102(1)	113(1)	126(1)	134.6(9)
C_{15} (GPa)	5.4(7)	7.0(5)	6.9(4)	8.0(4)	10.3(4)	10.1(5)	8.9(4)
C_{25} (GPa)	17(1)	18(1)	27.3(8)	24.2(9)	22.2(7)	13(1)	10.3(9)
C_{35} (GPa)	28.7(6)	26.3(5)	27.4(4)	25.9(4)	26.8(4)	26.4(5)	26.7(3)
C_{46} (GPa)	14.6(6)	9.5(5)	12.0(4)	9.8(4)	11.6(5)	16.4(7)	17.5(5)
K_S^R (GPa)	135.9(7)	144.6(6)	155.2(4)	166.5(4)	179.1(4)	195.0(6)	206.4(4)
G^R (GPa)	82.7(3)	86.8(3)	89.5(3)	92.6(2)	95.2(3)	96.7(4)	99.1(3)
K_S^V (GPa)	140.1(7)	148.9(6)	161.2(4)	171.8(4)	184.5(4)	198.8(6)	209.7(4)
G^V (GPa)	86.3(3)	90.0(3)	93.5(3)	96.3(2)	98.9(3)	100.8(4)	103.4(3)
K_S^{VRH} (GPa)	138(3)	147(3)	158(2)	169(3)	182(3)	197(2)	208(2)
G^{VRH} (GPa)	84(2)	88(2)	91(2)	94(2)	97(2)	99(2)	101(2)
Vp (km/s)	8.71(4)	8.86(3)	9.03(4)	9.18(3)	9.35(3)	9.53(3)	9.67(3)
Vs (km/s)	5.06(3)	5.12(3)	5.16(3)	5.19(3)	5.22(3)	5.23(3)	5.25(3)

Table IV.1. Single-crystal and aggregate elastic properties of jadeite at different Ps determined in this study.

for consistency, although the experimental results obtained using other experimental methods do not deviate far away from the values determined by Brillouin spectroscopy (e.g., sound velocities of diopside determined by Li and Neuville (2010) and Sang and Bass (2014) agree with each other very well). As shown in Figure IV.2, jadeite is clearly the fastest Cpx endmember for both Vp and Vs in the entire P range of this study.

Comparing the velocities of all the major upper mantle minerals with jadeite (Figure

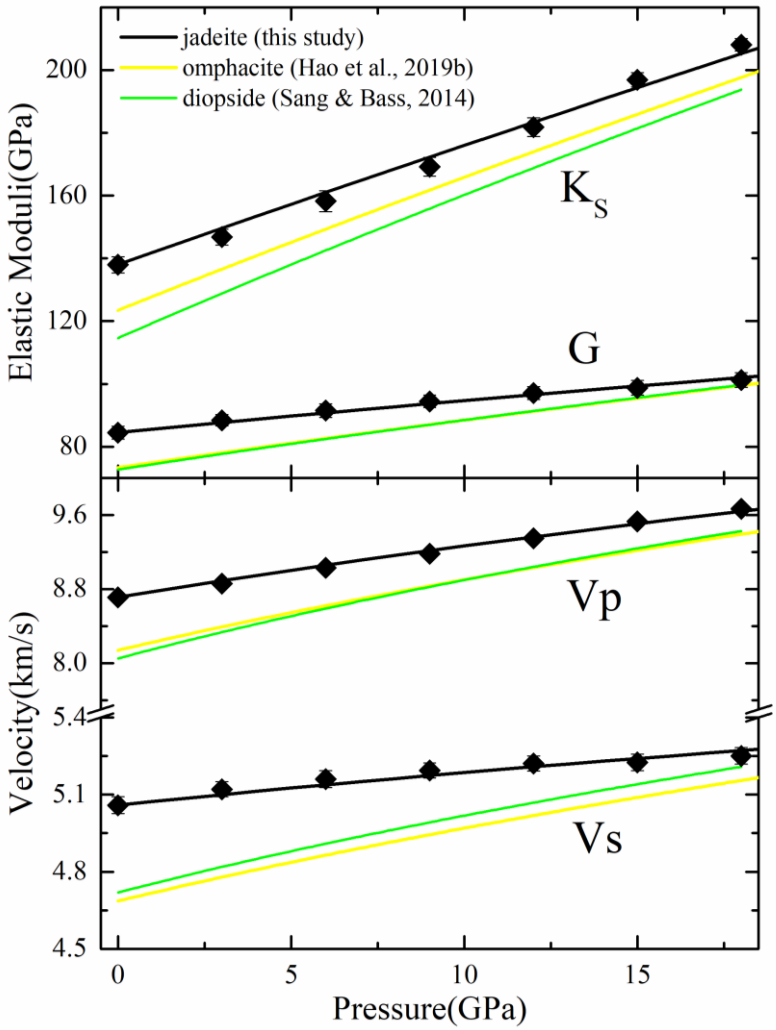

Figure IV.2. The high-P Ks, G, Vp, and Vs of jadeite in this study are compared with diopside (Sang & Bass, 2014) and omphacite (Hao et al., 2019b).

IV.S11), olivine and pyroxenes are all acoustically slower. It is worth noting that there are some discrepancies between previous EOS and elasticity studies of olivine when the P significantly exceeds its P stability range (Angel et al., 2018). However, within the P range we were modeling in this study, the difference is very small. Stishovite, as expected by its dense structure with 6 coordinated Si, is the fastest mineral phase. The Vp of jadeite is slightly slower than the garnet, whereas its Vs exceeds the garnet (Figure IV.S11). Overall, jadeite is among the fastest mineral phases in the Earth's upper mantle.

Figure IV.3 shows the finite strain fitting results of all C_{ij}s. Those are the first experimentally determined values for jadeite under high-P conditions. Kawai and Tsuchiya (2010) and Walker (2012) obtained the C_{ij}s of jadeite at 0 K used first-principles calculations (Figure IV.S12). Many of the computed C_{ij}s follow similar trends as the experimentally

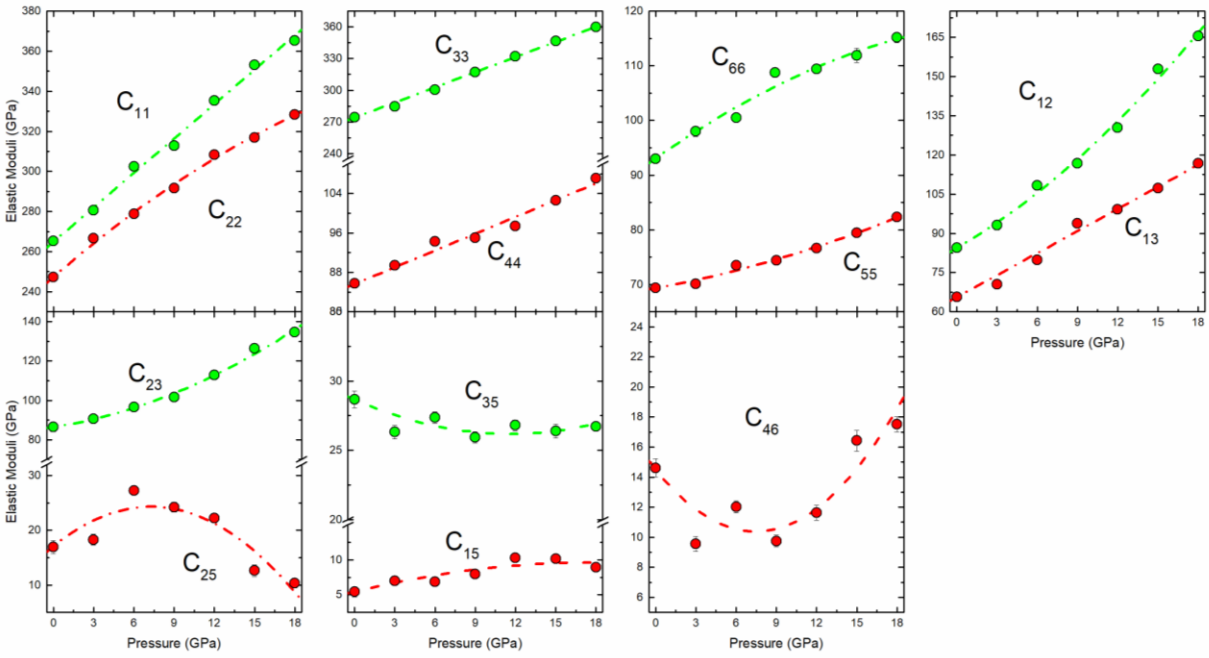

Figure IV.3. Single-crystal elastic moduli of jadeite at high-P conditions. The dashed lines represent the best fit finite-strain elastic models.

determined values in this study. For example, C_{11}, C_{22}, and C_{33} all increase with P; C_{33} is higher than C_{11} and C_{22} in the entire P range. However, it is also worth noting that the two computational studies at 0 K (Kawai & Tsuchiya, 2010; Walker, 2012) are not entirely consistent with each other. For some diagonal and off-diagonal C_{ij}s, such as C_{55}, C_{15}, C_{25}, and C_{35}, the two computational studies yield dramatically different results. It seems that the C_{25} and C_{35} values predicted by Kawai and Tsuchiya (2010) are closer to what were experimentally determined in this study, whereas the C_{55} calculated by Walker (2012) better matched the values measured in this study. Although both calculations were based on density functional theory, Kawai and Tsuchiya (2010) utilized the ab initio approach, whereas Walker (2012) utilized the plane wave and pseudopotentials in his calculation. These different technical treatments may contribute to the discrepancies shown in Figure IV.S12. Further computational studies at higher Ts may help to resolve these issues.

3.3. Elastic anisotropy of jadeite at high-P conditions

Seismic anisotropy is a powerful tool for studying the flow field and identifying possible chemical heterogeneities in the Earth's upper mantle (Hao et al., 2019b). During the slab subduction, the flow-induced lattice preferred orientation of omphacite, which is the solid solution of jadeite and diopside, is the main contributor of the seismic anisotropy of slab crust (e.g., Zhang et al., 2006) due to the elastically isotropic nature of the garnet (e.g., Sinogeikin & Bass, 2000). As the primary phase up to 50 vol% in the subducted continental sediments/crust, determination of the elastic anisotropy of jadeite is also crucial for locating the enriched mantle reservoirs in the Earth's deep interior.

In this study, we used 4 different elastic anisotropy indices: Universal Anisotropy Index (A^U), the Vp and Vs azimuthal anisotropy A^{Vp} and A^{Vs}, and Vs polarization anisotropy D^{Vs}

(Supporting Information, Text IV.S4, Equation IV.S6-IV.S9) to describe the anisotropy of jadeite.

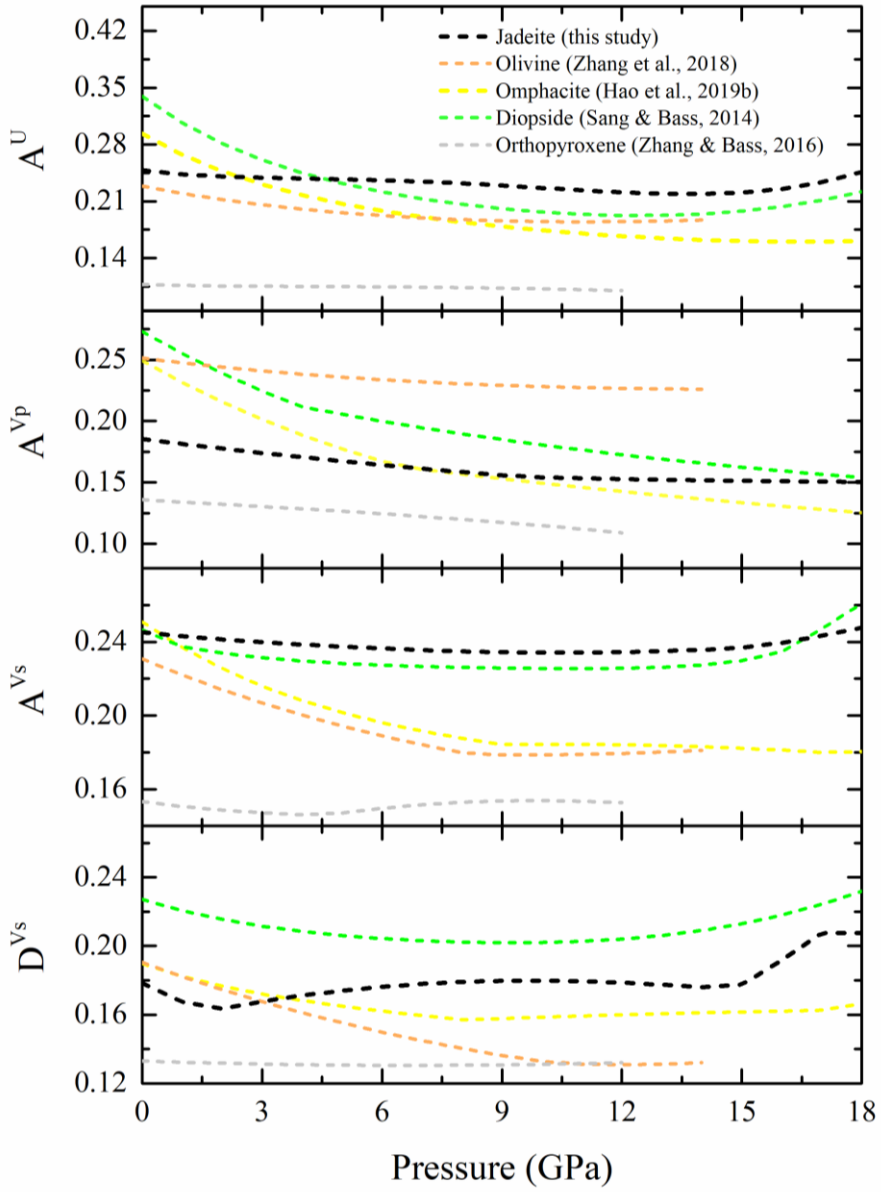

Figure IV.4. The anisotropy indices (A^U, A^{Vp}, A^{Vs}, and D^{Vs}) of jadeite, diopside (Sang & Bass, 2014), omphacite (Hao et al., 2019b), orthopyroxene (Zhang & Bass, 2016), and olivine (Zhang et al., 2018).

We calculated the anisotropy indices of jadeite up to 18 GPa and compared them with other major upper mantle anisotropic minerals (Figure IV.4, Zhang et al., 2018; Sang & Bass, 2014; Zhang & Bass, 2016; Hao et al., 2019b). The P dependences of the C_{ij}s for all the other major upper mantle minerals can be found in Table IV.S4. The decrease of the 4 anisotropy indices as a function of P is smaller for jadeite than the other minerals. When P exceeds ~5 GPa, the A^U of jadeite becomes the highest among all minerals. Olivine has the highest A^{Vp} in the entire P range. The A^{Vs} of jadeite remains the highest among all 5 minerals up to 16 GPa. Jadeite becomes more anisotropic in D^{Vs} than olivine and omphacite when P is higher than 4 GPa. These calculations suggest that the subducted sediments/crust can be highly anisotropic due to the enrichment of the jadeite component with strong intrinsic acoustic anisotropy.

3.4. Geophysical implications

Previous geochemical and petrological studies have suggested that the sediments/crust with continental origin may be recycled back into the deep mantle, down to perhaps the transition zone depth range (e.g., Chauvel et al., 1992; Liu et al., 2007). Due to the difference in major element composition, the seismic velocities of the subducted eclogitic oceanic crust, the subducted sediments/crust with continental origin, and the ambient mantle are different (Hao et al., 2019b; Irifune, et al., 1994; Wu et al., 2009). In this study, utilizing the thermoelastic parameters of jadeite and other relevant mineral phases (Wu et al., 2009; Irifune et al., 1994), we modeled the density and velocities of the subducted sediments/crust with continental origin along 1000 K (cold) and 1600 K (ambient) mantle adiabats from 200 km to 500 km depth (Stixrude & Lithgow-Bertelloni, 2005; Katsura et al., 2010). In a realistic case, the geotherm may lie in between the two. We also compared our results with the velocities calculated for oceanic crust (Aoki & Takahashi, 2004), the global 1-D seismic model AK135

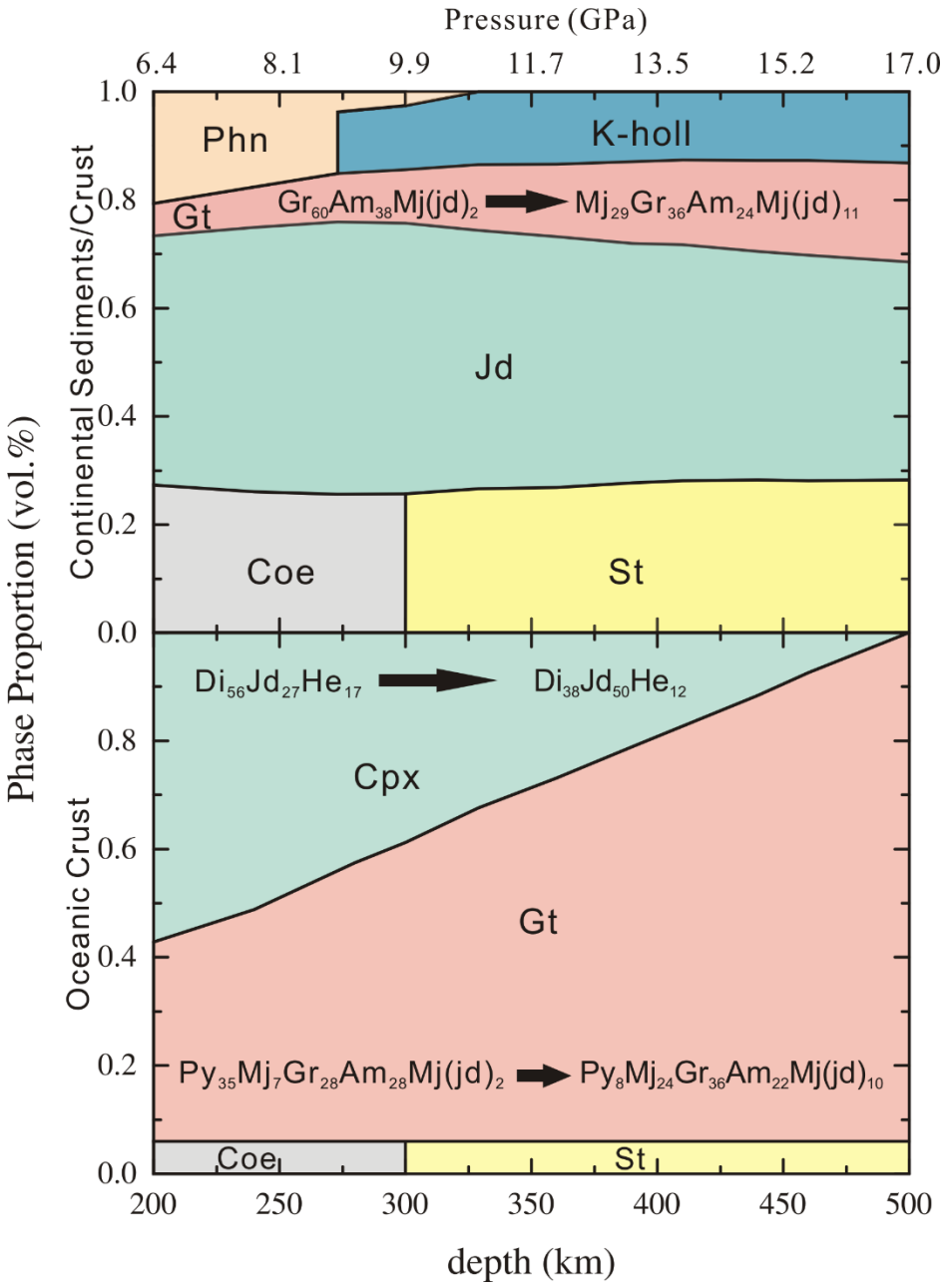

Figure IV.5. Phase proportions of the continental sediments/crust (Wu et al., 2009) and the oceanic crust (Aoki & Takahashi, 2004) as a function of depth (Coe: coesite; St: stishovite; Gt: garnet; Py: pyrope; Mj: majorite; Gr: grossular; Am: almandine; Mj(jd): jadeite-majorite; Cpx: clinopyroxene; Di: diopside; Jd: jadeite; He: hedenbergite; Phn: phengite; K-holl: K-hollandite).

(Kennett et al., 1995), and the ambient pyrolitic mantle (Xu et al., 2008). Table IV.5 shows the thermoelastic parameters we used for all the relevant mineral phases. We adopted the experimentally constrained high-P petrological models by Aoki and Takahashi (2004) for the density and velocity calculation of the basaltic oceanic crust, Wu et al. (2009) and Irifune et al. (1994) for the subducted continent-derived sediments/crust. The mineral proportions, as well as compositions, are both calculated as depth-dependent (Figure IV.5, Table IV.S6). We assumed ideal mixing between different mineral endmembers. Voigt-Reuss-Hill averaging scheme is used for estimating the densities and elastic moduli of the multi-component lithologies (Supporting Information, Text IV.S5 equation IV.S10-IV.S12). It is worth noting that the starting materials used in the 2 existing studies Irifune et al. (1994) and Wu et al. (2009) are similar yet both slightly different from the averaged upper continental crust composition (Rudnick & Fountain, 1995). The obtained petrological models of the subducted sediments/crust with continental origin are also different between Irifune et al. (1994) and Wu et al. (2009). In particular, the jadeite content in Irifune et al. (1994) decreased dramatically with P, and at 17 GPa it was less than 10 vol%. However, the jadeite content in Wu et al. (2009) was always higher than 30 vol%. In order to explore the effect of the small compositional difference of the starting materials on the high-P phase diagram of the continental sediments/crust (Irifune et al., 1994; Rudnick & Fountain, 1995; Wu et al., 2009), we performed additional PerpleX calculations to obtain the possible phase diagrams at high P-T conditions (Connolly, 2009; Supporting Information, Text IV.S6, Figure IV.S13). As shown in Figure IV.S13, the calculated and experimentally determined jadeite volume proportion (~30%-50%) in Wu et al. (2009) is closer to the calculated value (~30%-39%) for the average upper continental crust (Rudnick & Fountain, 1995). However, due to the limitations of

PerpleX software package (e.g., treatment of K), the calculation is still preliminary. It is also worth noting that the experimental run time in Wu et al. (2009) is significantly longer than Irifune et al. (1994). However, evaluating which petrological model is more reliable is beyond the scope of this study. Further high P-T phase equilibrium studies are needed to clarify the discrepancies between the 2 existing studies. In this study, we calculated the high P-T seismic properties of the continental sediments/crust based on both Wu et al. (2009) and Irifune et al. (1994), shown as Figure IV.6 and Figure IV.S14 in the Supporting Information, respectively. The differences in terms of seismic properties are small between the two models, and we focus on discussing the results based on the Wu et al. (2009) in the remainder of the text.

As shown in Figure IV.6, at depths shallower than ~300 km, the density of the continent-derived sediments/crust is significantly less than the oceanic crust and the ambient mantle. This is caused by the low densities of jadeite, phengite, and coesite compared with the major upper mantle mineral phases, such as olivine and garnet (Zhang et al., 2018; Chen et al., 2017). Although the seismic velocities of phengite and coesite in the continental sediments/crust are much slower than the most abundant upper mantle mineral olivine (Zhang et al., 2018; Chen et al., 2017; Vaughan & Guggenheim, 1986), the high jadeite content in the continental sediments/crust results in the similar Vp of the continental sediments/crust and the ambient mantle. On the other hand, the Vs of the continental sediments/crust is significantly lower than the ambient mantle. Thus, the elevated Vp/Vs values (1.88-1.92) are expected in regions enriched in continentally derived sediments/crust. This can be used as an alternative explanation for the high Vp/Vs regions in the shallower upper mantle in addition to partial melt (e.g., Nakajima et al., 2001).

At depth ~300 km, the phase transformation from coesite to stishovite causes the density and velocity jumps observed for both the continent-derived sediments/crust and

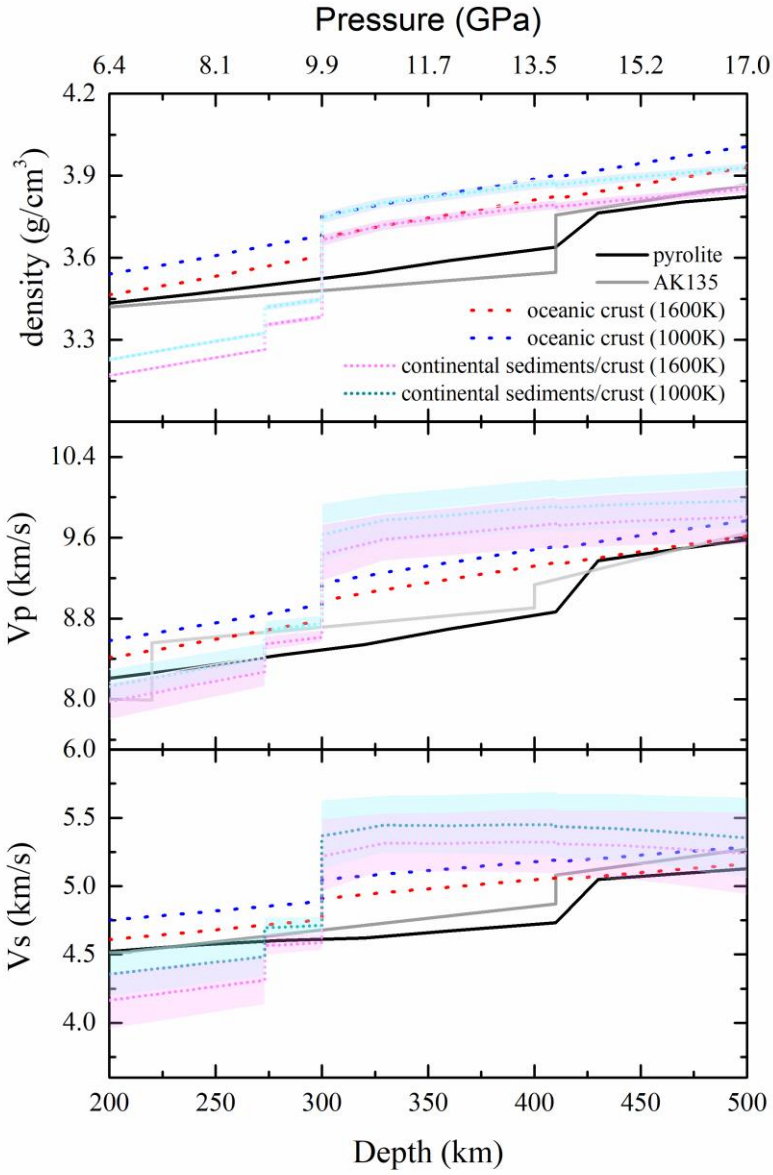

Figure IV.6. The density and seismic velocities of the subducted continental sediments/crust and oceanic crust, compared with the pyrolite model (Xu et al., 2008), and AK 135 model (Kennett et al., 1995). The blue and pink regions are bounded by Voigt and Reuss bounds at 1000 K and 1600 K adiabat, respectively.

oceanic crust (Chen et al., 2017; Yang & Wu, 2014). Due to the high silica content (>25 vol%), the density of the continental sediments/crust is similar to oceanic crust and higher than the ambient mantle. However, the density of oceanic crust exceeds that of the continent-derived sediments/crust at ~350 km depth because of the dissolution of Cpx into garnet (Aoki & Takahashi, 2004), though both of them are denser than the ambient mantle. The seismic velocities of the continent-derived sediments/crust increase by 9.5% and 13.8% for Vp and Vs, respectively at ~300 km depth. This velocity jump and the high volume fraction of jadeite make the continental sediments/crust the fastest petrological component in the deep upper mantle. Assuming the continent-derived sediments/crust are at the same T as the ambient mantle (along the 1600 K adiabat geotherm), the Vp and Vs difference between the continental sediments/crust and the ambient mantle can be as high as 11.8% and 14.7%, respectively at 300-410 km depth. If we consider the possibly lower T of the continental sediments/crust, then the maximum velocity contrast will be bracketed between 11.8%-13.9% and 14.7%-17.5% for Vp and Vs, respectively. The Vp and Vs of continent-derived sediments/crust are also 5.6% and 7.3% faster than those of the subducted oceanic crust.

At ~410 km depth, the density, Vp, and Vs of the ambient mantle increase by 2.9%, 5.0%, and 6.2%, respectively, due to the olivine to wadsleyite phase transformation (Xu et al., 2008). As a result, the density contrast between the ambient mantle, continental sediments/crust, and oceanic crust decreases to as small as 1.4%. The seismic velocities of the ambient mantle are similar to oceanic crust. The Vp and Vs of the continental sediments/crust are still significantly faster than the ambient mantle by 4.1% and 5.0%, respectively. At this depth, the Vs of the continental sediments/crust decrease fast with depth, because of the computationally predicted softening of the elastic properties of K-hollandite at 0 K (Kawai &

Tsuchiya, 2013). Future experimental investigations may help us further understand this interesting behavior.

As discussed above, the subducted continental sediments/crust are extremely fast geochemical heterogeneities between 300 km to 500 km depth. The fast seismic anomalies observed in the upper mantle can be easily explained by the existence of the recycled continental sediments/crust even without the need of any abnormal cold Ts. For example, the fast seismic anomalies at 300-550 km depth under Central Asia (Kufner et al., 2016) are as high as 4% for Vp, which requires >1000 K T difference assuming a pure thermal origin. However, a T of more than 1000 K lower than the surrounding mantle seems unrealistic. Considering the possible subduction of continental crust under the Tibetan plateau (e.g., Replumaz et al., 2010), this 4% Vp anomaly can easily be explained by ~34% continental crust at the same T with the ambient mantle or ~29% continental crust at about 200-300 K lower T. In addition, a few distinct enriched geochemical reservoirs have been identified under the South Pacific Ocean from previous studies (Hofmann, 1997), which is in agreement with the fast anomalies identified in global P-wave tomography models in the deep upper mantle (e.g., Li et al., 2008).

4. Conclusions

We have determined the thermal EOS and the single-crystal elastic properties of jadeite by synchrotron single-crystal XRD and Brillouin spectroscopy. The derived thermoelastic properties for jadeite are: K_{T0}=134.6 GPa, K_{T0}'=3.8(2), α_0=3.4(5) $\times 10^{-5}$ K^{-1}, K_{S0}=138(3) GPa, G_0=84(2) GPa, K_{S0}'=3.9(1), and G_0'=1.09(4). In the entire stability P range, the acoustic velocities of jadeite are faster than all the other Cpx. Based on the modeled density and seismic velocities of the subducted sediments/crust with continental origin, we found that the seismic

velocities of the continental sediments/crust are faster than the ambient upper mantle by ~11.8% and ~14.7% at depths greater than ~300 km for Vp and Vs, respectively. This huge velocity contrast can help to identify the enriched geochemical reservoirs and heterogeneities in the Earth's interior.

Acknowledgments

The authors would like to thank Mike Spilde for the help with Electron Microprobe Analysis experiments at the Institute of Meteoritics at UNM and Sergey Tkachev for the Neon gas loading of the DACs at GSECARS, APS, ANL. The use of the gas-loading system and 13-BM-C beamlines are supported by COMPRES, the Consortium for Materials Properties Research in Earth Sciences under NSF Cooperative Agreement EAR 1661511, and GSECARS is funded by NSF (EAR - 1634415) and Department of Energy (DOE) – GeoSciences (DE-FG02-94ER14466). This research used resources of the APS, a U.S. DOE Office of Science User Facility operated for the DOE Office of Science by ANL under Contract NO. DE-AC02-06CH11357. The X-ray Atlas instrument at the University of Hawaii was funded by NSF grant EAR 1541516 (PD). All the data presented in this study are available in the Supporting Information. We thank Suyu Fu for providing the original Matlab code for the C_{ij} sensitivity test and Brandon Schmandt for the insightful discussions with geophysical implications.

Funding: This work is supported by the National Science Foundation (NSF) under Grant EAR 1646527 (JZ) and the start-up fund from UNM (JZ). PD was supported by NSF grant EAR 1722969.

References

Angel, R. J., Alvaro, M., & Nestola, F. (2018). 40 years of mineral elasticity: a critical review and a new parameterisation of equations of state for mantle olivines and diamond inclusions. *Physics and Chemistry of Minerals, 45(2)*, 95-113.

Aoki, I., & Takahashi, E. (2004). Density of MORB eclogite in the upper mantle. *Physics of the Earth and Planetary Interiors*, *143*, 129-143.

Arevalo Jr, R., McDonough, W. F., & Luong, M. (2009). The K/U ratio of the silicate Earth: Insights into mantle composition, structure and thermal evolution. *Earth and Planetary Science Letters*, *278*(3-4), 361-369.

Cameron, M., Sueno, S., Prewitt, C. T., & Papike, J. J. (1973). High-Temperature Crystal Chemistry of Acmite, Diopside, Hedenbergite Jadeite, Spodumene and Ureyite. *American Mineralogist: Journal of Earth and Planetary Materials*, *58*(7-8), 594-618.

Chauvel, C., Hofmann, A. W., & Vidal, P. (1992). HIMU-EM: the French Polynesian connection. *Earth and Planetary Science Letters*, *110*(1-4), 99-119.

Chen, T., Liebermann, R. C., Zou, Y., Li, Y., Qi, X., & Li, B. (2017). Tracking silica in Earth's upper mantle using new sound velocity data for coesite to 5.8 GPa and 1073 K. *Geophysical Research Letters*, *44*(15), 7757-7765.

Connolly, J. A. D. (2009). The geodynamic equation of state: what and how. Geochemistry, Geophysics, Geosystems, 10(10).

Corgne, A., Keshav, S., Fei, Y., & McDonough, W. F. (2007). How much potassium is in the Earth's core? New insights from partitioning experiments. *Earth and Planetary Science Letters*, *256*(3-4), 567-576.

Davies, G. F., & Dziewonski, A. M. (1975). Homogeneity and constitution of the Earth's lower mantle and outer core. *Physics of the Earth and Planetary Interiors*, *10*(4), 336-343.

Dera, P., Zhuravlev, K., Prakapenka, V., Rivers, M. L., Finkelstein, G. J., Grubor-Urosevic, O.,

et al. (2013). High pressure single-crystal micro X-ray diffraction analysis with GSE_ADA/RSV software. *High Pressure Research*, *33*(3), 466-484.

Fei, Y., Ricolleau, A., Frank, M., Mibe, K., Shen, G., & Prakapenka, V. (2007). Toward an internally consistent pressure scale. *Proceedings of the National Academy of Sciences*, *104*(22), 9182-9186.

Hao, M., Pierotti, C. E., Tkachev, S., Prakapenka, V., & Zhang, J. S. (2019a). The single-crystal elastic properties of the jadeite-diopside solid solution and their implications for the composition-dependent seismic properties of eclogite. *American Mineralogist*, *104*(7), 1016-1021.

Hao, M., Zhang, J. S., Pierotti, C. E., Ren, Z., & Zhang, D. (2019b). High‐Pressure Single‐Crystal Elasticity and Thermal Equation of State of Omphacite and Their Implications for the Seismic Properties of Eclogite in the Earth's Interior. Journal of Geophysical Research: Solid Earth, 124(3), 2368-2377.

Hofmann, A. W. (1997). Mantle geochemistry: the message from oceanic volcanism. *Nature*, *385*(6613), 219.

Holland, T. J. B., & Powell, R. (2011). An improved and extended internally consistent thermodynamic dataset for phases of petrological interest, involving a new equation of state for solids. *Journal of Metamorphic Geology*, *29*(3), 333-383.

Irifune, T., Ringwood, A. E., & Hibberson, W. O. (1994). Subduction of continental crust and terrigenous and pelagic sediments: an experimental study. *Earth and Planetary Science Letters*, *126*(4), 351-368.

Kandelin, J., & Weidner, D. J. (1988). The single-crystal elastic properties of jadeite. *Physics of the Earth and Planetary Interiors*, *50*(3), 251-260.

Katsura, T., Yoneda, A., Yamazaki, D., Yoshino, T., & Ito, E. (2010). Adiabatic temperature profile in the mantle. *Physics of the Earth and Planetary Interiors*, *183*(1-2), 212-218.

Kawai, K., & Tsuchiya, T. (2010). Ab initio investigation of high-pressure phase relation and elasticity in the NaAlSi2O6 system. *Geophysical Research Letters*, *37*(17).

Kawai, K., & Tsuchiya, T. (2013). First-principles study on the high-pressure phase transition and elasticity of KAlSi3O8 hollandite. *American Mineralogist*, *98*(1), 207-218.

Kawai, K., & Tsuchiya, T. (2015). Elasticity of continental crust around the mantle transition zone. In *The Earth's Heterogeneous Mantle* (pp. 259-274). Springer, Cham.

Kennett, B. L., Engdahl, E. R., & Buland, R. (1995). Constraints on seismic velocities in the Earth from traveltimes. *Geophysical Journal International*, *122*(1), 108-124.

Kufner, S. K., Schurr, B., Sippl, C., Yuan, X., Ratschbacher, L., Ischuk, A., ... & Tilmann, F. (2016). Deep India meets deep Asia: Lithospheric indentation, delamination and break-off under Pamir and Hindu Kush (Central Asia). *Earth and Planetary Science Letters*, *435*, 171-184.

Li, B., & Neuville, D. R. (2010). Elasticity of diopside to 8 GPa and 1073 K and implications for the upper mantle. *Physics of the Earth and Planetary Interiors*, *183*(3-4), 398-403.

Li, C., van der Hilst, R. D., Engdahl, E. R., & Burdick, S. (2008). A new global model for P wave speed variations in Earth's mantle. *Geochemistry, Geophysics, Geosystems*, *9*(5).

Liu, L., Zhang, J., Green II, H. W., Jin, Z., & Bozhilov, K. N. (2007). Evidence of former stishovite in metamorphosed sediments, implying subduction to> 350 km. *Earth and Planetary Science Letters*, *263*(3-4), 180-191.

Mao, H. K., Bell, P. M., Shaner, J. T., & Steinberg, D. J. (1978). Specific volume measurements of Cu, Mo, Pd, and Ag and calibration of the ruby R 1 fluorescence pressure gauge from 0.06 to 1 Mbar. *Journal of applied physics*, *49*(6), 3276-3283.

McCarthy, A. C., Downs, R. T., & Thompson, R. M. (2008). Compressibility trends of the clinopyroxenes, and in-situ high-pressure single-crystal X-ray diffraction study of jadeite. *American Mineralogist*, *93*(1), 198-209.

Nakajima, J., Matsuzawa, T., Hasegawa, A., & Zhao, D. (2001). Three-dimensional structure of Vp, Vs, and Vp/Vs beneath northeastern Japan: Implications for arc magmatism and fluids. *Journal of Geophysical Research: Solid Earth*, *106*(B10), 21843-21857.

Nestola, F., Ballaran, T. B., Liebske, C., Bruno, M., & Tribaudino, M. (2006). High-pressure behaviour along the jadeite NaAlSi 2 O 6–aegirine NaFeSi 2 O 6 solid solution up to 10 GPa. *Physics and Chemistry of minerals*, *33*(6), 417-425.

Norris, S. (2008). Elastic properties of jadeite. Undergraduate Senior thesis, University of Illinois.

Pandolfo, F., Cámara, F., Domeneghetti, M. C., Alvaro, M., Nestola, F., Karato, S. I., & Amulele, G. (2015). Volume thermal expansion along the jadeite–diopside join. *Physics and Chemistry of Minerals*, *42*(1), 1-14.

Posner, E. S., Dera, P., Downs, R. T., Lazarz, J. D., & Irmen, P. (2014). High-pressure single-crystal X-ray diffraction study of jadeite and kosmochlor. *Physics and Chemistry of Minerals*, *41*(9), 695-707.

Replumaz, A., Negredo, A. M., Villasenor, A., & Guillot, S. (2010). Indian continental subduction and slab break-off during Tertiary collision. *Terra Nova*, *22*(4), 290-296.

Rudnick, R. L., & Fountain, D. M. (1995). Nature and composition of the continental crust: a lower crustal perspective. *Reviews of geophysics*, *33*(3), 267-309.

Sang, L., & Bass, J. D. (2014). Single-crystal elasticity of diopside to 14 GPa by Brillouin scattering. *Physics of the Earth and Planetary Interiors*, *228*, 75-79.

Sinogeikin, S. V., & Bass, J. D. (2000). Single-crystal elasticity of pyrope and MgO to 20 GPa by Brillouin scattering in the diamond cell. *Physics of the Earth and Planetary Interiors*, *120*(1-2), 43-62.

Stixrude, L., & Lithgow-Bertelloni, C. (2005). Thermodynamics of mantle minerals—I. Physical properties. Geophysical Journal International, 162(2), 610-632.

Tribaudino, M., Nestola, F., Bruno, M., Ballaran, T. B., & Liebske, C. (2008). Thermal expansion along the $NaAlSi_2O_6$–$NaFe^{3+}Si_2O_6$ and $NaAlSi_2O_6$–$CaFe^{2+}Si_2O_6$ solid solutions. *Physics and Chemistry of Minerals*, *35*(5), 241-248.

Vaughan, M. T., & Guggenheim, S. (1986). Elasticity of muscovite and its relationship to crystal structure. *Journal of Geophysical Research: Solid Earth*, *91*(B5), 4657-4664.

Walker, A. M. (2012). The effect of pressure on the elastic properties and seismic anisotropy of diopside and jadeite from atomic scale simulation. *Physics of the Earth and Planetary Interiors*, *192*, 81-89.

Wu, Y., Fei, Y., Jin, Z., & Liu, X. (2009). The fate of subducted upper continental crust: an experimental study. *Earth and Planetary Science Letters*, *282*(1-4), 275-284.

Xu, W., Lithgow-Bertelloni, C., Stixrude, L., & Ritsema, J. (2008). The effect of bulk composition and temperature on mantle seismic structure. *Earth and Planetary Science Letters*, *275*(1-2), 70-79.

Yang, R., & Wu, Z. (2014). Elastic properties of stishovite and the CaCl2-type silica at the mantle temperature and pressure: An ab initio investigation. *Earth and Planetary Science Letters*, *404*, 14-21.

Zhang, J., Green II, H. W., & Bozhilov, K. N. (2006). Rheology of omphacite at high temperature and pressure and significance of its lattice preferred orientations. *Earth and Planetary Science Letters*, *246*(3-4), 432-443.

Zhang, J. S., & Bass, J. D. (2016). Single-crystal elasticity of natural Fe-bearing orthoenstatite across a high-pressure phase transition. *Geophysical Research Letters*, *43*(16), 8473-8481.

Zhang, J. S., Bass, J. D., & Schmandt, B. (2018). The Elastic Anisotropy Change Near the 410-km Discontinuity: Predictions from Single-Crystal Elasticity Measurements of Olivine and Wadsleyite. *Journal of Geophysical Research: Solid Earth*, *123*(4), 2674-2684.

Zhao, Y., Von Dreele, R. B., Shankland, T. J., Weidner, D. J., Zhang, J., Wang, Y., & Gasparik, T. (1997). Thermoelastic equation of state of jadeite $NaAlSi_2O_6$: An energy-dispersive Reitveld Refinement Study of low symmetry and multiple phases diffraction. *Geophysical Research Letters*, *24*(1), 5-8.

Supporting Information

IV.1. Definition of the thermal-P EOS

The thermal-P EOS used in this study is defined as:

$$P(V,T) = P(V,T_0) + P_{th}(V,T) \quad \text{(IV.S1)}$$

The P(V, T_0) term corresponds to the P calculated at the reference temperature T_0 (300 K). In this study, we choose the 3rd order Birch-Murnaghan EOS (Birch, 1947) for the P(V, T_0) term. The thermal-P term P_{th}(V, T) is calculated using the Holland-Powell form:

$$P_{th}(V,T) = \alpha_0 K_{T0}\left(\frac{\theta_E}{\xi_0}\right)\left(\frac{1}{exp\left(\frac{\theta_E}{T}\right)-1} - \frac{1}{exp\left(\frac{\theta_E}{T_{ref}}\right)-1}\right) \quad \text{(IV.S2)}$$

where T_{ref} is 300 K in this study, and θ_E is the Einstein T, which is fixed to 537 K for jadeite according to Holland and Powell (2011). The ξ_0 can be calculated by:

$$\xi_0 = \frac{\left(\frac{\theta_E}{T_{ref}}\right)^2 exp\left(\frac{\theta_E}{T_{ref}}\right)}{\left(exp\left(\frac{\theta_E}{T_{ref}}\right)-1\right)^2}. \quad \text{(IV.S3)}$$

IV.2. Calculation of the ambient isothermal bulk modulus K_{T0}

In a typical high-P single-crystal XRD experiment, the sample crystal is loaded in a DAC with soft P-transmitting media and is subject to a relatively uniform stress field. Therefore, it would be expected to obey the Reuss (iso-stress) bound of the bulk modulus. The ambient isothermal bulk modulus K_{T0} can be calculated from the Reuss bound of the adiabatic bulk modulus K_{S0}^R using the equation:

$$K_{T0} = \frac{K_{S0}^R}{1+\alpha\gamma_G T} \quad \text{(IV.S4)}$$

Where α is the thermal expansion coefficient; γ_G is the Grüneisen parameter. The Reuss bound K_{S0}^R is calculated from the ambient C_{ij}s measured in this study (Section 3.2). The term $\alpha\gamma_G T$ is estimated to be ~ 0.01 for pyroxenes at 300 K (Nishihara et al., 2003). Thus, K_{T0} is calculated to be 134.6 GPa.

IV.3. Sensitivity test

It is essential to choose the proper combination of crystallographic orientations for Brillouin experiments to reliably invert the full single-crystal elasticity moduli C_{ij}s, especially for materials with low symmetries. From this perspective, the sensitivity test is important to ensure the robustness of our results.

In this study, we have modified the sensitivity test algorism shown in Fu et al. (2019) and rewrote the sensitivity testing code in Python. The sensitivity value S_x is defined as:

$$S_x = \left[\frac{\partial V_x / V_x}{\partial C_{ij} / C_{ij}}\right]_{maximum} \quad \text{(IV.S5)}$$

where V_x represents the sound velocities of different types of sound waves (Vp, Vs1, and Vs2). Assuming a 0.1% change of each C_{ij}, we calculated the relative change of Vp, Vs1, and Vs2 along all 39 crystallographic directions we have measured in this study. The S_x values represent the maximum relative change of Vp, Vs1, and Vs2 along the 39 different crystallographic directions that we experimentally measured in this study. Figure IV.S9 shows the final results for the orientation combination that were used in this study. Most C_{ij}s can be inverted with satisfactory sensitivity, and C_{15} is the only C_{ij} that can be improved with more measurements. However, the uncertainties of the C_{15} values determined in this study should not affect the robustness of our calculation result and conclusion, due to its minor role in calculating the aggregate elastic properties as well as seismic anisotropy.

IV.4. Definition of the anisotropy indices

A^U is used to describe the overall elastic anisotropy of minerals (Ranganathan & Ostoja-Starzewski, 2008). A^{Vp} or A^{Vs} shows the maximum velocity difference of all Vp or Vs propagating along different directions. D^{Vs} represents the maximum velocity difference between 2 orthogonally polarized shear waves propagating along the same direction.

Universal Anisotropy Index (A^U) is defined as:

$$A^U = 5\frac{G^V}{G^R} + \frac{K_S{}^V}{K_S{}^R} - 6 \quad \text{(IV.S6)}$$

The superscripts R and V denote the Reuss and Voigt bounds of the homogeneous isotropic aggregate under the VRH averaging scheme (Hill, 1963).

The Vp and Vs azimuthal anisotropy A^{Vp} and A^{Vs}, and Vs polarization anisotropy D^{Vs} are defined as:

$$A^{Vp} = \frac{Vp_{max} - Vp_{min}}{Vp_{VRH}} \quad \text{(IV.S7)}$$

$$A^{Vs} = \frac{Vs_{max} - Vs_{min}}{Vs_{VRH}} \quad \text{(IV.S8)}$$

$$D^{Vs} = \frac{|Vs_1 - Vs_2|_{max}}{Vs_{VRH}} \quad \text{(IV.S9)}$$

The subscript VRH represents the VRH average calculated from the known C_{ij}s (Hill, 1963).

IV.5. Voigt-Reuss-Hill average of multi-phase aggregates

The Voigt bound corresponds to uniform strain scenario and the Reuss bound corresponds to uniform stress. In a multi-phase aggregate, mathematically, they are defined as:

$$Voigt\ bound: E^V = f_a E_a + f_b E_b \quad \text{(IV.S10)}$$

$$Reuss\ bound: E^R = \left(\frac{f_a}{E_a} + \frac{f_b}{E_b}\right)^{-1} \quad \text{(IV.S11)}$$

$$Hill\ average: E^{VRH} = (E^V + E^R)/2 \quad \text{(IV.S12)}$$

where E^V, E^R, and E^{VRH} represent the aggregate material properties of Voigt bound, Reuss bound, and Hill average, respectively; E_a and E_b represent the properties of phase a and b, respectively; f_a and f_b represent the volume fractions of phase a and b, respectively.

The actual properties of the multi-phase aggregate should lie in between the Voigt and Reuss bounds. We used Voigt-Reuss-Hill average for our calculations and the two bounds are both plotted in Figure IV.6 and Figure IV.S14.

IV.6. PerpleX calculations

We used PerpleX (Connolly, 2009) to calculate the phase proportions of all mineral components with different starting compositions defined in Irifune et al. (1994), Rudnick and Fountain (1995), and Wu et al. (2009).

PerpleX could not incorporate the K element into the phase equilibrium calculation. Fortunately, K primarily exists in the K-hollandite phase and does not fit the crystallographic sites in the structures of garnet, jadeite, and SiO_2 polymorphs from 250 km to 500 km. Thus, in order to perform the PerpleX calculations, we have modified the starting compositions by subtracting the $KAlSi_3O_8$ from the initial chemical compositions which are defined in Irifune et al. (1994), Rudnick and Fountain (1995), and Wu et al. (2009). We assumed all K remains in K-hollandite, and the volume fraction of K-hollandite remains constant in the calculated depth range.

The calculated results are shown in Figure IV.S13.

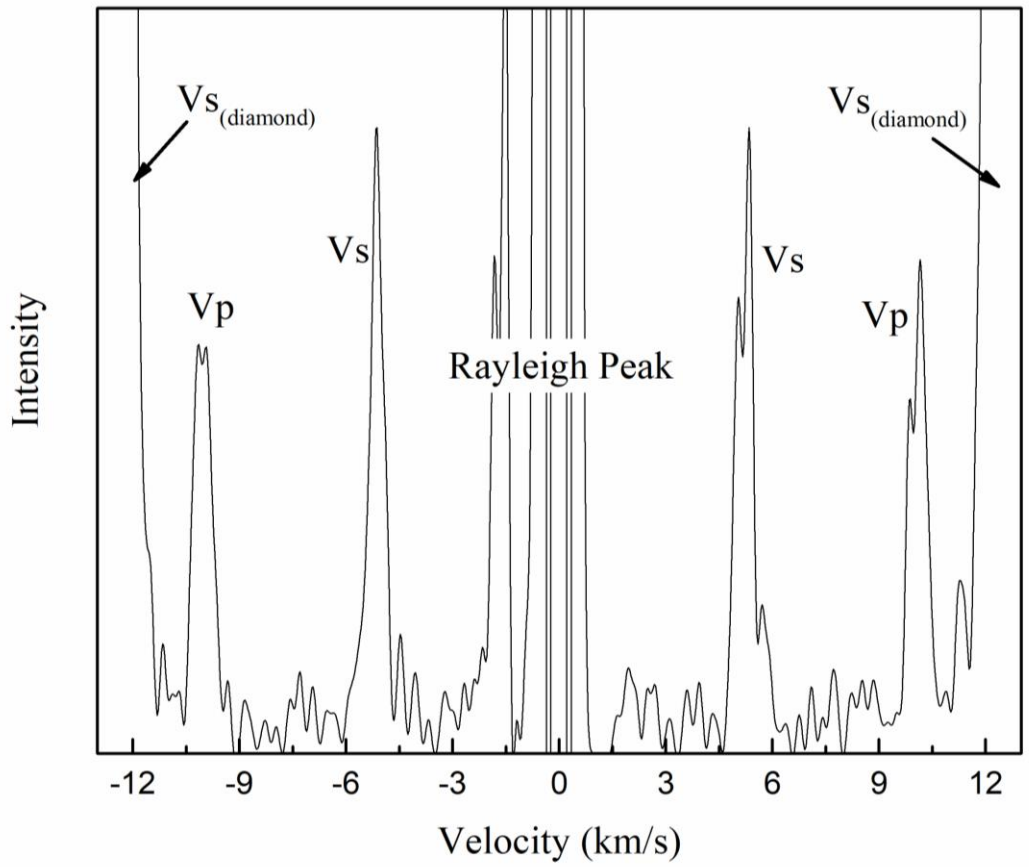

Figure IV.S7. A typical Brillouin spectrum at 18 GPa. Two Vs peaks and Vp peaks from the jadeite sample are observed. The Neon peaks are too weak to be observed at 18 GPa. The collection time is ~10 min. For anisotropic minerals, whether one or two Vs appears, and which Vs appears in a Brillouin spectrum, are controlled by the incoming and the outgoing laser polarization, as well as the selection of crystal orientations (e.g., Auld, 1973; Sandercock, 1982). The polarization direction of the incoming laser also strongly affects the Vp peak intensity, which is typically a lot smaller than the Vs peak intensities for silicate minerals. In most experiments, we optimized the laser polarization to maximize the Vp peak intensity, as shown here.

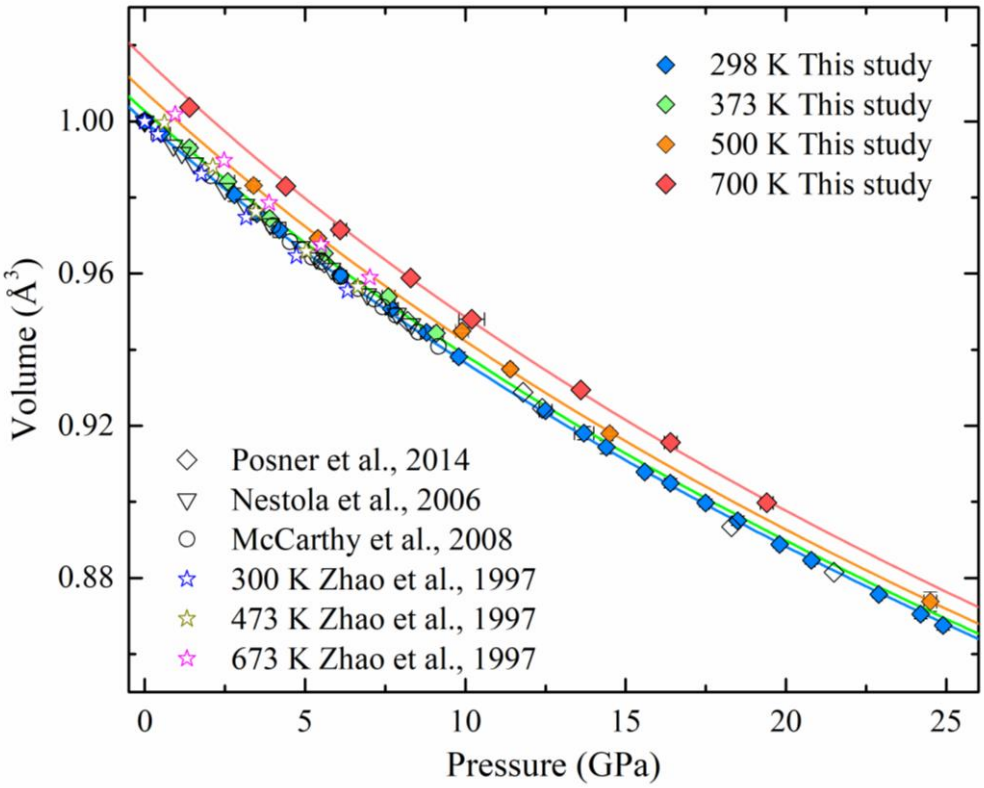

Figure IV.S8. P-V-T EOS and isothermal compression curves of the jadeite determined in this study compared with previous high-P studies (Nestola et al., 2006; McCarthy et al., 2008; Posner et al., 2014; Zhao et al., 1997).

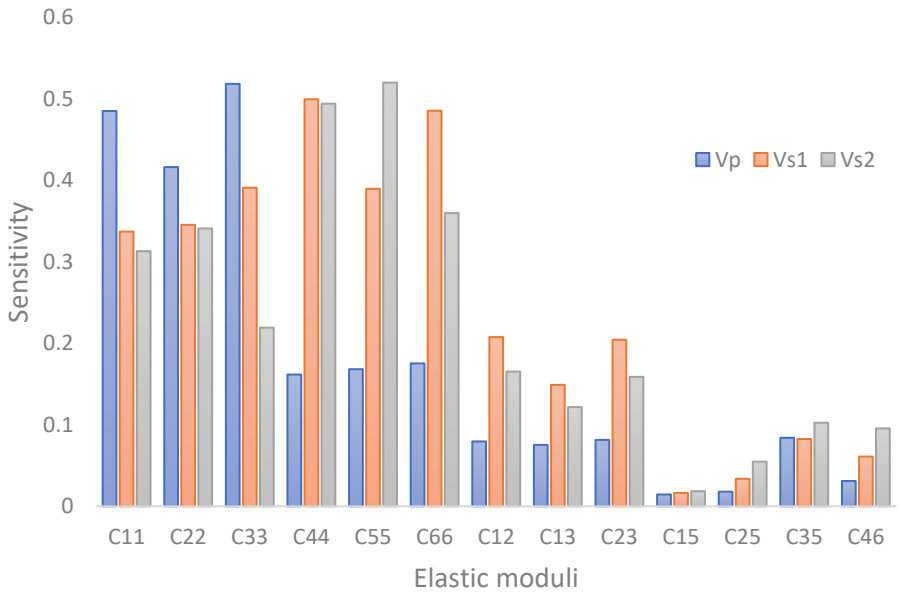

Figure IV.S9. The sensitivity test results for the orientation combination used in this study. The only C_{ij} that can be improved with more measurements is C_{15} (sensitivity coefficients from Vp, Vs1, and Vs2 are all smaller than 0.05). We did not perform more measurements to improve C_{15}, because C_{15} plays a very minor role in calculating the aggregate elastic properties.

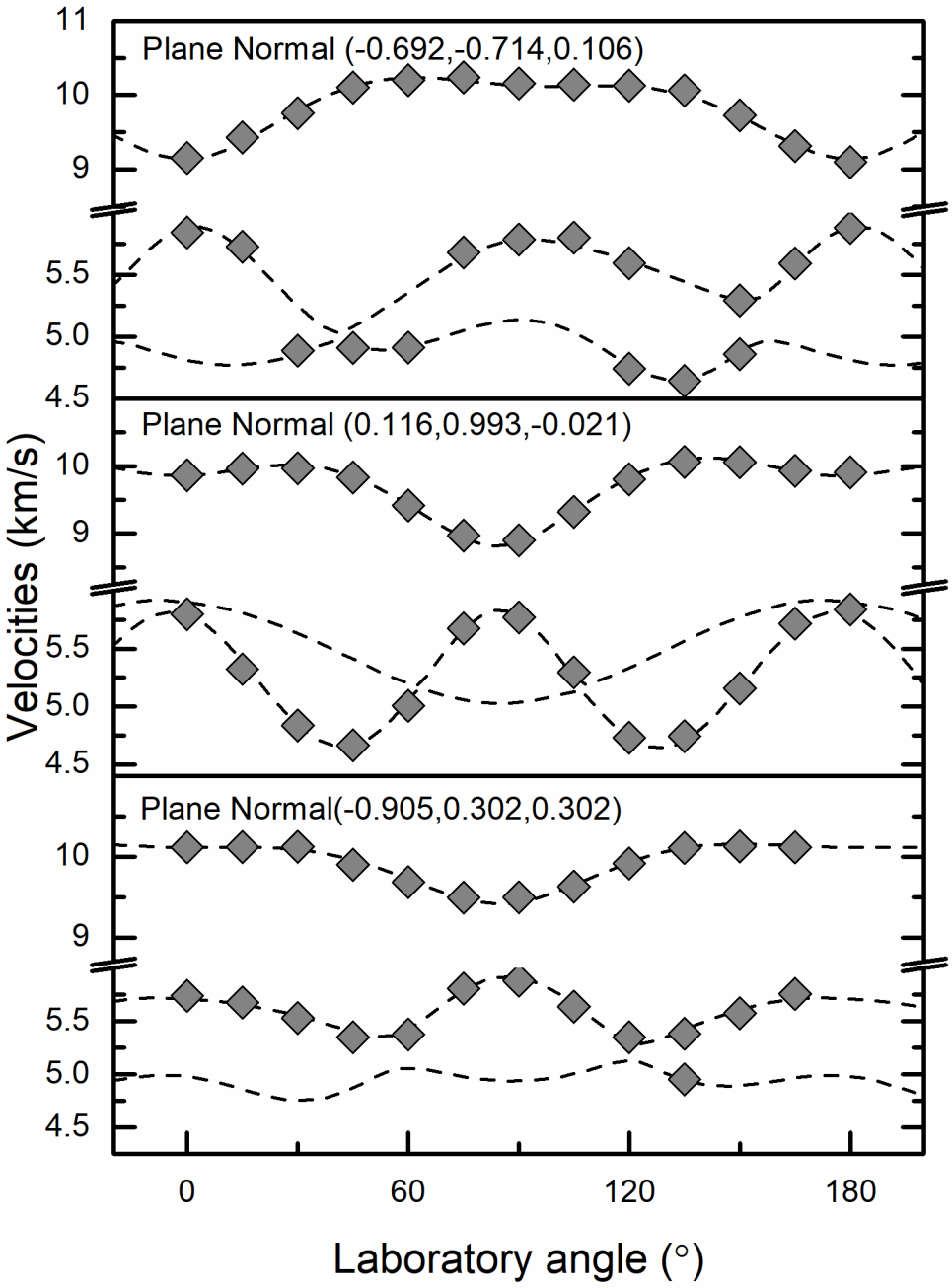

Figure IV.S10. Measured acoustic velocities of jadeite as a function of the laboratory Chi angles within the sample plane at 18 GPa. Dashed lines are the acoustic velocities calculated from the best-fit single-crystal elasticity model, and diamonds are the experimentally determined velocities. The errors of measured velocities are smaller than the symbols. The root-mean-square (RMS) error between the actual experimental data and the model is 32 m/s.

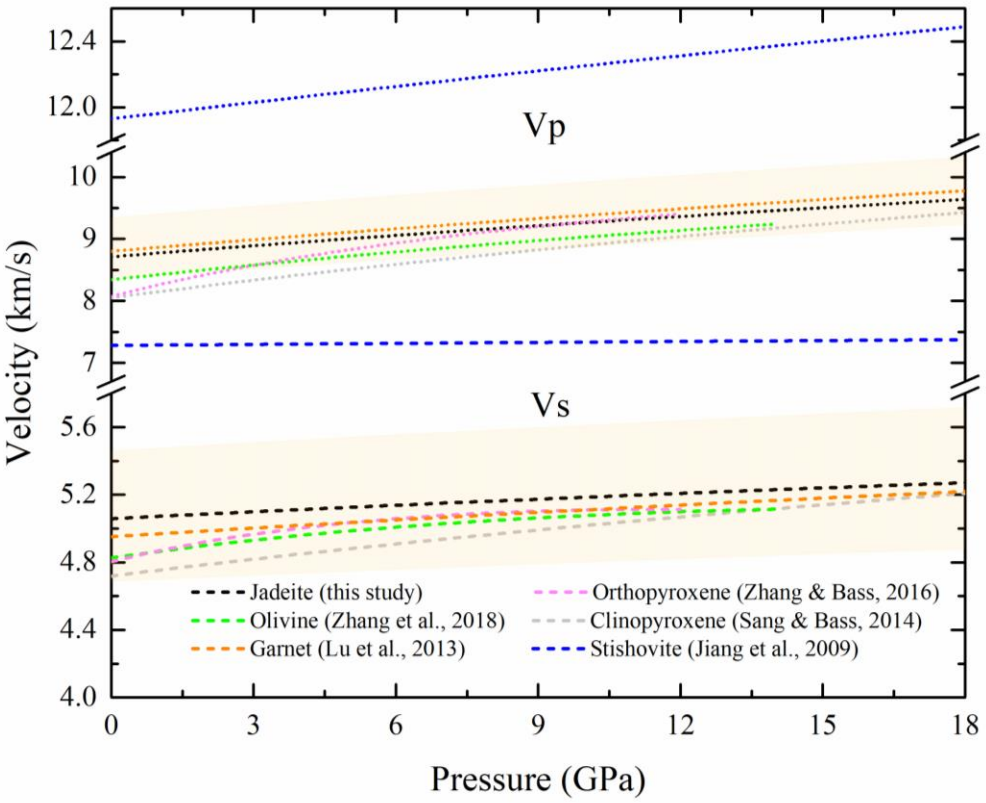

Figure IV.S11. The seismic velocities of the major upper mantle minerals, stishovite, and jadeite at 300 K. Dashed lines represent Vs and dotted lines represent Vp. The shadow regions represent the velocity variations caused by the extensive solid solutions between the 4 major mantle garnet chemical endmembers Pyrope-Grossular-Almandine-Majorite. The high-velocity limit is bounded by grossular (Gwanmesia et al., 2014) and the low-velocity limit is bounded by almandine (Arimoto et al., 2015). The chemical compositions of jadeite (this study), orthopyroxene (Zhang & Bass, 2016), olivine (Zhang et al., 2018), clinopyroxene (Sang & Bass, 2014), garnet (Lu et al., 2013), stishovite (Jiang et al., 2009) are $Jadeite_{0.96}Diopside_{0.04}$, Enstatite (with 10 mol% Fe and Al), $Forsterite_{0.9}Fayalite_{0.1}$, pure Diopside, $Pyrope_{0.695}Almandine_{0.251}Grossular_{0.054}$, and, pure Stishovite, respectively. Considering the higher almandine content up to 38.2 mol% (Wu et al., 2009) or 39.2 mol% (Irifune et al., 1994) in the continentally derived garnets at shallower depths (Table IV.S6), we expect the actual velocities of garnet in the continental sediments/crust to be significantly lower than what were measured by Lu et al. (2013).

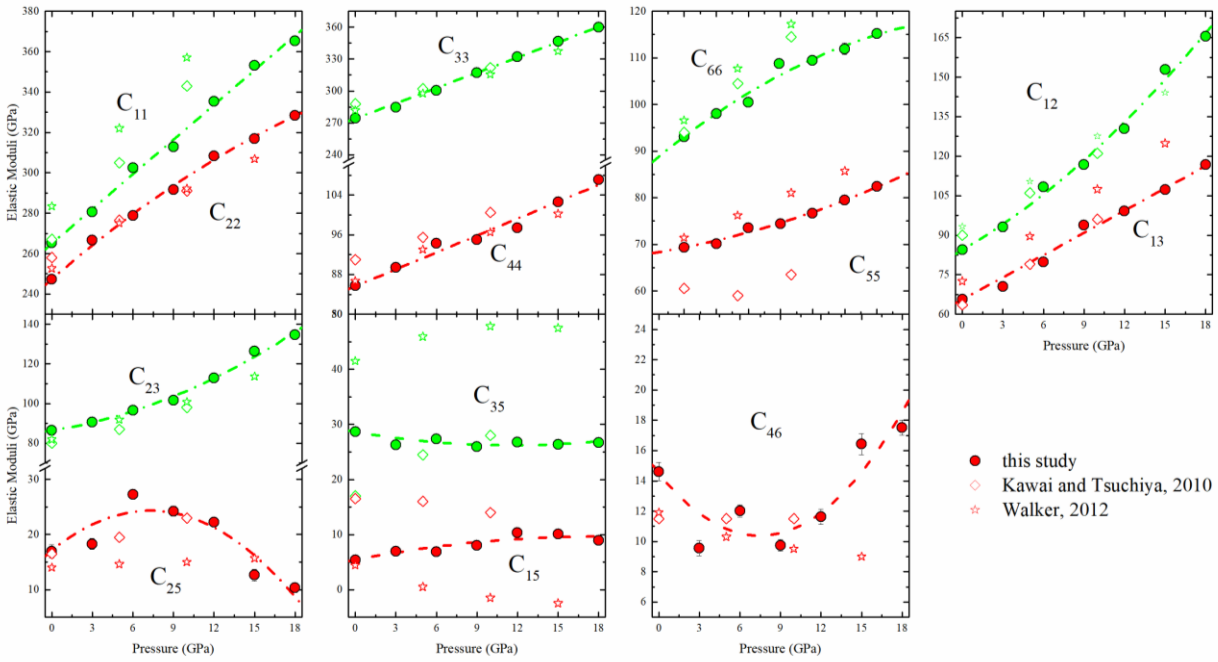

Figure IV.S12. The C_{ij}s obtained in this study compared with two previous first-principles computational studies at 0 K (Kawai & Tsuchiya, 2010; Walker, 2012). The dashed lines are the finite strain fitting results of the experimental data obtained in this study. It is worth noting that the two computational studies at 0 K (Kawai & Tsuchiya, 2010; Walker, 2012) are not consistent with each other. For some diagonal and off-diagonal C_{ij}s, such as C_{55}, C_{15}, C_{25}, and C_{35}, the two computational studies actually yield dramatically different results. It seems that the C_{25} and C_{35} values predicted by Kawai and Tsuchiya (2010) are closer to what were experimentally determined in this study, whereas the C_{55} calculated by Walker (2012) better matched the values measured in this study. Although both calculations are based on density functional theory, Kawai and Tsuchiya (2010) utilized the ab initio approach, whereas Walker (2012) utilized the plane-wave and pseudopotentials in his calculation. These different technical treatments may contribute to the discrepancies shown here. Further computational studies at higher Ts may help to resolve these issues.

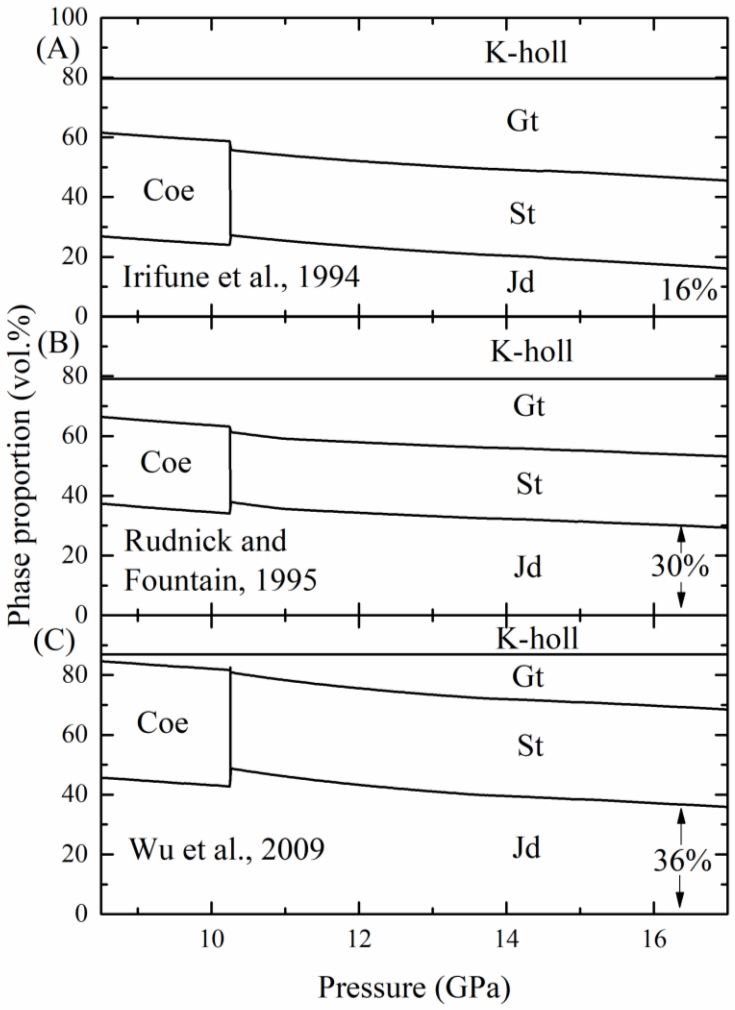

Figure IV.S13. The calculated phase diagrams using PerpleX with different starting compositions defined by Irifune et al. (1994), Rudnick and Fountain (1995), and Wu et al. (2009). (Coe: coesite; St: stishovite; Gt: garnet; Jd: jadeite; K-holl: K-hollandite. Note the Jd marked in the phase diagrams does not represent the pure jadeite endmember. The molar fraction of the jadeite component increases with P from ~70% to ~90%.) The calculated jadeite content at high P-T conditions using the starting composition from Irifune et al. (1994) is much smaller than the values obtained with the average upper continental crust composition (Rudnick & Fountain, 1995). The values obtained using the starting composition from Wu et al. (2009) is actually much closer.

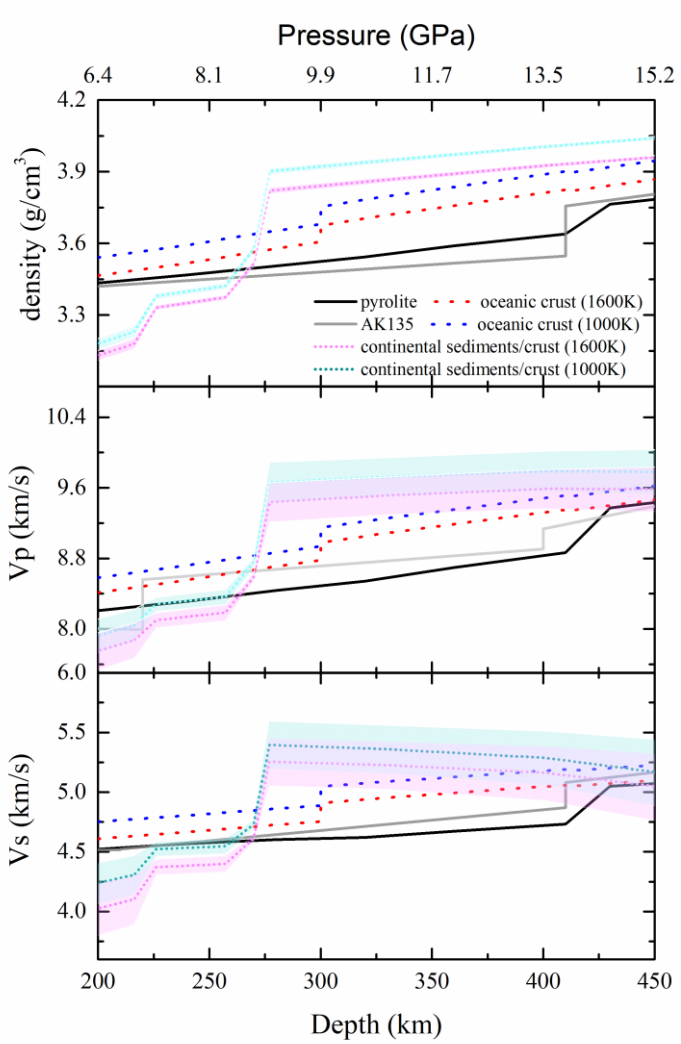

Figure IV.S14. The density and seismic velocities of the subducted continental sediments/crust based on the results from Irifune et al. (1994), compared with oceanic crust (Aoki & Takahashi, 2004), the pyrolite model (Xu et al., 2008), and AK 135 model (Kennett et al., 1995). The blue and pink regions are bounded by Voigt and Reuss bounds along the 1000 K and 1600 K adiabat, respectively. The seismic properties calculated using the petrological model from Irifune et al. (1994) are similar to those from Wu et al. (2009).

Elements	Wt%
Na	10.87
Mg	0.26
Al	12.93
Si	27.87
Ca	0.58
Fe	0.53
O	47.58
Total	100.62

Table IV.S2. Chemical composition of the jadeite sample. The EPMA experiment is performed using the JEOL 8200 Electron Microprobe facility hosted by the Institute of Meteoritics at UNM. Experimental conditions can be found in the main text section 2. The element standards were albite for Na, forsterite for Mg, almandine for Al and Fe, diopside for Si and Ca. Oxygen was calculated by stoichiometry from the cations.

T (K)	P (GPa)	a (Å)	b (Å)	c (Å)	β (°)	V (Å^3)
298	0	9.439(5)	8.583(4)	5.228(1)	107.50(2)	404.0(3)
298	0.5(3)	9.430(7)	8.572(8)	5.222(2)	107.46(4)	402.7(5)
298	2.8(1)	9.39(1)	8.50(1)	5.198(3)	107.33(5)	396.2(7)
298	3.5(1)	9.357(7)	8.506(7)	5.182(2)	107.11(4)	394.2(5)
298	4.2(2)	9.33(1)	8.53(1)	5.159(4)	107.05(7)	392.5(8)
298	6.1(1)	9.299(7)	8.463(8)	5.148(3)	106.87(4)	387.7(5)
298	7.7(2)	9.286(7)	8.418(9)	5.135(3)	106.87(5)	384.1(6)
298	8.8(2)	9.248(6)	8.426(7)	5.117(3)	106.83(4)	381.6(5)
298	9.8(1)	9.219(7)	8.407(8)	5.104(3)	106.66(4)	379.0(5)
298	12.5(2)	9.185(6)	8.356(7)	5.075(2)	106.57(2)	373.3(4)
298	13.7(3)	9.168(8)	8.34(1)	5.060(3)	106.61(5)	370.9(7)
298	14.4(1)	9.14(1)	8.34(1)	5.050(4)	106.36(6)	369.4(7)
298	15.6(1)	9.136(6)	8.294(7)	5.041(2)	106.25(4)	366.8(4)
298	16.4(1)	9.119(5)	8.292(8)	5.036(3)	106.22(4)	365.6(5)
298	17.5(1)	9.087(5)	8.283(7)	5.021(2)	105.89(4)	363.5(4)
298	18.5(1)	9.087(7)	8.262(8)	5.013(2)	106.11(4)	361.6(5)
298	19.8(1)	9.077(6)	8.225(7)	5.002(2)	105.95(4)	359.1(4)
298	20.8(1)	9.055(5)	8.219(7)	4.993(2)	105.91(4)	357.4(4)
298	22.9(1)	9.033(5)	8.189(7)	4.970(2)	105.75(4)	353.8(4)
298	24.2(1)	9.039(6)	8.160(8)	4.964(3)	106.12(5)	351.7(5)
298	24.9(1)	9.010(6)	8.152(8)	4.957(3)	105.7(4)	350.5(5)
373	1.4(1)	9.395(5)	8.59(1)	5.210(2)	107.33(4)	401.2(4)
373	2.6(2)	9.364(5)	8.564(7)	5.197(2)	107.42(4)	397.6(2)
373	3.9(1)	9.322(7)	8.550(7)	5.179(2)	107.46(3)	393.7(2)
373	5.6(1)	9.305(3)	8.504(6)	5.161(2)	107.22(4)	390.0(2)
373	7.6(2)	9.264(6)	8.469(6)	5.138(2)	107.05(4)	385.4(2)
373	9.1(2)	9.229(6)	8.442(7)	5.118(1)	106.9(4)	381.5(2)
500	3.4(1)	9.382(4)	8.53(1)	5.195(2)	107.19(3)	397.2(5)
500	5.4(1)	9.328(3)	8.497(6)	5.167(2)	107.00(2)	391.6(3)
500	11.4(1)	9.213(3)	8.389(5)	5.098(2)	106.54(2)	377.7(3)
500	9.9(2)	9.236(3)	8.434(4)	5.113(2)	106.56(2)	381.8(3)
500	14.5(1)	9.144(3)	8.329(5)	5.062(2)	105.89(2)	370.8(3)
500	24.5(2)	9.014(13)	8.15(2)	4.982(6)	105.3(1)	353(1)
700	8.3(1)	9.261(4)	8.502(6)	5.1432(7)	106.96(2)	387.4(3)
700	19.4(2)	9.072(7)	8.297(8)	5.026(2)	106.09(4)	363.5(2)
700	13.6(1)	9.188(7)	8.38(1)	5.087(2)	106.55(5)	375.5(2)
700	16.4(2)	9.171(7)	8.298(9)	5.068(2)	106.45(5)	369.9(2)
700	10.2(4)	9.237(6)	8.448(7)	5.129(1)	106.84(4)	383.0(2)
700	6.1(2)	9.324(8)	8.522(7)	5.169(1)	107.14(4)	392.5(2)
700	4.4(1)	9.383(8)	8.538(8)	5.191(1)	107.28(4)	397.1(2)
700	1.4(1)	9.447(8)	8.605(8)	5.231(3)	107.54(7)	405.5(3)

Table IV.S3. Unit cell parameters of the jadeite determined from single-crystal XRD experiments.

	Omphacite (Hao et al., 2019b)			Diopside (Sang & Bass, 2014)		
	M_0 (GPa)	$\partial M/\partial P$	$\partial M^2/\partial P^2$ (GPa^{-1})	M_0 (GPa)	$\partial M/\partial P$	$\partial M^2/\partial P^2$ (GPa^{-1})
C_{11}	231.5(8)	8.3(3)	-0.24(6)	229.0(4)	6.7(2)	-0.16(4)
C_{22}	201(1)	4.92(7)	0	179.0(4)	6.7(3)	-0.23(6)
C_{33}	253.8(8)	7.8(3)	-0.29(5)	242.5(4)	7.9(2)	-0.28(4)
C_{44}	79.1(5)	0.96(3)	0	78.9(3)	1.5(1)	0
C_{55}	68.9(4)	1.03(2)	0	68.1(2)	2.2(2)	-0.15(4)
C_{66}	74.0(4)	2.41(4)	0	78.2(3)	2.05(9)	0
C_{12}	84.4(9)	4.6(4)	-0.13(6)	78.0(7)	4.9(6)	-0.3(1)
C_{13}	76(1)	3.13(7)	0	69.8(6)	4.5(2)	-0.18(4)
C_{23}	60(2)	2.94(15)	0	58.0(7)	3.2(2)	0
C_{15}	5.8(5)	0	0	9.9(3)	-0.8(1)	0.10(3)
C_{25}	5.4(10)	0.5(1)	0	6.1(5)	-1.1(2)	0
C_{35}	39.8(5)	-2.3(1)	0.18(2)	40.9(3)	-1.3(2)	0.05(3)
C_{46}	5.9(4)	0.73(3)	-0.148(6)	6.6(2)	-1.7(3)	0.26(7)
	Olivine (Zhang et al., 2018)			Orthopyroxene (Zhang & Bass, 2016)		
	M_0 (GPa)	$\partial M/\partial P$	$\partial M^2/\partial P^2$ (GPa^{-1})	M_0 (GPa)	$\partial M/\partial P$	$\partial M^2/\partial P^2$ (GPa^{-1})
C_{11}	320.1(6)	7.2(3)	-0.05(1)	232.2(5)	12.6(4)	-1.3(1)
C_{22}	197.1(6)	5.9(1)	-0.08(1)	175.7(7)	10.2(4)	-0.8(1)
C_{33}	233.4(8)	5.3(1)	-0.03(1)	222.9(6)	13.5(6)	-1.3(2)
C_{44}	63.6(5)	1.91(4)	-0.037(2)	82.2(4)	3.0(2)	-0.42(5)
C_{55}	77.3(4)	1.53(5)	-0.023(2)	77.3(3)	2.6(2)	-0.34(8)
C_{66}	78(2)	2.11(6)	-0.024(2)	78.1(6)	4.4(5)	-0.6(2)
C_{12}	70(1)	3.8(1)	-0.03(1)	79.5(9)	6.9(3)	-0.5(1)
C_{13}	70.9(6)	3.7(1)	-0.011(4)	61.2(6)	8.6(5)	-0.9(2)
C_{23}	75.6(8)	3.35(7)	0	54.1(8)	8.4(4)	-0.7(1)

Table IV.S4. P derivatives of the single-crystal elastic moduli of omphacite, diopside, olivine, and orthopyroxene. $\partial M/\partial P$ and $\partial M^2/\partial P^2$ values presented here are the first and second P derivatives defined by the finite strain EOS in Davies (1974). M_0 represents the values at ambient conditions and is fixed in the inversion.

Mineral	Density (g/cm^3)	K_{S0} (GPa)	$\partial K_S/\partial P$	$\partial K_S/\partial T$ (GPa/K)	G_0 (GPa)	$\partial G/\partial P$	$\partial G/\partial T$ (GPa/K)	a_0 (10^{-4} K^{-1})	a_1 (10^{-8} K^{-2})	a_2 (K)
Jadeite[1]	3.302(5)	138(3)	3.9(1)	-0.012(1)	84(2)	1.09(4)	-0.011(1)	0.34(5)	0	0
Diopside[1]	3.272(6)	116.4(7)	4.9(1)	-0.012(1)	73.0(4)	1.6(1)	-0.011(1)	0.19	2.08	0
Pyrope[2,3,4,5,8]	3.56(2)	171.0(5)	4.4(1)	-0.014(3)	94.9(2)	1.15(6)	-0.011(2)	0.288	0.2787	-0.5521
Mg-majorite[2,3,4,5,8]	3.56(2)	162.0(5)	4.4(1)	-0.014(3)	86.2(2)	1.15(6)	-0.011(2)	0.288	0.2787	-0.5521
Jd-majorite[6,7]	3.644(7)	178(4)	4.47(2)	-0.0138(3)	125(2)	1.29(5)	-0.0128(2)	0.1951	0.8089	-0.4972
Grossular[7,8]	3.605(2)	171.2(8)	4.47(2)	-0.0138(3)	107.4(2)	1.29(5)	-0.0128(2)	0.1951	0.8089	-0.4972
Almandine[9]	4.3188(2)	174.2(12)	4.61(14)	-0.0267(7)	94.9(7)	1.06(6)	-0.0131(8)	0.26(5)	2.3(14)	0
Coesite[10,11]	2.91(2)	106.5(6)	2.7(15)	-0.0016(16)	60.7(3)	0.33(5)	-0.0044(5)	0.106(14)	-0.028(166)	-0.48(12)
Stishovite[12,13]	4.381(2)	296(5)	4.2(4)	-0.046(5)				0.126(11)	1.29(17)	0
Phengite[14,15]	2.844(30)	58(10)	6.2(14)	0	35(8)	0.76(3)	-0.011	0.28(4)	0	0
K-hollandite[16,17]	3.9	197	4.37(7);* -0.056(13)	-0.033(2)	107.9	0.95(4);* -0.515(5)	-0.011	0.332(5)	1.09(1)	0
Hedenbergite[1,8,18]	3.657(1)	120(4)	4	-0.012(1)	62(2)	1.6(1)	-0.011(1)	0.298	0	0

1. Li and Neuville (2010) 2. Irifune et al. (2008) 3. Liu et al. (2000) 4. Sinogeikin and Bass (2002) 5. Suzuki and Anderson (1983) 6. Reichmann et al. (2002) 7. Gwanmesia et al. (2014) 8. Fei (1995) 9. Arimoto et al. (2015) 10. Chen et al. (2017) 11. Kulik et al. (2018) 12. Yang and Wu (2014) 13. Nishihara et al. (2005) 14. Pavese et al. (1999) 15. Vaughan and Guggenheim (1986) 16. Nishiyama et al. (2005) 17. Kawai and Tsuchiya (2013) 18. Kandelin and Weidner (1988b) * The second values listed in the cells of $\partial K_S/\partial P$ and $\partial G/\partial P$ are the second P derivatives: $\partial^2 K_S/\partial P^2$and $\partial^2 G/\partial P^2$.

Table IV.S5. Thermoelastic parameters of all the relevant mineral phases for calculating the density and velocity. The a_0, a_1 and a_2 are the thermal expansion parameters, defined in Fei (1995): $a(T)=a_0+a_1T+a_2T^{-2}$. The thermal expansion parameters for jadeite using equation IV.3. The elasticity data of stishovite are directly obtained from the first-principles calculation study by Yang and Wu (2014). The parameters for stishovite listed in the table are for density calculation. The parameters (except the thermal expansion parameters) for pyrope and coesite are recalculated based on the experimental values presented in Irifune et al. (2008) and Chen et al. (2017). Due to the lack of data, we used the $\partial G/\partial P$ of antigorite for phengite due to their similar layered structures, and the $\partial G/\partial T$ for phengite and K-hollandite is fixed at -0.011 GPa/K, which is the averaged value of all the other minerals listed in the table. Some parameters are listed without uncertainties because the uncertainties were not reported in the references.

Depth (km)	Clinopyroxene in the oceanic crust (Aoki & Takahashi, 2004)	Garnet in the oceanic crust (Aoki & Takahashi, 2004)	Garnet in the continental sediments/crust (Wu et al., 2009)
200	$Di_{0.555}Jd_{0.272}He_{0.173}$	$Py_{0.346}Mj_{0.071}Gr_{0.283}Am_{0.276}Mj(jd)_{0.024}$	$Gr_{0.602}Am_{0.382}Mj(jd)_{0.016}$
300	$Di_{0.495}Jd_{0.348}He_{0.157}$	$Py_{0.247}Mj_{0.138}Gr_{0.308}Am_{0.259}Mj(jd)_{0.049}$	$Mj_{0.073}Gr_{0.536}Am_{0.342}Mj(jd)_{0.050}$
390	$Di_{0.442}Jd_{0.416}He_{0.143}$	$Py_{0.168}Mj_{0.188}Gr_{0.330}Am_{0.243}Mj(jd)_{0.071}$	$Mj_{0.175}Gr_{0.455}Am_{0.292}Mj(jd)_{0.078}$
440	$Di_{0.412}Jd_{0.454}He_{0.135}$	$Py_{0.129}Mj_{0.211}Gr_{0.342}Am_{0.234}Mj(jd)_{0.084}$	$Mj_{0.230}Gr_{0.412}Am_{0.265}Mj(jd)_{0.094}$
500	$Di_{0.376}Jd_{0.499}He_{0.125}$	$Py_{0.086}Mj_{0.236}Gr_{0.357}Am_{0.223}Mj(jd)_{0.099}$	$Mj_{0.291}Gr_{0.363}Am_{0.235}Mj(jd)_{0.111}$
Depth (km)	Clinopyroxene in the continental sediments/crust (Irifune et al., 1994)		Garnet in the continental sediments/crust (Irifune et al., 1994)
216	$Di_{0.241}Jd_{0.652}He_{0.107}$		$Mj_{0.249}Gr_{0.359}Am_{0.392}$
270	$Di_{0.199}Jd_{0.709}He_{0.092}$		$Mj_{0.245}Gr_{0.412}Am_{0.344}$
330	$Di_{0.154}Jd_{0.771}He_{0.075}$		$Mj_{0.243}Gr_{0.428}Am_{0.298}Mj(jd)_{0.031}$
460	$Di_{0.066}Jd_{0.892}He_{0.042}$		$Mj_{0.273}Gr_{0.374}Am_{0.247}Mj(jd)_{0.106}$

Table IV.S6. The depth-dependent chemical compositions of garnets and clinopyroxenes in the oceanic crust and continental sediments/crust. The clinopyroxene in continental sediments/crust from Wu et al. (2009) is pure jadeite. (Py: pyrope; Mj: majorite; Gr: grossular; Am: almandine; Mj(jd): jadeite-majorite; Di: diopside; Jd: jadeite; He: hedenbergite) The almandine content of the garnets in continental sediments/crust varies between 38.2 mol% to 23.5 mol%, 39.2 mol% to 24.7 mol% from 200-500 km depth in Wu et al. (2009) and Irifune et al. (1994), respectively.

Reference

Aoki, I., & Takahashi, E. (2004). Density of MORB eclogite in the upper mantle. *Physics of the Earth and Planetary Interiors*, *143*, 129-143.

Arimoto, T., Gréaux, S., Irifune, T., Zhou, C., & Higo, Y. (2015). Sound velocities of Fe3Al2Si3O12 almandine up to 19 GPa and 1700 K. *Physics of the Earth and Planetary Interiors*, *246*, 1-8.

Auld, B. A. (1973). Acoustic fields and waves in solids. Рипол Классик.

Birch, F. (1947). Finite elastic strain of cubic crystals. *Physical review*, *71*(11), 809.

Chen, T., Liebermann, R. C., Zou, Y., Li, Y., Qi, X., & Li, B. (2017). Tracking silica in Earth's upper mantle using new sound velocity data for coesite to 5.8 GPa and 1073 K. *Geophysical Research Letters*, *44*(15), 7757-7765.

Connolly, J. A. D. (2009). The geodynamic equation of state: what and how. Geochemistry, Geophysics, Geosystems, 10(10).

Davies, G. F. (1974). Effective elastic moduli under hydrostatic stress—I. quasi-harmonic theory. *Journal of Physics and Chemistry of Solids*, *35*(11), 1513-1520.

Fei, Y. (1995). Thermal expansion. In T. J. Ahrens *Mineral physics & crystallography: a handbook of physical constants* (Vol. 2, pp. 29-44). Washington, DC: American Geophysical Union.

Fu, S., Yang, J., Tsujino, N., Okuchi, T., Purevjav, N., & Lin, J. F. (2019). Single-crystal elasticity of (Al, Fe)-bearing bridgmanite and seismic shear wave radial anisotropy at the topmost lower mantle. *Earth and Planetary Science Letters*, *518*, 116-126.

Gwanmesia, G. D., Wang, L., Heady, A., & Liebermann, R. C. (2014). Elasticity and sound velocities of polycrystalline grossular garnet (Ca3Al2Si3O12) at simultaneous high pressures and high temperatures. *Physics of the Earth and Planetary Interiors*, *228*, 80-87.

Hao, M., Zhang, J. S., Pierotti, C. E., Ren, Z., & Zhang, D. (2019b). High‐Pressure Single‐Crystal Elasticity and Thermal Equation of State of Omphacite and Their Implications for the Seismic Properties of Eclogite in the Earth's Interior. Journal of Geophysical Research: Solid Earth, 124(3), 2368-2377.

Hill, R. (1963). Elastic properties of reinforced solids: some theoretical principles. *Journal of the Mechanics and Physics of Solids*, *11*(5), 357-372.

Holland, T. J. B., & Powell, R. (2011). An improved and extended internally consistent thermodynamic dataset for phases of petrological interest, involving a new equation of state for solids. *Journal of Metamorphic Geology*, *29*(3), 333-383.

Irifune, T., Higo, Y., Inoue, T., Kono, Y., Ohfuji, H., & Funakoshi, K. (2008). Sound velocities of majorite garnet and the composition of the mantle transition region. *Nature*, *451*(7180), 814.

Jiang, F., Gwanmesia, G. D., Dyuzheva, T. I., & Duffy, T. S. (2009). Elasticity of stishovite and acoustic mode softening under high pressure by Brillouin scattering. *Physics of the Earth and Planetary Interiors*, *172*(3-4), 235-240.

Kandelin, J., & Weidner, D. J. (1988b). Elastic properties of hedenbergite. Journal of Geophysical Research: Solid Earth, 93(B2), 1063-1072.

Kawai, K., & Tsuchiya, T. (2013). First-principles study on the high-pressure phase transition and elasticity of KAlSi3O8 hollandite. *American Mineralogist*, *98*(1), 207-218.

Kulik, E., Murzin, V., Kawaguchi, S., Nishiyama, N., & Katsura, T. (2018). Thermal expansion of coesite determined by synchrotron powder X-ray diffraction. *Physics and Chemistry of Minerals*, 1-9.

Li, B., & Neuville, D. R. (2010). Elasticity of diopside to 8 GPa and 1073 K and implications for the upper mantle. *Physics of the Earth and Planetary Interiors*, *183*(3-4), 398-403.

Lin, J. F., Mao, Z., Yang, J., & Fu, S. (2018). Elasticity of lower-mantle bridgmanite. Nature, 564(7736), E18-E26.

Liu, J., Chen, G., Gwanmesia, G. D., & Liebermann, R. C. (2000). Elastic wave velocities of pyrope–majorite garnets (Py62Mj38 and Py50Mj50) to 9 GPa. *Physics of the Earth and Planetary Interiors*, *120*(1-2), 153-163.

Lu, C., Mao, Z., Lin, J. F., Zhuravlev, K. K., Tkachev, S. N., & Prakapenka, V. B. (2013). Elasticity of single-crystal iron-bearing pyrope up to 20 GPa and 750 K. *Earth and Planetary Science Letters*, *361*, 134-142.

McCarthy, A. C., Downs, R. T., & Thompson, R. M. (2008). Compressibility trends of the clinopyroxenes, and in-situ high-pressure single-crystal X-ray diffraction study of jadeite. *American Mineralogist*, *93*(1), 198-209.

Nestola, F., Ballaran, T. B., Liebske, C., Bruno, M., & Tribaudino, M. (2006). High-pressure behaviour along the jadeite NaAlSi 2 O 6–aegirine NaFeSi 2 O 6 solid solution up to 10 GPa. *Physics and Chemistry of minerals*, *33*(6), 417-425.

Nishihara, Y., Nakayama, K., Takahashi, E., Iguchi, T., & Funakoshi, K. Ì. (2005). P-V-T equation of state of stishovite to the mantle transition zone conditions. *Physics and Chemistry of Minerals*, *31*(10), 660-670.

Nishihara, Y., Takahashi, E., Matsukage, K., & Kikegawa, T. (2003). Thermal equation of state of omphacite. *American Mineralogist*, *88*(1), 80-86.

Posner, E. S., Dera, P., Downs, R. T., Lazarz, J. D., & Irmen, P. (2014). High-pressure single-crystal X-ray diffraction study of jadeite and kosmochlor. *Physics and Chemistry of Minerals*, *41*(9), 695-707.

Ranganathan, S. I., & Ostoja-Starzewski, M. (2008). Universal elastic anisotropy index. *Physical Review Letters*, *101*(5), 055504.

Reichmann, H. J., Sinogeikin, S. V., Bass, J. D., & Gasparik, T. (2002). Elastic Moduli of Jadeite-Enstatite Majorite. *Geophysical research letters*, *29*(19).

Rudnick, R. L., & Fountain, D. M. (1995). Nature and composition of the continental crust: a lower crustal perspective. *Reviews of geophysics*, *33*(3), 267-309.

Sandercock, J. R. (1982). Trends in Brillouin scattering: studies of opaque materials, supported films, and central modes. In Light scattering in solids III (pp. 173-206). Springer, Berlin, Heidelberg.

Sang, L., & Bass, J. D. (2014). Single-crystal elasticity of diopside to 14 GPa by Brillouin scattering. *Physics of the Earth and Planetary Interiors*, *228*, 75-79.

Sinogeikin, S. V., & Bass, J. D. (2002). Elasticity of Majorite and a Majorite-Pyrope solid solution to high pressure: Implications for the Transition Zone. *Geophysical Research Letters*, *29*(2), 4-1.

Speziale, S., Marquardt, H., & Duffy, T. S. (2014). Brillouin scattering and its application in geosciences. Reviews in Mineralogy and Geochemistry, 78(1), 543-603.

Suzuki, I., & Anderson, O. L. (1983). Elasticity and thermal expansion of a natural garnet up to 1, 000K. *Journal of Physics of the Earth*, *31*(2), 125-138.

Yang, R., & Wu, Z. (2014). Elastic properties of stishovite and the CaCl2-type silica at the mantle temperature and pressure: An ab initio investigation. *Earth and Planetary Science Letters*, *404*, 14-21.

Zhang, J. S., & Bass, J. D. (2016). Single-crystal elasticity of natural Fe-bearing orthoenstatite across a high-pressure phase transition. *Geophysical Research Letters*, *43*(16), 8473-8481.

Zhang, J. S., Bass, J. D., & Schmandt, B. (2018). The Elastic Anisotropy Change Near the 410-km Discontinuity: Predictions from Single-Crystal Elasticity Measurements of Olivine and Wadsleyite. *Journal of Geophysical Research: Solid Earth*, *123*(4), 2674-2684.

Chapter V

Seismic visibility of eclogite in the Earth's upper mantle – implications from high pressure-temperature single-crystal elastic properties of omphacite

Abstract

Identifying and locating the geochemical and geophysical heterogeneities in the Earth's interior is one of the most important and challenging tasks for the deep Earth scientists. Subducted oceanic crust metamorphizes into the dense eclogite in the upper mantle and is considered a major cause of geochemical and geophysical heterogeneities in the deep Earth. In order to detect eclogitic materials inside the Earth, precise measurements of the high pressure-temperature single-crystal elasticity of major minerals in eclogite is thus exceedingly important. Omphacite, a Na,Al-bearing clinopyroxene, constitutes up to 75 vol% of eclogite. In the present study, we performed the first high pressure-temperature single-crystal elasticity measurements of omphacite using Brillouin spectroscopy. Utilizing the finite-strain approach, we obtained the following thermoelastic parameters for omphacite: K_{S0}'=4.5(1), G_0'=1.53(5), $\partial K_{S0}/\partial T$=-0.029(5) GPa/K, $\partial G_0/\partial T$=-0.013(5) GPa/K, with K_{S0}=123(3) GPa, G_0=74(2) GPa, and ρ_0=3.34(1) g/cm^3. We found that the seismic velocities of undeformed eclogite are similar to pyrolite at the depths of 200-300 and 410-500 km, thus eclogite is seismically invisible at these depths. Combined with the lattice-preferred orientations of the omphacite in naturally deformed eclogites, we also modeled seismic anisotropy of eclogite at various pressure-temperature conditions. A 10 km thick subducted eclogitic crust can result in ~0.2 s shear wave splitting in the Earth's upper mantle.

1. Introduction

The Earth's oceanic crust is primarily made of basalt. When oceanic lithosphere is subducted, the basaltic oceanic crust metamorphizes into eclogite when the pressure and temperature exceed 2 GPa and 1073 K (Ito & Kennedy, 1971). Due to its high density, the formation of eclogite further helps the slab subduction (Xu et al., 2008; Moghadam et al., 2010). Omphacite, the solid solution of diopside ($CaMgSi_2O_6$) and jadeite ($NaAlSi_2O_6$), is the major mineral phase in eclogite (up to 75 vol%) and can stably exist at depths up to 500 km. Due to the slow mixing and diffusion process within the Earth's interior, the recycled eclogitic materials can be preserved over the geological time as chemical heterogeneities in the deep Earth (Xu et al. 2008, Ballmer et al. 2017). To seismically identify those heterogeneities, the high pressure-temperature elastic properties of relevant minerals are needed.

Seismologists have found complex seismic anisotropy features near subduction zones (e.g. Niday & Humphreys, 2020; Long & Silver, 2008), which are generally explained as the result of the flow-induced lattice-preferred orientation (LPO) of the elastically anisotropic minerals. Understanding the seismic anisotropy observations as well as the mantle flow field requires knowledge of the single-crystal elasticity and the LPO of relevant minerals, such as omphacite in the subducted slab crust.

Although the elastic properties of the Ca,Mg endmember of clinopyroxene, diopside, have been thoroughly investigated (e.g. Sang & Bass, 2014; Li & Neuville, 2010; Walker, 2012; Sang et al., 2011; Isaak et al., 2006), the single-crystal elastic properties of omphacite, on the other hand, are less constrained. High-pressure single-crystal elasticity studies of omphacite are either performed at 0 K condition computationally (Skelton & Walker, 2015), or measured at 300 K condition experimentally (Hao et al., 2019). Our ability to trace the eclogitic materials in the deep Earth through seismic methods is substantially restricted by the

lack of knowledge on the temperature-dependent single-crystal elasticity of omphacite at high-pressure condition. Thus, building up on our previous high-pressure study on omphacite single crystals at 300 K (Hao et al., 2019), we further conducted single-crystal Brillouin spectroscopy experiments on the same crystals at simultaneously high pressure-temperature conditions up to 18 GPa and 700 K, and then modeled the isotropic and anisotropic seismic properties of the undeformed and deformed eclogite samples after combining the laboratory determined LPO with the updated pressure-temperature dependent single-crystal elastic properties of omphacite measured in this study. The results presented in this study will serve as the basis for detecting the recycled oceanic crust in the Earth's upper mantle.

2. Experiments

The omphacite crystals we utilized in this study are the same as the ones used in Hao et al. (2019), with the chemical composition of $Na_{0.289}Mg_{0.633}Ca_{0.68}Fe_{0.108}Al_{0.323}Si_{1.975}O_6$ determined by Electron Microprobe (EPMA). The selected crystals were hand-polished to 10-20 μm thick platelets using aluminum oxide lapping films. They are optically examined to be scratch-free and inclusion-free under the microscope. The crystals were then cut into smaller pieces with lateral dimensions between 40 and 60 μm for the diamond anvil cell (DAC) loading. The plane normals of different crystals were measured at 13-BM-D station of GeoSoilEnviroCARS (GSECARS). The technical details of the X-ray diffraction experiments for determining the crystal orientations can be found in Hao et al. (2019). The face normals of the polished crystals are: (-0.152, -0.969, 0.195), (0.242, 0.299, -0.923), and (0.651, -0.759, -0.005). The angular uncertainties are 1-2°. Based on the sensitivity test (Text V.S1.1) result shown in Figure V.S5, the sound velocity measurements within the three selected crystal

platelets could offer enough constraints for the 13 independent single-crystal elastic moduli (C_{ij}s) of the monoclinic omphacite.

We used resistively heated DACs for generating the high pressure-temperature conditions. A pair of 16-sided standard-cut diamond anvils with 450 μm cutlets were glued to two 90° opening standard WC seats, and then placed in a BX90 DAC (Kantor et al., 2012). The sample chamber was formed by the two diamond anvils and a ~50 μm thick pre-indented Re foil with a ~280 μm diameter hole. A Pt heater, which is made of a pyrophyllite ring base with 3 equal-length Pt wires (Lai et al., 2020), was placed between the two WC seats to heat up the sample chamber at high-pressure conditions. Two K-type thermocouples were placed in direct contact with the diamond on the same side, and as close as possible to the diamond culet. Additional cement was added on top of the conjunctions to insulate the thermocouples from the Pt heater. In addition, we filled the space within the DAC as well as the space between the DAC and the water-cooled Al DAC holder with high-temperature ceramic fiber, which also helped reduce the heat loss and the temperature gradient within the DAC. Figure V.S6 shows the power curve of the high pressure-temperature experiments, the power at the 700 K is about 85 W. The maximum difference between the temperature readings from the two thermocouples was ~8 K throughout the entire examined pressure-temperature range. We did not use any inert gas to protect the diamonds due to the relatively low temperature reached in this study. None of the diamonds used in this study showed any oxidation/ heat damage after the completion of the experiments. The DAC sample chambers were filled with a Neon pressure-transmitting medium using GSECARS's gas loading system (Rivers et al., 2008). Two ruby spheres were loaded with the crystal inside the DAC sample chamber and ruby fluorescence shift measurements were employed for pressure determination (Shen et al., 2020; Datchi et al.,

2007). We estimated pressure uncertainties from the temperature difference of the two thermocouples and the two pressure readings before and after each Brillouin experimental run.

We conducted all high pressure-temperature Brillouin spectroscopy measurements in the UNM laser spectroscopy laboratory. The spectroscopy system is equipped with a 300 mW 532 nm single-mode Spectra Physics diode-pumped solid-state laser, and a six-pass tandem Fabry-Perot interferometer with Hamamatsu H10682 detector. We use a line polarizer to adjust the laser beam power. The power reaching the DACs is ~80-100 mW. The incoming laser is focused onto the sample with a 9 mm diameter MgF_2 coated plano-convex lens with a focal length of 36 mm and the Brillouin scattered light is collected by a 30 mm diameter achromat with a focal length of 100 mm. The detailed experimental setup has been described in Zhang et al. (2015). The silica glass Corning 7980 is used to calibrate the scattering angle for the 50° scattering geometry, results in a scattering angle of 50.68(6)° (Zhang et al., 2011). We were able to observe both the shear (Vs) and compressional (Vp) modes in all Brillouin spectra we collected at thirteen different Chi angles (360, 345, 315, 285, 255, 225, 195, 180, 150, 120, 90, 60, 30) along the 360° azimuth for all three crystals at each pressure-temperature condition to avoid any geometrical errors. A typical high pressure-temperature Brillouin spectrum was shown in Figure V.S7 with a collection time of ~7 min.

3. Results and discussion

The elastic properties of omphacite at ambient condition (ρ_0=3.34(1) g/cm^3, K_{S0}=123(3) GPa, G_0=74(2) GPa) were adopted from Hao et al. (2019) and fixed in the following inversion process. The high pressure-temperature thermoelastic parameters of omphacite were iteratively calculated using the high pressure-temperature data obtained in this study combined with the room-temperature high-pressure data from Hao et al. (2019). Given as a starting single-crystal

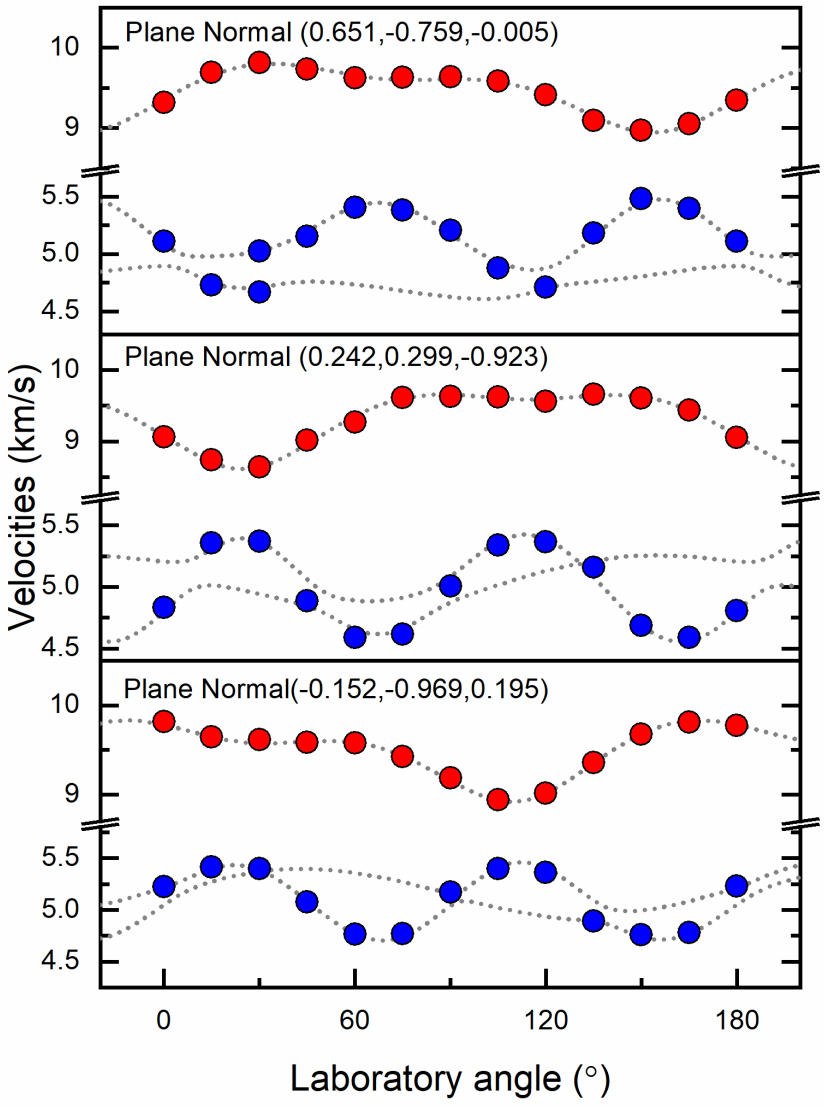

Figure V.1. Experimentally determined velocities of the omphacite crystals with different orientations at 18.4 GPa and 700 K. The dotted lines are calculated from the final C_{ij} model, and the circles represent the measured velocities. The phonon directions of the Vp and Vs measurements were calculated by matching the in-plane measured velocities with velocity dispersion curves predicted by the best-fit C_{ij} model. The uncertainties of the individual velocity measurements are smaller than the symbols. The root-mean-square (RMS) error between the experimental data and the model is 35 m/s.

C_{ij} model with hypothetical high pressure-temperature densities, we calculated the C_{ij}s, K_S, G, Vs, and Vp at each pressure-temperature condition through the least-squares inversion of the Christoffel equation. In this step, only Vs and Vp represent the true high pressure-temperature values, since they are independent of the assumed density. We then fit the temperature-dependent 3rd order finite-strain equation of state to the true Vs-Vp-pressure-temperature data set to acquire the true high pressure-temperature densities, and the pressure, temperature derivatives of G and K_S (Duffy & Anderson, 1989; Davies & Dziewonski, 1975). The last step is to update the C_{ij}s, G, and K_S, with true densities at high pressure-temperature condition. The actual measurements at 18.4 GPa 700 K and the velocities calculated from the final C_{ij} model are plotted together in Figure V.1. Table V.1 lists the density, Vs, Vp, C_{ij}s, G, K_S, and G under each pressure-temperature condition. Table V.S2 shows the trade-off coefficients of the 13 independent C_{ij}s at 3.8 GPa and 400 K.

The K_{S0}', G_0', $\partial K_{S0}/\partial T$, and $\partial G_0/\partial T$ were determined to be 4.5(1), 1.53(5), -0.029(5) GPa/K, and -0.013(5) GPa/K, respectively, with fixed K_{S0}=123(3) GPa, G_0=74(2) GPa, and ρ_0=3.34(1) g/cm^3. We used the thermal expansion coefficient α_0=2.7(8) $\times 10^{-5}$ K^{-1} for

	1.4(1) GPa 400 K	3.8(1) GPa 400 K	10.0(1) GPa 400 K	14.8(1) GPa 400 K	17.0(1) GPa 400 K	4.3(3) GPa 500 K	10.9(2) GPa 500 K
ρ (g/cm^3)	3.369	3.432	3.579	3.679	3.722	3.436	3.591
ρ* (g/cm^3)	3.369(10)	3.432(10)	3.580(10)	3.681(10)	3.725(10)	3.436(10)	3.591(10)
C_{11} (GPa)	237.9(6)	255(1)	296.1(7)	329.2(9)	341(1)	253(1)	297.8(7)
C_{22} (GPa)	201.1(9)	208(2)	241.7(9)	263(1)	275(2)	208(1)	241(1)
C_{33} (GPa)	258.2(6)	277(1)	312.4(9)	340.8(7)	352(1)	277.1(9)	313(1)
C_{44} (GPa)	78.8(4)	83.2(6)	87.6(6)	91.5(7)	93(1)	82.9(6)	87.9(7)
C_{55} (GPa)	68.9(4)	70.8(6)	79.1(4)	83.0(4)	84.8(6)	71.1(6)	78.5(4)
C_{66} (GPa)	75.4(3)	81.3(7)	96.1(4)	107.4(7)	112.2(8)	80.2(6)	95.3(5)
C_{12} (GPa)	85.3(7)	94(1)	118.6(8)	139(1)	145(1)	94(1)	120(1)
C_{13} (GPa)	75.6(7)	82(1)	103.2(9)	122(1)	132(1)	81(1)	104(1)
C_{23} (GPa)	62(2)	76(2)	93(3)	107(2)	111(3)	68(2)	92(3)
C_{15} (GPa)	8.4(4)	7.7(6)	6.8(4)	3.4(5)	4.7(8)	7.7(6)	5.3(4)
C_{25} (GPa)	8.0(9)	7(1)	5.4(8)	8(1)	9(2)	4(1)	6.2(9)
C_{35} (GPa)	34.6(4)	34.5(6)	25.5(5)	23.1(5)	21.6(7)	32.4(6)	27.8(5)

C_{46} (GPa)	7.1(3)	5.1(6)	4.8(4)	6.8(7)	1.3(9)	6.0(6)	7.0(5)
K_S^R (GPa)	121.8(4)	133.1(7)	160.9(7)	181.2(6)	189.2(8)	131.6(6)	160.9(8)
G^R (GPa)	73.3(2)	76.6(3)	85.9(3)	91.2(3)	94.0(4)	76.8(3)	85.3(3)
K_S^V (GPa)	127.0(4)	138.1(7)	164.5(7)	185.3(6)	193.5(8)	135.9(6)	164.9(8)
G^V (GPa)	76.2(2)	79.6(3)	88.2(3)	94.1(3)	96.6(4)	79.8(3)	88.1(3)
K_S^{VRH} (GPa)	124(3)	136(3)	163(2)	183(2)	191(3)	134(3)	163(3)
G^{VRH} (GPa)	75(2)	78(2)	87(1)	93(2)	95(2)	78(2)	87(2)
Vp (km/s)	8.16(4)	8.36(4)	8.83(3)	9.13(3)	9.25(3)	8.33(3)	8.81(3)
Vs (Km/s)	4.71(3)	4.77(3)	4.93(2)	5.02(2)	5.06(2)	4.77(3)	4.91(2)

	14.9(2) GPa 500 K	16.9(2) GPa 500 K	2.7(4) GPa 700 K	11.5(4) GPa 700 K	14.9(4) GPa 700 K	18.4(3) GPa 700 K
ρ (g/cm^3)	3.673	3.713	3.374	3.587	3.658	3.727
ρ* (g/cm^3)	3.674(10)	3.713(10)	3.374(10)	3.586(10)	3.658(10)	3.726(10)
C_{11} (GPa)	327(1)	337(1)	233(1)	293(1)	319(1)	341.1(8)
C_{22} (GPa)	258(1)	270(1)	196(2)	237(2)	255(2)	272(1)
C_{33} (GPa)	337.5(9)	345(1)	251(1)	304(1)	335(1)	348.7(7)
C_{44} (GPa)	89.8(7)	92.8(9)	75.4(7)	86.2(9)	88(1)	92.6(8)
C_{55} (GPa)	81.8(5)	84.4(5)	68(1)	77.1(6)	79.5(5)	84.8(4)
C_{66} (GPa)	105.5(7)	110.6(7)	71.5(6)	93.4(7)	103.3(8)	109.5(5)
C_{12} (GPa)	137(1)	142(1)	81(1)	114(1)	132(1)	143.9(8)
C_{13} (GPa)	118(1)	128(1)	71(1)	100(1)	117(1)	128.5(9)
C_{23} (GPa)	110(3)	115(3)	61(3)	94(4)	99(3)	117(2)
C_{15} (GPa)	3.0(7)	5.3(7)	9.2(7)	5.7(7)	4.0(7)	6.0(5)
C_{25} (GPa)	10(1)	13(1)	7(1)	10(1)	13(1)	14.1(9)
C_{35} (GPa)	21.7(6)	21.6(7)	33.0(8)	30.0(8)	18.8(7)	19.8(4)
C_{46} (GPa)	3.4(7)	0.5(6)	7.4(7)	6.2(7)	1.0(8)	2.5(6)
K_S^R (GPa)	179.8(7)	186.8(7)	118.1(8)	157(1)	173.5(8)	188.7(5)
G^R (GPa)	89.8(3)	92.7(4)	71.5(4)	83.9(4)	88.9(4)	93.1(3)
K_S^V (GPa)	183.9(7)	191.4(7)	122.9(8)	161(1)	178.2(8)	193.4(5)
G^V (GPa)	92.6(3)	95.4(4)	74.2(4)	86.4(4)	91.5(4)	95.5(3)
K_S^{VRH} (GPa)	182(3)	189(3)	121(3)	159(3)	176(3)	191(3)
G^{VRH} (GPa)	91(2)	94(2)	73(2)	85(2)	90(2)	94(2)
Vp (km/s)	9.09(3)	9.21(3)	8.06(4)	8.72(3)	9.00(3)	9.22(3)
Vs (Km/s)	4.98(2)	5.04(2)	4.67(3)	4.87(2)	4.97(2)	5.03(2)

Table V.1. Density, C_{ij}s, K, G, Vp, and Vs of omphacite at each pressure-temperature condition determined in this study. The Reuss and Voigt bounds of the homogeneous isotropic aggregate under the VRH averaging scheme are denoted by the superscripts R and V. The density values obtained using the temperature dependent finite-strain equation of state derived from the Vp-Vs-pressure-temperature data set in this study are reported as ρ, and for comparison, the density values calculated using the thermal equation of state in Hao et al. (2019) are presented as ρ*.

omphacite (Hao et al., 2019), and the K_{S0}' and G_0' calculated using the high pressure-temperature data set in this study are consistent with previous high-pressure ambient-temperature experiments on the same crystals (Hao et al., 2019). Figure V.2 and Figure V.S8 shows the G, K_S, Vs, and Vp of the sample under high pressure-temperature conditions. Li and Neuville (2010) conducted ultrasonic acoustic measurements at high pressure-temperature conditions for diopside, and obtained K_{S0}=116.4(7) GPa, K_{S0}'=4.9(1), $\partial K_{S0}/\partial T$=-0.012(1) GPa/K, G_0=73.0(4) GPa, $\partial G_0/\partial T$=-0.011(1) GPa/K. Compared with the values determined for

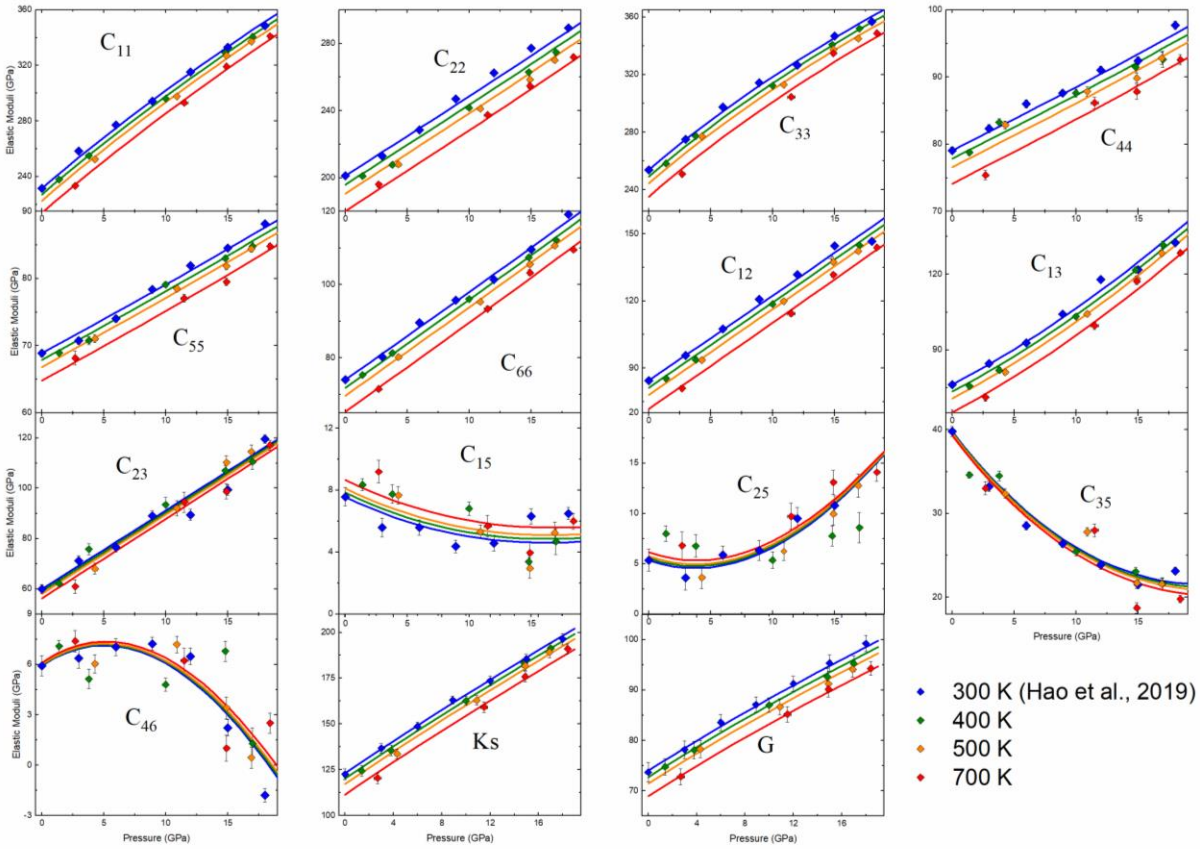

Figure V.2. The high pressure-temperature C_{ij}s, Ks, and G of omphacite determined in this study. The blue, green, orange, and red solid lines represent the finite strain fitting results at 300 K, 400 K, 500 K, and 700 K, respectively.

diopside (Li & Neuville, 2010), the K_{S0} and G_0 of omphacite measured in this study are higher than diopside as expected, whereas the pressure derivatives are lower. On the other hand, the temperature derivatives of K_{S0} and G_0 of omphacite are higher than diopside. Therefore, higher jadeite component in the clinopyroxene decreases the pressure dependence but increases the temperature dependence of the elastic moduli.

Figure V.2 shows the first experimentally measured C_{ij}s and the finite strain fitting results for omphacite at high pressure-temperature conditions. All the diagonal C_{ij}s, C_{12}, and C_{13} decrease with temperature. However, the temperature effects for C_{23}, C_{15}, C_{25}, C_{35}, and C_{46} are less significant, especially considering the relatively large uncertainties of C_{15}, C_{25}, and C_{46}. Isaak et al. (2006) measured the single-crystal elastic properties of diopside up to 1300 K at ambient pressure and found that C_{15}, C_{25}, and C_{46} are the only C_{ij}s increasing with temperature. The results obtained in this study are consistent with what were found in Isaak et al. (2006).

4. Implications

Subducted or delaminated basaltic materials are important geophysical and geochemical heterogeneities in the deep Earth (Xu et al., 2008). Better constrained seismic properties of basaltic materials help us in identifying the possibly eclogite-rich regions in the deep Earth. In the following sections, we will focus on modeling both the seismic anisotropy and the isotropic seismic velocities of eclogite aggregates.

4.1. Seismic anisotropy of the deformed eclogite in the subducted slab crust

The stresses in the subducting slab are controlled by tectonic forces, and the slab curst which is adjacent to the slab-mantle interface, is likely to experience extreme stress during subduction. As a result, the eclogite formed under these conditions is expected to be strongly

deformed depending on the subduction speed and geometry (Royden & Husson, 2006). Therefore, we need to combine the pressure-temperature dependent single-crystal elasticity with the rock textures (in particular, the LPO of omphacite) to derive the anisotropic seismic properties of the subducted and deformed slab crust.

Wang et al. (2009) measured the LPO of naturally deformed eclogite samples from the Sulu ultrahigh-pressure metamorphic terrane. These eclogite samples are believed to originate from >125 km depth, and thus are likely to represent the subducted basaltic crust which was quickly exhumed to the Earth's surface afterwards. They found that even though garnet, which is nearly elastically isotropic (Sinogeikin & Bass, 2000), is the volumetrically more abundant phase in some of their samples (up to 87 vol%), omphacite dominates seismic anisotropy of eclogite. This is consistent with the results shown in Kim et al. (2018). During the subduction, the LPO of anisotropic omphacite induced by ductile deformation is the main contributor to seismic anisotropy of the subducted crust in the upper mantle (e.g., Zhang et al., 2006). Therefore, estimating the seismic anisotropies of deformed omphacite at elevated P-T conditions is essential for interpreting seismic anisotropy near subduction zones.

Combing the experimentally determined single-crystal C_{ij}s with microstructure of naturally deformed eclogite, seismic anisotropy caused by the LPO of omphacite can be modeled at elevated pressure-temperature conditions. Using the MTEX software package (Mainprice et al., 2011) and the electron backscatter diffraction (EBSD) measurements of eclogite by Wang et al. (2009), we modeled the Vs polarization anisotropy D^{Vs}, Vp, Vs1, and Vs2 distributions of omphacite for two naturally deformed eclogite samples B270 and B295 (Supporting Information, Equation V.S2-V.S5). The calculated pole figures of sample B270 and B295 are shown in Figure 3 and Figure S5, respectively. The overall textures of the two

samples are similar, although sample B270 shows higher anisotropy. It is worth noting that seismic anisotropy of B295 calculated in Wang et al. (2009) is different from the results in this study, which is due to the use of different C_{ij} models of omphacite. Wang et al. (2009) utilized

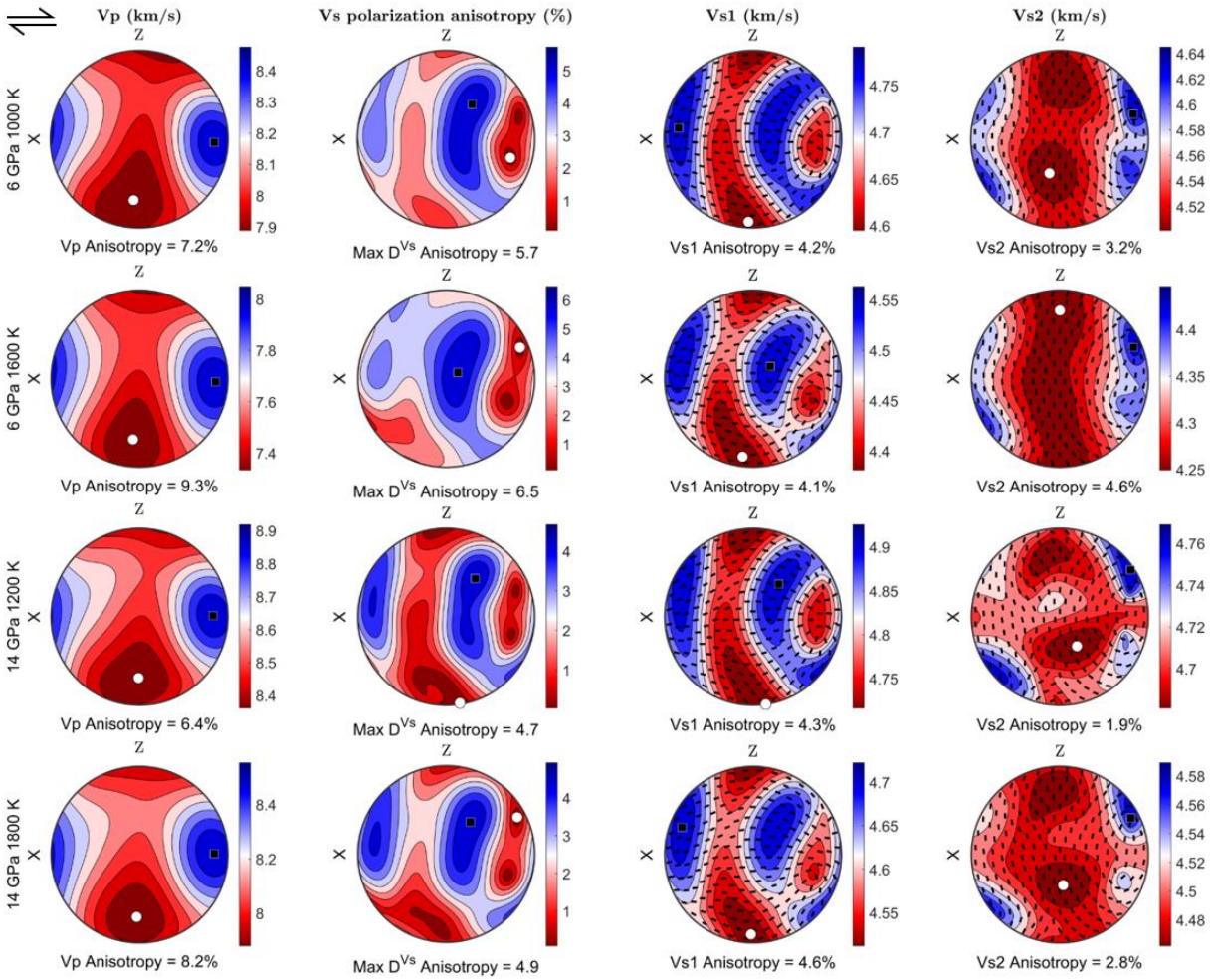

Figure V.3. Calculated seismic anisotropy of omphacite in deformed eclogite sample B270 at high pressure-temperature conditions (Wang et al., 2009). Equal area projection, lower hemisphere. The direction perpendicular to the foliation (Z) is shown vertical and the lineation (X) is horizontal. The black square and white circle mark the highest and lowest values, respectively, in each pole figure. Vs1 presents the fast Vs and the black bars are the polarization directions of Vs.

the C_{ij}s of a jadeite-rich omphacite sample measured at ambient condition by Bhagat et al. (1992), whereas we employ the high pressure-temperature C_{ij}s of a diopside-rich omphacite sample from this study. With weaker fabrics in sample B295, the use of different C_{ij} models has a stronger impact on its overall calculated seismic anisotropy. The discussion below is based on the modeling results of sample B270 which shows a stronger texture than B295.

As shown in Figure V.3, the fastest Vp direction of sample B270 is always subparallel to the lineation and the slowest Vp direction is subnormal to the foliation. The Vp anisotropy clearly increases with temperature and decreases with pressure. At relatively low pressure-temperature conditions (6 GPa and 1000 K), the Vp anisotropy of omphacite is ~ 7.2%. Considering the omphacite volume fraction of ~70% and the mild deformation of the nearly isotropic garnet (Sinogeikin & Bass, 2000; Wang et al., 2009; Kim et al., 2018) in eclogite, the Vp anisotropy of eclogite is on the order of 5-6 % in the shallower upper mantle. When reaching ~14 GPa and 1800 K at transition zone depths, the Vp anisotropy of omphacite increases to 8.2%. However, considering that the volume fraction of omphacite decreases from ~70% at the top of the upper mantle to ~20% in the transition zone (Aoki & Takahashi, 2004), the Vp anisotropy of eclogite is only at the level of ~2% in the transition zone.

The D^{Vs} pole figures are complex. At lower pressures, the direction with lowest D^{Vs} is subparallel to the lineation and the direction with highest D^{Vs} is sub-perpendicular to the lineation and subparallel to the foliation direction. However, at higher pressures, the directions with the lowest D^{Vs} appear both along the lineation and perpendicular to the foliation direction. Temperature does not affect the overall shape of the pole figures of D^{Vs}, although temperature does increase the strength of seismic anisotropy.

Mantle flow geometries near a subducting slab are complicated. Near the slab wedge, there are two dominating mantle flow fields: the 2-D corner flow is along the dipping direction and perpendicular to the trench, and the 3-D around flow is parallel to the trench (Figure V.S10, Long & Silver, 2008; Eakin et al., 2010). In this study, we assumed a seismic ray with nearly normal incidence, similar to what is expected in the SKS splitting measurements. For the 2-D corner flow, the fast Vs polarization will be perpendicular to the trench with a small dipping angle, or parallel to the trench with a high dipping angle. The 3-D around flow always results in fast Vs polarization parallel to the trench and the dipping angle does not matter. Considering the fact that garnet is nearly isotropic and does not show clear LPO in the deformed eclogite (Sinogeikin and Bass 2000; Kim et al., 2018), the Vs splitting of the entire subducted oceanic crust are primarily caused by the LPO of omphacite. According to Figure V.3, a 10 km thick subducted eclogitic crust can lead to ~0.2 s shear wave splitting in the upper mantle, which cannot be ignored when interpreting seismic data in subduction zones (Eakin et al., 2010; Niday & Humphreys, 2020).

4.2. Isotropic seismic velocities of undeformed eclogite

In addition to the slab crust, lower continental crust is also believed to be compositionally basaltic (Wedepohl, 1995). Delamination of the basaltic continental root is another way to recycle shallow materials down to the deep Earth (Kay & Mahlburg-Kay, 1991). Weaker stress fields are associated with the delamination processes compared to subduction zones, and eclogite involved in the delamination process is less likely to form strong deformation textures. It is thus worth to reevaluate the isotropic seismic properties of eclogite as an end member case, based on the pressure-temperature dependent elastic properties of omphacite and other relevant mineral phases (Aoki & Takahashi, 2004; Table V.S3).

In this study, we considered two geotherm profiles at 200-500 km depth: one along the 1000 K mantle adiabat, and the other along the 1600 K adiabat (Katsura et al., 2010; Stixrude & Lithgow-Bertelloni, 2005), representing the cold and normal mantle temperature conditions. We also compared the velocities of eclogite with those for the pyrolitic mantle (Xu et al., 2008), as shown in Figure V.4 and Figure V.S11. We calculated the mineral compositions and proportions both as depth-dependent, and for solid solution we considered the simplest ideal

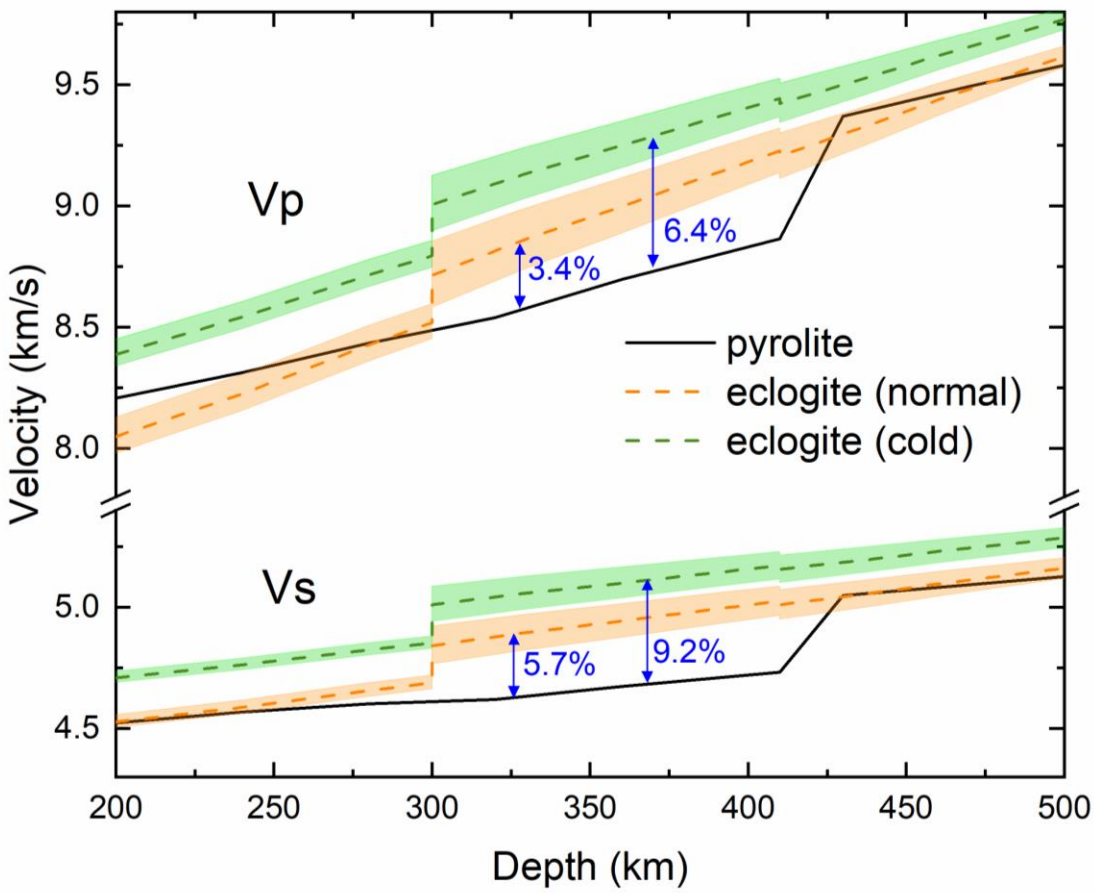

Figure V.4. Seismic velocities of undeformed eclogite determined in this study and pyrolite shown in Xu et al., (2008). The shaded green and orange regions represent the Voigt and Reuss bounds along the normal (1600 K) and cold (1000 K) geotherm, respectively.

mixing scenario. To calculate the elastic moduli and densities for the multi-component systems, we adopted the Voigt-Reuss-Hill averaging scheme (Text V.S1.3, Equation V.S6-V.S8). Instead of assuming all clinopyroxenes share the same temperature dependence of elastic moduli and using previously determined values for diopside, we remodeled the seismic velocities of eclogite using the new thermoelastic parameters of omphacite determined in this study.

The new results showed ~2% slower seismic velocities of eclogite compared to what were calculated in Hao et al. (2019), although the maximum Vs and Vp differences still appear between ~300-410 km. Along normal geotherm, the Vs and Vp of eclogite are ~5.7% and ~3.4% higher than those of the pyrolitic mantle, respectively. The possible lower temperature of eclogite enhances the velocity contrast to ~5.7%-9.2% and ~3.4%-6.4% for Vs and Vp, respectively.

At depth shallower than 300 km or deeper than 410 km, the Vp and Vs of eclogite are practically indistinguishable from pyrolite. This is the major revision to what was found in Hao et al. (2019). The difference is caused by the use of diopside's $\partial K_{S0}/\partial T$ and $\partial G_0/\partial T$ for omphacite in the calculation in Hao et al. (2019). The T dependence of K_{S0} and G_0 of omphacite measured in this study are higher than diopside, resulting in lower Vp and Vs for the model eclogite calculated in this study. Our model suggests that the seismic anomalies observed at depth shallower than 300 km and deeper than 410 km are primarily caused by temperature variations rather than compositional heterogeneities due to recycled eclogite. In other words, eclogitic materials are seismically invisible at those depth ranges. Only when interpreting seismic observations of subduction zones at depth between 300-410 km depth, the composition-induced velocity differences need to be taken into consideration.

5. Conclusions

We have measured the single-crystal elastic properties of omphacite using Brillouin spectroscopy at simultaneously high pressure-temperature condition up to 18 GPa and 700 K. The new thermoelastic parameters of omphacite determined in this study are: K_{S0}=123(3) GPa, G_0=74(2) GPa, K_{S0}'=4.5(1), G_0'=1.53(5), $\partial K_{S0}/\partial T$=-0.029(5) GPa/K, and $\partial G_0/\partial T$=-0.013(5) GPa/K. Combing the EBSD measurements of naturally deformed eclogite, we modeled seismic anisotropy of deformed eclogite at high pressure-temperature conditions. We found that the LPO of anisotropic omphacite can result in shear-wave splitting time of ~0.2 s for a 10-km-thick eclogitic crust. The isotropic seismic velocities of undeformed eclogite are indistinguishable from the pyrolitic mantle at the depths between 200-300 km and 410-500 km. As a result, the seismic anomalies observed at shallower upper mantle and the upper transition zone are primarily of thermal origin rather than caused by the compositional heterogeneities of eclogitic materials.

Acknowledgments

The authors would like to thank Jane Silverstone for providing the omphacite sample, Caroline E. Pierotti for polishing the samples, Mike Spilde for the help with EPMA measurements, Lowell Miyagi for the advice on anisotropy calculations, and Sergey Tkachev for the help in experiments at GSECARS as well as the Neon gas loadings. The use of the gas-loading system is supported by COMPRES, the Consortium for Materials Properties Research in Earth Sciences under NSF Cooperative Agreement EAR 1661511, and GSECARS are funded by NSF (EAR - 1634415) and Department of Energy (DOE) – GeoSciences (DE-FG02-94ER14466). This research used resources of APS, a U.S. DOE Office of Science User Facility operated for the DOE Office of Science by Argonne National Laboratory under Contract NO.

DE-AC02-06CH11357. The presented data can be found in the UNM digital data repository at https://digitalrepository.unm.edu/eps_fsp/10.

Funding: This work is supported by the National Science Foundation (NSF) under Grant EAR 1646527 (JZ) and the start-up fund from UNM (JZ).

References

Aoki, I., & Takahashi, E. (2004). Density of MORB eclogite in the upper mantle. *Physics of the Earth and Planetary Interiors*, *143*, 129-143.

Arimoto, T., Gréaux, S., Irifune, T., Zhou, C., & Higo, Y. (2015). Sound velocities of Fe3Al2Si3O12 almandine up to 19 GPa and 1700 K. *Physics of the Earth and Planetary Interiors*, *246*, 1-8.

Ballmer, M. D., Houser, C., Hernlund, J. W., Wentzcovitch, R. M., & Hirose, K. (2017). Persistence of strong silica-enriched domains in the Earth's lower mantle. *Nature Geoscience*, *10*(3), 236.

Bhagat, S. S., Bass, J. D., & Smyth, J. R. (1992). Single-crystal elastic properties of omphacite-C2/c by Brillouin spectroscopy. *Journal of Geophysical Research: Solid Earth*, *97*(B5), 6843-6848.

Datchi, F., Dewaele, A., Loubeyre, P., Letoullec, R., Le Godec, Y., & Canny, B. (2007). Optical pressure sensors for high-pressure–high-temperature studies in a diamond anvil cell. High Pressure Research, 27(4), 447-463.

Davies, G. F., & Dziewonski, A. M. (1975). Homogeneity and constitution of the Earth's lower mantle and outer core. *Physics of the Earth and Planetary Interiors*, *10*(4), 336-343.

Duffy, T. S., & Anderson, D. L. (1989). Seismic velocities in mantle minerals and the mineralogy of the upper mantle. Journal of Geophysical Research: Solid Earth, 94(B2), 1895-1912.

Eakin, C. M., Obrebski, M., Allen, R. M., Boyarko, D. C., Brudzinski, M. R., & Porritt, R. (2010). Seismic anisotropy beneath Cascadia and the Mendocino triple junction: Interaction of the subducting slab with mantle flow. Earth and Planetary Science Letters, 297(3-4), 627-632.

Gwanmesia, G. D., Wang, L., Heady, A., & Liebermann, R. C. (2014). Elasticity and sound velocities of polycrystalline grossular garnet (Ca3Al2Si3O12) at simultaneous high pressures and high temperatures. *Physics of the Earth and Planetary Interiors*, *228*, 80-87.

Hao, M., Zhang, J. S., Pierotti, C. E., Ren, Z., & Zhang, D. (2019). High-Pressure Single-Crystal Elasticity and Thermal Equation of State of Omphacite and Their Implications for the Seismic Properties of Eclogite in the Earth's Interior. Journal of Geophysical Research: Solid Earth, 124(3), 2368-2377.

Hao, M., Zhang, J. S., Pierotti, C. E., Zhou, W. Y., Zhang, D., & Dera, P. (2020). The seismically fastest chemical heterogeneity in the Earth's deep upper mantle—implications from the single-crystal thermoelastic properties of jadeite. Earth and Planetary Science Letters, 543, 116345.

Irifune, T., Higo, Y., Inoue, T., Kono, Y., Ohfuji, H., & Funakoshi, K. (2008). Sound velocities of majorite garnet and the composition of the mantle transition region. *Nature*, *451*(7180), 814.

Isaak, D. G., Ohno, I., & Lee, P. C. (2006). The elastic constants of monoclinic single-crystal chrome-diopside to 1,300 K. *Physics and Chemistry of Minerals*, *32*(10), 691-699.

Ito, K., & Kennedy, G. C. (1971). An experimental study of the basalt - garnet granulite - eclogite transition. The structure and physical properties of the Earth's crust, 14, 303-314.

Kantor, I., Prakapenka, V., Kantor, A., Dera, P., Kurnosov, A., Sinogeikin, S., et al. (2012). BX90: A new diamond anvil cell design for X-ray diffraction and optical measurements. *Review of Scientific Instruments*, *83*(12), 125102.

Katsura, T. (2022). A revised adiabatic temperature profile for the mantle. *Journal of Geophysical Research: Solid Earth*, *127*(2), e2021JB023562.

Kay, R. W., & Mahlburg-Kay, S. (1991). Creation and destruction of lower continental crust. Geologische Rundschau, 80(2), 259-278.

Kim, D., Kim, T., Lee, J., Kim, Y., Kim, H., & Lee, J. I. (2018). Microfabrics of omphacite and garnet in eclogite from the Lanterman Range, northern Victoria Land, Antarctica. Geosciences Journal, 22(6), 939-953.

Lai, X., Zhu, F., Zhang, J. S., Zhang, D., Tkachev, S., Prakapenka, V. B., & Chen, B. (2020). An Externally-Heated Diamond Anvil Cell for Synthesis and Single-Crystal Elasticity Determination of Ice-VII at High Pressure-Temperature Conditions. JoVE (Journal of Visualized Experiments), (160), e61389.

Li, B., & Neuville, D. R. (2010). Elasticity of diopside to 8 GPa and 1073 K and implications for the upper mantle. *Physics of the Earth and Planetary interiors*, *183*(3-4), 398-403.

Long, M. D., & Silver, P. G. (2008). The subduction zone flow field from seismic anisotropy: A global view. science, 319(5861), 315-318.

Mainprice, D., Hielscher, R., & Schaeben, H. (2011). Calculating anisotropic physical properties from texture data using the MTEX open-source package. Geological Society, London, Special Publications, 360(1), 175-192.

Moghadam, R. H., Trepmann, C. A., Stöckhert, B., & Renner, J. (2010). Rheology of synthetic omphacite aggregates at high pressure and high temperature. *Journal of Petrology*, *51*(4), 921-945.

Niday, W., & Humphreys, E. (2020). Complex upper mantle anisotropy in the Pacific Northwest: Evidence from SKS splitting. Earth and Planetary Science Letters, 540, 116264.

Rivers, M., Prakapenka, V. B., Kubo, A., Pullins, C., Holl, C. M., & Jacobsen, S. D. (2008). The COMPRES/GSECARS gas-loading system for diamond anvil cells at the Advanced Photon Source. *High Pressure Research*, *28*(3), 273-292.

Royden, L. H., & Husson, L. (2006). Trench motion, slab geometry and viscous stresses in subduction systems. Geophysical Journal International, 167(2), 881-905.

Sang, L., & Bass, J. D. (2014). Single-crystal elasticity of diopside to 14 GPa by Brillouin scattering. *Physics of the Earth and Planetary Interiors*, *228*, 75-79.

Sang, L., Vanpeteghem, C. B., Sinogeikin, S. V., & Bass, J. D. (2011). The elastic properties of diopside, CaMgSi2O6. *American Mineralogist*, *96*(1), 224-227.

Shen, G., Wang, Y., Dewaele, A., Wu, C., Fratanduono, D. E., Eggert, J., ... & IPPS task group. (2020). Toward an international practical pressure scale: A proposal for an IPPS ruby gauge (IPPS-Ruby2020). High Pressure Research, 40(3), 299-314.

Sinogeikin, S. V., & Bass, J. D. (2000). Single-crystal elasticity of pyrope and MgO to 20 GPa by Brillouin scattering in the diamond cell. *Physics of the Earth and Planetary Interiors*, *120*(1-2), 43-62.

Skelton, R., & Walker, A. M. (2015). The effect of cation order on the elasticity of omphacite from atomistic calculations. *Physics and Chemistry of Minerals, 42*(8), 677-691.

Stixrude, L., & Lithgow-Bertelloni, C. (2005). Thermodynamics of mantle minerals—I. Physical properties. Geophysical Journal International, 162(2), 610-632.

Xu, W., Lithgow-Bertelloni, C., Stixrude, L., & Ritsema, J. (2008). The effect of bulk composition and temperature on mantle seismic structure. *Earth and Planetary Science Letters*, *275*(1-2), 70-79.

Walker, A. M. (2012). The effect of pressure on the elastic properties and seismic anisotropy of diopside and jadeite from atomic scale simulation. *Physics of the Earth and Planetary Interiors*, *192*, 81-89.

Wang, Q., Burlini, L., Mainprice, D., & Xu, Z. (2009). Geochemistry, petrofabrics and seismic properties of eclogites from the Chinese Continental Scientific Drilling boreholes in the Sulu UHP terrane, eastern China. Tectonophysics, 475(2), 251-266.

Wedepohl, K. H. (1995). The composition of the continental crust. Geochimica et cosmochimica Acta, 59(7), 1217-1232.

Zhang, J., Green II, H. W., & Bozhilov, K. N. (2006). Rheology of omphacite at high temperature and pressure and significance of its lattice preferred orientations. *Earth and Planetary Science Letters*, *246*(3-4), 432-443.

Zhang, J. S., Bass, J. D., Taniguchi, T., Goncharov, A. F., Chang, Y. Y., & Jacobsen, S. D. (2011). Elasticity of cubic boron nitride under ambient conditions. Journal of Applied Physics, 109(6), 063521.

Zhang, J. S., Bass, J. D., & Zhu, G. (2015). Single-crystal Brillouin spectroscopy with CO2 laser heating and variable q. Review of Scientific Instruments, 86(6), 063905.

Supporting Information

V.S1. Sensitivity test

It is essential to choose the proper combination of crystallographic orientations for Brillouin experiments to reliably invert the full single-crystal elasticity moduli C_{ij}s, especially for materials with low symmetries. From this perspective, the sensitivity test is important to ensure the robustness of our results.

The sensitivity value S_x is defined as:

$$S_x = \left[\frac{\partial V_x / V_x}{\partial C_{ij} / C_{ij}} \right]_{maximum} \quad \text{(V.S1)}$$

where V_x represents the sound velocities of different types of sound waves (Vp, Vs1, and Vs2). Assuming a 0.1% change of each C_{ij}, we calculated the relative change of Vp, Vs1, and Vs2 along all 39 crystallographic directions we have measured in this study. The S_x values represent the maximum relative change of Vp, Vs1, and Vs2 along the 39 different crystallographic directions that we experimentally measured in this study. Figure V.S5 shows the final results for the orientation combination that were used in this study. Most C_{ij}s can be inverted with satisfactory sensitivity, and C_{25} can be improved with more measurements. However, the uncertainties of C_{25} determined in this study should not affect the robustness of our calculation result and conclusion, due to its minor role in calculating the aggregate elastic properties as well as seismic anisotropy.

V.S2. Anisotropy indices

Vs polarization (D^{Vs}), Vp, Vs1, and Vs2 anisotropy indices are defined as:

$$D^{Vs} = 2 * \frac{|Vs_1 - Vs_2|_{max}}{Vs_1 + Vs_2} \quad \text{(V.S2)}$$

$$Vp\ anisotropy = 2 * \frac{Vp_{max} - Vp_{min}}{Vp_{max} + Vp_{min}} \quad \text{(V.S3)}$$

$$Vs1\ anisotropy = 2 * \frac{Vs1_{max} - Vs1_{min}}{Vs1_{max} + Vs1_{min}} \quad \text{(V.S4)}$$

$$Vs2\ anisotropy = 2 * \frac{Vs2_{max} - Vs2_{min}}{Vs2_{max} + Vs2_{min}} \quad \text{(V.S5)}$$

V.S3. Voigt-Reuss-Hill average of multi-phase aggregates

The Voigt bound corresponds to uniform strain scenario and the Reuss bound corresponds to uniform stress. In a multi-phase aggregate, mathematically, they are defined as:

$$Voigt\ bound: E^V = f_a E_a + f_b E_b \quad \text{(V.S6)}$$

$$Reuss\ bound: E^R = \left(\frac{f_a}{E_a} + \frac{f_b}{E_b} \right)^{-1} \quad \text{(V.S7)}$$

$$Hill\ average: E^{VRH} = (E^V + E^R)/2 \quad \text{(V.S8)}$$

where E^V, E^R, and E^{VRH} represent the aggregate material properties of the Voigt bound, the Reuss bound, and the Hill average, respectively; E_a and E_b represent the properties of phase a and b, respectively; f_a and f_b represent the volume fractions of phases a and b, respectively.

The actual properties of the multi-phase aggregate should lie in between the Voigt and Reuss bounds (Hill, 1963). We used Voigt-Reuss-Hill average for our calculations in Figure V.4.

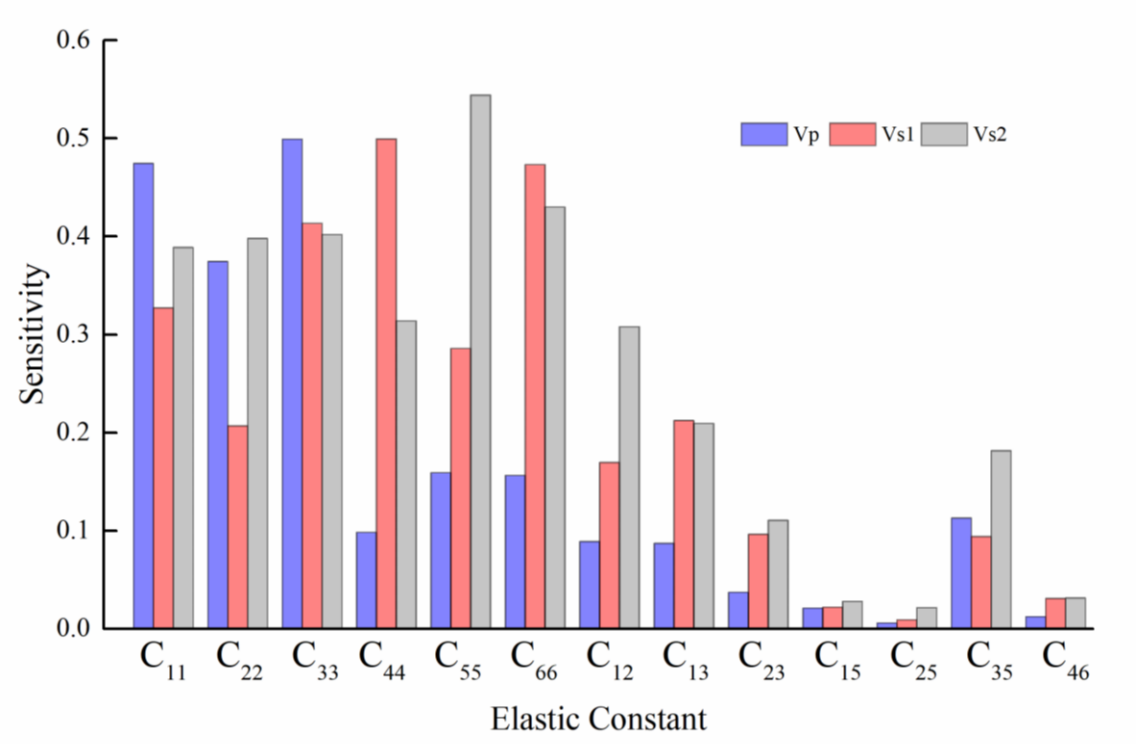

Figure V.S5. The sensitivity test results for the orientation combination used in this study. The C_{ij}s that can be improved with more measurements is C_{25}. However, C_{25} plays a minor role in calculating the aggregate elastic properties. Thus, we did not perform additional experiments to improve the constrain on C_{25}.

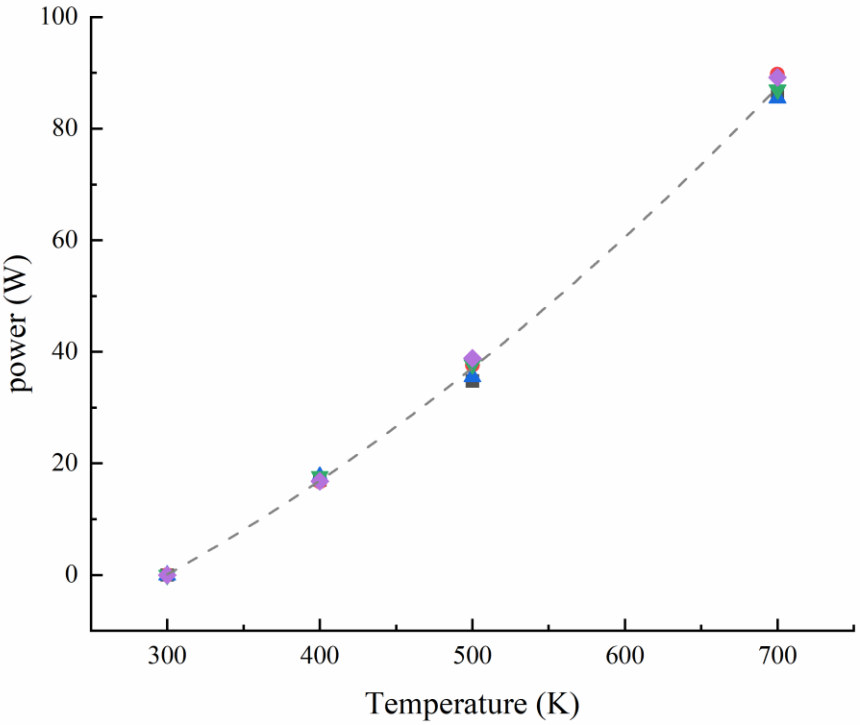

Figure V.S6. The power curve of the resistively heated DACs used in this study. Different symbols represent different experimental runs. The gray dashed line shows the fitting results using second-order polynomial: $P=-30(4)+0.05(2)*T+0.00017(2)*T^2$, $R^2=0.9986$.

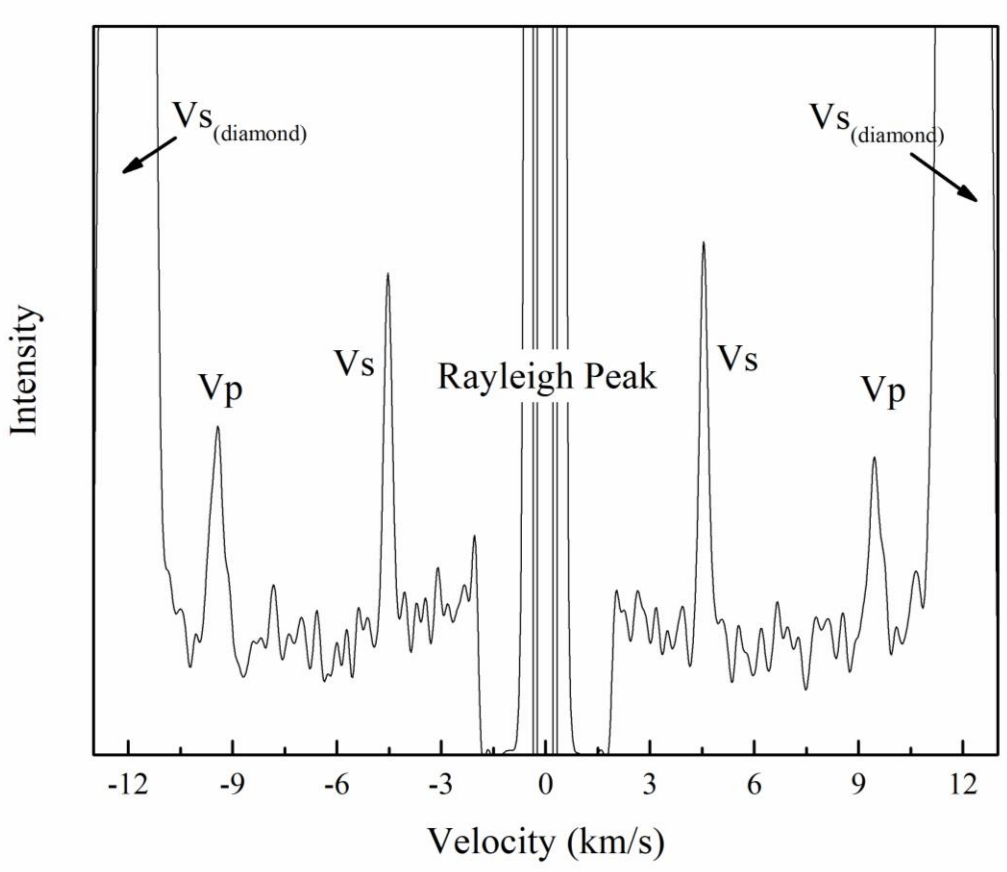

Figure V.S7. A typical Brillouin spectrum at 18.4 GPa and 700 K. Two Vs peaks and Vp peaks from the omphacite sample are observed. The Neon peaks are too weak to be observed at 18.4 GPa. The collection time is ~7 min.

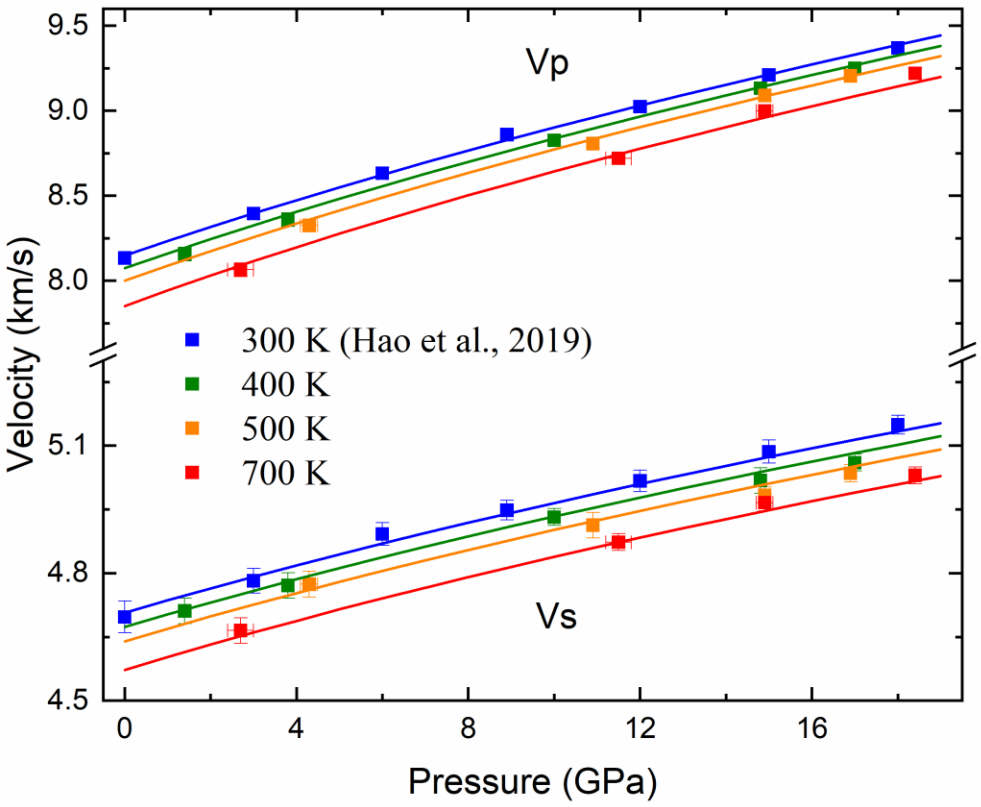

Figure V.S8. The high pressure-temperature velocities of omphacite determined in this study.

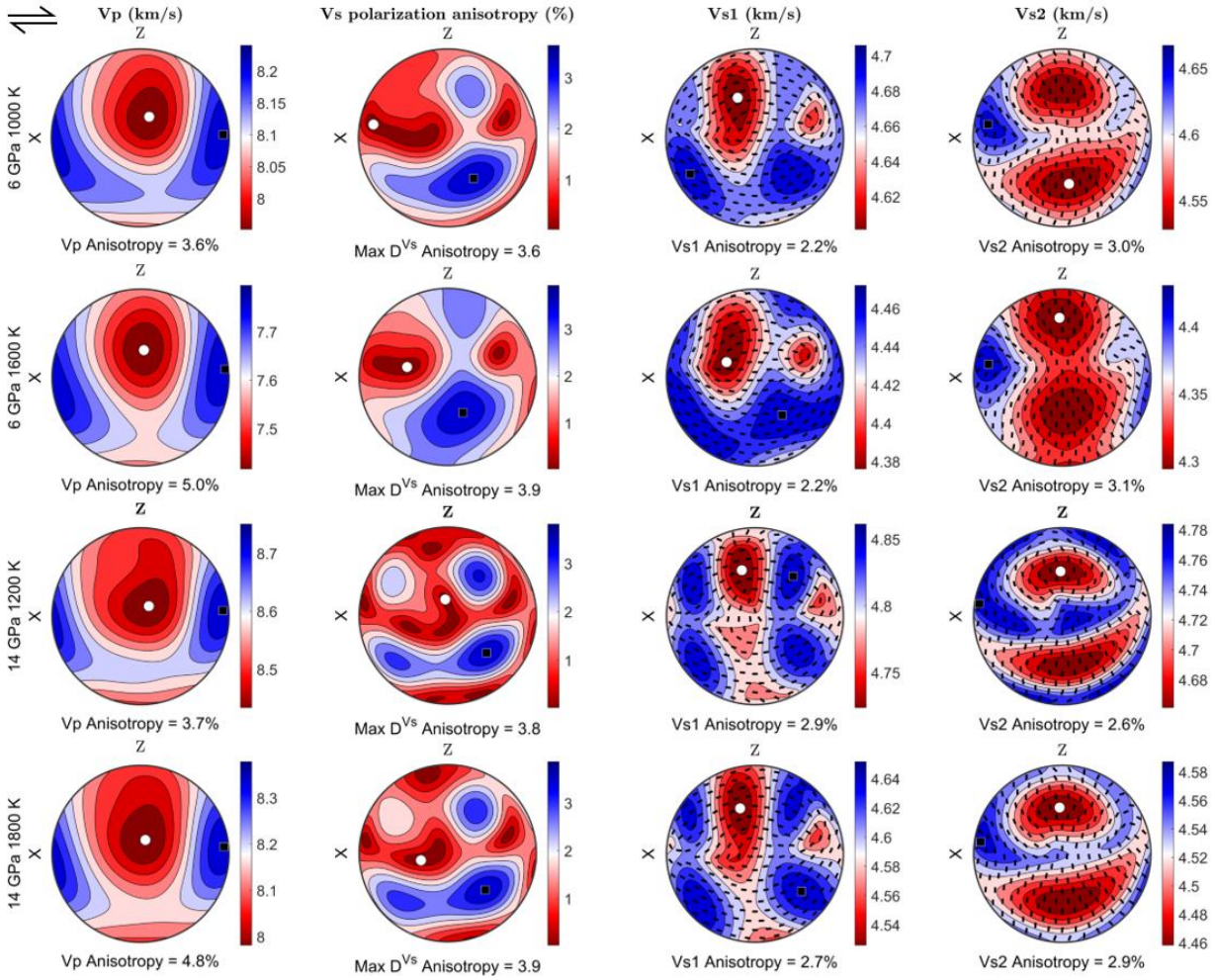

Figure V.S9. Calculated seismic anisotropy of omphacite at high pressure-temperature conditions (sample B295 in Wang et al., 2009). Equal area projection, upper hemisphere. Perpendicular to the foliation (Z) is vertical and the lineation (X) is horizontal. The black square and white circle mark the highest and lowest values, respectively, in each pole figure.

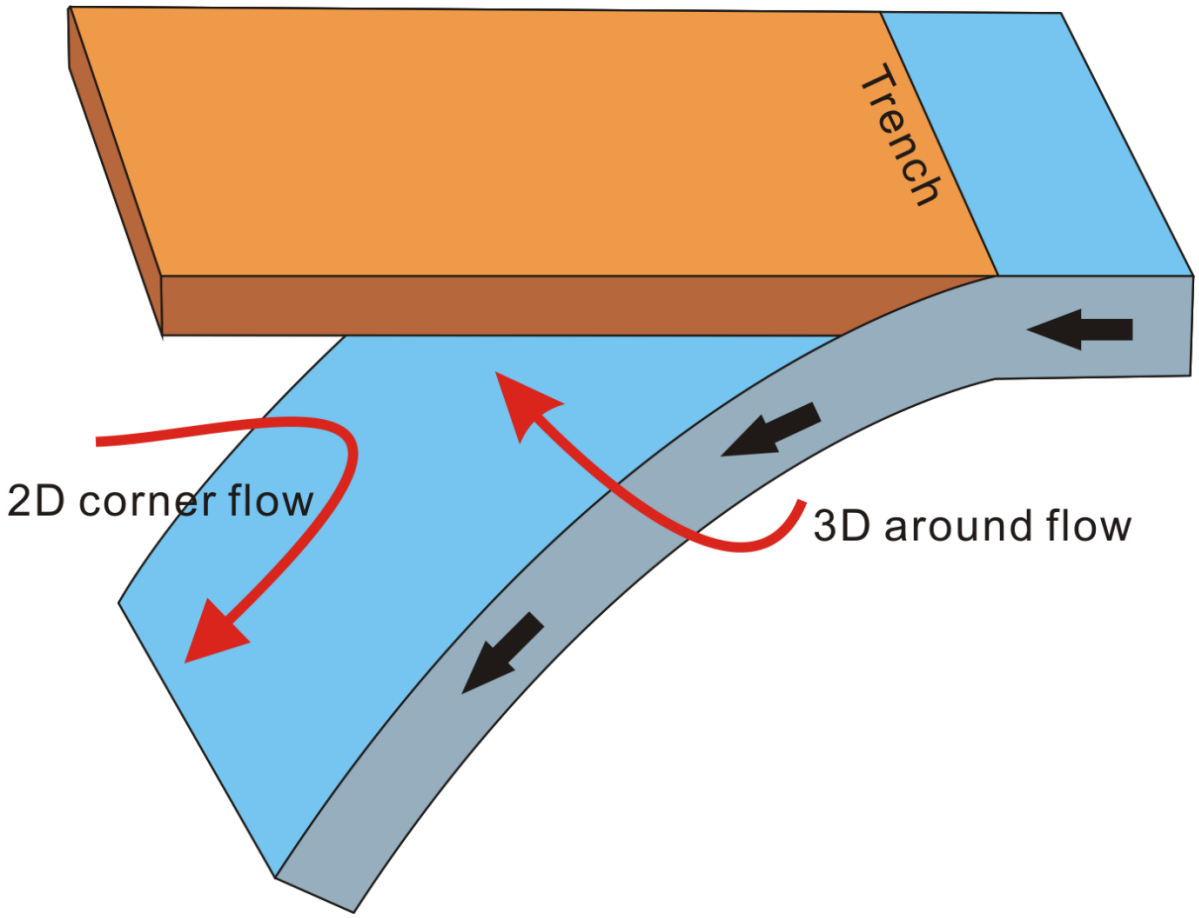

Figure V.S10. The schematic diagram of mantle flows (modified from Long & Silver, 2008).

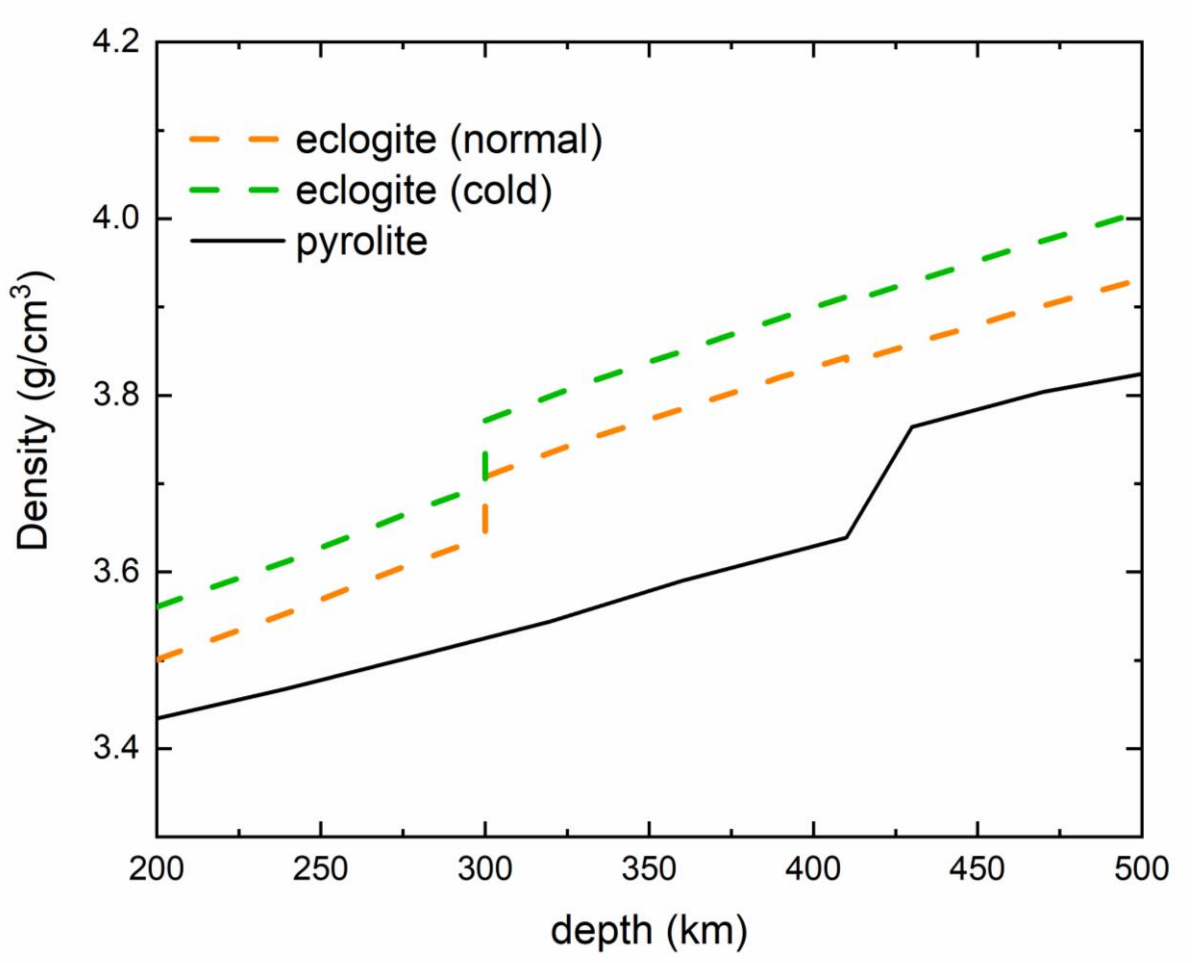

Figure V.S11. Densities of eclogite determined in this study compared with pyrolite in Xu et al. (2008).

C_{ij}s	C_{11}	C_{22}	C_{33}	C_{44}	C_{55}	C_{66}	C_{12}	C_{13}	C_{23}	C_{15}	C_{25}	C_{35}	C_{46}
C_{11}	1.0	.0114	.0016	-.0017	.0077	.0063	-.0021	-.0043	.0009	.0057	-.0020	.0024	-.002
C_{22}	.0121	1.0	-.0018	.0084	-.0009	.0156	-.0284	.0027	.0223	-.0033	.0082	.0018	-.0025
C_{33}	.0016	-.0017	1.0	.0040	.0079	.0001	.0002	-.0065	.0155	-.0006	.0002	.0037	-.0007
C_{44}	-.0017	.0077	.0039	1.0	.0033	.0032	-.0002	-.0002	-.0032	-.0012	-.0078	-.0009	.0059
C_{55}	.0075	-.0008	.0077	.0033	1.0	.0005	.0008	.0024	-.0011	.0009	.0014	-.0037	-.0021
C_{66}	.0061	.0142	.0001	.0032	.0005	1.0	.0084	.0009	-.0070	.0002	-.0005	-.0003	-.0005
C_{12}	-.0021	-.0270	.0002	-.0002	.0009	.0087	1.0	.0018	.0200	-.0038	.0013	.0039	.0022
C_{13}	-.0044	.0026	.0066	.0002	.0025	.0010	.0018	1.0	.0255	.0015	.0180	.0048	-.0036
C_{23}	.0011	.0268	.0197	-.0042	-.0015	-.0092	.0253	.0317	1.0	.0184	-.0240	-.0181	.0050
C_{15}	.0055	-.0030	-.0005	-.0012	.0009	.0002	-.0037	.0014	.0140	1.0	-.0023	.0005	.0047
C_{25}	-.0021	.0079	.0002	-.0083	.0014	-.0005	.0013	.0181	-.0194	-.0024	1.0	.0000	.0122
C_{35}	.0023	.0016	.0036	-.0009	-.0037	-.0003	.0037	.0046	-.0138	.0005	.0000	1.0	.0021
C_{46}	-.0002	-.0023	-.0007	.0059	-.0021	-.0005	.0021	-.0034	.0038	.0047	.0115	.0021	1.0

Table V.S2. The trade-off coefficients of the 13 C_{ij}s of the measured omphacite sample at 400 K 3.8 GPa.

Mineral	Density (g/cm^3)	K_{S0} (GPa)	$\partial K_S/\partial P$	$\partial K_S/\partial T$ (GPa/K)	G_0 (GPa)	$\partial G/\partial P$	$\partial G/\partial T$ (GPa/K)	a_0 (10^{-4} K^{-1})	a_1 (10^{-8} K^{-2})	a_2 (K)
Jadeite[1]	3.302(5)	138(3)	3.9(1)	-0.029(5)	84(2)	1.09(4)	-0.013(5)	0.34(5)	0	0
Diopside[2]	3.272(6)	116.4(7)	4.9(1)	-0.029(5)	73.0(4)	1.6(1)	-0.013(5)	0.19	2.08	0
Pyrope[3,4,5,6,8]	3.56(2)	171.0(5)	4.4(1)	-0.014(3)	94.9(2)	1.15(6)	-0.011(2)	0.288	0.2787	-0.5521
Mg-majorite[3,4,5,6,9]	3.56(2)	162.0(5)	4.4(1)	-0.014(3)	86.2(2)	1.15(6)	-0.011(2)	0.288	0.2787	-0.5521
Jd-majorite[7,8]	3.644(7)	178(4)	4.47(2)	-0.0138(3)	125(2)	1.29(5)	-0.0128(2)	0.1951	0.8089	-0.4972
Grossular[8,9]	3.605(2)	171.2(8)	4.47(2)	-0.0138(3)	107.4(2)	1.29(5)	-0.0128(2)	0.1951	0.8089	-0.4972
Almandine[10]	4.3188(2)	174.2(12)	4.61(14)	-0.0267(7)	94.9(7)	1.06(6)	-0.0131(8)	0.26(5)	2.3(14)	0
Coesite[11,12]	2.91(2)	106.5(6)	2.7(15)	-0.0016(16)	60.7(3)	0.33(5)	-0.0044(5)	0.106(14)	-0.028(166)	-0.48(12)
Stishovite[13,14]	4.381(2)	296(5)	4.2(4)	-0.046(5)				0.126(11)	1.29(17)	0
Hedenbergite[9,15]	3.657(1)	120(4)	4	-0.029(5)	62(2)	1.6(1)	-0.013(5)	0.298	0	0

1. Hao et al. (2020) 2. Li and Neuville (2010) 3. Irifune et al. (2008) 4. Liu et al. (2000) 5. Sinogeikin and Bass (2002) 6. Suzuki and Anderson (1983) 7. Reichmann et al. (2002) 8. Gwanmesia et al. (2014) 9. Fei (1995) 10. Arimoto et al. (2015) 11. Chen et al. (2017) 12. Kulik et al. (2018) 13. Yang and Wu (2014) 14. Nishihara et al. (2005) 15. Kandelin and Weidner (1988)

Table V.S3. Thermoelastic parameters of all the relevant mineral phases for calculating the density and velocity. The a_0, a_1 and a_2 are the thermal expansion parameters, defined in Fei (1995): $a(T)=a_0+a_1T+a_2T^{-2}$. The thermal expansion parameters for jadeite using the equations in Hao et al. (2020). The elasticity data of stishovite are directly obtained from the first-principles calculation study by Yang and Wu (2014). The parameters for stishovite listed in the table are for density calculation. The parameters (except the thermal expansion parameters) for pyrope and coesite are recalculated based on the experimental values presented in Irifune et al. (2008) and Chen et al. (2017). Some parameters are listed without uncertainties because the uncertainties were not reported in the references.

Reference

Arimoto, T., Gréaux, S., Irifune, T., Zhou, C., & Higo, Y. (2015). Sound velocities of Fe3Al2Si3O12 almandine up to 19 GPa and 1700 K. *Physics of the Earth and Planetary Interiors*, *246*, 1-8.

Chen, T., Liebermann, R. C., Zou, Y., Li, Y., Qi, X., & Li, B. (2017). Tracking silica in Earth's upper mantle using new sound velocity data for coesite to 5.8 GPa and 1073 K. *Geophysical Research Letters*, *44*(15), 7757-7765.

Fei, Y. (1995). Thermal expansion. In T. J. Ahrens *Mineral physics & crystallography: a handbook of physical constants* (Vol. 2, pp. 29-44). Washington, DC: American Geophysical Union.

Gwanmesia, G. D., Wang, L., Heady, A., & Liebermann, R. C. (2014). Elasticity and sound velocities of polycrystalline grossular garnet (Ca3Al2Si3O12) at simultaneous high tes and high temperatures. *Physics of the Earth and Planetary Interiors*, *228*, 80-87.

Hill, R. (1963). Elastic properties of reinforced solids: some theoretical principles. *Journal of the Mechanics and Physics of Solids*, *11*(5), 357-372.

Irifune, T., Higo, Y., Inoue, T., Kono, Y., Ohfuji, H., & Funakoshi, K. (2008). Sound velocities of majorite garnet and the composition of the mantle transition region. *Nature*, *451*(7180), 814.

Kandelin, J., & Weidner, D. J. (1988). Elastic properties of hedenbergite. Journal of Geophysical Research: Solid Earth, 93(B2), 1063-1072.

Kulik, E., Murzin, V., Kawaguchi, S., Nishiyama, N., & Katsura, T. (2018). Thermal expansion of coesite determined by synchrotron powder X-ray diffraction. *Physics and Chemistry of Minerals*, 1-9.

Li, B., & Neuville, D. R. (2010). Elasticity of diopside to 8 GPa and 1073 K and implications for the upper mantle. *Physics of the Earth and Planetary Interiors*, *183*(3-4), 398-403.

Liu, J., Chen, G., Gwanmesia, G. D., & Liebermann, R. C. (2000). Elastic wave velocities of pyrope–majorite garnets (Py62Mj38 and Py50Mj50) to 9 GPa. *Physics of the Earth and Planetary Interiors*, *120*(1-2), 153-163.

Nishihara, Y., Nakayama, K., Takahashi, E., Iguchi, T., & Funakoshi, K. Ì. (2005). P-V-T equation of state of stishovite to the mantle transition zone conditions. *Physics and Chemistry of Minerals*, *31*(10), 660-670.

Reichmann, H. J., Sinogeikin, S. V., Bass, J. D., & Gasparik, T. (2002). Elastic Moduli of Jadeite-Enstatite Majorite. *Geophysical research letters*, *29*(19).

Sinogeikin, S. V., & Bass, J. D. (2002). Elasticity of Majorite and a Majorite-Pyrope solid solution to high pressure: Implications for the Transition Zone. *Geophysical Research Letters*, *29*(2), 4-1.

Suzuki, I., & Anderson, O. L. (1983). Elasticity and thermal expansion of a natural garnet up to 1, 000K. *Journal of Physics of the Earth*, *31*(2), 125-138.

Wang, Q., Burlini, L., Mainprice, D., & Xu, Z. (2009). Geochemistry, petrofabrics and seismic properties of eclogites from the Chinese Continental Scientific Drilling boreholes in the Sulu UHP terrane, eastern China. Tectonophysics, 475(2), 251-266.

Yang, R., & Wu, Z. (2014). Elastic properties of stishovite and the CaCl2-type silica at the mantle temperature and pressure: An ab initio investigation. *Earth and Planetary Science Letters*, *404*, 14-21.

Chapter VI

Fast Seismic Anomalies under Continents Explained by the Delaminated Lower Continental Crust – Implications from High Pressure-Temperature Elasticity of Jadeite

Abstract

Various seismic models (e.g., GLAD-M25) have shown that the shear wave velocities (Vs) under continents, especially under continental cratons are extremely fast at 100-200 km depth. The elevated Vs (up to 4.8-4.9 km/s), which is more than 7% faster than the ambient mantle (~4.5 km/s), is difficult to be explained by low temperatures or high Mg# only. Alternatively, the delaminated lower continental crust (eclogitic materials) has been proposed to explain these fast seismic anomalies. However, due to the lack of knowledge of the thermoelastic properties of clinopyroxene which is dominated mineral phase (up to 60 vol%) in the delaminated lower continental crust, our understanding of the seismic properties of the potentially delaminated lower continental crust is still limited. Due to the high Na content (2.5-3.5 wt%), the clinopyroxene in the potentially delaminated lower continental crust is jadeite-rich (up to 60-80 mol%). Thus, the elastic properties of jadeite under high pressure-temperature conditions are needed. In this study, we measured the single-crystal elasticity of jadeite by Brillouin spectroscopy under high pressure-temperature conditions for the first time. We found that the temperature dependence of Vs of jadeite is extremely small if not negligible. As a result, the Vs of jadeite is much higher than all the other major upper mantle minerals at upper mantle conditions. Utilizing the chemical compositions of the lower continental crust under different tectonic settings, we calculated the mineral proportions of those chemically different lower continental crusts using Perple_X. The subsequently modeled seismic velocities of the

potentially delaminated lower continental crusts were found to match the widely observed fast seismic anomalies under cratons between 100-200 km depth.

1. Introduction

Delamination of the lower continental crust, which is usually referred to the sinking of the gradationally unstable basaltic crust into the Earth's upper mantle, is an important geological process for understanding the heterogeneities of the upper mantle (Kay & Kay, 1993; Levander et al., 2011). The trace elements (e.g., Sr/Y and La/Yb) and isotope (e.g., $^{87}Sr/^{86}Sr$ and ε_{Nd}) data of the adakitic intrusive rocks suggest that the potentially delaminated lower continental crust (PDLCC) could affect intra-plate volcanism (Xu et al., 2002; Lustrino 2005). In addition, the isotope and trace element distribution (e.g., $^{206}Pb/^{204}Pb$ and $^{87}Sr/^{86}Sr$ ratios) of the ocean island basalts (OIB) suggests that the origin of the enriched mantle (EM) is related to the recycling of the continental crust (Willbold & Stracke, 2010; Hofmann, 1997). Thus, identification of the PDLCC is necessary for interpreting the geochemical heterogeneities in the mantle. In addition, the PDLCC also has important geophysical implications: On one hand, the PDLCC may contribute to the observed seismic anomalies in the cratonic lithosphere (Garber et al., 2018; Levander et al., 2011); On the other hand, the enrichment of the heat-generation elements (e.g., U and K) in the recycled continental crust is important for the thermal evolution of the mantle (Arevalo et al., 2009).

Although the trace element and isotope observations of OIBs (Willbold & Stracke, 2010) and mantle xenoliths (Wang et al., 2018) have provided evidence for the PDLCC, seismically locating the recycled PDLCC remains challenging. Under high pressure-temperature conditions, the basaltic lower continental crust will transform to eclogitic materials which contain up to 60 vol% clinopyroxene. Due to the high Na content of the lower

continental crust (Rudnick & Fountain, 1995), the jadeite component in the clinopyroxene is up to 60-80 mol%. Therefore, the thermoelastic properties of jadeite under high pressure-temperature conditions are needed to constrain the seismic properties of the PDLCC. However, the elastic properties of jadeite have only been measured at room-temperature and high-pressure conditions (Hao et al., 2020) or computed at 0 K and high-pressure conditions (Walker, 2012; Kawai & Tsuchiya, 2010). In this study, we performed single-crystal Brillouin spectroscopy experiments on jadeite up to 18 GPa and 700 K at the high-pressure laser spectroscopy laboratory at University of New Mexico (UNM).

In addition, the mineral proportions and composition change with depth in the PDLCC has never been investigated because the chemical composition of the lower continental crust varies with tectonic environments (Rudnick & Fountain, 1995). The lack of the mineral proportions also prohibits us from linking various the seismic observations to the delamination process. Therefore, we used Perple_X software package for phase equilibrium calculation combined with thermodynamic properties of relevant minerals (Stixrude & Lithgow-Bertelloni, 2011) to calculate the mineral proportions and compositions of the PDLCC under mantle conditions. Finally, combining the thermoelastic properties of all relevant minerals, we modeled the seismic properties of the PDLCC from 30 to 500 km depth.

2. Experimental methods

2.1 High pressure-temperature Brillouin experiments

The jadeite crystals used in this study were selected from a natural jadeitite sample. The chemical composition, $Na_{0.954}Mg_{0.021}Ca_{0.029}Fe_{0.019}Al_{0.966}Si_{2.002}O_6$, was determined by the JEOL 8200 Electron Microprobe at UNM (Hao et al., 2020). The experimental current and

accelerating voltage were 20 nA and 15 kV, respectively. The element standards were forsterite for Mg, diopside for Si and Ca, albite for Na, and almandine for Al and Fe. Oxygen was calculated by stoichiometry from the cations. The hand-picked inclusion-free crystals were polished into platelets with 15-20 um thickness. Then the scratch-free crystals were broken into small pieces with diameters of 40-50 um and loaded into diamond anvil cells (DACs). The plane normals of the three selected crystals were (-0.692, -0.714, 0.106), (0.116, 0.993, -0.021), and (-0.896, -0.338, 0.289) measured at Sector 13-BMC, GeoSoilEnviroCARS (GSECARS), Advanced Photon Source (APS), Argonne National Laboratory (ANL). The two crystals with (-0.692, -0.714, 0.106) and (0.116, 0.993, -0.021) orientations are the same ones which were used in Hao et al. (2020), and the crystal with (-0.896, -0.338, 0.289) orientation was used for this study only. The angular uncertainties of the plane normals are ~0.5º. As shown in Figure VI.S6, the measured Vp and Vs of the selected three jadeite crystals are enough to constrain the thirteen independent single-crystal elastic moduli (C_{ij}s) of jadeite.

450 um culet diamonds were glued on tungsten carbide seats with 90º optical opening and put inside BX90 DACs for high pressure-temperature Brillouin experiments. Pre-indented rhenium gaskets with thicknesses of 50-55 um were drilled with ~280 um diameter holes and served as sample chambers. Neon was loaded into sample chambers as the pressure medium at GSECARS, APS, ANL (Rivers et al., 2008). Two ruby spheres were loaded into the sample chamber as pressure markers (Datchi et al., 2007; Mao et al., 1986). The pressure uncertainties were determined from the four pressure readings from the ruby fluorescence measurements of the two ruby spheres before and after the experiments. Pt wires were twined on pyrophyllite heaters, and two K-type thermocouples were placed near the diamond culet for temperature

measurements. The differences between the temperature readings from the two thermocouples are less than 7-10 K.

A single-mode 300 mW 532 nm solid-state laser was used for Brillouin experiments at UNM. A standard silica glass (Corning 7980) was used to calibrate the symmetric forward scattering angle as 50.6(1)º. The three jadeite crystals with known plane normals were measured at thirteen different Chi angles (0, 30, 60, 90, 120, 150, 180, 195, 225, 255, 285, 315, 345) to reduce the geometrical errors. Figure VI.S7 shows a typical Brillouin spectrum.

2.2 Perple_X calculations

To calculate the mineral proportions and compositions of the PDLCC under high pressure-temperature conditions, we used Perple_X software (Connolly, 2009) which is based on Gibbs free energy minimization. We adopted the most recent thermodynamic database from Stixrude and Lithgow-Bertelloni (2022) for the Perple_X calculation. The starting compositions of lower continental crust under different tectonic settings (Platform Shield, Mesozoic-Cenozoic Contractions, Mesozoic-Cenozoic Extensions, Continental Arcs, and Active Rifts) are obtained from Rudnick and Fountain (1995) (Table VI.S1). We calculated the phase proportions and chemical compositions of individual mineral phases from 30 km to 500 km depth. Different geotherms were used in our calculations based on their tectonic settings (Figure VI.S8; Reston & Morgan, 2004; Artemieva, 2019; Katsura, 2022). K element cannot be included in the Perple_X calculation. Since K_2O content is relatively low (<1 wt%) in the lower continental crust and the behavior of K is similar to Na in the eclogitic materials (Aoki & Takahashi, 2004), we treated all the K as Na in our calculation.

3. Results

3.1. High pressure-temperature single-crystal elasticity of jadeite

Given an initial guess of the C_{ij}s and density of jadeite, we conducted least-squares inversions of the Christoffel equation to obtain the best-fit C_{ij} model at every pressure-temperature condition. The aggregate elastic properties Vp, Vs, K_S, and G at each pressure-temperature condition can then be calculated through Voigt-Reuss-Hill (VRH) averaging scheme. The obtained Vp and Vs are independent of the assumed density and thus represent true values at high pressure-temperature conditions. Then we fit the temperature-dependent third order finite strain equation of state to the P-T-Vp-Vs dataset obtained from both this study and Hao et al. (2020) to get the true densities and the temperature and pressure derivatives of K_S and G (Duffy & Anderson, 1989; Davies & Dziewonski, 1975). During the inversion process, the elastic properties of jadeite at ambient condition (K_{S0}=123(3) GPa, G_0=74(2) GPa, and ρ_0=3.302(5) g/cm) from Hao et al. (2020) were fixed. The K_s, G, and C_{ij}s at each pressure-temperature condition are then recalculated utilizing the updated true densities (Table VI.S2). Figure VI.S9 shows the measured velocities at different Chi angles and the velocities predicted from the best-fit C_{ij} model at 16.7(2) GPa 500 K.

Using the experimentally determined thermal expansion coefficient α_0=3.4(5) $\times 10^{-5}$ K^{-1} for the same jadeite sample in Hao et al. (2020), the fitting of the high pressure-temperature data yields K_{S0}'=3.76(5), G_0'=1.11(2), $\partial K_{S0}/\partial T$=-0.028(2) GPa/K, and $\partial G_0/\partial T$=-0.004(1) GPa/K with K_{S0}=138(3) GPa, G_0=84(2) GPa, and ρ_0=3.302(5) g/cm^3. The K_{S0}' and G_0' determined in this study are consistent with the values reported in Hao et al. (2020) within uncertainties. Figure VI.1 shows the measured Vp, Vs, K_S, and G of jadeite under high pressure-temperature conditions. The most interesting feature is the extremely small temperature dependence of G and Vs of jadeite. As a result, at mantle temperature (1700 K),

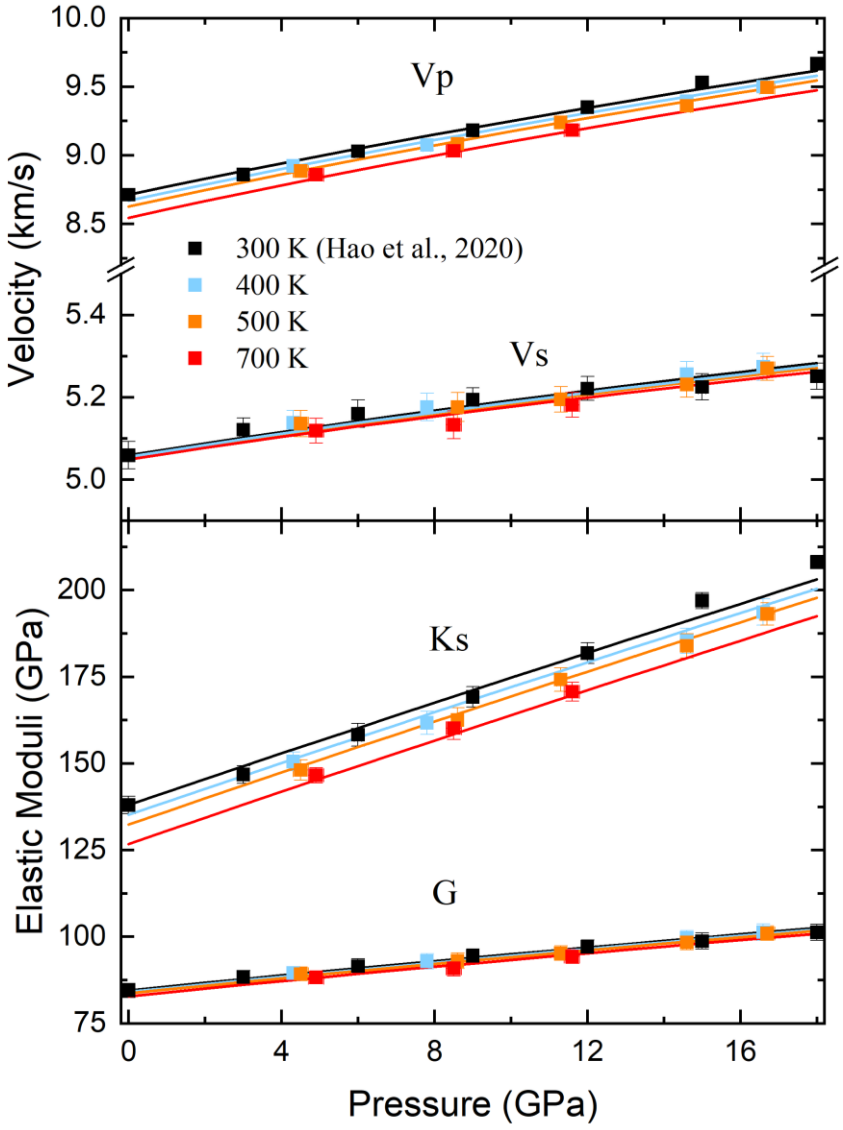

Figure VI.1. The high pressure-temperature Vp, Vs, Ks, and G of jadeite.

the Vs of jadeite is much higher than all the other major upper mantle minerals (Figure VI.S10). It is even faster than pyrope which is the fast endmember of garnet (Figure VI.S10).

Figure VI.2 shows all the high pressure-temperature C_{ij}s of jadeite determined in this study. Most of the C_{ij}s increase with pressure and decrease with temperature. The temperature

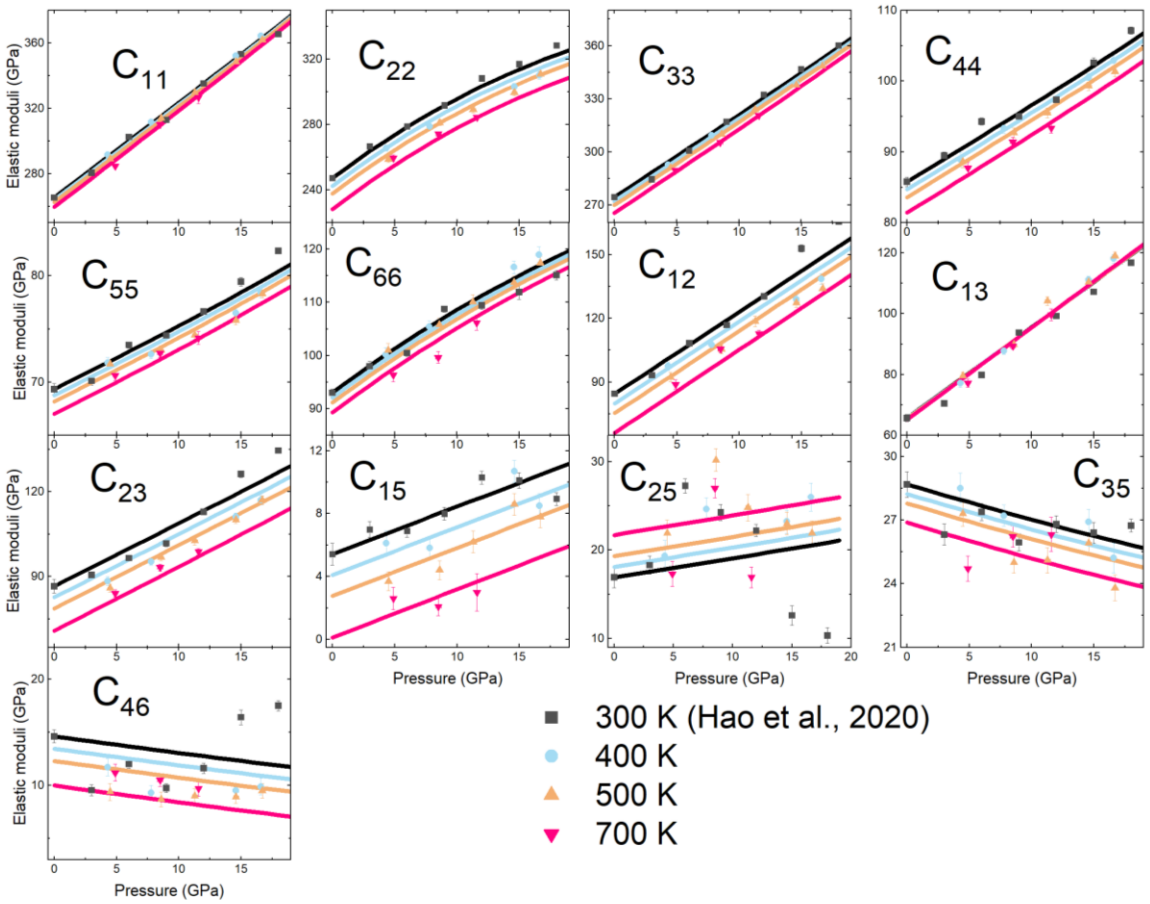

Figure VII.2. The high pressure-temperature C_{ij}s of jadeite. Solid lines are the finite strain equation of state fittings of the C_{ij}s.

dependences of many C_{ij}s (e.g., C_{13}) are very small, which agrees with the extremely small temperature dependence of G.

3.2. The compositions and proportions of the major minerals in PDLCC at high pressure-temperature conditions

Figure VI.3 shows the calculated mineral proportions of the PDLCC under different tectonic settings from 30 km to 500 km depth. From the top of the upper mantle down to the middle of the mantle transition zone, clinopyroxene and garnet are always the dominated

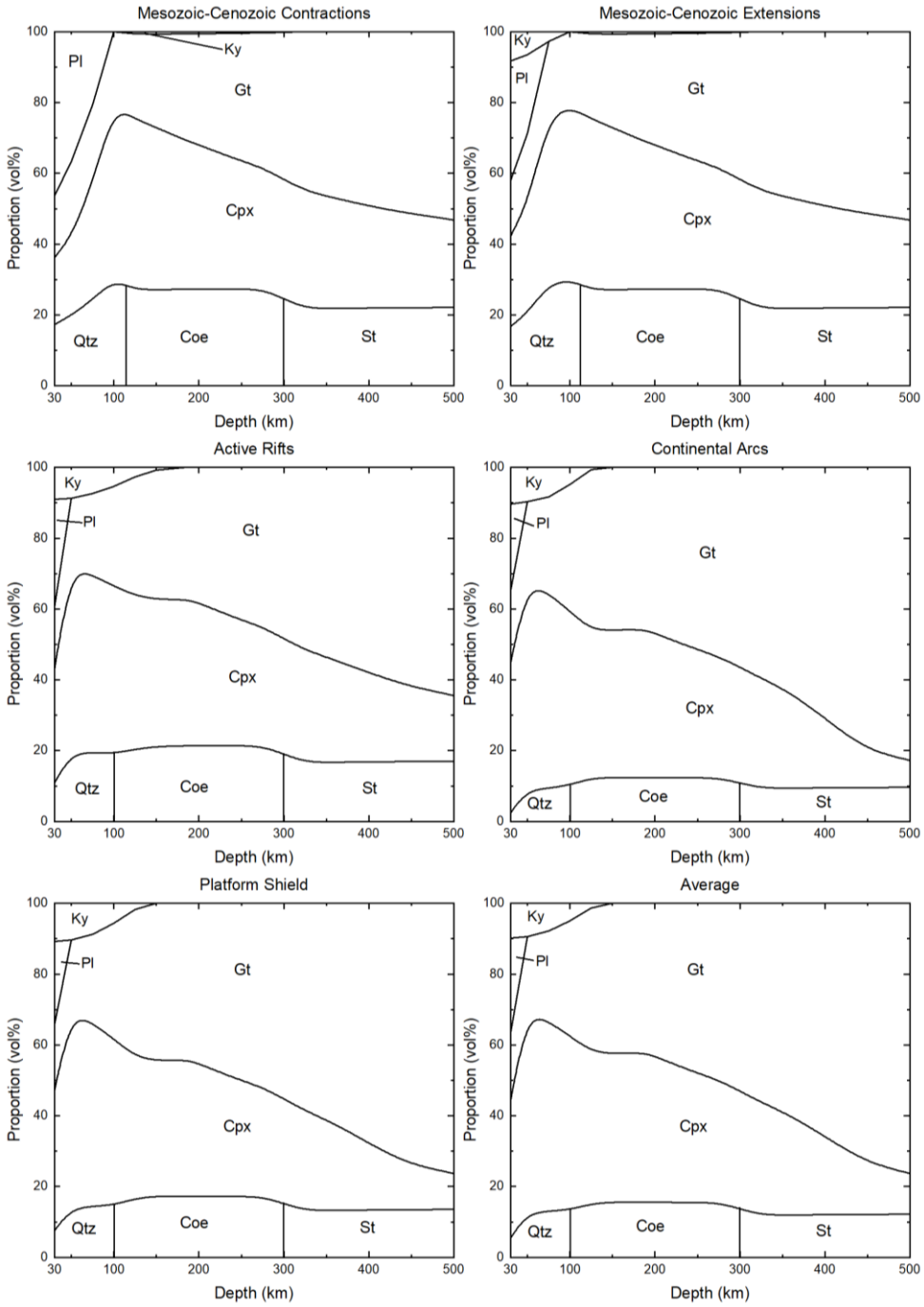

Figure VI.3. The calculated mineral proportions of the PDLCCs under different tectonic environments. (Pl: plagioclase; Ky: kyanite; Gt: garnet; Cpx: clinopyroxene; Qtz: quartz; Coe: coesite; St: stishovite)

mineral phases (sum up to ~70-80 vol%) regardless of the tectonic environments. The proportion of silica phases (~10-20 vol%) remains constant throughout the entire upper mantle. Due to the high Al content in the PDLCC (Rudnick & Fountain, 1995), kyanite (Al_2SiO_5) exists at the top of the upper mantle and gradually dissolves into garnet and/or clinopyroxene at 100-150 km depth. Plagioclase only appears at top of the upper mantle.

The chemical compositions of clinopyroxene and garnet gradually change with depth. Although the exact chemical compositions of garnet and clinopyroxene vary with tectonic settings, the general trend is similar: for clinopyroxene, the jadeite component increases with depth whereas both the diopside and hedenbergite component decrease with depth; for garnet, the grossular and majorite component always increase with depth and almandine component decreases with depth. The pyrope component in garnet increases with depth up to ~200 km and then gradually decreases with depth. These compositional changes are consistent with what was found in previous studies on mid-ocean ridge basalt and are mostly caused by the dissolution of pyroxenes into the garnet (Aoki & Takahashi, 2004).

4. Implications

Previous geochemical studies have suggested the potential existence of the PDLCC in the mantle. For example, the oxygen isotopes of the mantle xenoliths found underneath the North China Cratons (NCC) suggest the intracontinental recycling of delaminated crust (Wang et al., 2018). As explained in the introduction, we would like to evaluate different hypotheses, in particular the existence of PDLCC, that have been proposed to explain the fast seismic anomalies at 100-200 km depth under continental cratons. Utilizing the calculated mineral proportions/compositions and the experimentally determined elasticity of jadeite and other minerals from this study and previous studies (Table VI.S3), we calculated the density and

seismic velocities of PDLCC under different tectonic environments from 30 km to 500 km depth. Considering the chemical compositions of clinopyroxene and garnet change with depth, we assumed ideal mixing of different endmembers for the calculation (Hao et al., 2019; Leitner et al., 1980; Table VI.S3). To estimate the densities and elastic moduli of the multi-phase system, we used VRH averaging scheme (Text S1).

4.1. 1-D seismic properties of PDLCC

As shown in Figure VI.4a, compared to the Ak135 1-D seismic model, the density of the PDLCC along cold geotherms (active rifts, continental arcs, platform shield, and average) is higher than ambient mantle at depths greater than 40-50 km. This clear density contrast between 40-200 km depth makes the thickened continental crust gravitationally unstable. At 200-300 km depth, the density of the PDLCC becomes similar to the ambient mantle.

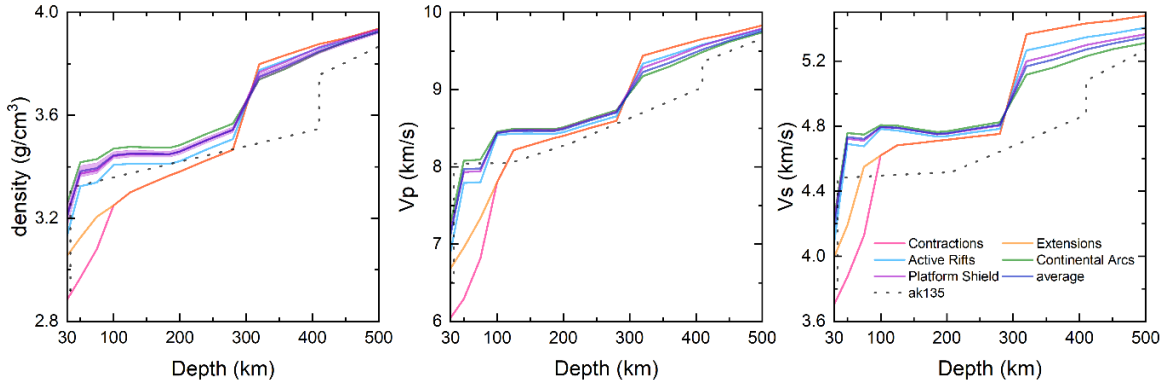

Figure VI.4. The density, Vp, and Vs of the PDLCCs under different tectonic environments from 30 km to 500 km depth. The dotted line represents the Ak135 seismic model. The density and velocities of PDLCC under contraction and extension environments overlap with each other at depths greater than 100 km. The purple shaded regions represent the uncertainties calculated for the average PDLCC composition.

Delamination of the lower continental crust is not as easy compared at shallower depths. The density of the PDLCC under contraction or extension environments is lower than the ambient mantle at 30-300 km depth due to the higher mantle temperatures under these tectonic environments. Thus, delamination is unlikely to take place under these tectonic environments.

Figure VI.4b shows the Vp of different PDLCCs from 30 km to 500 km depth. The Vp of the PDLCC along cold geotherms is similar to or higher than the Ak135 seismic model at depths greater than ~50 km. At depths of ~50-90 km, ~200-300 km, and ~400-500 km, the Vp of the PDLCC along cold geotherms is similar to ambient upper mantle. However, at depths of ~90-200 km and ~300-410 km, the Vp is higher than the Ak135 seismic model by ~ 5% and 6%, respectively. Due to the higher temperatures, the Vp of the PDLCC under contraction or extension environments is lower than the ambient mantle at 30-100 km depth and becomes comparable to the ambient mantle from 100 km to 300 km depth. At depths greater than 300 km, the Vp of the PDLCC under contraction or extension environments is higher than normal mantle by ~8% (bottom of the upper mantle) to ~2.5% (mantle transition zone) due to the existence of stishovite.

As shown in Figure VI.3c, the Vs of the PDLCC along cold geotherms is higher than the Ak135 seismic model at depths greater than 40 km. Due to the higher temperatures under extension or contraction environments, the Vs of PDLCC is only higher than Ak135 seismic model at depths greater than ~80-100 km. The largest Vs contrast between the PDLCC along cold geotherms and normal mantle exists at 100-200 km depth (~5%-7%) and 300-410 km depth (~7.4%-10.7%). The Vs of the PDLCC under extension or contraction environments is higher than the Ak135 seismic model by 3.5%, 13.3%, and 5.2% at depths of 100-300 km, 300-410 km, and 410-500 km, respectively.

4.2. The fast seismic anomalies at 100-200 km under continental cratons

The fast Vs anomalies under continental cratons have been observed globally in different seismic models (e.g., SEMum2, GLAD-M25, and DR2020s) between 100-200 km depth (French et al., 2013; Debayle et al., 2020; Lei et al., 2020). The SEMum2, GLAD-M25, and DR2020s models all show similar geographic distributions of fast Vs anomalies at ~150 km depth with the highest Vs ranging from ~4.8 km/s to 4.9 km/s (Figure VI.5a, VI.S11). In this study, we focus on the most recent GLAD-M25 model (Lei et al., 2020), which is a global adjoint tomography model utilizing both surface and body waves.

To evaluate different hypotheses for explaining the fast Vs anomalies under continental cratons, we calculated the Vs (Voigt bound) of pyrolite, harzburgite, and eclogite at 150 km depth under different temperatures assuming different Mg#s in the constituting mafic minerals (Figure VI.5b). The pyrolite, harzburgite, and eclogite represent ambient mantle (~60 vol% olivine), olivine-rich lithosphere (~80 vol% olivine), and PDLLC, respectively. The bulk chemical composition of the eclogite here, which represents the PDLCC, is the average lower continental crust chemical composition from Rudnick and Fountain (1995) as shown in Table VI.S1. Two different temperatures are assumed at 150 km depth under craton: one is 300 K lower than the adiabatic ambient mantle representing cold temperatures expected under the “normal” cratons; the other one is at ~1000 K, which is expected to be seen only under extremely cold cratons (Figure VI.S8). According to the studies of mantle xenoliths, the Mg# of the mafic minerals in continental lithosphere might increase from ~89 in the ambient mantle to ~92-93 (e.g., Kopylova and Russell, 2000; Jaques et al., 1990). Thus, we considered pyrolite, harzburgite, and eclogite with ~30% less Fe (Mg# ~92.3) compared with the ambient mantle.

As shown in Figure VI.5b, along normal cold geotherms, even with Mg# as high as

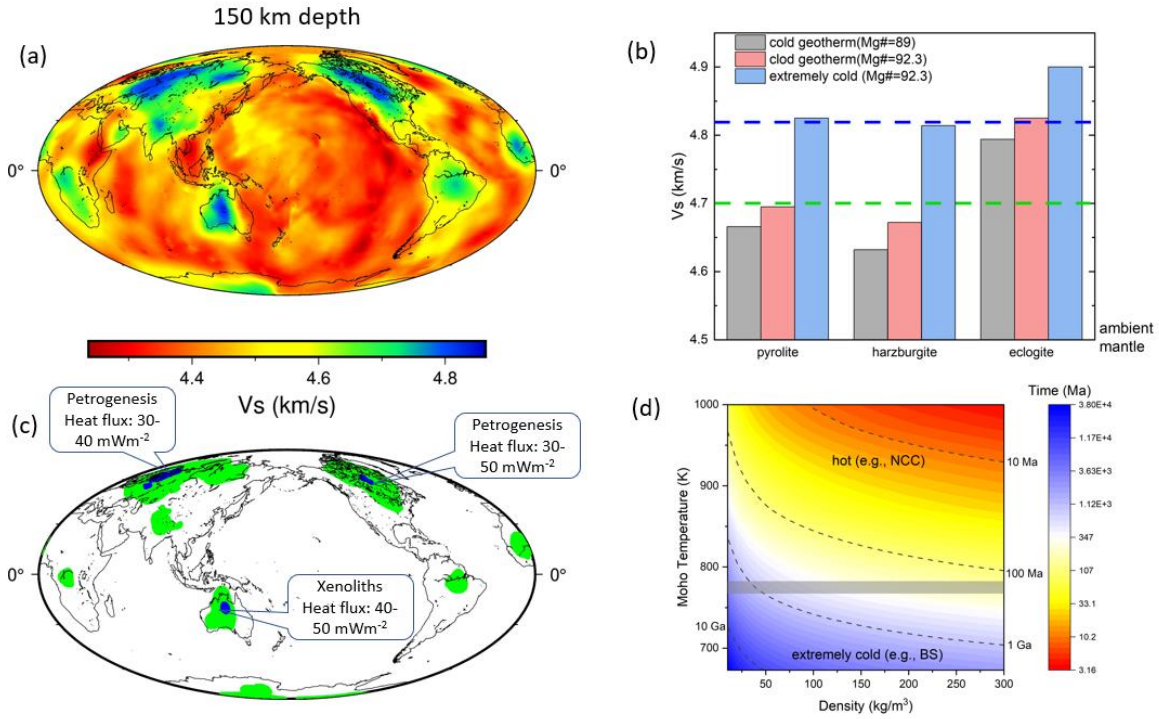

Figure VI.5. (a) The global Vs map at 150 km depth from the GLAD-M25 model (Lei et al., 2020). (b) The Vs (Voigt bound) comparison of pyrolite, harzburgite, and eclogite with different temperatures and Mg#. The blue and green dashed lines marked the Vs of 4.82 km/s and 4.7 km/s, respectively. (c) The global distribution of the potentially delaminated eclogitic materials based on the global Vs model. Bule and green regions are with Vs > 4.82 km/s and Vs between 4.82 to 4.7 km/s, respectively. (d) The instability time of a 10-km thick dense eclogitic lower continental crust changes with Moho temperature and density contrast, adopted from Jull and Kelemen (2001) and Hacker et al. (2015). The grey line shows the Moho temperature along a regular cold cratonic geotherm. (NCC: North China Craton; BS: Baltic Shield)

92.3, the Vs of pyrolite/harzburgite could only reach ~4.7 km/s, whereas the Vs of eclogite is higher than 4.8 km/s. Along an extremely cold geotherm (1000 K at 150 km depth), the Vs of

pyrolite/harzburgite is ~4.82 km/s, whereas the Vs of eclogite could reach 4.9 km/s. We identified two regions in GLAD-M25 model (Figure VI.5c): blue regions with Vs larger than 4.82 km/s, which could only be explained by delaminated eclogitic materials; green regions with Vs between 4.7 and 4.82 km/s, which could be explained by either the extremely low temperatures or the presence of small amounts of PDLCC. As shown in Figure VI.5c, the blue regions only exist in Eastern Canada, Western Australia, and Eastern Europe, where the xenoliths or petrogenesis studies support potential delamination processes taking place in the past (Whalen et al., 2010; Kovalenko et al., 2005; Smithies & Champion, 1999). The green regions are widely distributed under different cratons, including Northern North America, Central Southern America, Western Australia, Southern and Northern Asia, Southern and Eastern Africa, and Eastern Europe.

Delamination of lower continental crust depends on many factors, such as Moho temperature, density contrast, and the thickness of the eclogitic layer. Adopting the crustal delamination model presented in Jull and Kelemen (2001) and Hacker et al. (2005), we plotted the instability time that is needed for delaminating a 10 km thick dense eclogitic layer as part of the lower continental crust as a function of Moho temperature and density contrast (Figure VI.5d). The Moho temperature has a huge effect on the instability time. Under normal cold cratons, the instability time is between 100 Ma to 1 Ga. If the Moho temperature is high (e.g., NCC), the instability time can be as short as only ~10 Ma. However, if the Moho temperature is extremely low (e.g., Baltic Shield), the instability time increases to ~1Ga or more, and delamination of the lower continental crust is difficult to occur on geological time scales. The local continental heat flux can be a good indicator of the Moho temperatures (Mareschal & Jaupart, 2013). For example, compared with the global average (~65 $mW \cdot m^{-2}$), the high heat

flux of NCC (>100 $mW \cdot m^{-2}$) suggests a fairly hot Moho. The instability time of the eclogitic lower crust under NCC would be on the order of 10 Ma or less. As a result, the delaminated eclogitic materials under NCC may have already sunk to the deeper part of the Earth, which explains the disappearance of the fast Vs anomalies under NCC between 100-200 km depth. On the other hand, the heat flux of Eastern Canada, Western Australia, and Eastern Europe, which are the blue regions in Figure VI.5c, is ~30-50 $mW \cdot m^{-2}$, suggesting a reasonably cold Moho which yields hundreds of Ma instability time. Typical cratons are ~1.5-2.5 Ga old, and it is thus possible to observe the delaminated eclogitic lower continental crust at 100-200 km depth under these cratons with a reasonably long instability time.

5. Conclusions

In this study, we measured high pressure-temperature single-crystal elastic properties of jadeite by Brillouin spectroscopy. The extremely small temperature dependence of the G makes the Vs of jadeite higher than all the other major minerals in the upper mantle. We also calculated the mineral proportions of the PDLCC under different tectonic environments using different lower crustal compositions constrained from geochemical studies. The dominated mineral phases in the upper mantle are always garnet and clinopyroxene regardless of their tectonic settings. Utilizing the calculated mineral proportions, compositions, and elastic properties of relevant minerals, we modeled the seismic properties of the PDLCCs. We found that the thickened lower continental crust along cold geotherms is gravitationally unstable. The high seismic velocities, especially Vs, of the PDLCC could contribute to the observed seismic anomalies under continental cratons at 100-200 km depth.

Acknowledgments

This study is supported by NSF EAR 1646527 (JSZ) and 1847707 (JSZ). The authors would like to thank Sergey Tkachev for the Neon gas loading of the DACs at GSECARS, APS, ANL. The use of the gas-loading system and 13-BM-C beamlines are supported by COMPRES, the Consortium for Materials Properties Research in Earth Sciences under NSF Cooperative Agreement EAR 1661511, and GSECARS is funded by NSF (EAR - 1634415) and Department of Energy (DOE) – GeoSciences (DE-FG02-94ER14466). This research used resources of the APS, a U.S. DOE Office of Science User Facility operated for the DOE Office of Science by ANL under Contract NO. DE-AC02-06CH11357. The X-ray Atlas instrument at the University of Hawaii was funded by NSF grant EAR 1541516 (PD). All the data presented in this study are available in the Supporting Information.

Funding: This work is supported by the National Science Foundation (NSF) under Grant EAR 1646527 (JZ) and 1847707 (JSZ). PD was supported by NSF grant EAR 1722969.

References

Aoki, I., & Takahashi, E. (2004). Density of MORB eclogite in the upper mantle. *Physics of the Earth and Planetary Interiors*, *143*, 129-143.

Artemieva, I. M. (2019). Lithosphere structure in Europe from thermal isostasy. *Earth-Science Reviews*, *188*, 454-468.

Connolly, J. A. D. (2009). The geodynamic equation of state: what and how. Geochemistry, Geophysics, Geosystems, 10(10).

Datchi, F., Dewaele, A., Loubeyre, P., Letoullec, R., Le Godec, Y., & Canny, B. (2007). Optical pressure sensors for high-pressure-high-temperature studies in a diamond anvil cell. *High Pressure Research*, *27*(4), 447–463.

Davies, G. F., & Dziewonski, A. M. (1975). Homogeneity and constitution of the Earth's lower mantle and outer core. *Physics of the Earth and Planetary Interiors*, *10*(4), 336–343.

Debayle, E., Bodin, T., Durand, S., & Ricard, Y. (2020). Seismic evidence for partial melt below tectonic plates. *Nature*, *586*(7830), 555-559.

Duffy, T. S., & Anderson, D. L. (1989). Seismic velocities in mantle minerals and the mineralogy of the upper mantle. *Journal of Geophysical Research*, *94*(B2), 1895–1912.

French, S., Lekic, V., & Romanowicz, B. (2013). Waveform tomography reveals channeled flow at the base of the oceanic asthenosphere. *Science*, *342*(6155), 227-230.

Garber, J. M., Maurya, S., Hernandez, J. A., Duncan, M. S., Zeng, L., Zhang, H. L., ... & Stixrude, L. (2018). Multidisciplinary constraints on the abundance of diamond and eclogite in the cratonic lithosphere. *Geochemistry, Geophysics, Geosystems*, *19*(7), 2062-2086.

Green, D. H., & Ringwood, A. E. (1967). An experimental investigation of the gabbro to eclogite transformation and its petrological applications. *Geochimica et Cosmochimica Acta*, *31*(5), 767-833.

Hacker, B. R., Kelemen, P. B., & Behn, M. D. (2015). Continental lower crust. *Annual Review of Earth and Planetary Sciences*, *43*(1), 167-205.

Hao, M., Zhang, J. S., Pierotti, C. E., Zhou, W. Y., Zhang, D., & Dera, P. (2020). The seismically fastest chemical heterogeneity in the Earth's deep upper mantle—implications from the single-crystal thermoelastic properties of jadeite. *Earth and Planetary Science Letters*, *543*, 116345.

Hao, M., Pierotti, C. E., Tkachev, S., Prakapenka, V., & Zhang, J. S. (2019). The single-crystal elastic properties of the jadeite-diopside solid solution and their implications for the composition-dependent seismic properties of eclogite. *American Mineralogist: Journal of Earth and Planetary Materials*, *104*(7), 1016-1021.

Hofmann, A. W. (1997). Mantle geochemistry: the message from oceanic volcanism. *Nature*, *385*(6613), 219.

James, D. E., Boyd, F. R., Schutt, D., Bell, D. R., & Carlson, R. W. (2004). Xenolith constraints on seismic velocities in the upper mantle beneath southern Africa. Geochemistry, Geophysics, Geosystems, 5(1).

Jaques, A. L., O'Neill, H. S. C., Smith, C. B., Moon, J., & Chappell, B. W. (1990). Diamondiferous peridotite xenoliths from the Argyle (AK1) lamproite pipe, Western Australia. *Contributions to Mineralogy and Petrology*, *104*(3), 255-276.

Jull, M., & Kelemen, P. Á. (2001). On the conditions for lower crustal convective instability. *Journal of Geophysical Research: Solid Earth*, *106*(B4), 6423-6446.

Katsura, T. (2022). A revised adiabatic temperature profile for the mantle. *Journal of Geophysical Research: Solid Earth*, *127*(2), e2021JB023562.

Kawai, K., & Tsuchiya, T. (2010). Ab initio investigation of high-pressure phase relation and elasticity in the NaAlSi2O6 system. *Geophysical Research Letters*, *37*(17).

Kay, R. W., & Kay, S. M. (1993). Delamination and delamination magmatism. *Tectonophysics*, *219*(1-3), 177-189.

Kennett, B. L., Engdahl, E. R., & Buland, R. (1995). Constraints on seismic velocities in the Earth from traveltimes. *Geophysical Journal International*, *122*(1), 108-124.

Kopylova, M. G., & Russell, J. K. (2000). Chemical stratification of cratonic lithosphere: constraints from the Northern Slave craton, Canada. *Earth and Planetary Science Letters*, *181*(1-2), 71-87.

Kovalenko, A., Clemens, J. D., & Savatenkov, V. (2005). Petrogenetic constraints for the genesis of Archaean sanukitoid suites: geochemistry and isotopic evidence from Karelia, Baltic Shield. *Lithos*, *79*(1-2), 147-160.

Lee, C. T. A. (2003). Compositional variation of density and seismic velocities in natural peridotites at STP conditions: Implications for seismic imaging of compositional heterogeneities in the upper mantle. Journal of Geophysical Research: Solid Earth, 108(B9).

Lei, W., Ruan, Y., Bozdağ, E., Peter, D., Lefebvre, M., Komatitsch, D., ... & Pugmire, D. (2020). Global adjoint tomography—model GLAD-M25. *Geophysical Journal International*, *223*(1), 1-21.

Leitner, B. J., Weidner, D. J., & Liebermann, R. C. (1980). Elasticity of single crystal pyrope and implications for garnet solid solution series. *Physics of the Earth and Planetary Interiors*, *22*(2), 111-121.

Lustrino, M. (2005). How the delamination and detachment of lower crust can influence basaltic magmatism. *Earth-Science Reviews*, *72*(1-2), 21-38.

Mao, H. K., Xu, J. A., & Bell, P. M. (1986). Calibration of the ruby pressure gauge to 800 kbar under quasi-hydrostatic conditions. *Journal of Geophysical Research: Solid Earth*, *91*(B5), 4673-4676.

Mareschal, J. C., & Jaupart, C. (2013). Radiogenic heat production, thermal regime and evolution of continental crust. *Tectonophysics*, *609*, 524-534.

Reston, T. J., & Morgan, J. P. (2004). Continental geotherm and the evolution of rifted margins. *Geology*, *32*(2), 133-136.

Rivers, M., Prakapenka, V., Kubo, A., Pullins, C., Holl, C., & Jacobsen, S. (2008). The COMPRES/GSECARS gas-loading system for dia- mond anvil cells at the Advanced Photon Source. *High Pressure Research*, *28*(3), 273–292.

Rudnick, R. L., & Fountain, D. M. (1995). Nature and composition of the continental crust: a lower crustal perspective. *Reviews of geophysics*, *33*(3), 267-309.

Smithies, R. H., & Champion, D. C. (1999). Late Archaean felsic alkaline igneous rocks in the Eastern Goldfields, Yilgarn Craton, Western Australia: a result of lower crustal delamination?. *Journal of the Geological Society*, *156*(3), 561-576.

Stixrude, L., & Lithgow-Bertelloni, C. (2022). Thermal expansivity, heat capacity and bulk modulus of the mantle. Geophysical Journal International, 228(2), 1119-1149.

Walker, A. M. (2012). The effect of pressure on the elastic properties and seismic anisotropy of diopside and jadeite from atomic scale simulation. *Physics of the Earth and Planetary Interiors*, *192*, 81-89.

Wang, C. G., Xu, W. L., Yang, D. B., Liu, Y. S., Pei, F. P., Li, Q. L., & Zhou, Q. J. (2018). Olivine oxygen isotope evidence for intracontinental recycling of delaminated continental crust. *Geochemistry, Geophysics, Geosystems*, *19*(7), 1913-1924.

Whalen, J. B., Wodicka, N., Taylor, B. E., & Jackson, G. D. (2010). Cumberland batholith, Trans-Hudson Orogen, Canada: Petrogenesis and implications for Paleoproterozoic crustal and orogenic processes. *Lithos*, *117*(1-4), 99-118.

Willbold, M., & Stracke, A. (2010). Formation of enriched mantle components by recycling of upper and lower continental crust. *Chemical Geology*, *276*(3-4), 188-197.

Xu, J. F., Shinjo, R., Defant, M. J., Wang, Q., & Rapp, R. P. (2002). Origin of Mesozoic adakitic intrusive rocks in the Ningzhen area of east China: partial melting of delaminated lower continental crust?. *Geology*, *30*(12), 1111-1114.

Supporting Information

Text VI.S1. Voigt-Reuss-Hill average of multi-phase aggregates

The calculations of Voigt bound, which represents uniform strain scenario, and the Reuss bound, which represents uniform stress scenario are:

$$Voigt\ bound: E^V = f_a E_a + f_b E_b \quad \text{(VI.S1)}$$

$$Reuss\ bound: E^R = (\frac{f_a}{E_a} + \frac{f_b}{E_b})^{-1} \quad \text{(VI.S2)}$$

where E^V and E^R represent the density or elastic moduli of the multi-component system of Voigt and Reuss bounds, respectively; E_a and E_b represent the density or elastic moduli of phase a and b, respectively; f_a and f_b represent the volume fractions of phase a and b, respectively.

The actual properties of the multi-phase aggregate should lie in between the Voigt and Reuss bounds. The equation for calculate Hill average (E^{VRH}) is:

$$Hill\ average: E^{VRH} = (E^V + E^R)/2 \quad \text{(VI.S3)}$$

The seismic velocities are calculated based on the density and elastic moduli of the Hill average.

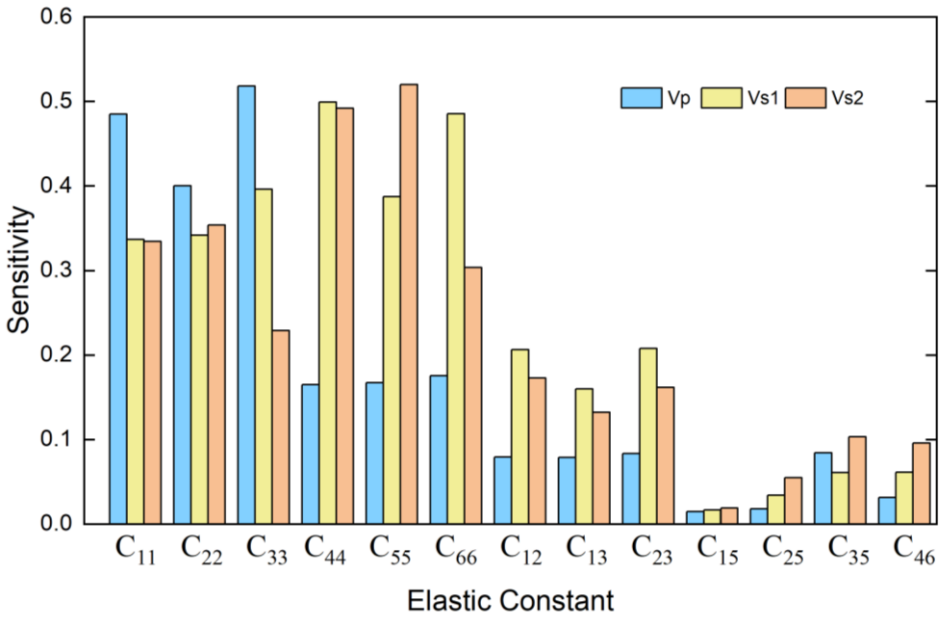

Figure VI.S6. The sensitivity of Vp, Vs1, and Vs2 to all the C_{ij}s using the orientation combination in this study.

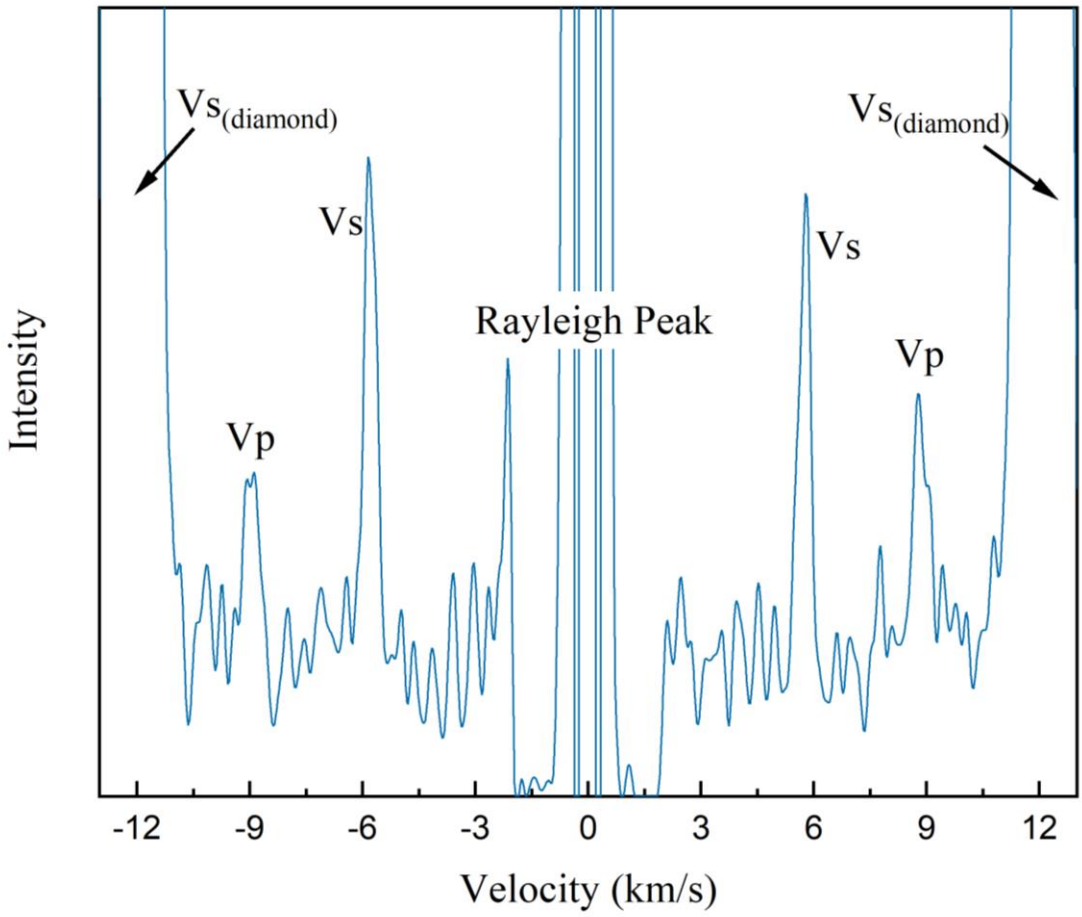

Figure VI.S7. Typical Brillouin spectrum of jadeite sample at 16.7(2) GPa 500 K. The peaks of Ne are too weak to be seen.

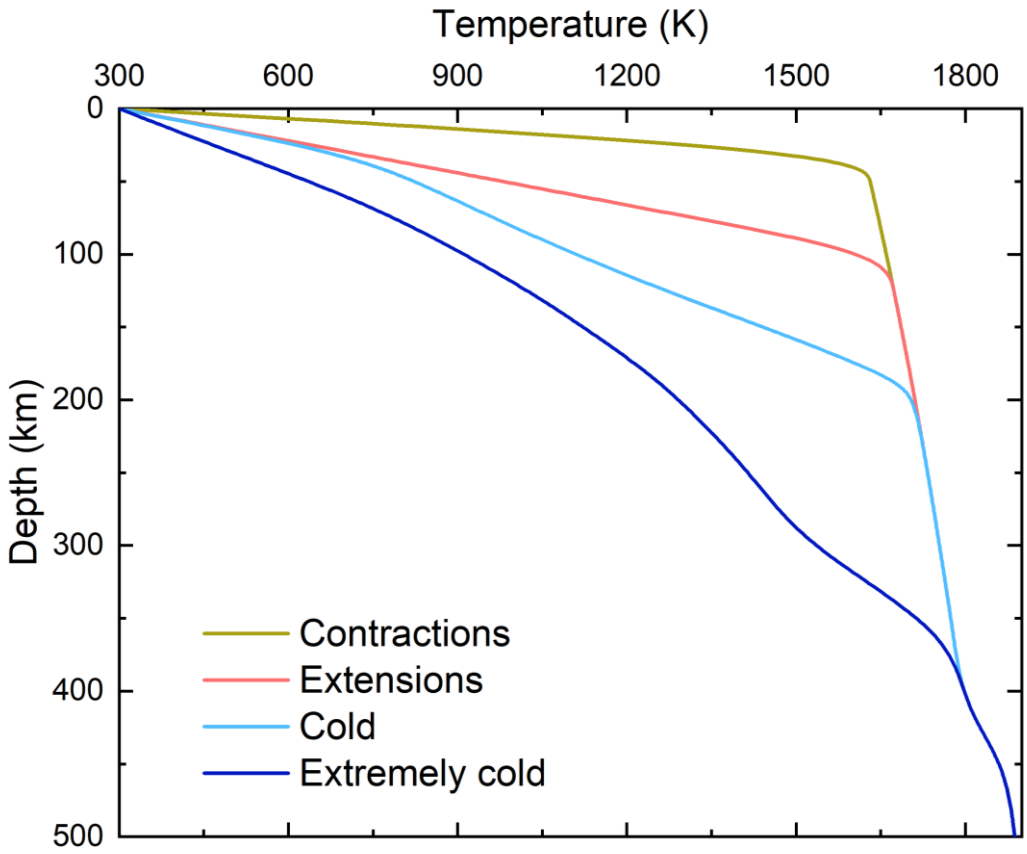

Figure VI.S8. The geotherms used for the Perple_X calculations. The cold geotherm is used for Platform Shield, Continental Arcs, Active Rifts, and average lower continental crust. The extremely cold geotherm are adopted from Artemieva (2019) and used for extremely cold cratons. At 350 km depth, all geotherms merge to the 1600 K mantle adiabat.

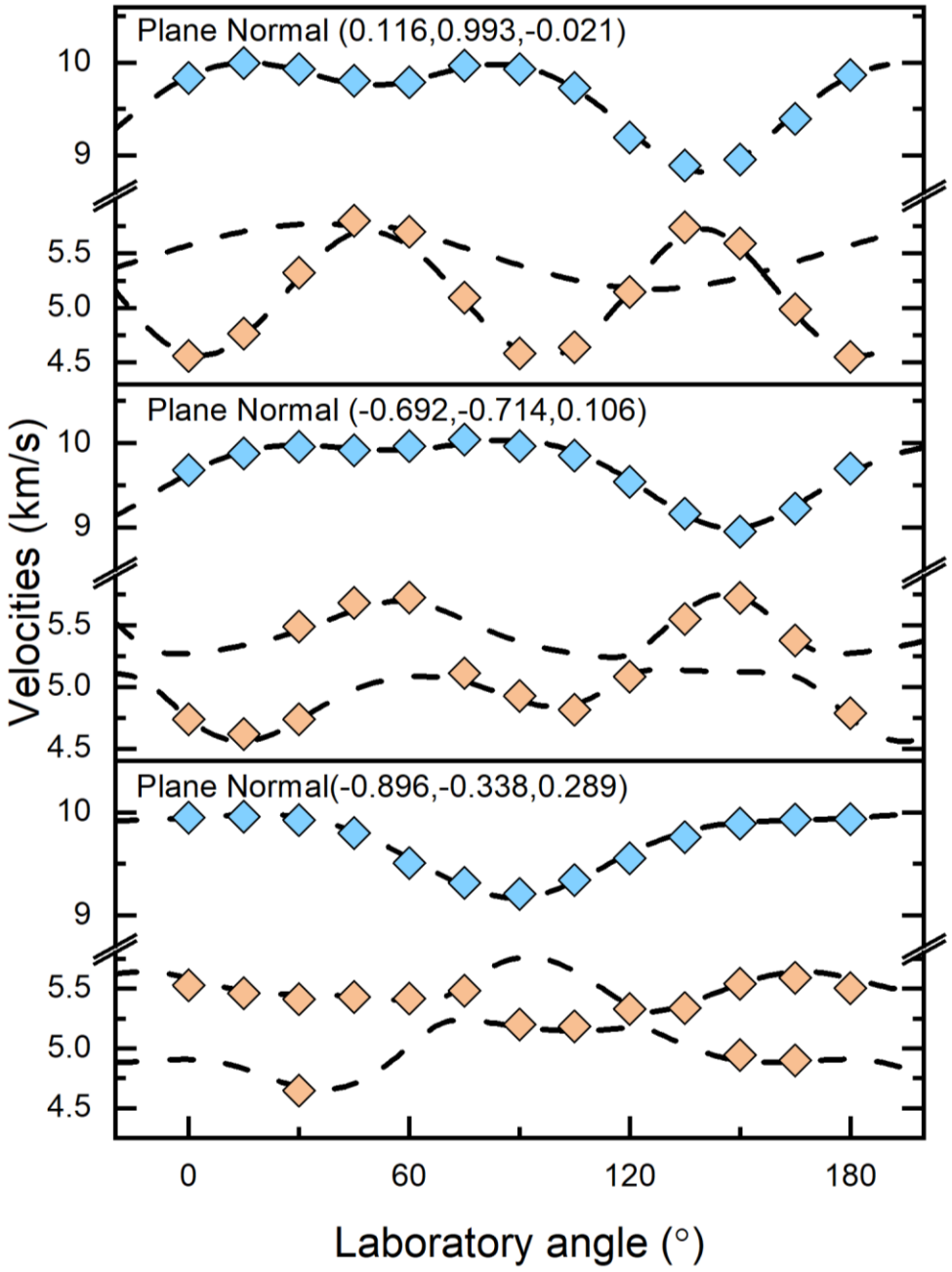

Figure VI.S9. Measured acoustic velocities of jadeite as a function of the laboratory Chi angles within the sample plane at 16.7(2) GPa 500 K. Dashed lines are the calculated velocities from the best-fit single-crystal elasticity model, and diamonds are the experimentally determined velocities. The errors of measured velocities are smaller than the symbols.

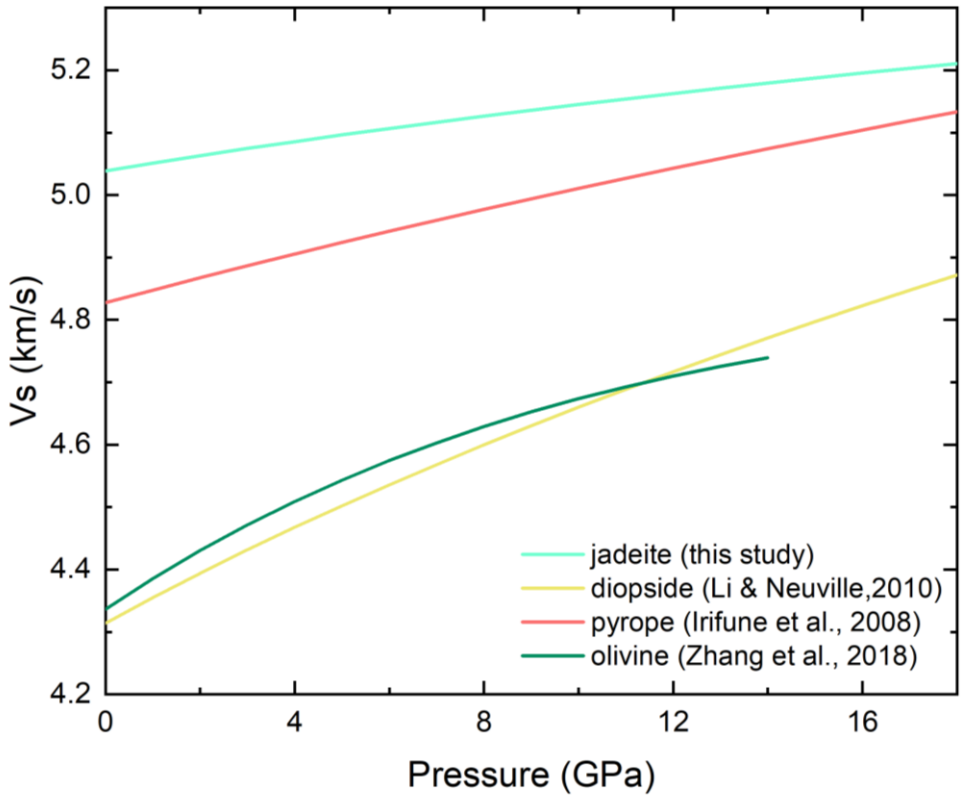

Figure VI.S10. The Vs of the major upper mantle minerals at 1700 K.

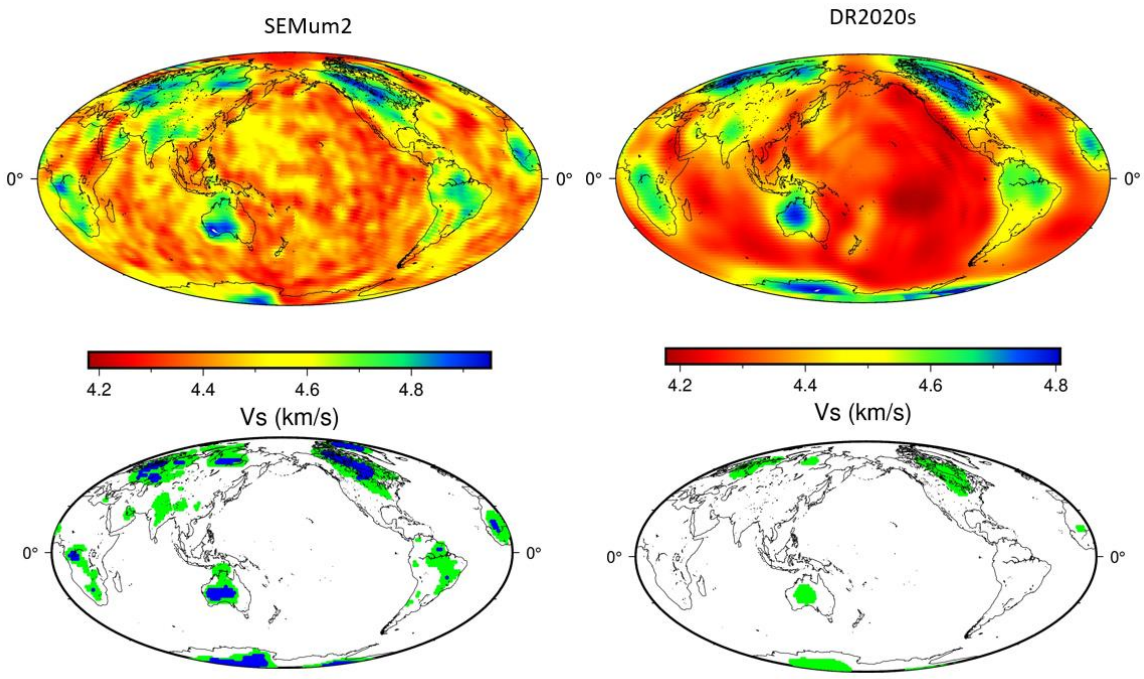

Figure VI.S11. The global Vs map at 150 km depth of SEMum2 and DR2020s seismic models and the distribution of the potentially delaminated eclogitic materials based on the global Vs model.

Oxides	Contraction/Extension	Platform Shield	Continental Arcs	Active Rifts	Average
SiO_2	57.7	52.4	50.8	54.9	52.3
Al_2O_3	16.0	16.5	16.9	16.4	16.6
FeO	7.3	8.2	8.8	7.9	8.4
MgO	4.8	7.1	7.7	6.0	7.1
CaO	6.7	9.5	10.1	8.0	9.4
Na_2O	3.0	2.7	2.5	2.8	2.6
K_2O	1.0	0.6	0.4	0.8	0.6

Table VI.S1. Chemical composition of lower continental crusts at different tectonic settings.

	4.3(1) GPa 400 K	4.5(2) GPa 500 K	4.9(3) GPa 700 K	7.8(1) GPa 400 K	8.6(2) GPa 500 K	8.5(4) GPa 700 K
ρ (g/cm^3)	3.390	3.383	3.368	3.467	3.473	3.449
C_{11} (GPa)	292(1)	289(1)	285(1)	312(1)	314(1)	310(1)
C_{22} (GPa)	266(2)	259(2)	260(2)	279(2)	281(2)	274(2)
C_{33} (GPa)	293(2)	290.9(8)	289.7(9)	309.2(8)	310.1(8)	305.4(7)
C_{44} (GPa)	89(1)	88.6(8)	87.7(8)	93.3(7)	92.7(7)	91.5(6)
C_{55} (GPa)	71.8(5)	71.7(4)	70.6(5)	72.6(4)	73.0(4)	72.7(4)
C_{66} (GPa)	100(1)	101(1)	96(1)	105(1)	106(1)	100(1)
C_{12} (GPa)	98(2)	92(2)	89(2)	108(2)	106(2)	106(2)
C_{13} (GPa)	77(1)	80(1)	77(1)	88(1)	90(1)	89(1)
C_{23} (GPa)	88(2)	86(1)	84(1)	95(1)	97(1)	93(1)
C_{15} (GPa)	6.1(8)	3.7(6)	2.6(7)	5.8(6)	4.4(6)	2.1(6)
C_{25} (GPa)	19(2)	22(1)	17(1)	25(1)	30(1)	27(1)
C_{35} (GPa)	28.5(7)	27.3(6)	24.7(6)	27.2(5)	25.0(5)	26.2(5)
C_{46} (GPa)	11.7(8)	9.4(8)	11.2(8)	9.3(7)	8.7(7)	10.5(6)
K_S^R (GPa)	148.2(4)	145.7(8)	144.9(8)	158.9(7)	159.5(6)	157.4(7)
G^R (GPa)	87.7(2)	87.5(4)	86.6(4)	90.9(3)	90.9(3)	88.9(3)
K_S^V (GPa)	152.9(4)	150.5(8)	148.3(8)	164.5(7)	165.5(6)	162.9(7)
G^V (GPa)	91.3(2)	91.0(4)	89.9(4)	94.9(3)	95.2(3)	92.9(3)
K_S^{VRH} (GPa)	151(3)	148(3)	147(2)	162(3)	162(3)	160(3)
G^{VRH} (GPa)	89(2)	89(2)	88(2)	93(2)	93(2)	91(2)
Vp (km/s)	8.92(3)	8.89(4)	8.86(3)	9..08(4)	9.08(4)	9.03(4)
Vs (Km/s)	5.14(3)	5.14(3)	5.12(3)	5.18(3)	5.18(3)	5.13(3)
	11.3(3) GPa 500 K	11.6(3) GPa 700 K	14.6(2) GPa 400 K	14.6(3) GPa 500 K	16.6(1) GPa 400 K	16.7(2) GPa 500 K
ρ (g/cm^3)	3.529	3.515	3.604	3.595	3.642	3.635
C_{11} (GPa)	330(1)	327(4)	352(1)	349(1)	364(1)	362(1)
C_{22} (GPa)	289(2)	284(2)	303(2)	300(2)	310(2)	311(2)
C_{33} (GPa)	324(1)	321(1)	338.4(8)	337.8(8)	350(1)	348.5(9)
C_{44} (GPa)	95.5(7)	93.4(7)	100.5(6)	99.3(6)	102.9(8)	101.3(7)
C_{55} (GPa)	74.4(5)	74.1(6)	76.5(4)	75.8(4)	78.4(5)	78.3(4)
C_{66} (GPa)	110(1)	106(1)	117(1)	114(1)	119(2)	117(1)
C_{12} (GPa)	119(3)	113(2)	129(2)	127(2)	139(3)	134(2)
C_{13} (GPa)	104(1)	100(2)	111(1)	110(1)	118(1)	119(1)

C_{23} (GPa)	103(2)	99(1)	111(1)	110(1)	117(2)	117(2)
C_{15} (GPa)	6.2(7)	3(1)	10.7(7)	8.6(7)	8.5(8)	7.8(7)
C_{25} (GPa)	25(2)	17(1)	23(1)	23(1)	26(2)	22(1)
C_{35} (GPa)	25.1(6)	26.3(8)	26.9(6)	25.9(5)	25.2(7)	23.8(6)
C_{46} (GPa)	9.0(7)	9.7(7)	9.5(6)	8.9(6)	9.9(8)	9.5(7)
K_S^R (GPa)	171.4(8)	169(1)	182.1(6)	180.9(7)	190.4(8)	190.5(8)
G^R (GPa)	93.3(3)	92.6(4)	97.6(3)	96.4(3)	99.2(4)	99.1(4)
K_S^V (GPa)	177.0(8)	173(1)	188.5(6)	186.8(7)	196.8(8)	195.7(8)
G^V (GPa)	97.2(3)	96.1(4)	101.6(3)	100.3(3)	103.4(4)	102.8(4)
K_S^{VRH} (GPa)	174(3)	171(3)	185(3)	184(3)	194(4)	193(3)
G^{VRH} (GPa)	95(2)	94(2)	100(2)	98(2)	101(2)	101(2)
Vp (km/s)	9.24(4)	9.18(3)	9.39(4)	9.36(4)	9.50(4)	9.50(3)
Vs (Km/s)	5.20(3)	5.18(3)	5.26(3)	5.23(3)	5.27(3)	5.27(3)

Table VI.S2. Density, C_{ij}s, K, G, Vp, and Vs of jadeite at each pressure-temperature condition determined in this study. The Reuss and Voigt bounds of the homogeneous isotropic aggregate under the VRH averaging scheme are denoted by the superscripts R and V.

Mineral	Density (g/cm^3)	K_{S0} (GPa)	$\partial K_S/\partial P$	$\partial K_S/\partial T$ (GPa/K)	G_0 (GPa)	$\partial G/\partial P$	$\partial G/\partial T$ (GPa/K)	a_0 (10^{-4} K^{-1})	a_1 (10^{-8} K^{-2})	a_2 (K)
Jadeite[1]	3.302(5)	138(3)	3.75(5)	-0.028(2)	84(2)	1.11(2)	-0.004(1)	0.34(5)	0	0
Diopside[1]	3.272(6)	116.4(7)	4.9(1)	-0.012(1)	73.0(4)	1.6(1)	-0.011(1)	0.19	2.08	0
Pyrope[2,3,4,5,8]	3.56(2)	171.0(5)	4.4(1)	-0.014(3)	94.9(2)	1.15(6)	-0.011(2)	0.288	0.2787	-0.5521
Mg-majorite[2,3,4,5,8]	3.56(2)	162.0(5)	4.4(1)	-0.014(3)	86.2(2)	1.15(6)	-0.011(2)	0.288	0.2787	-0.5521
Jd-majorite[6,7]	3.644(7)	178(4)	4.47(2)	-0.0138(3)	125(2)	1.29(5)	-0.0128(2)	0.1951	0.8089	-0.4972
Grossular[7,8]	3.605(2)	171.2(8)	4.47(2)	-0.0138(3)	107.4(2)	1.29(5)	-0.0128(2)	0.1951	0.8089	-0.4972
Almandine[9]	4.3188(2)	174.2(12)	4.61(14)	-0.0267(7)	94.9(7)	1.06(6)	-0.0131(8)	0.26(5)	2.3(14)	0
Coesite[10,11]	2.91(2)	106.5(6)	2.7(15)	-0.0016(16)	60.7(3)	0.33(5)	-0.0044(5)	0.106(14)	-0.028(166)	-0.48(12)
Stishovite[12,13]	4.381(2)	314	4.7(6)	-0.038(5)	221	2.0(3)	-0.025(2)	0.126(11)	1.29(17)	0
Quartz[14,15,16]	2.648	37.8	6.2(2)	-0.022	44.4	0.9(1)	-0.0036	0.1417	9.6581	-1.6973
Kyanite[17]	3.669	186(2)	7.2(6)	-0.023(2)	125(1)	2.3(2)	-0.017(1)	0.21	0	0
Hedenbergite[1,8,18]	3.657(1)	120(4)	4	-0.012(1)	62(2)	1.6(1)	-0.011(1)	0.298	0	0
Albite[8,19,20]	2.623(3)	51.7	4.7	-0.016	33.7	2.9	-0.01	0.2199	1.0271	-0.8714
Anorthite[8,19,20]	2.757(3)	87	4.7	-0.016	39	2.9	-0.01	0.1394	0.0597	0
Olivine[21,22]	3.348	129(2)	4.01(9)	-0.018(2)	78(2)	1.9(2) -0.105(9)*	-0.013(1)	0.3034	0.7422	0.5381
Orthopyroxene[23,24]	3.288(4)	113(1)	8.8(1) -0.68(6)*	-0.0263(3)	75.9(7)	2.9(1) -0.40(2)*	-0.0136(3)	0.297(16)	0.57(11)	0

1. Li and Neuville (2010) 2. Irifune et al. (2008) 3. Liu et al. (2000) 4. Sinogeikin and Bass (2002) 5. Suzuki and Anderson (1983) 6. Reichmann et al. (2002) 7. Gwanmesia et al. (2014) 8. Fei (1995) 9. Arimoto et al. (2015) 10. Chen et al. (2017) 11. Kulik et al. (2018) 12. Yang and Wu (2014) 13. Nishihara et al. (2005) 14. Ackerman and Sorrell (1974) 15. Wang et al. (2015) 16. Ohno et al. (2006) 17. Gaida et al. (2021) 18. Kandelin and Weidner (1988) 19. Brown et al. (2016) 20. Mookherjee et al. (2016) 21. Núñez-Valdez et al. (2013) 22. Zhang et al. (2018) 23. Zhang and Bass (2016) 24. Jackson et al. (2006).

* The second value represents the second pressure derivative.

Table VI.S3. Thermoelastic parameters of all the relevant mineral phases for calculating the density and velocity. The a_0, a_1 and a_2 are the thermal expansion parameters, defined in Fei (1995): $a(T)=a_0+a_1T+a_2T^{-2}$. The thermal expansion parameters for jadeite using equation in Hao et al. (2020). The parameters (except the thermal expansion parameters) for stishovite, pyrope and coesite are recalculated based on the values presented in Yang and Wu (2014), Irifune et al. (2008), and Chen et al. (2017), respectively. Due to the lack of data, the $\partial K_S/\partial T$ and $\partial G/\partial T$ for albite and anorthite are fixed as -0.016 GPa/K and -0.01 GPa/K, which are the averaged value of all the other minerals listed in the table. Some parameters are listed without uncertainties because the uncertainties were not reported in the references.

Reference

Ackermann, R. J., & Sorrell, C. A. (1974). Thermal expansion and the high–low transformation in quartz. I. High-temperature X-ray studies. *Journal of Applied Crystallography*, *7*(5), 461-467.

Arimoto, T., Gréaux, S., Irifune, T., Zhou, C., & Higo, Y. (2015). Sound velocities of Fe3Al2Si3O12 almandine up to 19 GPa and 1700 K. *Physics of the Earth and Planetary Interiors*, *246*, 1-8.

Brown, J. M., Angel, R. J., & Ross, N. L. (2016). Elasticity of plagioclase feldspars. *Journal of Geophysical Research: Solid Earth*, *121*(2), 663-675.

Chen, T., Liebermann, R. C., Zou, Y., Li, Y., Qi, X., & Li, B. (2017). Tracking silica in Earth's upper mantle using new sound velocity data for coesite to 5.8 GPa and 1073 K. *Geophysical Research Letters*, *44*(15), 7757-7765.

Fei, Y. (1995). Thermal expansion. In T. J. Ahrens *Mineral physics & crystallography: a handbook of physical constants* (Vol. 2, pp. 29-44). Washington, DC: American Geophysical Union.

Gaida, N. A., Gréaux, S., Kono, Y., Ohfuji, H., Kuwahara, H., Nishiyama, N., ... & Hasegawa, M. (2021). Elasticity of nanocrystalline kyanite at high pressure and temperature from ultrasonic and synchrotron X-ray techniques. *Journal of the American Ceramic Society*, *104*(1), 635-644.

Gwanmesia, G. D., Wang, L., Heady, A., & Liebermann, R. C. (2014). Elasticity and sound velocities of polycrystalline grossular garnet (Ca3Al2Si3O12) at simultaneous high pressures and high temperatures. *Physics of the Earth and Planetary Interiors*, *228*, 80-87.

Hao, M., Zhang, J. S., Pierotti, C. E., Zhou, W. Y., Zhang, D., & Dera, P. (2020). The seismically fastest chemical heterogeneity in the Earth's deep upper mantle—implications from the single-crystal thermoelastic properties of jadeite. *Earth and Planetary Science Letters*, *543*, 116345.

Irifune, T., Higo, Y., Inoue, T., Kono, Y., Ohfuji, H., & Funakoshi, K. (2008). Sound velocities of majorite garnet and the composition of the mantle transition region. *Nature*, *451*(7180), 814.

Jackson, J. M., Sinogeikin, S. V., & Bass, J. D. (2007). Sound velocities and single-crystal elasticity of orthoenstatite to 1073 K at ambient pressure. *Physics of the Earth and Planetary Interiors*, *161*(1-2), 1-12.

Kandelin, J., & Weidner, D. J. (1988b). Elastic properties of hedenbergite. Journal of Geophysical Research: Solid Earth, 93(B2), 1063-1072.

Kulik, E., Murzin, V., Kawaguchi, S., Nishiyama, N., & Katsura, T. (2018). Thermal expansion of coesite determined by synchrotron powder X-ray diffraction. *Physics and Chemistry of Minerals*, 1-9.

Li, B., & Neuville, D. R. (2010). Elasticity of diopside to 8 GPa and 1073 K and implications for the upper mantle. *Physics of the Earth and Planetary Interiors*, *183*(3-4), 398-403.

Liu, J., Chen, G., Gwanmesia, G. D., & Liebermann, R. C. (2000). Elastic wave velocities of pyrope–majorite garnets (Py62Mj38 and Py50Mj50) to 9 GPa. *Physics of the Earth and Planetary Interiors*, *120*(1-2), 153-163.

Mookherjee, M., Mainprice, D., Maheshwari, K., Heinonen, O., Patel, D., & Hariharan, A. (2016). Pressure induced elastic softening in framework aluminosilicate-albite (NaAlSi3O8). *Scientific reports*, *6*(1), 1-10.

Nishihara, Y., Nakayama, K., Takahashi, E., Iguchi, T., & Funakoshi, K. Ì. (2005). P-V-T equation of state of stishovite to the mantle transition zone conditions. *Physics and Chemistry of Minerals*, *31*(10), 660-670.

Núñez-Valdez, M., Wu, Z., Yu, Y. G., & Wentzcovitch, R. M. (2013). Thermal elasticity of (Fex, Mg1− x) 2SiO4 olivine and wadsleyite. *Geophysical Research Letters*, *40*(2), 290-294.

Ohno, I., Harada, K., & Yoshitomi, C. (2006). Temperature variation of elastic constants of quartz across the α-β transition. *Physics and Chemistry of Minerals*, *33*(1), 1-9.

Reichmann, H. J., Sinogeikin, S. V., Bass, J. D., & Gasparik, T. (2002). Elastic Moduli of Jadeite-Enstatite Majorite. *Geophysical research letters*, *29*(19).

Sinogeikin, S. V., & Bass, J. D. (2002). Elasticity of Majorite and a Majorite-Pyrope solid solution to high pressure: Implications for the Transition Zone. *Geophysical Research Letters*, *29*(2), 4-1.

Suzuki, I., & Anderson, O. L. (1983). Elasticity and thermal expansion of a natural garnet up to 1, 000K. *Journal of Physics of the Earth*, *31*(2), 125-138.

Wang, J., Mao, Z., Jiang, F., & Duffy, T. S. (2015). Elasticity of single-crystal quartz to 10 GPa. *Physics and Chemistry of Minerals*, *42*(3), 203-212.

Yang, R., & Wu, Z. (2014). Elastic properties of stishovite and the CaCl2-type silica at the mantle temperature and pressure: An ab initio investigation. *Earth and Planetary Science Letters*, *404*, 14-21.

Zhang, J. S., & Bass, J. D. (2016). Single-crystal elasticity of natural Fe-bearing orthoenstatite across a high-pressure phase transition. *Geophysical Research Letters*, *43*(16), 8473-8481.

Zhang, J. S., Bass, J. D., & Schmandt, B. (2018). The Elastic Anisotropy Change Near the 410-km Discontinuity: Predictions from Single-Crystal Elasticity Measurements of Olivine and Wadsleyite. *Journal of Geophysical Research: Solid Earth*, *123*(4), 2674-2684.

Chapter VII

The ultra-low viscosity of volatile-rich kimberlite magma

Abstract

The volatile-rich kimberlite magma originates from depths > 200 km in the Earth's interior. Study of the kimberlite magma formation and migration provides an important window to the volatile recycling processes in the deep Earth. Various simulation models have suggested the ultra-fast ascent speed during the eruption processes of kimberlite magma. However, the viscosity of kimberlite magma, which is crucial for understanding their migration in the deep Earth remains poorly constrained. In this study, we conducted in-situ falling-sphere viscometry experiments of kimberlite magma with different volatile contents (0-5 wt% H_2O and 2-8 wt% CO_2) up to 5.3 GPa 2173 K. The results show that volatiles, especially H_2O, can significantly decrease the viscosity of kimberlite magma. The viscosity of kimberlite magma is ~1-2 orders of magnitude lower than what was determined in previous studies and mid-ocean ridge basalt (MORB) under similar pressure-temperature conditions and comparable to the ultra-mobile pure carbonate melt. The updated viscosity data obtained in this study is also used for modeling the upwelling and eruption process of kimberlite magma.

Main text

Kimberlite magma, as the host of diamonds, is among the most important terrestrial magmas due to its volatile-rich nature and its ultra-deep origin (e.g., > 200 km; Wilson & Head Iii, 2007; Foley et al., 2019; Nickel & Green, 1985; Mitchell, 2013). They are excellent geochemical probes of the deep Earth (Pearson et al, 2019; Tappe et al., 2017). For example, the Mg/Si ratios of kimberlite magma and the mantle xenoliths embedded in can help to

constrain the chemical compositions of the local lithospheric mantle (Pearson et al., 2019). The similarity and differences of the trace elements (e.g., Ce/Pb and Ba/Nb) and radiogenic isotopes (e.g., $^{187}Os/^{188}Os$) between the kimberlite magma and ocean island basalts provide important information about different geochemical reservoirs (e.g., EM-1) in the Earth's interior (Pearson et al., 2019; Tappe et al., 2013; Araujo et al., 2001). Typical kimberlite magma originates from partial melting of CO_2-bearing peridotite (Dasgupta et al., 2013; Becker & Roex, 2006; Price et al., 2000) or subducted carbonated slab crust (Tappe et al., 2013; Sun & Dasgupta, 2019) at depths greater than ~200 km, possibly in the mantle transition zone (Foley et al., 2019; Sun & Dasgupta, 2019; Kiseeva et al., 2013).

Kimberlite samples collected in the field are geochemically complicated (Wilson & Head Iii, 2007; Pearson et al., 2019; Kamenetsky et al., 2009). In addition to the alteration process after the crystallization of kimberlite magma on the surface, the potential reactions between the kimberlite magma and the nearby rocks along its upwelling path can also be important. For example, the $^{87}Sr/^{86}Sr$ ratio difference between the group II and group I kimberlites can result from the interaction by the enriched geochemical reservoirs with the primitive kimberlite magma (Pearson et al., 2019; Smith et al., 1985). However, the extent of these chemical reactions during the kimberlite magma ascent and eruption process heavily depends on the migration speed of the kimberlite magma at depth.

Sparks et al. (2006) simulated the eruption process of kimberlite magma and suggested that a low enough viscosity would enable the extremely fast eruption process (e.g., ~5-20 m/s) under the turbulent regime. Wilson and Head Lii (2007) and Russell et al. (2012) also found that the CO_2 fluid or gas exsolved from the kimberlite magma at lower pressures could contribute to its fast magma ascent and eruption processes.

However, the viscosity of volatile-rich kimberlite magma is not experimentally well constrained. Previous in-situ falling-sphere viscometry experiments showed that the viscosities of calcite and dolomite melts were lower than 0.01 Pa·s (Kono et al., 2014a) which is more than an order of magnitude lower than that of MORB at similar pressure-temperature conditions. Considering the fact that typical kimberlite magma is CO_2-rich, its viscosity is likely low. However, a recent study using quenched falling sphere experiments found that the viscosity of kimberlite magma is comparable to or even higher than MORB under high pressure-temperature conditions and does not depend on the H_2O content (Persikov et al., 2017). Such high viscosity values do not support the fast ascent speed of kimberlite magma, as suggested by previous simulation models (Wilson & Head Iii, 2007; Sparks et al., 2006).

To fill in this knowledge gap, we conducted in-situ falling-sphere viscometry measurements of kimberlite magma with 2-8 wt% CO_2 and 0-5 wt% H_2O up to 5.3 GPa 2173 K using the Paris-Edinburgh cell at Sector 16-BM-B, HPCAT, Advanced Photon Source (Kono et al., 2014b; Figure VII.S5, Table VII.S1). The viscosity of kimberlite magma under different pressure-temperature conditions was calculated using the terminal velocities, which are the maximum sphere falling speeds determined from the X-ray images taken via a high-speed camera. Utilizing the viscosity data obtained in this study, we further modeled the kimberlite magma ascent and eruption processes starting at a depth of 220 km and extending to the Earth's surface.

The experimental results are summarized in Figure VII.1. Previous experiments on hydrous silicate melts have suggested that addition of H_2O could decrease the viscosities of silicate magmas by interacting with network-forming cations to depolymerize the magma (Robert et al., 2013; Whittington et al., 2009). This effect has been observed in this study as

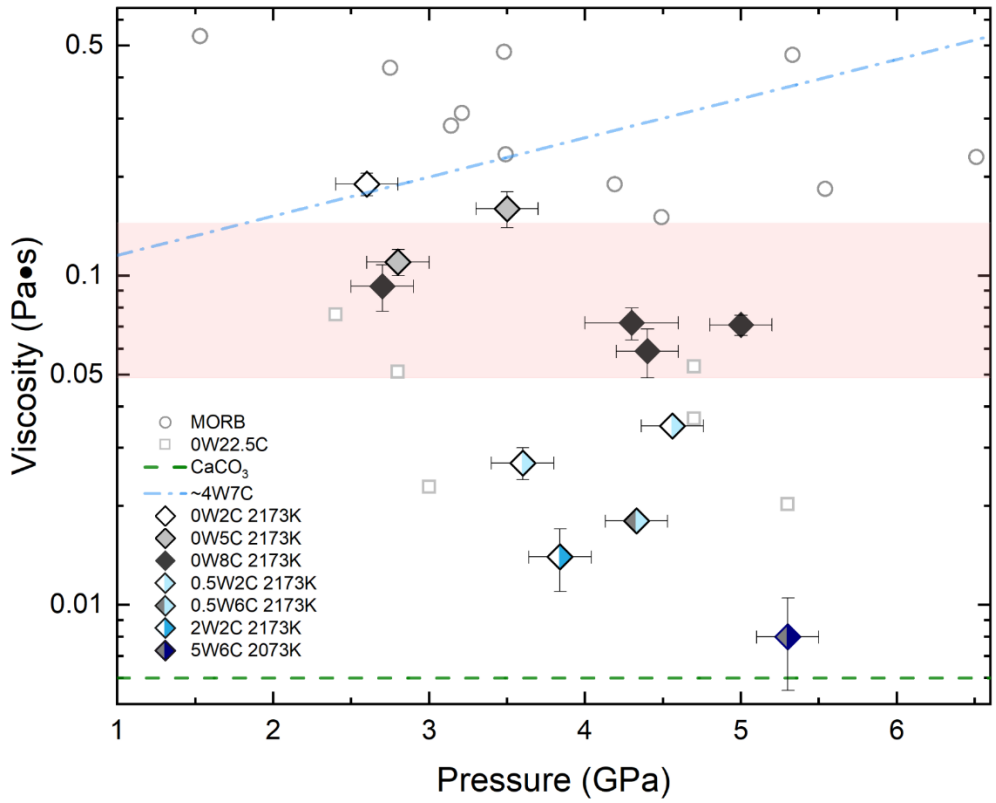

Figure VII.1. The viscosities of kimberlite, MORB, CaCO3, and carbonate-silicate transitional melts under high pressure-temperature conditions. The numbers before the "W" and "C" represent the wt% of the H_2O and CO_2 in the melts, respectively. The diamond symbols represent the viscosity values of kimberlite magmas with different CO_2 and H_2O contents measured in this study. The gray circles and squares represent the viscosity measurements of MORB (Sakamaki et al., 2013) and carbonate-silicate transitional melts with ~22.5 wt% CO_2 (Stagno et al., 2020), respectively. The blue dash-dotted line represents the viscosity values of kimberlite magma measured by the quenched experiments (Persikov et al., 2017). The green dash line represents the viscosity of pure carbonate melts (Kono et al., 2014a). The pink shaded area shows the critical viscosity value range at 2173 K to enable the turbulent flow regime during the kimberlite magma eruption process (Supporting Information Text VII.S1, VII.S3).

well. As shown in Figure VII.1, with only 0.5 wt% H_2O added, the viscosity of kimberlite magma decreases by a factor of ~6 from ~0.1-0.2 Pa·s to only 0.02-0.03 Pa·s. With 2 wt% of H_2O added, the viscosity of kimberlite magma decreases by more than an order of magnitude. When the H_2O content reaches 5 wt%, the viscosity of kimberlite magma is less than 0.01 Pa·s, which is close to that of pure carbonate melts (Kono et al., 2014a) at similar pressure-temperature conditions and on the same order of the viscosity of liquid water at ambient condition. Addition of CO_2 could also decrease the viscosity of kimberlite magma, which is consistent with the ultra-low viscosity values of pure carbonate and carbonate-silicate transitional melts reported in previous studies (Kono et al., 2014a; Stagno et al., 2020). However, our results indicate that H_2O has a stronger effect than CO_2. For example, with only 0.5 wt% H_2O and 2 wt% CO_2 added, the viscosity of kimberlite magma is similar to the anhydrous carbonate-silicate transitional melts with ~22.5 wt% CO_2 (Stagno et al., 20).

Persikov et al. (2017) is the only existing experimental study on the viscosity of hydrous kimberlite magma at high pressure-temperature conditions. The viscosity values presented in Persikov et al. (2017) are between 0.1-0.7 Pa·s which are comparable to the viscosity of MORB at similar pressure-temperature conditions determined using in-situ falling-sphere viscometry (Sakamaki et al., 2013). The viscosity of hydrous kimberlite magma determined in Persikov et al. (2017) is even higher than MORB at pressures higher than ~3.5 GPa. However, according to the experimental data we obtained in this study, which also used the in-situ falling-sphere viscometry method, the viscosity values of kimberlite magma with different volatile contents are always lower than MORB in the investigated pressure-temperature range (~2-5 GPa 2073-2173K). The significantly higher viscosity values reported in Persikov et al. (2017) may result from the lower velocities of falling spheres measured using

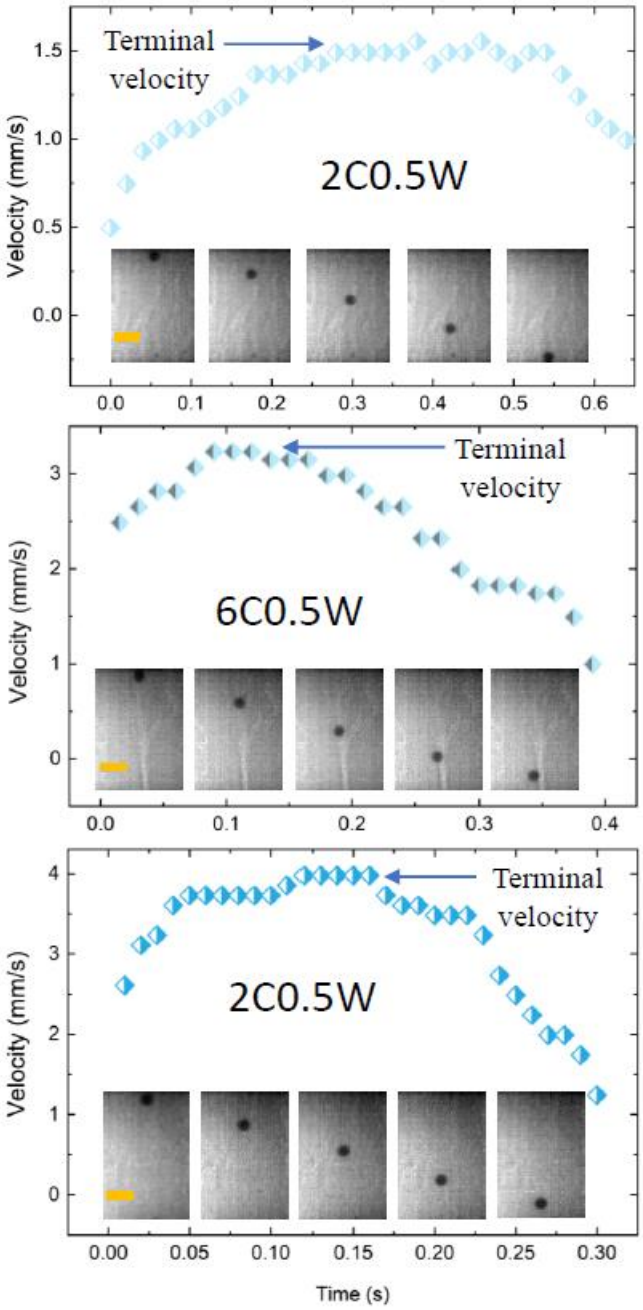

Figure VII.2. Movements of the Re spheres and the velocity evolution during the Falling-sphere viscosity measurements. The numbers before the "W" and "C" represent the wt% of the H_2O and CO_2 in the melts, respectively. All spheres reached terminal velocities during the experiments. The orange bars in the images represent 0.2 mm.

the quenched method. In the quenched experiments, the sphere falling process was not directly recorded, and thus the average sphere falling speed instead of the terminal velocity was obtained (Figure VII.2). As a result, the viscosity values calculated using the average sphere falling speeds determined in the quenched experiments are the upper limits rather than the true viscosity values of the liquids. In contrast, as shown in Figure VII.2, we can calculate the velocity change as a function of time during the entire sphere falling process from X-ray radiography images. Thus, we can accurately determine the terminal velocities, which are the maximum velocities reached for all experimental runs.

Previous kimberlite magma eruption models have suggested that the migration of kimberlite magma under turbulent flow regimes is required for its ultra-fast eruption (Sparks et al., 2006). The formation of turbulent flows during the kimberlite magma eruption is possible only if the effective magma viscosity is lower than a critical viscosity value of ~1-4 Pa·s (Sparks et al., 2006; Supporting Information Text VII.S3). As the ascending magma approaches the Earth's surface, crystals and bubbles formed through exsolution and fractional crystallization can significantly increase its effective viscosity (Persikov et al., 2018; Petford, 2009; Supporting Information Text VII.S1). Thus, the critical effective viscosity value of ~1-4 Pa·s for the near-surface crystal and bubble-bearing kimberlite magma corresponds to a corrected critical viscosity value of ~0.049-0.145 Pa·s of the bubble and crystal-free kimberlite magma under experimental conditions (Supporting Information Text VII.S1), as shown by the pink area in Figure VII.1. The corrected critical viscosity value of ~0.049-0.145 Pa·s is significantly lower than the viscosity of hydrous kimberlite magma determined in Persikov et al. (2017), but similar to the viscosity of CO_2-bearing but anhydrous kimberlite magma in this study. However, with a small amount of H_2O added, which is expected in natural primitive

kimberlite magma (Kamenetsky et al., 2009; Soltys et al., 2018; Kjarsgaard et al., 2009; Nielsen & Sand, 2008; Table VII.S1), the viscosity is consistently lower than the corrected critical viscosity (Figure VII.1), which ensures the turbulent flow regime during the kimberlite magma eruption process.

Utilizing the viscosity data of kimberlite magma obtained in this study, we calculated the kimberlite magma migration velocity change as a function of depth during its ascent and eruption process (Figure VII.3). The primitive kimberlite magma may originate from different mantle sources and thus carry different amounts of volatiles (e.g., the H_2O content varies from

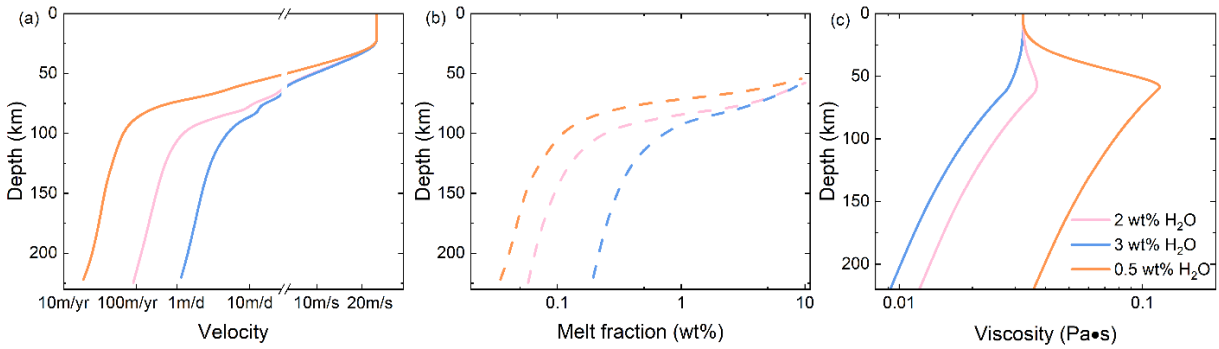

Figure VII.3. The kimberlite magma migration velocity, melt fraction, and viscosity change as a function of depth. (a) The ascent and eruption velocities calculated for kimberlite magma with 0.5 wt%, 2 wt%, and 3 wt% H_2O. The horizontal axes are in log scale. (b) The melt fractions change with depth from Dasgupta et al. (2013). (c) The kimberlite magma viscosity change with depth. The viscosity gradually increases from 220 km to ~50 km depth and then decreases again after the input of groundwater takes place. The final H_2O content in the erupted kimberlite magma ranges between 0.5 wt% to 8 wt% and depends on groundwater input. The final viscosity value of the erupted kimberlite magma at depths shallower than 50 km was calculated assuming an average H_2O content of ~5 wt% (Kamenetsky et al., 2009).

~0.5 wt% to ~8 wt%; Table VII.S1). It is hard to constrain the exact CO_2 content in the primitive kimberlite magma, and the effect of CO_2 on the viscosity of kimberlite magma is not as strong as H_2O. Thus, as shown in Figure VII.4, we assumed that the CO_2 content gradually decreases from >20 wt% (Dasgupta et al., 2013; Russell et al., 2012) in the primitive kimberlite magma at ~200 km depth to ~6 wt% in the erupted kimberlite magma at the Earth's surface (Kamenetsky et al., 2009). We focus on three different primitive kimberlite magma compositions with different H_2O contents which originate from different reservoirs in the Earth's mantle: 1. primitive kimberlite magma with 2 wt% of H_2O originated from the ambient

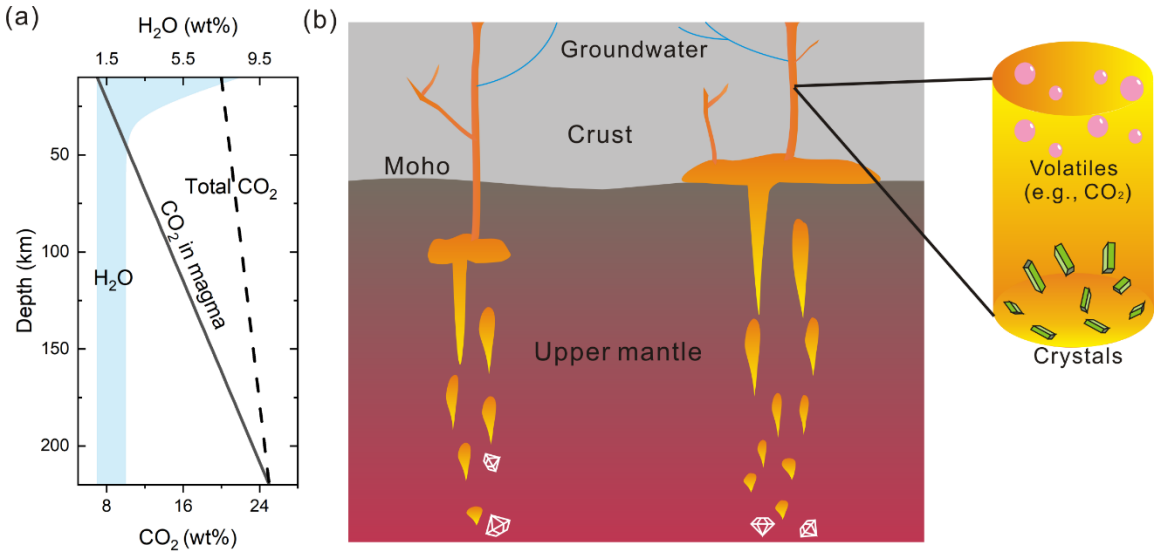

Figure VII.4. Kimberlite magma ascent, evolution, and eruption process. (a) The depth dependent CO_2 and H_2O content. The H_2O content is shown by the blue area. The dashed and solid black lines represent the total CO_2 content in the system (including the dissolved CO_2 in magma and the exsolved CO_2 fluid or gas) and CO_2 content in magma, respectively (Russell et al., 2012; Dasgupta et al., 2013). (b) Schematic illustration of the kimberlite magma ascent and eruption process. The ascent velocity will gradually increase from the source mantle to the magma chamber. Then the magma erupts to the surface with crystals and bubbles.

mantle with ~200 ppm H_2O (Masuti et al., 2016; Wang et al., 2008); 2. primitive kimberlite magma with 0.5 wt% of H_2O originated from volatile-depleted regions in the mantle with ~50 ppm H_2O; 3. primitive kimberlite magma with 3 wt% of H_2O originated from a volatile-enriched reservoir in the mantle with ~300 ppm H_2O. Because of the negligible pressure dependence of the H_2O partitioning coefficient between melts and upper mantle minerals (Hirschmann et al., 2009) and the lack of the experimental constraint on the H_2O content in primitive kimberlite magma, the H_2O content is assumed to be constant before it approaches shallower depth where the groundwater input could be significant (Figure VII.4). The change of melt fraction as a function of depth is directly adopted from previous experiments (Figure VII.3; Dasgupta et al., 2013). The detailed calculation procedures for the ascent and eruption velocities are shown in Supporting Information Text VII.S1-VII.S3.

Figure VII.3 shows the calculated viscosities as well as the ascent and eruption velocities of kimberlite magma with different H_2O contents that originate from different regions in the mantle. It is clear that the kimberlite magma sourced from a hydrated mantle reservoir with relatively low viscosity values ascends much faster at the level of 400-1600 m/yr compared with only 20-60 m/yr for the kimberlite magma that originates from the volatile-poor regions in the Earth's interior. As shown in Figure VII.3a, from the source mantle to ~100 km depth, the melt fraction gradually increases[9], which is expected due to decompression melting. The CO_2-enriched melts will also gradually react with the silicate upper mantle and release the low-density CO_2 fluid (Russell et al., 2012), which further increases the density contrast between kimberlite magma and the upper mantle (Supporting Information Text VII.S2). The increase of melt fraction and density contrast can speed up the magma ascent process (McKenzie, 1989; von Bargen & Waff, 1986). For the kimberlite magma originated

from the relatively dry mantle, because of the low melt fraction and the relatively high viscosity, the ascent velocities (~20-60 m/yr at 200-100 km depth) are the lowest. For the kimberlite magma originated from moderately or highly hydrated part of the mantle, the ascent velocities are ~90-370 m/yr and ~400-1600 m/yr, respectively, from 200-100 km depth. Overall, the kimberlite magma ascent velocity is much higher than that of the basaltic magma constrained from isotopes (~10 m/yr; Richardson & McKenzie, 1994; Rubin & Macdougall, 1988) because of the ultra-low viscosity of kimberlite magma (Figure VII.3c). When the kimberlite magma reaches ~100 km depth, the ascent velocities increase from ~1 m/d to >100 m/d at the uppermost mantle depths range due to the high melt fractions (Figure VII.3b).

The eruption process of kimberlite magma is likely similar to other silicate magmas. Before the final eruption takes place, kimberlite magma gradually ascends and accumulates at the bottom of the crust or in the uppermost mantle forming a primitive magma chamber (Figure VII.4; Huppert & Sparks, 1981). During the final stage of eruption (depths < 50 km), the exsolved CO_2 bubbles and crystals in the kimberlite magma will increase the effective viscosity (Figure VII.4; Persikov et al., 2018; Petford, 2009). However, the groundwater may also enter the magma chamber through faults or fractures (Figure VII.4; Buttner et al., 1999; Kamenetsky et al., 2014), which would significantly decrease the viscosity of the magma. The magma migration speed in the final eruption stage is fast (~20 m/s), but less constrained due to the combined effect from these two competing processes.

To sum up, in this study, we measured the viscosity of volatile-rich kimberlite magma, which is 1 to 2 orders lower than previous studies (Sparks et al., 2006; Persikov et al., 2017). Based on the viscosity data of kimberlite magma measured in this study, we modeled its fast ascent and eruption process. The rapid ascent and eruption of kimberlite magma could help to

preserve the high-pressure mineral phases (e.g., ringwoodite) in the super-deep diamonds (Pearson et al., 2014; Walter et al., 2011) as well as the major elements, trace elements, and isotope signatures of the local mantle sampled by the xenoliths (Peslier et al., 2008).

Methods

Different oxides, carbonates, and hydroxides with purity > 99% were mixed according to the compositions shown in Extended Data Table 1 as starting materials (Kamenetsky et al., 2009). The high pressure-temperature in-situ falling sphere experiments were carried out at Sector 16-BM-B, HPCAT, Advanced Photon Source using Paris-Edinburgh cell with graphite capsules (Kono et al., 2014b), with 1.5 mm in diameter and 2.0 mm in height (Figure VII.S5). The temperatures were calculated from the pre-calibrated power-temperature curves and the pressures were determined using the equation of state of MgO (Kono et al., 2014b). The volatile contents of the quenched samples were re-examined using Thermal Fisher Continuum microscope with the Nicolet Nexus 670 Fourier Transform Infrared Spectrometer at the University of New Mexico after the completion of experiments (Figure VII.S6; Mercier et al., 2010). Due to the ultra-fast nature of these falling-sphere experiments, the volatile loss was negligible.

Parallel beam polychromatic X-rays were used for imaging the sample chamber (Figure VII.2). A high-speed camera (Photron FASTCAM SA3) with 1000 frames per second was used to capture the sample chamber images during the sphere falling process. A WC sphere with a 497 μm diameter was used to calibrate the size of the pixels of the camera. Re spheres with diameters of ~80-190 μm were used to do falling-sphere viscometry measurements. The position of the Re spheres recorded by the high-speed camera was analyzed by ImageJ software to calculate sphere falling speeds. The terminal velocities (v), which are the maximum sphere

falling speeds, are calculated from the velocity-time curves (Figure VII.2). The viscosity (η) was calculated with the Stokes equation outlined in Kono et al. (2014b):

$$\eta = \frac{g d_s^2 (\rho_s - \rho_l) F}{18 v E} \tag{VII.1}$$

$$F = 1 - 2.104\left(\frac{d_s}{d_l}\right) + 2.09\left(\frac{d_s}{d_l}\right)^3 - 0.95\left(\frac{d_s}{d_l}\right)^5 \tag{VII.2}$$

$$E = 1 + \frac{9 d_s}{16 Z} + (\frac{9 d_s}{16 Z})^2 \tag{VII.3}$$

where g is gravitational acceleration, d and ρ are diameters and densities of the sphere (s) and liquid (l). Z is the height of the sample capsule.

Acknowledgments

This work was supported by WeR1 Faculty Success Fund from the University of New Mexico (J. S. Z.). The experiments were performed at HPCAT (Sector 16), Advanced Photon Source (APS), Argonne National Laboratory. HPCAT operation is supported by DOE-NNSA under Award No. DE-NA0001974, with partial instrumentation funding from NSF. The Advanced Photon Source is a U.S. Department of Energy (DOE) Office of Science User Facility operated for the DOE Office of Science by Argonne National Laboratory under Contract No. DE-AC02-06CH11357.

References

Araujo, Ana, et al. "Petrology of kamafugites and kimberlites from the Alto Paranaiba alkaline province, Minas Gerais, Brazil." *Contributions to Mineralogy and Petrology* 142.2 (2001): 163-177.

Becker, Megan, and Anton P. Le Roex. "Geochemistry of South African on-and off-craton, Group I and Group II kimberlites: petrogenesis and source region evolution." *Journal of Petrology* 47.4 (2006): 673-703.

Büttner, Ralf, Pierfrancesco Dellino, and Bernd Zimanowski. "Identifying magma–water interaction from the surface features of ash particles." *Nature* 401.6754 (1999): 688-690.

Dasgupta, Rajdeep, et al. "Carbon-dioxide-rich silicate melt in the Earth's upper mantle." *Nature* 493.7431 (2013): 211-215.

Foley, Stephen F., Gregory M. Yaxley, and Bruce A. Kjarsgaard. "Kimberlites from source to surface: insights from experiments." *Elements: An International Magazine of Mineralogy, Geochemistry, and Petrology* 15.6 (2019): 393-398.

Hirschmann, Marc M., et al. "Dehydration melting of nominally anhydrous mantle: The primacy of partitioning." *Physics of the Earth and Planetary Interiors* 176.1-2 (2009): 54-68.

Huppert, Herbert E., and R. Stephen J. Sparks. "The fluid dynamics of a basaltic magma chamber replenished by influx of hot, dense ultrabasic magma." *Contributions to Mineralogy and Petrology* 75.3 (1981): 279-289.

Kamenetsky, Vadim S., et al. "How unique is the Udachnaya-East kimberlite? Comparison with kimberlites from the Slave Craton (Canada) and SW Greenland." *Lithos* 112 (2009): 334-346.

Kamenetsky, Vadim S., et al. "Towards a new model for kimberlite petrogenesis: Evidence from unaltered kimberlites and mantle minerals." *Earth-Science Reviews* 139 (2014): 145-167.

Kiseeva, Ekaterina S., et al. "Melting and phase relations of carbonated eclogite at 9–21 GPa and the petrogenesis of alkali-rich melts in the deep mantle." *Journal of Petrology* 54.8 (2013): 1555-1583.

Kjarsgaard, B. A., et al. "Geochemistry of hypabyssal kimberlites from Lac de Gras, Canada: comparisons to a global database and applications to the parent magma problem." *Lithos* 112 (2009): 236-248.

Kono, Yoshio, et al. "Ultralow viscosity of carbonate melts at high pressures." *Nature Communications* 5.1 (2014a): 1-8.

Kono, Yoshio, et al. "Toward comprehensive studies of liquids at high pressures and high temperatures: Combined structure, elastic wave velocity, and viscosity measurements in the Paris–Edinburgh cell." Physics of the Earth and Planetary Interiors 228 (2014b): 269-280.

Masuti, Sagar, et al. "Upper-mantle water stratification inferred from observations of the 2012 Indian Ocean earthquake." *Nature* 538.7625 (2016): 373-377.

McKenzie, Dan. "Some remarks on the movement of small melt fractions in the mantle." *Earth and planetary science letters* 95.1-2 (1989): 53-72.

Mercier, M., Di Muro, A., Métrich, N., Giordano, D., Belhadj, O., & Mandeville, C. W. (2010). Spectroscopic analysis (FTIR, Raman) of water in mafic and intermediate glasses and glass inclusions. *Geochimica et Cosmochimica Acta*, *74*(19), 5641-5656.

Mitchell, Roger H. *Kimberlites: mineralogy, geochemistry, and petrology*. Springer Science & Business Media, 2013.

Nickel, K. G., and D. H. Green. "Empirical geothermobarometry for garnet peridotites and implications for the nature of the lithosphere, kimberlites and diamonds." *Earth and Planetary Science Letters* 73.1 (1985): 158-170.

Nielsen, Troels FD, and Karina K. Sand. "The Majuagaa kimberlite dike, Maniitsoq region, West Greenland: constraints on an Mg-rich silicocarbonatitic melt composition from groundmass mineralogy and bulk compositions." *The Canadian Mineralogist* 46.4 (2008): 1043-1061.

Pearson, D. G., et al. "Hydrous mantle transition zone indicated by ringwoodite included within diamond." *Nature* 507.7491 (2014): 221-224.

Pearson, D. Graham, Jon Woodhead, and Philip E. Janney. "Kimberlites as geochemical probes of Earth's mantle." *Elements: An International Magazine of Mineralogy, Geochemistry, and Petrology* 15.6 (2019): 387-392.

Persikov, E. S., P. G. Bukhtiyarov, and A. G. Sokol. "Viscosity of hydrous kimberlite and basaltic melts at high pressures." *Russian Geology and Geophysics* 58.9 (2017): 1093-1100.

Persikov, Eduard S., Pavel G. Bukhtiyarov, and Alexander G. Sokol. "Viscosity of haplokimberlitic and basaltic melts at high pressures: Experimental and theoretical studies." *Chemical Geology* 497 (2018): 54-63.

Peslier, Anne H., Alan B. Woodland, and John A. Wolff. "Fast kimberlite ascent rates estimated from hydrogen diffusion profiles in xenolithic mantle olivines from southern Africa." *Geochimica et Cosmochimica Acta* 72.11 (2008): 2711-2722.

Petford, Nick. "Which effective viscosity?." *Mineralogical Magazine* 73.2 (2009): 167-191.

Price, S. E., J. K. Russell, and M. G. Kopylova. "Primitive magma from the Jericho Pipe, NWT, Canada: constraints on primary kimberlite melt chemistry." *Journal of Petrology* 41.6 (2000): 789-808.

Richardson, C., and D. McKenzie. "Radioactive disequilibria from 2D models of melt generation by plumes and ridges." *Earth and Planetary Science Letters* 128.3-4 (1994): 425-437.

Robert, Geneviève, et al. "The effect of water on the viscosity of a synthetic calc-alkaline basaltic andesite." *Chemical Geology* 346 (2013): 135-148.

Rubin, K. H., and J. D. Macdougall. "226 Ra excesses in mid-ocean-ridge basalts and mantle melting." *Nature* 335.6186 (1988): 158-161.

Russell, James K., et al. "Kimberlite ascent by assimilation-fuelled buoyancy." *Nature* 481.7381 (2012): 352-356.

Sakamaki, Tatsuya, et al. "Ponded melt at the boundary between the lithosphere and asthenosphere." *Nature Geoscience* 6.12 (2013): 1041-1044.

Smith, C. B., et al. "Geochemical character of southern African kimberlites: a new approach based on isotopic constraints." *Transactions of the Geological Society of South Africa* 88.2 (1985): 267-280.

Soltys, Ashton, Andrea Giuliani, and David Phillips. "A new approach to reconstructing the composition and evolution of kimberlite melts: a case study of the archetypal Bultfontein kimberlite (Kimberley, South Africa)." *Lithos* 304 (2018): 1-15.

Sparks, R. S. J., et al. "Dynamical constraints on kimberlite volcanism." *Journal of Volcanology and Geothermal Research* 155.1-2 (2006): 18-48.

Stagno, Vincenzo, et al. "The Viscosity of Carbonate-Silicate Transitional Melts at Earth's Upper Mantle Pressures and Temperatures, Determined by the In Situ Falling-Sphere Technique." *Carbon in Earth's Interior* (2020): 223-236.

Sun, C., & Dasgupta, R. (2019). Slab–mantle interaction, carbon transport, and kimberlite generation in the deep upper mantle. *Earth and Planetary Science Letters*, *506*, 38-52.

Tappe, Sebastian, et al. "Mantle transition zone input to kimberlite magmatism near a subduction zone: origin of anomalous Nd–Hf isotope systematics at Lac de Gras, Canada." *Earth and Planetary Science Letters* 371 (2013): 235-251.

Tappe, Sebastian, et al. "Sources and mobility of carbonate melts beneath cratons, with implications for deep carbon cycling, metasomatism and rift initiation." *Earth and Planetary Science Letters* 466 (2017): 152-167.

von Bargen, Nikolaus, and Harve S. Waff. "Permeabilities, interfacial areas and curvatures of partially molten systems: results of numerical computations of equilibrium microstructures." *Journal of Geophysical Research: Solid Earth* 91.B9 (1986): 9261-9276.

Wang, Duojun, et al. "The electrical conductivity of upper-mantle rocks: water content in the upper mantle." *Physics and Chemistry of Minerals* 35.3 (2008): 157-162.

Walter, M. J., et al. "Deep mantle cycling of oceanic crust: evidence from diamonds and their mineral inclusions." *Science* 334.6052 (2011): 54-57.

Whittington, Alan G., et al. "The viscosity of hydrous dacitic liquids: implications for the rheology of evolving silicic magmas." *Bulletin of Volcanology* 71.2 (2009): 185-199.

Wilson, Lionel, and James W. Head Iii. "An integrated model of kimberlite ascent and eruption." *Nature* 447.7140 (2007): 53-57.

Supporting Information

Text VII.S1. Calculation of the (effective) viscosity during magma ascent and eruption process

Assuming the viscosity of all silicate melts at infinite temperature is $10^{-4.6}$ Pa·s, the temperature effects of the viscosity were calculated by fitting the equation (Persikov et al., 2018; Giordano et al., 2008):

$$log\eta = 1000b/T - 4.6 \quad \text{(VII.S1)}$$

where T is temperature and b is a numerical constant, which can be fitted by the experimental results. According to our results and previous studies (Stagno et al., 2020), pressure has subtle influences on the viscosity of kimberlite magma. Therefore, we did not consider the pressure effects in the model presented in this study.

During the kimberlite magma eruption process, the exsolved volatile bubbles and crystals also affect the effective viscosity (η_e) and the η_e can be estimated by (Persikov et al., 2018):

$$\eta_e = \eta_0(1 - V_c)^{-3.35} \quad \text{(VII.S2)}$$

$$\eta_e = \eta_0(1 - 1.5V_b)^{-0.55} \quad \text{(VII.S3)}$$

where η_0 is the viscosity of the pure liquid and V_c and V_b are the volume fractions of the crystals and bubbles, respectively. Utilizing the data presented in Stagno et al. (2020) and this study, the effects of CO_2 content on the viscosity of anhydrous kimberlite magma (η_a) at 2173 K are fitted to the empirical equation:

$$\eta_a = 0.2744x^{0.547} \quad \text{(VII.S4)}$$

where x is the weight percentage of the CO_2. For the effects of H_2O content (0-5 wt%) on the viscosity of magma at 2173 K, the fitting based on the data in this study to empirical equation yields:

$$\eta = \frac{\eta_a}{11.624\ln(y+1)+1.07} \quad \text{(VII.S5)}$$

where y is the weight percentage of H_2O.

We firstly utilized empirical equations (VII.S4) and (VII.S5) to calculate the viscosity of volatile-rich kimberlite magma at 2173 K. Then equation (VII.S1) is used for temperature correction. In this study, we adopted an adiabatic geotherm with a potential temperature of 1350 ℃ (Dasgupta et al., 2013). Equations (VII.S2) and (VII.S3) are used to calculate the final effective viscosity for bubble and crystal-bearing kimberlite magma when needed.

Text VII.S2. Calculation of kimberlite magma ascent velocities

The magma ascent velocities in the Earth's mantle are calculated by (McKenzie et al., 1989):

$$k = \frac{a^2\varphi^n}{C} \quad \text{(VII.S6)}$$

$$v = \frac{k\Delta\rho g}{\eta\varphi} \quad \text{(VII.S7)}$$

where k is the permeability, a is the grain size, φ is the melt fraction, n and C are numerical constant, $\Delta\rho$ is the density contrast, g is gravitational acceleration, and η is the viscosity. In this study, we assumed a grain size of 5 mm and adopted the melt fractions from previous experimental studies on hydrous carbonated peridotite (Dasgupta et al., 2013). The n and C are fixed to be 2 and 1600, respectively, when melt fractions are less than 3 wt% (von Bargen &

Waff, 1986) and 3 and 100, respectively, when melt fractions exceed 3 wt% (McKenzie et al., 1989). The density of the ascent kimberlite magma is calculated using the density of the released CO_2 fluid (Russell et al., 2012) with the density of the original kimberlite magma (Persikov et al., 2018). Comparing the calculated density of the kimberlite magma with the ambient mantle density obtained from the PREM model (Dziewonski & Anderson, 1981), the density contrast increases from ~400 kg/m^3 to ~ 1150 kg/m^3 from ~220 km depth to the top of the mantle (~50 km). The viscosity calculations procedures are shown in Text VII.S1.

Text VII.S3. Calculation of kimberlite magma eruption velocities

The viscosity is a key factor affecting the kimberlite eruption process in the dykes, which controls the flow regime. When the viscosity is lower than the critical viscosity (η_c), the flow will be in the turbulent regime (Sparks et al., 2006). η_c can be calculated by:

$$\eta_c = \left(\frac{2\Delta P \rho w^3}{3hRe}\right)^{0.5} \quad \text{(VII.S8)}$$

where ΔP is the overpressure, ρ is the density of the magma, w is the width of the dyke, h is the vertical length of the dyke, and Re is Reynolds number. If the Re is high (>1000), then the flow will be in the turbulent regime. Assuming ΔP = 10 MPa, ρ = 2700 kg/m^3, w = 0.2-0.5 m, h = 100 km, and Re = 1000 (Persikov et al., 2018; Sparks et al., 2006), the critical viscosity is ~1-4 Pa·s, which is the effective viscosity of the crystal and bubble-bearing kimberlite magma during the eruption. Assuming 20 vol% of crystals and bubbles existed in the erupting magma, the viscosity at 2173 K is only ~0.049-0.145 Pa·s in the corresponding primitive kimberlite magma which are bubble and crystal-free.

The eruption velocities (u) of kimberlite magma in the turbulent regime are calculated by:

$$u = 7.7g\Delta\rho\left(\frac{w^5}{\eta(\rho g\Delta\rho)^3}\right)^{1/7}. \quad \text{(VII.S9)}$$

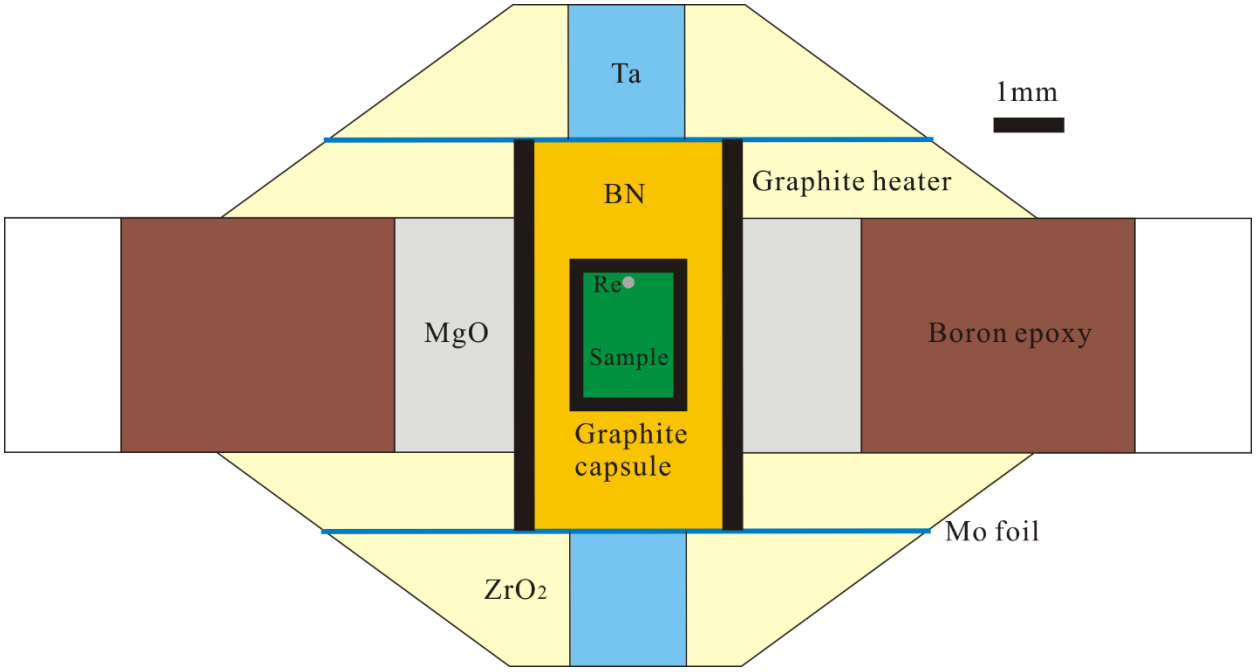

Figure VII.S5. Schematic illustration of the Paris-Edinburgh cell assembly used in this study (Kono et al., 2014).

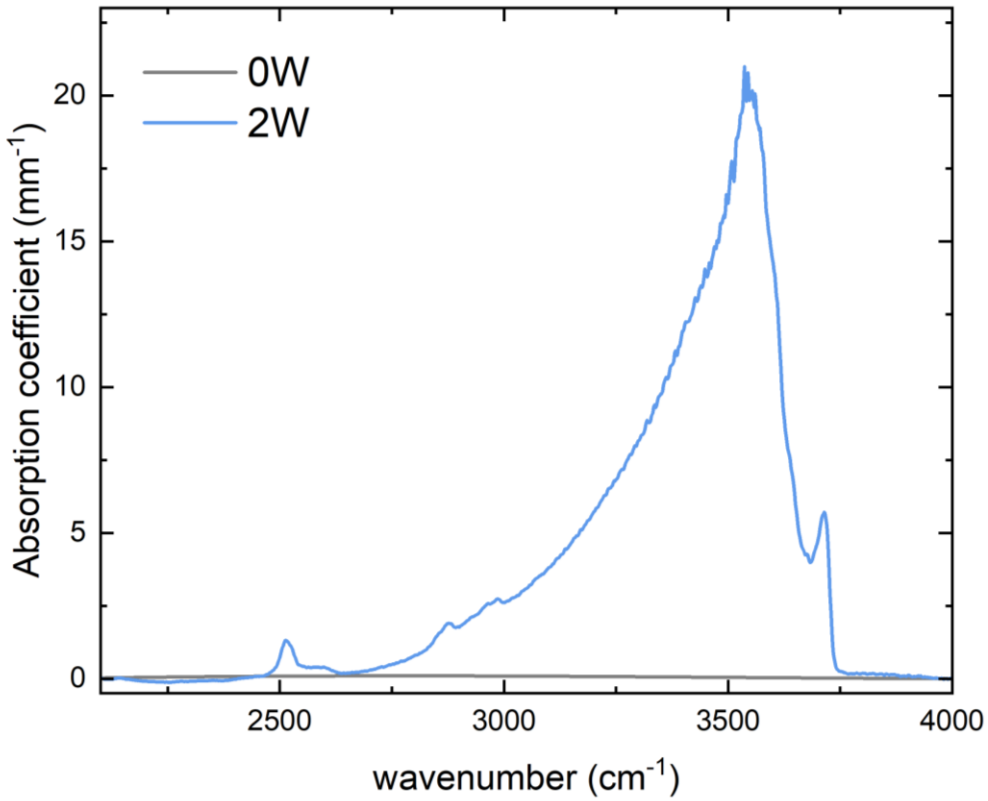

Figure VII.S6. Typical Fourier Transform Infrared spectra of the quenched run products collected using the Thermal Fisher Continuum microscope with the Nicolet Nexus 670 spectrometer at the laser spectroscopy lab at the University of New Mexico. The spectra were collected from 2100 cm^{-1} to 4000 cm^{-1} using an IR light source, a CaF_2 beam splitter and an MCT-A cooled using liquid nitrogen. The H_2O content of the anhydrous sample is under the detection limit. The H_2O content of the hydrous samples was calculated using the calibration of basalt[43], due to the lack of the specific calibration for kimberlite. The calculated H_2O content of the hydrous sample containing 2 wt% H_2O in the starting materials shown in this figure is ~2.1(1) wt%, suggesting negligible loss of water during the experiments.

	South Africa (Soltys et al., 2018)		Canada (Kjarsgaard et al., 2009)		Greenland (Nielsen & Sand, 2008)		Russia (Kamenetsky et al., 2009)			Natural kimberlite sample composition Range (Kamenetsky et al., 2009)	This study
	kimberlite	primitive melts	kimberlite	primitive melts	kimberlite	primitive melts	low H_2O	high H_2O	primitive melts		
SiO_2	30.1-31.6	25.5-26.9	32.46	27.5-31.8	25.84	17.47	26.71	29.29	-	25.6-40	31.3
TiO_2	1.1-1.3	1.4-1.7	0.6	0.7-1.1	3.62	4.99	1.25	1.27	-	0.3-3.6	1.4
Al_2O_3	1.2-1.4	1.1-1.3	2.01	2.5-3.1	1.42	2.27	1.75	1.79	-	1.4-3.0	2.1
FeO	9.1-9.5	9.2-9.7	7.59	7.3-8.3	10.32	10.61	8.09	8.34	-	6.6-10.3	8.3
MgO	31.2-33.8	25.4-27.6	34.28	27.5-30.8	33.36	23.98	31.33	33.14	-	25.2-38.6	32.5
CaO	10.4-12.0	16.7-18.6	8.34	9.2-14.2	10.72	17.27	12.19	11.84	-	4.1-12.2	9.2
Na_2O	0.2	0.2-0.3	0.07	0.1	0.09	0.13	3.23	0.31	6.2	0.1-3.2	0.52
K_2O	0.8-1.0	0.7-0.9	0.72	0.6-1.0	0.2	0.32	1.33	1.01	-	0.2-1.5	0.96
H_2O	2.3-2.7	3.0-3.5	6.54	6.1-8.7	-	-	0.38	2.84	<1	0.4-7.8	0-5
CO_2	6.8-8.3	9.3-11.2	6.07	5.1-12.2	-	-	9.42	7.96	-	2.6-9.4	2-8

Table VII.S1. The chemical compositions of different kimberlite samples and their corresponding primitive kimberlite melts. The last two columns show the composition range of natural kimberlite samples and composition of the samples used in this study. We adopted the average major element compositions of the kimberlite samples from different locations (Kamenetsky et al., 2009).

References

Dasgupta, Rajdeep, et al. "Carbon-dioxide-rich silicate melt in the Earth's upper mantle." *Nature* 493.7431 (2013): 211-215.

Dziewonski, Adam M., and Don L. Anderson. "Preliminary reference Earth model." *Physics of the earth and planetary interiors* 25.4 (1981): 297-356.

Giordano, Daniele, James K. Russell, and Donald B. Dingwell. "Viscosity of magmatic liquids: a model." *Earth and Planetary Science Letters* 271.1-4 (2008): 123-134.

Kamenetsky, Vadim S., et al. "How unique is the Udachnaya-East kimberlite? Comparison with kimberlites from the Slave Craton (Canada) and SW Greenland." *Lithos* 112 (2009): 334-346.

Kjarsgaard, B. A., et al. "Geochemistry of hypabyssal kimberlites from Lac de Gras, Canada: comparisons to a global database and applications to the parent magma problem." *Lithos* 112 (2009): 236-248.

Kono, Yoshio, et al. "Ultralow viscosity of carbonate melts at high pressures." *Nature Communications* 5.1 (2014): 1-8.

McKenzie, Dan. "Some remarks on the movement of small melt fractions in the mantle." *Earth and planetary science letters* 95.1-2 (1989): 53-72.

Mercier, Maxime, et al. "Spectroscopic analysis (FTIR, Raman) of water in mafic and intermediate glasses and glass inclusions." *Geochimica et Cosmochimica Acta* 74.19 (2010): 5641-5656.

Nielsen, Troels FD, and Karina K. Sand. "The Majuagaa kimberlite dike, Maniitsoq region, West Greenland: constraints on an Mg-rich silicocarbonatitic melt composition from groundmass mineralogy and bulk compositions." *The Canadian Mineralogist* 46.4 (2008): 1043-1061.

Persikov, Eduard S., Pavel G. Bukhtiyarov, and Alexander G. Sokol. "Viscosity of haplokimberlitic and basaltic melts at high pressures: Experimental and theoretical studies." *Chemical Geology* 497 (2018): 54-63.

Russell, James K., et al. "Kimberlite ascent by assimilation-fuelled buoyancy." *Nature* 481.7381 (2012): 352-356.

Soltys, Ashton, Andrea Giuliani, and David Phillips. "A new approach to reconstructing the composition and evolution of kimberlite melts: a case study of the archetypal Bultfontein kimberlite (Kimberley, South Africa)." *Lithos* 304 (2018): 1-15.

Sparks, R. S. J., et al. "Dynamical constraints on kimberlite volcanism." *Journal of Volcanology and Geothermal Research* 155.1-2 (2006): 18-48.

Stagno, Vincenzo, et al. "The Viscosity of Carbonate-Silicate Transitional Melts at Earth's Upper Mantle Pressures and Temperatures, Determined by the In Situ Falling-Sphere Technique." *Carbon in Earth's Interior* (2020): 223-236.

von Bargen, Nikolaus, and Harve S. Waff. "Permeabilities, interfacial areas and curvatures of partially molten systems: results of numerical computations of equilibrium microstructures." *Journal of Geophysical Research: Solid Earth* 91.B9 (1986): 9261-9276.